Transcostal focused ultrasound surgery

treatment through the ribcage

Jing Gao

2012

University of Dundee

Transcostal Focused Ultrasound Surgery: Treatment through the Ribcage

by

JING GAO

A Thesis Submitted in Fulfilment of the Requirements of the University of Dundee for the Degree of Doctor of Philosophy (Ph.D.) in Mechanical Engineering.

August 2012

TABLE OF CONTENTS

DECLARATION

I hereby declare that this thesis has been compiled by myself, that it is a record of work completed by myself and that it has not previously been accepted for a higher degree at this University or any other institution of learning.

…………………………..

Jing Gao

CERTIFICATE

This is to certify that Jing Gao has done this research under my supervision and that she has fulfilled the conditions of Ordinance 39 of the University of Dundee, so that she is qualified to submit for the Degree of Doctor of Philosophy.

…………………………..

Dr. Zhihong Huang

The School of Engineering, Physics and Mathematics

COPYRIGHT

The copyright of this thesis submitted to the degree of Doctor of Philosophy (Ph.D.) belongs to the School of Engineering, Physics and Mathematics, University of Dundee, Dundee, United Kingdom, DD1 4HN.

ACKNOWLEDGEMENTS

ABSTRACT

Two issues hindering the clinical application of image-guided transcostal focused ultrasound surgery (FUS) are the organ motion caused by cardiac and respiratory movements and the presence of the ribcage. Intervening ribs absorb and reflect the majority of ultrasound energy excited by an acoustic source, resulting in insufficient energy delivered to the target organs of the liver, kidney, and pancreas. Localized hot spots also exist at the interfaces between the ribs and soft tissue and in highly absorptive regions such as the skin. The aim of this study is to assess the effects of transmitted beam distortion and frequency-dependent rib heating during trans-costal FUS, and to propose potential solutions to reduce the side effects of rib heating and increase ultrasound efficacy.

Direct measurements of the transmitted beam propagation were performed on a porcine rib cage phantom, an epoxy rib cage phantom and an acoustic absorber rib cage phantom, in order of their similarities to the human rib cage. Finite element analysis was used to investigate the rib cage geometry, the position of the target tissue relative to the rib cage, and the geometry and operating frequency of the transducer. Of particular importance, frequency-dependent heating at the target and the intervening ribs were estimated along with experimental verification. The ratio of ultrasonic power density at the target and the ribs, the time-varying spatial distribution of temperature, and the ablated focus of each sonication are regarded as key indicators to determine the optimal frequency. Following that, geometric rib-sparing was evaluated by investigating the operation of 2D matrix arrays to optimize focused beam shape and intensity at target.

Trans-costal FUS is most useful in treating tumours that are small and near the surface of the abdominal organs, such as the liver, kidney and pancreas. However, for targets deep inside these organs, severe attenuation of acoustic energy occurs, suggesting that pure ultrasound thermal ablation with different heating patterns will have limited effects in improving the treatment efficacy. Results also demonstrate that the optimal ultrasound frequency is around 0.8 MHz for the configurations considered, but that it may shift to higher frequencies with changes in the axial and lateral positions of the tumours.

In this work, I aimed to reduce the side effects of rib heating and increase the ultrasound efficacy at the focal point in trans-costal treatment. However, potential advanced techniques need to be explored for further enhanced localized heating in trans-costal FUS.

LIST OF ABBREVIATIONS AND SYMBOLS

APS	Ammonium persulfate
BBB	Blood brain barrier
BIS	N,N'-methylene-bis-acrylamide
BSA	Bovine Serum Albumin
CEM	Cumulative equivalent minutes
CT	Computed tomography
FDA	Food and Drug Administration
FEA	Finite element analysis
FOM	Figure of merit
FUS	Focused ultrasound surgery
HCC	Hepatocellular carcinoma
HIFU	High intensity focused ultrasound
KZK	Khokhlov-Zabolotskaya-Kuznetsov parabolic nonlinear equation
LMA	Levenberg-Marquardt algorithm
MI	Mechanical index
MRI/MR	Magnetic resonance imaging
ODE	Ordinary differential equation
PDE	Partial differential equation
PML	Perfectly matched layer
PNP	Peak negative pressure
PZT	Lead zirconate titanate
SAR	Specific absorption rate
SRMs	Small renal masses
TACE	Transcatheter arterial chemoembolization
TD	Thermal dose
TEMED -	N,N,N',N'-tetramethylethylene diamine
TMM	Tissue-mimicking material
tPA	Tissue plasminogen activator
TPS	Transient plane source
US	B-mode ultrasound imaging

A	Area; Amplitude
a	Aperture
c	Speed of sound; Stiffness
C	Specific heat capacity
d	Piezoelectric charge constant
d_r	Diameter of the -3dB focal zone
D	Distance between the transducer and surface of the phantom
D_z	Distance from the source to the frontal surface of the rib plane
D_y	Distance from the target to the centre of one rib in the transverse direction
e	Piezoelectric stress constant
f	Frequency
f_a	Anti-resonant frequency / mechanical resonance
f_r	Resonant frequency / electrical resonance
$f\#$	F-number
F	Force; Fourier number
g	Piezoelectric voltage constant
h	Piezoelectric stiffness constant
H	Thickness of the rib mimics.
I	Electric current; Sound intensity / acoustic intensity
I_{sata}	Spatial average, temporal average intensity
I_{spta}	Spatial peak, temporal average intensity
I_{sapa}	Spatial average, pulse average intensity
I_{sppa}	Spatial peak, pulse average intensity
I_{satp}	Spatial average, temporal peak intensity
I_{sptp}	Spatial peak, temporal peak intensity
k	Thermal conductivity; Real wave number
k_c	Complex wave number
k_p	Electromechanical coupling coefficient
k_t	Electromechanical coupling coefficient of thickness expander plate
L	Width of one period of the rib structure
L_r	Width of the rib mimics
L_i	Width of the inter-costal spaces
p	Sound pressure / acoustic pressure

p_0	Initial pressure
P	Electric driving power
P_{ac}	Sound power / acoustic power
Q_m	Mechanical damping; Volumetric metabolic heat
Q_v	Heat source term / absorbed ultrasound power density
r	First sidelobe point
R	Reflection coefficient; Resistance
R_e	Effective beam radius in the frontal rib plane
R_s	Radius of the ultrasonic source
t_{on}	Sonication duration
t_{off}	Cooling-off period
T	Transpose; Temperature; Transmission coefficient
T_c	Curie temperature
u	Displacement
v	Velocity
w_b	Perfusion rate
x_{sh}	Shock formation distance
X	Reactance
Z	Acoustic impedance; Electrical impedance; Focal length of the ultrasonic source
$|Z|$	Impedance magnitude
$Z - D_z$	Depth of the target measured from the frontal surface of the rib plane
Δx	Element size
Δt	Time difference; Time step
α	Attenuation coefficient; Thermal diffusivity
β	Coefficient of nonlinearity / nonlinear parameter
β_p	Sensitivity coefficient
γ	Correlation coefficient
δ	Diffusivity
$\tan \delta$	Dielectric loss
ε	Permittivity
$\varepsilon_R{}^s$	Relative permittivity at constant stress
$\varepsilon_R{}^T$	Relative permittivity at constant strain

θ	Impedance phase
θ_c	Critical angle
θ_i	Incident angle
θ_r	Reflection angle
θ_t	Transmission angle
λ	Wavelength
ρ	Density
τ	Stability factor / CFL number; Period
ω	Angular frequency
ϑ	Dilatation

LIST OF FIGURES

LIST OF TABLES

CHAPTER 1 INTRODUCTION

1.1 Background

The safety and efficacy of focused ultrasound surgery (FUS), also known as high intensity focused ultrasound (HIFU), in the treatment of tumours including those of the prostate, uterus, breast, bone, liver, kidney, and pancreas is now established. The mechanism of this technique is to use a focused ultrasonic source (single-element transducer or phased array) to generate localized thermal coagulation necrosis at depth within the body while leaving surrounding healthy tissue minimally affected. The small ablation zones caused by single ultrasonic exposures are combined to form a larger ablation zone until the entire target volume is covered. Under the guidance of advanced imaging modalities such as real-time diagnostic ultrasound (US) or magnetic resonance imaging (MRI), the intended tumours can be accurately targeted and the extent of the ablation process can be precisely monitored.

As a minimally invasive or truly non-invasive tumour ablation technique, FUS offers advantages over other treatment modalities such as radiofrequency and microwave radiation in terms of its low risk of side effects. However, there are a number of technical challenges hindering its widespread clinical application. One of these is the presence of the rib cage, necessitating extracorporeal treatment of organs in the upper abdomen e.g. liver, kidney, and pancreas. Because of the strong reflection and attenuation of ultrasonic energy by the ribs, general side effects such as skin burns and overheating of the ribs have been reported frequently. The beam defocusing and splitting caused by the periodic spatial structure of the rib cage have produced multiple hot spots and reduction of peak intensity in the target area, leading to decreased treatment efficacy. Furthermore, the abdominal organ motion caused by respiration or the heartbeat during the delivery of FUS may lead to severe target mislocation and potential damage to surrounding healthy tissue.

Since 1990, several research groups have reported attempts to avoid or minimize overheating of the ribs and overlying tissue, whilst also enhancing localized heating at targets within the rib cage. However, no systematic understanding of the HIFU fields

affected by the ribs is known yet. Further technological and methodological refinements are still necessary to address the long treatment times required in trans-costal FUS due to the large targeted tumour size and the small focal volume. Although FUS has been investigated both *in vitro* and *in vivo* for the treatment of hepatic, renal, and pancreatic tumours, and has gained preliminary acceptance as a treatment option, limited clinical data is available. Large randomized clinical trials with long-term follow up periods are therefore necessary to fully understand the clinical effectiveness and complications of trans-costal FUS.

1.2 Project Aims and Objectives

As noted previously in trans-costal FUS studies, the intervening ribs absorb and reflect the majority of ultrasound energy excited by a focused ultrasonic source, resulting in insufficient energy being delivered to the target organs of liver, kidney, and pancreas. Common side effects of localized hot spots at the interfaces between the ribs and soft tissue or in the highly absorptive regions like the skin are reported. This thesis presents research aimed towards the successful extracorporeal FUS treatment of the liver, kidney, and pancreas tumours. The key to this technique is to deliver sufficient ultrasonic energy to the target tumours whilst also possibly reducing the energy blocked by the ribs. The work focuses on the comprehensive parametric investigations of related parameters in this non-invasive tumour ablation technique; especially for achieving the optimal treatment outcomes, two-dimensional multi-element phased arrays can be used to generate versatile beam forms to efficiently avoid the rib obstacles in between. Preliminary results of the interaction of the modified HIFU beams with the intervening ribs and over a specific volume of target tissues will enable initial conclusions to be drawn about the effectiveness of binary manipulation of elements in these phased arrays.

1.3 Contents of the Thesis

The work presented in this thesis aims to explore the basic acoustic and thermal effects of HIFU and thereafter its specific applications via trans-costal route. To facilitate this, several acoustic devices used for focused ultrasound generation are presented. Experimental techniques to enable beam profile measurement and thermal ablative experimentation are developed, and a temperature-sensitive tissue-mimicking material for

use in high power applications is presented and characterized in terms of its acoustic and thermal properties. Relationships between the experimental measurements and numerical predictions are clarified, and the heating effects of various influencing factors in HIFU are determined numerically. For potential use in the treatment of hepatic, renal, and pancreatic tumours behind the rib cage, experimental investigations are made on different rib cage samples and mimics. Numerical exploration of the influence of various treatment parameters related in the trans-costal sonications is carried out using a finite element method that will provide useful information in the determination of optimizing treatment protocols. Further studies in this direction to minimize the side effects and to develop the most successful strategy of irradiation for a specific situation are therefore important, and potential solutions for utilizing the multi-element phased arrays may be proved efficient in trans-costal FUS applications.

1.4 List of Publications Arising From this Work

Peer-Reviewed Journal Articles

1. Gao, J., You, J., Cochran, S., Corner, G., Huang, Z., 'Simultaneous Measurement of Thermophysical Properties of Tissue-Mimicking Phantoms for High Intensity Focused Ultrasound (HIFU) Exposures', International Journal of Thermophysics 2012, Volume 33 Number 3, pp. 495-504.
2. Gao, J., Huang, Z., Cochran, S., 'Ultrasound Beam Distortion and Pressure Reduction in Trans-costal Focused Ultrasound Surgery'. (submitted to the journal of Applied Acoustics)
3. Gao, J., Huang, Z., Cochran, S., 'Optimal Sonication Protocols for Trans-costal Focused Ultrasound Surgery', (In preparation)
4. Gao, J., Huang, Z., Cochran, S., 'Avoid Overheating of Ribs by Optimized Operation of 2D Phased Arrays', (In preparation)

Proceedings and Abstracts

5. Qiu Z., Gao J., Cochran S., Huang Z., Corner G., Song C., 'The development of therapeutic ultrasound with assistance of robotic manipulator', Engineering in Medicine and Biology Society (EMBC), Minneapolis, USA, 2009, pp. 733-736.

6. Corner G., Daglish S., Qiu Z., Gao J., Brodie G., Cochran S., Melzer A., Mayne K., Huang Z. and Gourlay T., "Characterisation and Application of a Custom-made HIFU transducer for Robotic Manipulation", 9th International Symposium on Therapeutic Ultrasound (ISTU), Aix-en-Provence, France, 2009.

7. Gao, J., Demore C., Corner G., Huang, Z., and Cochran S., 'Exploration of thermal issues in treatment planning for focused ultrasound surgery', 22nd International Conference of Society for Medical Innovation and Technology (SMIT), Trondheim, Norway, 2010.

8. Gao, J., You, J., Cochran S., Corner G., Huang, Z., 'Simultaneous measurements of thermo-physical properties of egg white phantoms for HIFU by using the step wise transient plane source technique', 11th International Symposium on Therapeutic Ultrasound (ISTU), New York, USA, 2011 (In press).

9. Gao, J., Volovick, A., Pekelny, Y., Huang, Z., Cochran, S., Melzer, A., 'Focusing through the rib cage for MR-guided transcostal FUS', 11th International Symposium on Therapeutic Ultrasound (ISTU), New York, USA, 2011, (In press).

10. Gao, J., Shi, L., Volovick, A., Cochran, S., Huang, Z., 'Effect of split-focus associated with the rib cage in transcostal focused ultrasound therapy', The 4th International Congress on Image and Signal Processing & The 4th International Conference on BioMedical Engineering and Informatics (CISP'11~EMBI'11), Shanghai, China, 2011, pp. 2286-2289.

11. Song S., Gao J., Huang Z., Jeng D., 'Effects of blood flow on high intensity focused ultrasound ablation', The 4th International Congress on Image and Signal Processing & The 4th International Conference on BioMedical Engineering and Informatics (CISP'11~EMBI'11), Shanghai, China, 2011, pp. 2290-2293.

12. Gao J., Volovick A., Pekelny Y., Cao R., Nabi G., Cochran S., Melzer A., Huang Z., 'Factors influencing treatment efficacy of trans-costal focused ultrasound surgery and possible solutions', 9th meeting of the UK Therapy Ultrasound Group (THUGS), London, 2012.

13. Gao J., Volovick A., Pekelny Y., Cao R., Nabi G., Cochran S., Melzer A., Huang Z., 'Optimizing sonication protocols for trans-costal focused ultrasound surgery', 12th International Symposium on Therapeutic Ultrasound (ISTU), Heidelberg, Germany, 2012.

14. Cao R., Gao J., Corner G., Nabi G., Huang Z., 'A rapid 3D model of abdominal organs for transcostal HIFU therapy'. 12th International Symposium on Therapeutic Ultrasound (ISTU), Heidelberg, Germany, 2012.

CHAPTER 2 LITERATURE REVIEW

An emergent medical therapy known as high-intensity focused ultrasound (HIFU) or focused ultrasound surgery (FUS) is now being developed for, and in clinical use for the treatment of the various types of tumours. The principle of this technique is to use a focused ultrasonic source (single element transducer or phased array) to generate ultrasound-induced localized thermal coagulation necrosis at a target tissue, but leaving surrounding healthy tissue minimally affected, and viable. The primary advantages of FUS over other therapies (radiofrequency or microwave radiation) include: non-invasive therapy, with the ultrasound source located outside body; precise treatment region minimizes impact on healthy tissues; and *in situ* monitoring of therapy via ultrasound or magnetic resonance imaging (MRI). In China, since the end of 1997, more than 40,000 patients have received FUS for tumours in the uterus, bone, breast, liver, kidney, and pancreas. Meanwhile, more than 1000 similar cases have been reported outside China (Khokhlova et al., 2010). Studies of treatment outcomes and side effects to date have demonstrated non-invasive FUS to be safe, effective and feasible in clinical applications.

This chapter presents an overview of the literature relevant to the work presented in this thesis. It firstly addresses the theory underpinning this work in Section 2.1. The relevant material is organized into the following sub-sections: 2.1.1 Generation of high-intensity focused ultrasound (HIFU); 2.1.2 HIFU propagation in soft tissues; 2.1.3 Heat generation and transfer in biological tissues; 2.1.4 Cavitation. By presenting this in the workflow of generation, propagation, and functional mechanisms of HIFU, this section provides important theoretical bases on the direction of the work. As shall be shown in Section 2.1.3.3, the occurrence of the ultrasound-induced thermal lesion can be predicted by the cumulative equivalent minutes, a criterion of great significance in conventional ultrasound hyperthermia or HIFU here. The breadth of the application area is such that the Section 2.2 is addressed in three parts: 2.2.1 History of focused ultrasound surgery; 2.2.2 Existing applications, and 2.2.3 Promising applications, thus presenting a brief introduction to the therapeutic applications of focused ultrasound surgery (FUS) in the past, present, and possible future. This discussion is extended in Section 2.3, in which the technical challenges of FUS in the treatment of liver, kidney, and pancreas tumours are stated, encompassing issues of presence of rib cage, abdominal organ motion caused by

respiratory movement, highly perfused organs, and prolonged treatment times. Finally, in support of this research, more advanced topics related to the technical improvements in terms of the imaging unit, treatment unit, positioning unit, and advanced treatment planning are presented in Section 2.4.

2.1 Physical Principles of Focused Ultrasound Surgery

2.1.1 Generation of High-Intensity Focused Ultrasound

In physics, the term 'ultrasound' means mechanical vibrations of a medium that are similar to sound waves, but with frequencies higher than the upper frequency limit of human hearing (20 kHz) (Cracknell, 1980). The development of modern technology of ultrasonics in applications of ultrasound imaging and therapy has mainly resulted from the development of piezoelectricity and modern electronic techniques. The principle of piezoelectricity was first discovered by the Curie brothers in 1880 (Curie and Curie, 1880), whereby certain solid materials having this property develop an internal electric field when they are under some external mechanical stress. In the following year, Lippmann predicted the inverse piezoelectric effect, namely a mechanical deformation of certain materials can appear when it is in external electric field (Lippmann, 1881; Curie and Curie, 1881). However, the piezoelectricity and its reversible effect, as shown in Figure 2.1, were not successfully applied in the detection and generation of ultrasound until the first world war, for the detection of enemy submarines.
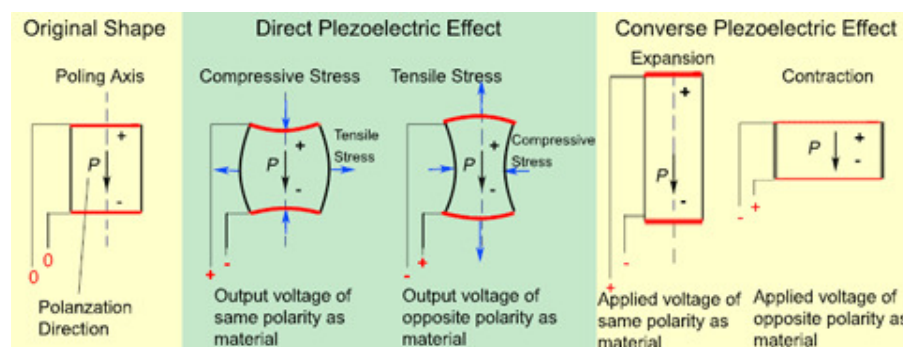
Figure 2.1 Direct and converse piezoelectric effects, *from Siu Wing OR, 2002*

In the context of ultrasound, piezoelectricity is exhibited in a number of materials, e.g., quartz, tourmaline and sodium potassium tartrate, which have been used as transducers

for many years. Applying an alternating voltage to the piezoelectric active element causes its dimensions to oscillate and the electrical energy is converted into mechanical energy, thus generating ultrasound waves in the propagating medium in front of the transducer.

Currently, the piezoelectric materials are divided into three main groups: piezo-ceramics, piezo-composites and passive materials (Mulvana, 2007). The most popular ceramic material is lead zirconate titanate, $Pb(ZrTi)O_3$ (PZT), a ferroelectric polycrystalline material widely used in medical devices for its high piezoelectric figure of merit (FOM = $d_{33}.g_{33}$) and good electromechanical coupling coefficient; it is relatively easy and cost effective to fabricate and offers versatility when complex shapes are required (Demore, 2006). The ceramic is poled to establish piezoelectric behaviour. As shown in Figure 2.2, the poling procedure refers to the heating of the material, sometimes over its Curie temperature (T_c, the temperature at which changes of crystalline structure occur), and subsequent application of a DC electric charge to affect a net dipolar arrangement. Once the ceramic has cooled down to room temperature and the electrical charge has been removed, a high degree of dipolar arrangement remains and the material is permanently polarized.
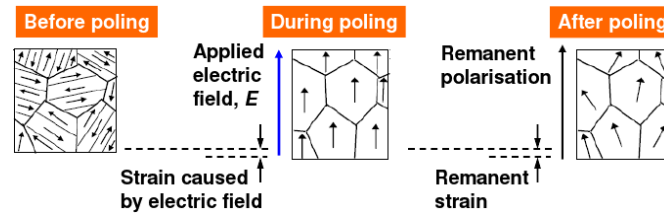
Figure 2.2 Poling effect, *from Xu, 1991*

The particular set of material properties indicating the ceramic's acoustic characteristics is discussed below. Specifically, these are the coupling coefficient, *k*, referring to the efficiency of mechanical and electrical energy conversion of the material; the acoustic impedance, Z, especially when compared to the acoustic impedance of the propagating medium; and the permittivity, *ε*, which affects the electrical impedance of the device and also the efficiency of the associated electrical driving system (Mulvana, 2007). Generally, a higher *k* value is desirable to ensure high sensitivity and efficient power conversion in the receiving or transmitting mode. Considering the acoustic impedance of tissue is approximately 1.5 MRayl, while that of PZT-5A ceramic is around 33.5 MRayl, a significant portion of energy is reflected back from the front surface of the ceramic,

which decreases the proportion of the drive signal that can be transmitted into the propagation medium. As the electrical impedance relates inversely to the capacitive reactance (a function of the permittivity of the material, its area and thickness), the permittivity of the material will therefore influence its suitability into an external electrical system.

For high power applications, the ability to withstand high temperatures without de-poling is of significance. The PZT-4 'hard' ceramic is less likely to be depoled because of its high Curie temperature and gives better performance during use. The new PZ50 range of ceramics (Ferroperm, Denmark) intended specifically for use in HIFU, offer improved high power performance, and allows small volume elements to be used to generate high power output. The piezo-composite (Figure 2.3) uses a passive material, usually polymer, to embed the piezoelectric material and aims for improved acoustic performance (increased electromechnical coupling and reduced acoustic impedance). Comparing with the ceramic with the acoustic impedance of 33.5 MRayl, a composite of PZT-5A can have a much decreased acoustic impedance of 10 MRayl. Composite materials may thus offer better results in tissue or water coupled applications.
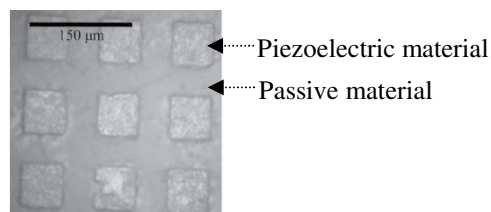
Figure 2.3 Image showing square pillars surrounded by the HY 1300/CY 1301 epoxy, *from Bernassau et al., 2011*
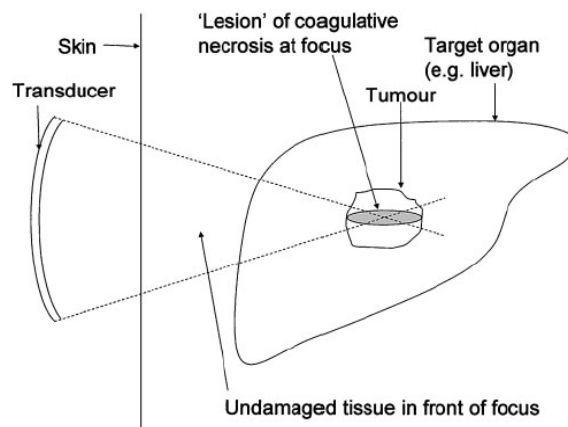
Figure 2.4 Diagram representing HIFU lesion production, *from Kennedy et al., 2003*

For therapeutic applications of ultrasound, transducers are capable of focusing the ultrasound beam to a tight cigar-shaped volume, as shown in Figure 2.4. The transducers in the shape of curved bowl or multi-element phased array are used to generate HIFU beams (ter Haar, 1999; ter Haar, 2000; ter Haar, 2001; ter Haar, 2007a; ter Haar, 2007b). However, the principle behind the multi-element phased array is the wave physics of phasing, varying the amplitude and time of a series of ultrasonic waves so that the individual propagating wave fronts generated by the array elements add to (constructive interference) or cancel (destructive interference) each other in order to effectively steer and shape the acoustic beam. The beam can be dynamically steered very quickly (in a small fraction of a second) in such a way that the beam can be scanned through multiple angles or with multiple focal depths.

2.1.2 HIFU Propagation in Soft Tissues

To achieve a particular clinical outcome of raising tissue temperature and relieving pain, focused ultrasound beams at frequencies of around 1 MHz are delivered into small-volume targeted tissue at a variety of energy and time settings. In this part, I will consider the propagation of focused ultrasound waves in a tissue material first.

2.1.2.1 Longitudinal and Shear Waves

In practice, several types of ultrasonic waves exist, but of primary interest is the longitudinal wave (Figure 2.5), in which the particles of the medium move backwards and forwards parallel to the same line as that in which the wave is travelling. This one-dimensional wave is sometimes referred to as a compressional wave. The instantaneous value of the longitudinal displacement as a function of x is sinusoidal. There are two reasons for this: first, ultrasound is usually produced by conversion of single frequency sinusoidal electromagnetic oscillations into ultrasonic waves; second, any wave can be Fourier analyzed into components which are pure sinusoidal waves (Cracknell, 1980). With the development in time, the particles of the medium will rearrange themselves by oscillating about their equilibrium positions and hence the compressions (increase in material density) and rarefactions (decrease in material density) will travel from their original places. The longitudinal waves propagate fast in soft tissues

at a velocity of approximately 1500 m/s and can reach tissue around 70 - 100 wavelengths deep.

The other type of bulk elastic body wave is the shear wave, or transverse wave, in which the particles move perpendicular to the direction of wave propagation. The waves travel through the elastic medium and the main restoring force results from the shear effects. In soft tissues, the shear wave has low propagation velocity (up to 10 - 40 m/s) and is highly attenuated when the frequency is higher than 1 MHz and can therefore be neglected. The shear wave velocity in solid bone (1995 m/s) is almost half of its longitudinal wave velocity (3736 m/s). Mode conversion of longitudinal and shear waves occur when a longitudinal wave hits an interface between materials of different acoustic impedances and the incident angle is not normal to the interface, whereby the mode conversion may introduce extra energy losses (Duncan, 2010).
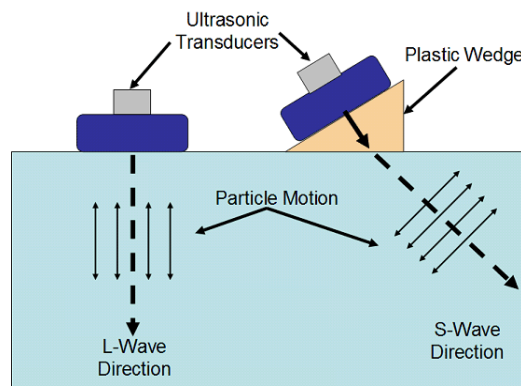
Figure 2.5 Longitudinal and shear waves

2.1.2.2 Pressure, Intensity, Power

The propagation of ultrasound occurs as the vibrating particles interact with neighboring particles within the material medium, causing a periodic change in pressure. Here, we provide a brief summary of acoustic parameters regarding the HIFU exposures, as listed in Table 2.1. In practical terms, medical ultrasound exposures and thermal doses are described by intensity, pressure, time, frequency, etc (ter Haar, 2009). In an ultrasound wave, the field parameters e.g. acoustic pressure and power, can be measured in water; however, there is no way of measuring intensity directly. The sound pressure, p (unit: Pa), is the deviation from the local ambient pressure induced by a sound wave at a given

location and given instant in time, and can be detected by hydrophones (Johns et al., 2007; Howard and Zanelli, 2007). The sound power generated by ultrasonic equipment, P_{ac} (in Watts), can be measured in two main ways: measurement of power from intensity (planar scanning using hydrophones) and radiation force method (Shou et al., 2006). The result is not depending on the position providing that the whole ultrasonic beam is included in the measurement. The requirement of spatially integrating the temporal average intensity over the entire 2-D beam area makes the procedure time-consuming, but may be the only option for diagnostic ultrasound field characterization. In the alternative radiation force method, as shown in Figure 2.6, a target placed in the beam path experiences a radiation force that is proportional to the power transferred in the beam. By connecting to an appropriate force-measuring device, the power output of the testing device can be determined.

Table 2.1 Typical acoustic parameters of HIFU, *from Khokhlova, 2009*

Parameter	
Ultrasound frequency, MHz	0.5 – 10
Acoustic wavelength, mm	0.15 – 3
Pressure amplitude level, MPa	3 – 30
Intensity level, W/cm^2	300 – 30000
Power level, W	50 – 2500
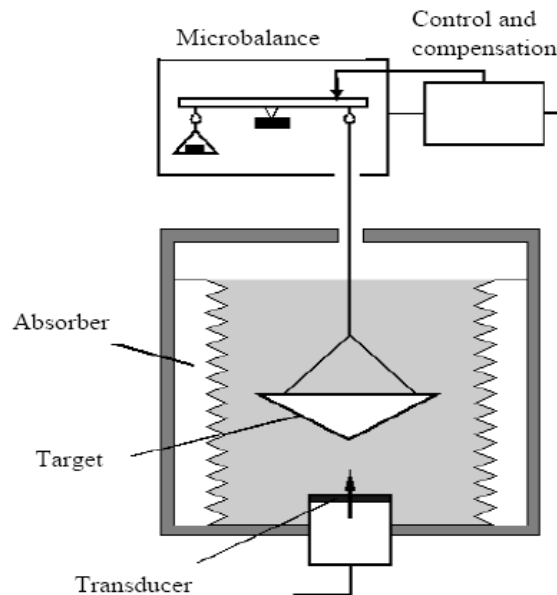
Figure 2.6 Radiation force balance for power measurement, *from ter Haar*, *2009*

The sound intensity, I (unit: W/m^2), is defined as the sound power per unit area. For a plane wave, the sound intensity can be written as:

$$I = \frac{p^2}{2\rho c}$$

(2 - 1)

where ρ and c are the density and speed of sound.

Intensity is calculated either from total acoustic power averaged over the beam area or from a peak pressure measurement. As it is varied in space and time, putting together spatial and temporal considerations, we have up to six intensities: I_{sata} (spatial average, temporal average, most quickly determined and most frequently quoted), I_{spta} (spatial peak, temporal average), I_{sapa} (spatial average, pulse average), I_{sppa} (spatial peak, pulse average), I_{satp} (spatial average, temporal peak), and I_{sptp} (spatial peak, temporal peak). In this thesis, I use I_{sata} for description except where otherwise mentioned.

2.1.2.3 Linear Propagation Effects

Reflection and Refraction

The propagation of ultrasonic waves through a medium is dependent on its physical properties and wave types. Neglecting attenuation, linear acoustic waves will propagate through the medium until a change in acoustic impedance is encountered. The acoustic impedance, Z (unit: Rayl), is equal to density of the material, ρ, multiplied by the propagation speed, c, and is the determining factor in the wave reflection. In cases of simple geometries and perpendicular incidence, the amplitudes of reflected echoes and transmitted waves depend on the incident signal at the boundary and the impedances of the media on either side (Cracknell, 1980).

$$R_x = \left(\frac{Z_1 - Z_2}{Z_1 + Z_2}\right)^2,$$

$$T_x = 1 - R_x = \frac{4Z_1 Z_2}{(Z_1 + Z_2)^2}$$

(2 - 2)

where R_x and T_x represent the intensity or energy reflection coefficient and transmission coefficient when waves propagate through medium 1 and encounter medium 2 at a normal angle. Thereby, strong reflections occur with respect to bone or gas containing

tissue, for example at the interface between soft tissue (1.63 MRayl) and bone (7.8 MRayl), R_x and T_x equal 0.428 and 0.572, respectively, resulting in nearly half of the incident energy reflected back.

However, as shown in Figure 2.7, when an incident wave encounters the boundary at an oblique angle, θ_i, the reflected wave will leave the boundary at an angle equal to the incidence, $\theta_r = \theta_i$, while the transmitted (refracted) wave will leave at an angle, θ_t.
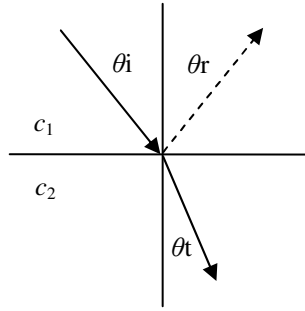
Figure 2.7 Reflection and refraction at a boundary between media with different sound speeds

$$\frac{\sin \theta_i}{c_1} = \frac{\sin \theta_t}{c_2} \qquad (2 - 3)$$

Corresponding pressure amplitudes of the reflected and transmitted waves could be:

$$\frac{p_r}{p_i} = \frac{Z_2 \cos \theta_i - Z_1 \cos \theta_t}{Z_2 \cos \theta_i + Z_1 \cos \theta_t},$$
$$\frac{p_t}{p_i} = \frac{2Z_2 \cos \theta_i}{Z_2 \cos \theta_i + Z_1 \cos \theta_t} \qquad (2 - 4)$$

where i, r, and t represent the incident, reflected and transmitted waves, respectively.

At the soft tissue/bone interface, i.e., $c_2 > c_1$, at angles greater than the critical angle, θ_c, transmission is no longer possible and the incident wave is completely reflected;

$$\sin \theta_c = \frac{c_1}{c_2} \qquad (2 - 5)$$

When the incident angle is less than the critical angle, mode conversion may occur for the

transmitted wave and shear waves will result. However, for the bone/soft tissue interface, only longitudinal waves will be transmitted, as transverse waves are not effectively supported in soft tissues (Duncan, 2010).

Attenuation

Suppose that a parallel acoustic wave is propagating through a medium, and the intensity or the excess pressure amplitude is measured at the reference position 0, and at a distance *x*. The attenuation is used to describe the total reduction in the intensity or excess pressure amplitude in between. The deflection of energy from the beam path is due to the reflection, refraction, scattering and diffraction by the medium between 0 and *x*, though most commonly it is described as the result of absorption and scattering (Wu and Nyborg, 2006).

$$I(x) = I(0)\exp(-2\alpha x) \tag{2 - 6}$$

where α is the attenuation coefficient in units of dB/cm/MHz.

Table 2.2 Typical values of attenuation in tissue *from Khokhlova, 2009*

Tissue	Attenuation (1 MHz), dB/cm
Water	2.5×10^{-4}
Blood	0.02
Liver	0.12
Muscle	0.12
Brain	0.07
Lungs	3.5

The absorption refers to the transformation of ultrasonic energy into some other form, mainly heat; and it is highly dependent on the material properties of the medium as well as the frequency (of the order of f^2 for water and f^1 for tissue) (Preston 1991). In the cases of reflection, refraction, scattering and diffraction, the acoustic beam is simply travelling in a different direction to that of the original wave. The reflection and refraction occur at the boundaries between media with different acoustic impedances; the scattering losses (20 - 40 % of total attenuation) are caused by the structure of the material, for example, any interface that is irregular at a small scale (sub-wavelength); while the diffraction will occur at barriers that are intersected in the beam path.

Focusing

The acoustic beam profiles of the circular or rectangular cross-sectional devices have been well presented before (Kino, 1987). The field of an unfocused transducer (aperture, *a*) is made up of the near- and far-field regions, with the division between the two regions occurring at a point Z_0,

$$Z_0 = \frac{4a^2 - \lambda^2}{4\lambda} \tag{2 - 7}$$

where λ is the wavelength. The two zones show two distinct solutions for wave amplitude along the transducer axis direction, *z*. In the near field, i.e., $z^2 << a^2$, the intensity along the beam axis can be expressed as

$$I(z) = 4I(0)\sin^2\frac{\pi a^2}{2\lambda z} \tag{2 - 8}$$

whereas for the far field case, it can be written as

$$I(z) = \left(\frac{\pi a^2}{\lambda z}\right)^2 I(0) \tag{2 - 9}$$

The graphical presentation of the near and far fields is shown in Figure 2.8. It can be seen that the far field is more uniform than the near field. And the distinction of the near- and far-fields is produced by the interaction between the propagating plane waves and edge waves caused by the aperture effect.
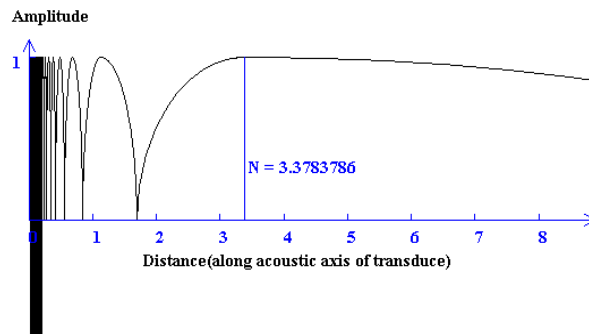
Figure 2.8 Acoustic pressure distribution along the transducer axis, *from Kino, 1987*

16

In therapeutic ultrasound applications, it is necessary that high energy concentrations are achieved over specific volumes of tissue, in which the focusing techniques are concerned. For a single-element transducer, focusing can be achieved by adding a concave lens or manufacturing the piezoelectric element in the shape of a spherical bowl. The spherically shaped transducer will produce a focused beam near its centre of curvature. The intensity amplitude of the beam near its focal point, z_0, can be determined using:

$$\frac{I(0, z_0)}{I(0)} = \left(\frac{\pi a^2}{z_0 \lambda} \right)^2 \qquad (2 - 10)$$

and will be significantly higher than the beam intensity at the transducer surface, 0, providing that $z_0 < \pi a^2 / \lambda$, where in this case, $2a$ is the transducer diameter. The relation is based on the use of the Rayleigh-Sommerfield theory, which will be covered in Section 2.1.2.5. The diameter of the -3dB focal zone, d_r, can be calculated using:

$$d_r = \frac{0.51 z_0 \lambda}{a} = 1.02 \lambda F \qquad (2 - 11)$$

where the F-number of the focused transducer is defined as $f\# = z_0 / 2a$. The intensity amplitude of the transducer falls rapidly from the focal point as described by the function $\text{jinc}^2 X$, as illustrated in Figure 2.9,
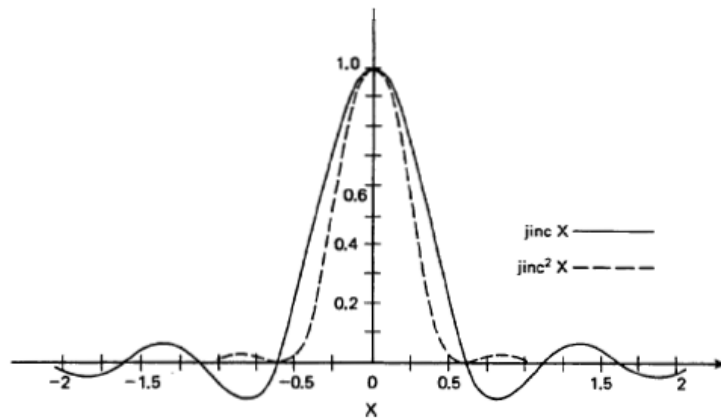
Figure 2.9 Plot of jinc X and jinc^2 X, where jinc $X = J_1(2\pi X)/\pi X$, *from Kino 1987*

in which,

$$\frac{I(r,z_0)}{I(0)} = \left(\frac{\pi a^2}{z_0 \lambda}\right)^2 \left(\mathrm{jinc}\,\frac{ra}{\lambda z_0}\right)^2 \tag{2 - 12}$$

The first sidelobe will be observed at the point, r,

$$r = \frac{0.82 z_0 \lambda}{a} \tag{2 - 13}$$

where the amplitude is 17.6 dB lower than at the focal point.

2.1.2.4 Nonlinear Propagation Effects

As discussed in Section 2.1.2.3, the linear propagation effects refer to wave behaviour in most situations when the assumption of a small-signal wave propagating through a homogeneous medium under adiabatic conditions is considered. In reality as the signal amplitude increases, the linear approximation of wave behaviour becomes inaccurate. The nonlinearity of the medium is important as it will change the wave speed at a local region, and hence cause the wave distortions at higher pressure conditions (Gooberman, 1969; Welsby, 1970). The effects of nonlinear propagation can therefore be observed with both increasing amplitude of the wave of interest and increasing wave propagation distance.

In order to fully describe the wave behaviour, the nonlinear term, i.e., the higher order components in the Taylor series expansion, that have been considered negligible to the wave speed in the linear approximation must be considered. The nonlinearity of a propagation medium can be described by the term, B/A, where A and B are temperature dependent coefficients in the Taylor series expansion for wave propagation, and $\beta = 1 + B/2A$ is well known as the coefficient of nonlinearity (Hamilton & Blackstock, 1998). However, it is currently quite challenging to accurately evaluate the value of B/A.

$$p = p_0(\rho) + A\left(\frac{\rho - \rho_0}{\rho_0}\right) + \frac{1}{2}B\left(\frac{\rho - \rho_0}{\rho_0}\right)^2 + \ldots$$
$$\rho_0\left(\frac{\partial^2 \rho}{\partial \rho^2}\right)_0 = B, c_0^2 = \rho_0^2\left(\frac{\partial \rho}{\partial \rho}\right)_0 = A \tag{2 - 14}$$

18

$$\beta=1+\frac{\rho_0}{2c_0^2}\left(\frac{\partial^2\rho}{\partial\rho^2}\right)_0=1+\frac{1}{2}B/A$$

Table 2.3 Typical values of nonlinear parameter in tissue, *from Khokhlova, 2009*

Tissue	nonlinear parameter β
Water	3.5
Blood	4
Non fat tissues	4.1 – 5
Fatty tissues	5.8 - 6.6

As a harmonic sine wave propagates through a nonlinear homogeneous medium, it exerts compressive and tensile forces during the corresponding phases, displaying positive and negative pressure amplitudes. Compression of the nonlinear medium results in a local increase in the density and speed of sound, in such a way that the sine wave travels through the area of higher pressure under a particular acceleration while on the contrary, it encounters a local retardation as it travels through the rarefaction area (Mulvana, 2007). Hence, the speed of sound in the nonlinear medium is no longer uniform after propagation through a few wavelengths, and the pure sine wave can be modified to become increasingly saw-tooth in shape due to the variation in speed between the positive and negative portions. When the negative slope gets smaller and smaller and approaches infinity, the result is an acoustic shock, as illustrated in Figure 2.10. Suppose $p\,(x = 0) = p_0\sin(\omega_0\tau)$, the shock formation distance, x_{sh}, is:

$$x_{sh}=\frac{c_0^3\rho_0}{\beta p_0\omega_0}\qquad\qquad(2\text{ - }15)$$
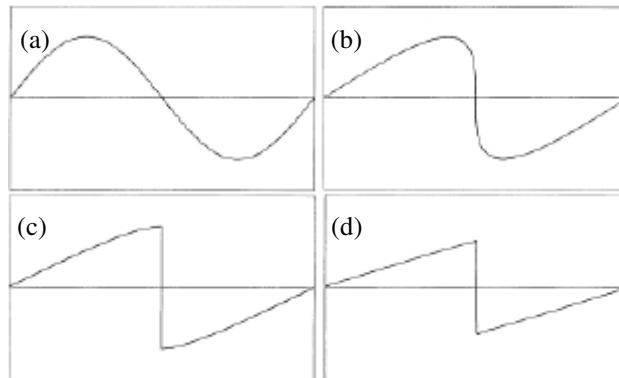
Figure 2.10 Development of a harmonic sine wave into a saw-tooth wave: (a) $x = 0$, (b) $x = x_{sh}$, (c) $x = \pi x_{sh}/2$, (d) $x = 3\pi x_{sh}$, *from Khokhlova 2009*

The modification of sine wave into a saw-tooth shape can be visualized by displaying the signal received by a hydrophone on an oscilloscope and it can be observed more clearly with increasing driving signal amplitude and propagation distance between the transmit and receive devices (Zhou et al., 2006; Canney et al., 2008). The distortion or shock generation associated with nonlinear wave propagation increases the harmonic contents of the wave and introduces higher harmonics along with the initial frequency (Filonenko and Khokhlova, 2001; Khokhlova et al., 2006; Khokhlova et al., 2007). The additional higher frequency harmonics (Figure 2.11a) increase the absorption and heating, typically in the focal region of a focused ultrasound transducer. Once the shock front has formed in the profile, the dissipative losses in the medium increase and the wave amplitude decreases, causing the nonlinear effects to be reduced and the linear approximation to be valid again (Figure 2.11b).
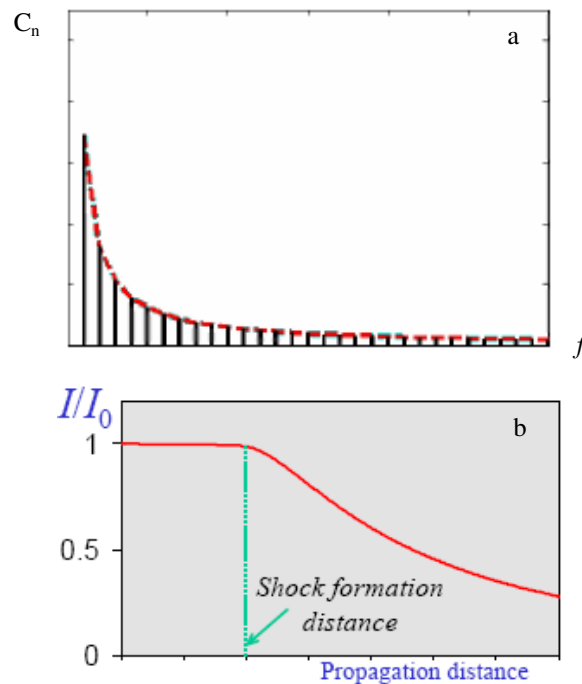
Figure 2.11 (a) Generation of higher frequency harmonics, and (b) Efficient nonlinear absorption on the shocks, *from Khokhlova 2009*

In typical HIFU applications, the wave distorts and steep shock fronts develop as the ultrasound propagates nonlinearly through the soft tissue. The waveform distortion together with the production of more rapidly absorbed higher harmonics can reduce the HIFU intensity and enhance tissue heating. The nonlinearity is concentrated and localized in the focal zone only, which results in amplified focal heating. In brief, consideration of

nonlinearity contributes to our understanding of HIFU sonication, although simplifications and assumptions about the propagation medium and the thermal environment need to be improved further.

2.1.2.5 Modelling of HIFU Propagation in Soft Tissues

In the literature, various linear and nonlinear models have been used for quantifying the acoustic wave behaviour and field responses during focused ultrasound thermal ablation, such as the full wave equation for inhomogeneous tissue, Rayleigh integral for acoustic field in water and homogenous tissue, evolution equations for directional beams in inhomogeneous tissue, plane wave approximation, etc (Khokhlova, 2009). In this section, we will discuss the Rayleigh-Sommerfeld integral and the KZK parabolic nonlinear equation only.

Rayleigh-Sommerfeld Integral

The Rayleigh-Sommerfeld integral applying to calculate the focused acoustic field was derived from the classical Rayleigh integral that was used for calculation of a flat circular radiator in a linear, homogeneous, and non-attenuating medium.

$$\mathbf{p}(\mathbf{r}) = \frac{j\rho c k}{2\pi} \int_{S'} \mathbf{u}(\mathbf{r}') \frac{e^{-jk|\mathbf{r}-\mathbf{r}'|}}{|\mathbf{r}-\mathbf{r}'|} dS' \qquad (2 - 16)$$

where $k = 2\pi/\lambda$ is the real wave number, S' is the surface area of the radiating source, $\boldsymbol{u}$ is the particle velocity normal to the radiating source, $\boldsymbol{r}$ and $\boldsymbol{r}'$ are, respectively, the control point (field point of interest) and the source point, and $p(\mathbf{r})$ is the complex acoustic pressure at the location of the control point.

Compared with other modelling techniques, this Rayleigh-Sommerfeld integral method is more applicable to calculations concerning the shape of the transducer, e.g. with a hole in the centre to incorporate an ultrasound scanner and in the case of multi-element phased arrays (Ebbini et al., 1988; Ebbini and Cain, 1989; Ebbini and Cain, 1991). For an N-element phased array transducer with arbitrary geometry (each element is small

enough to be treated as a point source), the discretized Rayleigh-Sommerfeld integral can be written as,

$$\mathbf{p}(\mathbf{r}) = \frac{j\rho ck}{2\pi} \sum_{n=1}^{N} \mathbf{u}_n(\mathbf{r}_n') \int_{S_n'} \frac{e^{-jk|\mathbf{r}-\mathbf{r}_n'|}}{|\mathbf{r}-\mathbf{r}_n'|} dS_n' \qquad (2 - 17)$$

where r_n' and S_n' are, respectively, the source point and the surface area of the nth element on the phased array transducer; $u_n(r_n')$ presents the particle velocity normal to the nth element on the array with the amplitude A_n and phase θ_n, which can be written as:

$$\mathbf{u}_n(\mathbf{r}_n) = A_n e^{j(\omega t+\theta_n)} \qquad (2 - 18)$$

Equation (2 – 17) suggests that the pressure at a point of interest can be obtained by summation of the pressure of each individual transducer element over the array. Using the pseudoinverse technique proposed in Ebbini and Main (1989), the excitation signal (amplitude and phase) of each single element can be determined for optimal synthesis of pressure patterns. In equations (2 – 16) and (2 – 17), the effects of attenuation can be included by replacing k with k_c, where $k_c = k - j\alpha$ is the complex wave number with attenuation coefficient α.

To solve the multi-layer tissue problem as concerned in the abdominal applications, e.g., for uterine fibroids, a modified Rayleigh-Sommerfeld integral method taking into account the reflection and refraction during propagation of ultrasonic wave through a layered structure was developed (Fan and Hynynen, 1992; Fan and Hynynen, 1994; Fan and Hynynen, 1996). As shown in Figure 2.12, considering a two layer media separated by a smooth interface, the idea is to regard the interface as a new radiator (dividing the interface into N elements), and approximate the infinitesimal area of the interface as a plane.
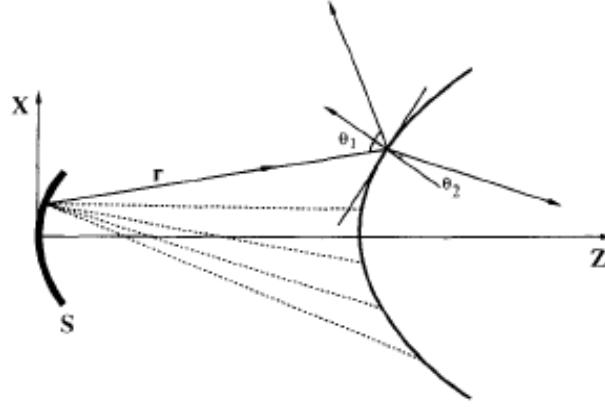
Figure 2.12 Two layer media separated by a curved interface, *from Fan et al, 1994*

The particle velocity normal to the interface due to the radiator, v, can be calculated by

$$v = \frac{jk_1}{2\pi} \sum_{n=1}^{N} u_n \frac{e^{-jk_1 r_n}}{r_n} \cdot \left(1 - j\frac{1}{k_1 r_n}\right) \Delta S_n \cdot T(\theta_1^n) \cdot \cos(\theta_2^n) \tag{2 - 19}$$

where k_1 and k_2 are the wave number in medium 1 and 2 on both sides of the interface, θ_1 and θ_2 represent the incident angle of the ultrasonic wave relative to the normal direction of the plane and the new radiation direction in medium 2, and T is the particle velocity transmission coefficient given as,

$$T = \frac{2\rho_1 c_1 \cos \theta_1}{\rho_2 c_2 \cos \theta_1 + \rho_2 c_2 \cos \theta_2} \tag{2 - 20}$$

where ρ_1 and ρ_2 are the density of the media, and c_1 and c_2 are the speed of sound in the media.

The acoustic velocity potential in the second medium, ψ', can be obtained by

$$\psi' = \frac{1}{2\pi} \sum_{n=1}^{N} v_n \frac{e^{-jk_2 r_n}}{r_n} \Delta S_n \tag{2 - 21}$$

The acoustic pressure in medium 2, p, can then be calculated as

$$p = \rho_2 \, \partial \psi' / \partial t = jk_2 \rho_2 c_2 \psi' \tag{2 - 22}$$

However, there are limitations need to be overcome in this method; for example, it can only be expanded to multi-layer tissue when the layer thickness is larger than the wavelength and the effects of scattering, diffraction and nonlinearity are not included (Fan and Hynynen, 1994).

KZK Parabolic Nonlinear Equation

The Khokhlov-Zabolotskaya-Kuznetsov (KZK) parabolic nonlinear equation is widely used to numerically model the three dimensional nonlinear acoustic field generated for high-intensity ultrasound applications and lithotripsy (Filonenko and Khokhlova, 2001; Khokhlova et al., 2006; Khokhlova et al., 2007). The axisymmetric form of pressure can be written as,

$$\frac{\partial^2 p}{\partial z \partial \tau} = \frac{c_0}{2} \nabla_\perp^2 p + \frac{\delta}{2c_0^3} \frac{\partial^3 p}{\partial \tau^3} + \frac{\beta}{2\rho_0 c_0^3} \frac{\partial^2 p^2}{\partial \tau^2} \qquad (2\text{ - }23)$$

where p is the acoustic pressure, z is the coordinate along the beam axis, $\tau = t - z/c_0$ is the retarded time, ρ_0 and c_0 are the ambient fluid density and small signal speed of sound, δ is the diffusivity parameter, $\beta = 1 + B/2A$ is the coefficient of nonlinearity, and $\nabla_\perp$ is the Laplace operator with transverse coordinates $r = (x, y)$. The first term on the right hand side represents the effects of diffraction, and the following terms dictate the thermo viscous attenuation/absorption and nonlinearity.

Equation (2 – 23) is valid when $ka/2 \gg 1$, where k is the wave number and $2a$ is the width of the acoustic source. The KZK equation can be numerically solved in the frequency domain and also in the time domain with finite differences and operator splitting. Although very effective for numerical studies of shocks in uniform acoustic media, this approach does not readily generalize to propagation and scattering in inhomogeneous acoustic and elastic media. However, one most important limitation of the KZK equation relies on the parabolic approximation, which assumes that the dimension of the source is much larger than a wavelength and the field is in a narrow beam. For this reason, the KZK equation may become less accurate for off-axis positions (Pinton, 2007).

2.1.3 Heat Generation and Transfer in Biological Tissues

The main mechanism of focused ultrasound induced heating refers to the conversion of ultrasonic energy into thermal energy via absorption. As scattering is assumed to be ignored, all the attenuated/absorbed energy is deposited into heat. The absorption occurs when there is a phase difference between the pressure and density (Cobbold, 2007). In fluids, this phase difference is caused by classical viscous friction. While for biological tissues, it is dominated by relaxation processes, as noted elsewhere, the various theories of the relaxation mechanisms can be divided into four groups: kinetic theory, irreversible thermodynamics, statistical thermodynamics, and the phenomenological approach.

2.1.3.1 Ultrasonic Radiation induced Heat Generation

When using an external ultrasound applicator to heat a homogeneous and uniformly attenuating medium, the absorbed ultrasound power density (Q_v), sometimes named as the specific absorption rate (SAR), at a given position x in the medium is proportional to the wave energy flux, which is equivalent to the magnitude of the ultrasound intensity (Lin et al., 2001; Cochard et al., 2009). Here it is assumed that the ultrasound intensities are not high enough to cause wave distortion and/or transient cavitation.

$$Q_v(x) = -\frac{dI(x)}{dx} = 2\alpha_a(x) \cdot I(x) \qquad (2 - 24)$$

where $I(x)$ is the time averaged intensity of the ultrasonic wave at the measurement location x, and $\alpha_a(x)$ is the ultrasonic absorption coefficient at position x in the medium. Two alternatives for the average rate of ultrasound radiation induced heat deposition can be given as:

$$Q_v = \frac{\alpha_a(x)}{\rho(x)c(x)}|p(x,f_c)|^2 \qquad (2 - 25)$$

and:

$$Q_v = \rho(x)c(x)\alpha_a(x)|v(x,f_c)|^2 \qquad (2 - 26)$$

where $\rho(x) \cdot c(x)$ is the acoustic impedance at point x. $p(x, f_c)$ and $v(x, f_c)$ are the pressure and velocity amplitudes at point x at the central frequency f_c, respectively.

The spatially variable, Q_v, (or named as the *SAR*, in W / cm^3) is actually a time-averaged, pressure-related value:

$$Q_v = \frac{1}{\tau} \int_{t'}^{t'+\tau} \frac{2\alpha}{\rho c \omega^2} \left(\frac{\partial p}{\partial t} \right)^2 dt \qquad (2 - 27)$$

where τ and ω are the period and the angular frequency of the ultrasound wave, respectively, and t' presents a specific time point beyond which the acoustic field is relatively constant-wave in character. This variable Q_v can thus be demonstrated as the gathered acoustic energy deposition in a unit volume of tissue over one single cycle.

The Q_v (or *SAR*) gain is defined as the ratio of Q_v at the target to the value at the point to spare. In practical terms, the heat source term Q_v is complex as it depends on the nature of the focused field produced by the transmitting transducer. But since Q_v represents the time derivative of incremental energy absorbed by the medium mass per unit volume, it can be calculated from the initial rate of temperature increase as the conduction effect is negligible at the beginning of heating (Sun et al., 2008):

$$Q_v = \rho C_p \left(\frac{\partial T}{\partial t} \right) \bigg|_{t=0^+} \qquad (2 - 28)$$

where C_p is the specific heat capacity of the medium at constant pressure.

2.1.3.2 Heat Transfer in Living Tissue

The possible thermal processes in living tissues including convection, conduction, radiation and perfusion (the process by which heat is removed from warmer regions by blood flowing through capillaries and blood vessels, and redistributed to cooler regions), can be described using the Pennes' bio-heat transfer equation (Damianou et al., 1995; Shih et al., 2005; Li et al., 2006; Cobbold, 2007):

$$\rho_t C_t \frac{\partial T}{\partial t} = k_t \nabla^2 T - w_b C_b (T - T_a) + Q_m + Q_v \qquad (2\text{ - }29)$$

where ρ_t, C_t, and k_t are the density, specific heat capacity, and thermal conductivity of the tissue; w_b, C_b, and T_a are respectively the blood perfusion rate in the heated region, specific heat capacity of blood, and temperature of arterial blood. The variables Q_m and Q_v represent the volumetric metabolic heat and the heat source term which is equivalent to the absorbed ultrasound power density in the tissue (Section 2.1.3.1).

Considering the short HIFU sonication duration as well as the small value of Q_m (~ 0.0001 cal/(cm^3·s)), the effects of the blood perfusion rate and heat production rate due to biological reactions can be neglected. The processes of heat energy transfer are thus mainly dominated by the ultrasound power deposition in tissue, Q_v, and the thermal conduction term, $k_t \nabla^2 T$. Although it neglects the effects of discrete blood vessels and the redistribution of thermal energy within the local vascular network, the Pennes' bio-heat transfer equation is still a good and practical approach for modelling the bio-thermal processes.

In calculating the tissue temperature distribution from the acoustical results, the model always neglects the small changes in acoustic properties with temperature. However, changes in wave velocity with temperature may lead to the phenomenon of thermal lensing (Connor and Hynynen, 2002; Connor and Hynynen, 2004), which indicates that the focus of the ultrasound moves as the sonicated material becomes hotter. This effect is particularly caused by heating in the pre-focal region, which can be interpreted as accumulated changes in phase as the ultrasound beam passes through this heated region. In order to integrate the thermal lensing effect in the thermal model, one needs to rerun the acoustic model after each period of thermal calculation. However, this effect is small in focused ultrasound sonications in which the pre-focal heating is always small compared with the heating at the focus.

2.1.3.3 Thermal Dosimetry for Heat induced Tissue Damage

The thermal damage and necrotic volume of tissue induced by HIFU exposures can be predicted using the cumulative equivalent minutes (CEM) proposed by Sapareto and

Dewey (Sapareto and Dewey, 1984), which converts a known temperature time history at a given location (x, y, z) to an equivalent time period of constant thermal exposure at 43 ℃, as follows:

$$t_{43}(x, y, z) = \int_0^{t_{final}} R\left(T(t)\right)^{43-T(t)} dt \approx \sum_0^{t_{final}} R\left(T(t)\right)^{43-T(t)} \Delta t \qquad (2\text{ - }30)$$

where the function $R(T)$ is typically approximated as an empirical piecewise-constant:

$$R(T) = \begin{cases} 0.5 & \text{if } T > 43°C \\ 0.25 & \text{if } 37°C < T < 43°C \\ 0 & \text{otherwise} \end{cases} \qquad (2\text{ - }31)$$

Based on the thermal dose (TD) formula, an exponential relationship exists between the temperature and the exposure time required to thermally destroy the cells in *in vivo* systems. The threshold TD value for tumour tissue coagulation was taken to be 240 equivalent minutes at 43℃, though it may vary within different organs. This limit value provides an effective way to estimate the margin of necrotic tissue by locating the 240 min iso-dose line around the focus (Damianou and Hynynen, 1994; Nell and Myers, 2010; Nandlall et al., 2009). In previous experience, it is unable to produce thermal injury when the temperature near the target area is below 55 ℃.

2.1.4 Cavitation

As described in Section 2.1.3, the fundamental physical mechanism of HIFU is known primarily as the thermal coagulation and ablation. HIFU however is associated with the other phenomenon named as cavitation. Cavitation concerns the small gas inclusions that exist within the propagation medium that is exposed to the HIFU field (Flynn, 1964; Miller, 1987). Cavitation bubbles may form due to boiling of fluid or by the growth of cavitation nuclei within the propagation medium, e.g., in the blood or tissue within the body. Bubble formation from tiny cavitation nuclei may be initiated above a threshold value that is dependent on the peak negative pressure (PNP) of the acoustic wave, the frequency of the ultrasound, the duration and rate of repetition, the properties of the propagating medium (the hydrostatic pressure, density, viscosity, compressibility, heat

conductivity and surface tension), etc (ter Haar & Duck, 2000). Once initiated, the cavitation bubbles oscillate in two forms, i.e. stable cavitation which refers to the radial oscillation of bubbles (as shown in Figure 2.13) or inertial cavitation which means the sudden collapse of these bubbles during the higher intensity sonications. For underwater and *in vitro* studies, cavitation can be detected using a hydrophone and a frequency analyzer to record and analyse the acoustic signal emitted by the bubble cloud (Prat et al., 1994; Khokhlova et al., 2006), however, it is difficult to detect the cavitation *in vivo* because of the short duration of the bubble cloud.
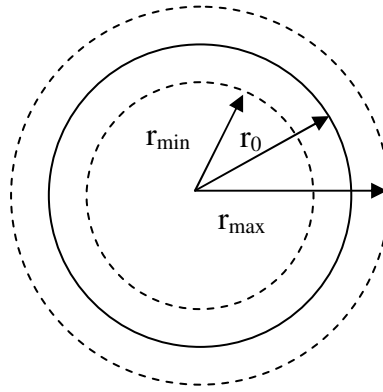
Figure 2.13 Schematic illustration of the radial oscillation of a gas bubble

In cases of high intensity applications, the excess pressure amplitude of the acoustic wave is greater than the hydrostatic pressure of the liquid, and then small bubbles will evolve as a result of the peak negative pressure corresponding to the peak rarefaction pressure of the propagating waveform (Mulvana, 2007). The positive and negative pressure half cycles exert pressure on the bubbles created, causing them to expand and retract in a stable way. When the acoustic intensity reaches a sufficient high level, the change of the negative pressure to the positive initiates the bubble implosion, and the inertia imported into the surrounding liquid results in bubble collapse.

The likelihood of cavitation occurring during a given ultrasound exposure increases as the ultrasonic frequency decreases, as given by the quantitative indicator of the mechanical index (MI)

$$MI = \frac{PNP}{\sqrt{f}}$$

(2 - 32)

where PNP is measured in MPa, and f is the centre frequency of the ultrasound beam (MHz). Typically, ultrasound-induced cavitation occurs above the characteristic threshold of MI = 0.7. As found in other studies, the intensity thresholds for acoustic cavitation in tissue increase with frequency and can be approximated regarding the thresholds in water. It is assumed that intensities greater than 10^5 W/m^2 are required to initiate cavitation in completely degassed water, as shown in Figure 2.14. In Church and Yang, 2005, the inertial cavitation thresholds for bubbles of 1 mm radius excited by 1 MHz ultrasound are 0.1 MPa for blood, 0.2 MPa for liver, 1 MPa for kidney and 1.05 – 1.25 MPa for smooth muscle, respectively.
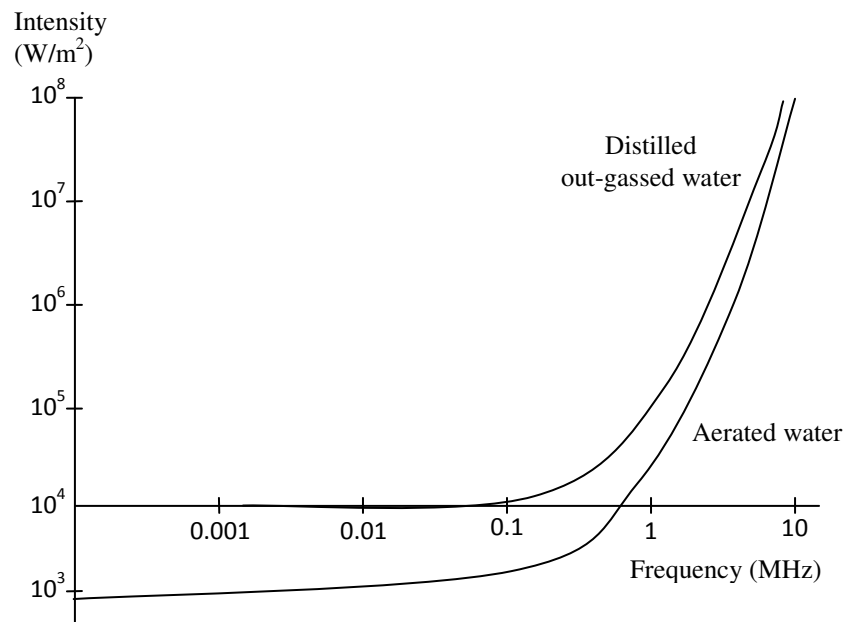
Figure 2.14 Approximate cavitation thresholds for various frequencies in out-gassed and aerated water, *from Cracknell 1980*

These stable and inertial bubble activities in tissue may cause considerable stress to surrounding media, and the collapse of the bubble caused by the rapid change of the negative and positive pressures releases a huge amount of energy, which at some therapeutic intensity levels may cause cellular structure and tissue damage (Prat et al., 1994; Liu et al., 2004). The exact amount of energy can be calculated by the ratio of r_{max} / r_0 (Figure 2.13), together with the surface tension of the liquid. The effects of inertial cavitation present safety concerns to human tissue, and are therefore more significant in clinical therapy. In certain cases, cavitation nuclei, e.g., ultrasound contrast

agents, may be introduced to the target tissue to enhance cavitation effects for therapeutic purposes, so that the threshold intensity values required for cavitation in biological media can be greatly reduced (Miller and Thomas, 1995; Chen et al., 2003). Apart from this, another promising use of the exerted forces is their potential use in mediation of drug/gene delivery (Unger et al., 2001; Bekeredjian et al., 2005).

2.2 Therapeutic Applications of Focused Ultrasound Surgery

Focused ultrasound energy (FUS) also referred to as HIFU, is a noninvasive or minimally invasive ablation technique that has been developed for the treatment of benign and malignant masses. In the past two decades, clinical FUS treatment has been attempted for a number of tumors in different areas of the body, such as prostate cancer, bladder cancer (Vallancien et al., 1996), uterine fibroids, breast cancer, bone metastases, etc. These selected sites are easy for FUS targeting due to the following reasons: (i) the organ remains relatively stationary during the treatment period, (ii) the acoustic window is free from gas and bone, and (iii) the acoustic path is well known. Moreover, recently published research in the field of FUS showed rising interests for non-invasive treatment of brain tumour shielded by the skull and other neurosurgical applications; and for liver, kidney, and pancreas cancer that are located behind the rib cage and can be affected by tissue movement. However, not limited to direct cancer therapy, FUS may also be used for the relief of chronic pain of malignant origin, haemostasis management, and treatment of cardiac conduction and congenital anomalies (Ter Haar, 2007a; Jolesz and McDannold, 2008; Hynynen, 2010).

2.2.1 History of Focused Ultrasound Surgery

The use of FUS as a therapeutic modality was first studied by Wood and Loomis in 1927, in which they found that ultrasound could induce lasting changes such as injury and cell death in biological systems of unicellular organisms, frogs and fish (Wood and Loomis, 1927). In 1942, Lynn and his colleagues succeeded in producing highly localized thermal lesions deep in bovine liver using focused ultrasound beams, without damaging intervening or surrounding tissue (Lynn et al., 1942). In the 1950s, the Fry brothers contributed significantly to the early investigation of this intense focused ultrasound technique towards successful medical applications, such as noninvasive thermal ablation

of localized regions in the brain (Fry et al., 1954; Fry et al., 1955) and the treatment of Parkinson's disease (Fry, 1958). During the same period, Burov et al. (1956) proposed that the high intensity, short duration ultrasound protocols could be used for the treatment of malignant disease. Experiments were also performed by applying FUS to treat malignancies, such as liver and kidney carcinoma (Linke et al., 1973; Frizzell et al., 1977).

Between the 1970s and 1980s, Fred Lizzi's group reported considerable research on the early use of FUS in the treatment of ophthalmological problems, including glaucoma, retinal tears, and traumatic capsular tears (Lizzi et al., 1978; Coleman et al., 1985a, b; Coleman et al., 1986), however, the rising medical laser technique has restrained the use of FUS in most of these clinical applications.

Encouraging FUS outcomes began to be published since 1990, with the advent of advanced medical imaging techniques such as computed tomography (CT), B-mode ultrasound imaging, and magnetic resonance imaging (MRI) for accurate targeting and monitoring purposes (Hynynen et al., 1993; Cline et al., 1993), as well as technical improvements in transducer design. With the recent pioneering research in several groups led by Dr. Gail ter Haar (The Institute of Cancer Research, UK), Dr. Feng Wu (Chongqing Medical University, China; Churchill Hospital, UK), Dr. Kullervo Hynynen (University of Toronto, Canada), Dr. Ferenc A. Jolesz (Brigham and Women's Hospital, US), Dr. Jean-Yves Chapelon (INSERM, France), and others, it is recognized that the development of image guidance is of greatest importance towards the aim of an ideal non-invasive surgery solution. Considering the requirements of accuracy, resolution, radiation safety and the ability of generating thermal information, ultrasound and MR are the two most widely used imaging techniques for now.

2.2.2 Existing Applications

2.2.2.1 Prostate Cancer

Prostate cancer is one of the most prevalent types of cancer and is the second cause of death from cancer in men in the UK. Due to the substantial side effects of current standard curative methods such as prostatectomy and radiotherapy, opportunities exist for

the alternative therapy of image-guided FUS that does not exclude other treatment modalities and can be repeated in the case of local failure. The intracavitary FUS systems for the treatment of benign prostate hyperplasia and localized prostate cancer include the Sonablate 500 (Focus Surgery, Inc., USA), Ablatherm (EDAP TMS, France) and others, but all have limited treatment follow up data. Those published references (Sanghvi et al., 1996; Madersbacher et al., 2000; Gelet et al., 2000; Blana et al., 2004; Uchida et al., 2005; Poissonnier et al., 2007; Blana et al., 2008) revealed promising clinical results, but with occasional complications such as skin burn, thermal injury to adjacent vital structures, transient urinary retention, stress incontinence, rectal fistulas, urinary infections, bleeding, gastrointestinal toxicity, etc. Other limitations of this transurethral or trans-rectal approach might be concluded as the requirement of spinal or general anesthesia, the probability of inaccurate targeting, and lengthy treatment times. And the responses are greatly complicated by the close proximity of the neurovascular bundles, external striated sphincter, rectum striated sphincter, rectal wall, etc. Nevertheless, those early promising results offer the potential that FUS may become a well-accepted treatment option in the near future.

2.2.2.2 Uterine Fibroid

Uterine fibroid is the most common benign tumour in females and its occurrence rate is between 20 to 40 % among reproductive-aged women, mostly in their middle and later reproductive years. The image-guided FUS may prove to surpass all previously described techniques such as surgery, radiofrequency ablation, endometrial ablation, etc, due to its non-invasiveness and organ preservation capability. The ultrasound-guided Model-JC high intensity focused ultrasound tumour therapy systems (HAIFU[TM] Technology Company, China) and the ExAblate magnetic resonance-guided focused ultrasound systems (InSightec Ltd., Israel) are the two most widely used extracorporeal system series around the world and produced most of the clinical references in this thesis. In 2004, the ExAblate 2000 system was first approved by U.S. Food and Drug Administration (FDA) for the clinical treatment of uterine fibroids. A successful treatment can result in a slowly shrinking and decreased volume of fibroid (Tempany et al., 2003; Stewart et al., 2003; Hindley et al., 2004; Rabinovici et al., 2007). Occasional complications were reported as urinary infection, temporary nerve irritation, skin redness and others. However, all these complications can be avoided by accurate and careful treatment planning and monitoring.

For safe operation, one needs to clear the beam pathway from the abdominal wall to the fibroid without passing through the bladder or bowel and make sure that there are no abdominal scars there (Zhang et al., 2010; Zaher et al., 2010). As the typical dimensions of a single lesion are substantially small, another particular concern is thus the improvement of treatment efficiency when a large fraction of the volume of uterine fibroids is to be ablated (Morita et al., 2009).

2.2.2.3 Breast Cancer

Breast cancer comprises 31% of all cancer incidences among women in the UK, and it is the third most common cause of cancer death here. Conventional treatment methods for patients with breast cancer include surgery followed by adjuvant therapy (chemotherapy, radiation, or both). While the image-guided FUS technique, as discussed above, can offer distinct advantages of decreased complication risks (bleeding, infection, seroma formation, chronic incisional pain, etc) and cosmetic outcome (avoiding surgical removal) (Hynynen et al., 2001a; Gianfelice et al., 2003; Wu et al., 2003a; Wu et al., 2005a). This extracorporeal FUS therapy or adjunct therapy can be performed under conscious sedation and patients may leave the hospital the next day after the operation, making a significant reduction in cost. However, there are still problems in terms of increased treatment time for larger tumours and possible side effects such as skin burn (Furusawa et al., 2006; Wu et al., 2007). Prior to becoming more commonly used and widely accepted, long-term randomized studies of FUS to treat breast tumours are still required (Schmitz et al., 2008).

2.2.2.4 Bone Metastasis

Malignant bone tumours (< 1 % of all malignant tumours) rarely occur as a primary tumour, but more generally from metastatic disease from cancer originating elsewhere in the body. After lungs and liver, bone is the third most common site of metastatic spread. Bone metastases at the ribs, pelvis and spine may be found in up to 85 % of patients dying from breast, prostate or lung cancer. Severe pain is the most common symptom found in 70 % of patients with bone metastases. Standard care of palliative radiation therapy provides pain relief in most of patients, while the image-guided FUS may offer significant advantages over current treatment options in that there is no radiation, the

treatment can be repeated as many times as needed for pain control, and limb sparing (Catane et al., 2007; Gianfelice et al., 2008; Liberman et al., 2009). A multicentre study to evaluate the safety and effectiveness of the ExAblate 2100 conformal bone system (InSightec Ltd., Israel) in the treatment of pain resulting from metastatic bone tumours has been under way. The FUS technique has been initially shown to have minimal or no side effects, however further large-scale, long-term randomized studies need to be performed. Of particular importance, attention should be paid to avoiding thermal damage to adjacent organs, nerves, bowel wall, or affecting bone breaking. As the ultrasound absorption in bone is much higher than that in soft tissue, FUS may also be ideal for bone tumour heating or thermal ablation of tissue at the interfaces with bone (Smith et al., 2001; Chen et al. 2010).

2.2.3 Promising Applications

2.2.3.1 Brain Cancer and Neurosurgery Applications

Brain cancer comprises 1.4 % of all cancer types and 2.4 % of all cancer deaths. In the UK, in 2008, there were 3,674 deaths as a result of brain and other central nervous system cancers (data from Cancer Research UK). Considering other treatment needs such as clot lysis for stroke, functional brain and neurological disorders, it is highly recommended to develop an ideally truly non-invasive transcranial ablation method, for example the image-guided FUS. The earliest experience with FUS was associated with applications for brain tumour treatment (Fry et al., 1954; Fry et al., 1955), however, the lack of adequate image guidance and accurate control of energy deposition patterns has prevented its use in clinical research. The presence of human skull distorts the ultrasound beam severely due to the heterogeneity and variable thickness of the bone structure. Also, because of the higher ultrasound absorption in bone, overheating of the skull may be found during the procedure.

In recent studies, adaptive focusing techniques based on manipulation of multi-element phased arrays have been developed (Thomas and Fink, 1996; Tanter et al., 1998; Hynynen and Sun, 1999). In these methods, the geometric and density information of the skull is derived from CT images (Aubry et al., 2003) and the skull model is reconstructed accordingly. These proposed techniques allow for correction of skull-induced ultrasound

beam aberrations without overheating the skull (Hynynen et al., 2004; Pernot et al., 2007; Pulkkinen et al., 2011). Based on the above mentioned studies, two FUS systems were designed for clinical brain applications: the ExAblate 4000 system (InSightec Ltd., Israel) and the SuperSonic brain therapy system (SuperSonic Imagine, France). In a feasibility study in clinical research, ten patients diagnosed with recurrent glioblastoma multiforme have been recruited to be treated using the ExAblate 4000 system (McDannold et al., 2010). Their preliminary results obtained from three patients showed that focused ultrasound can thermally ablate target tissue transcranially, eliminating the necessity of craniotomy and its associated risks and costs. These nonivasive operations induced minimal skull heating, as shown in Figure 2.15, and no neurological deficits were noted during or after these procedures.
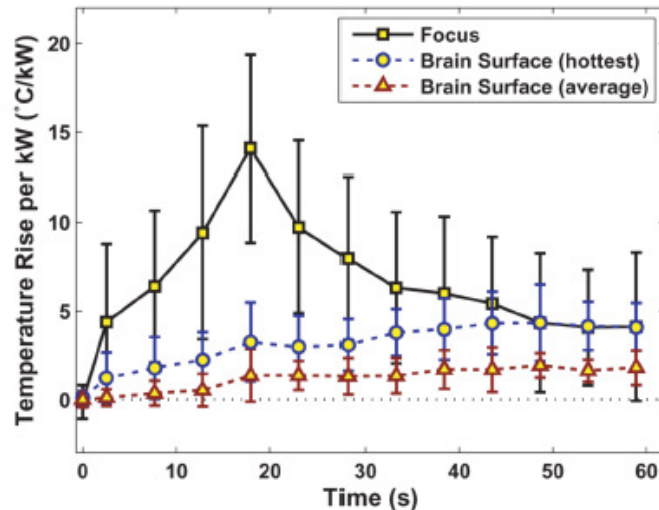
Figure 2.15 Temperature rise normalized to applied acoustic power as a function of time at the focus and on the brain surface, *from McDannold et al., 2010*

Patients with hemorrhagic and ischemic stroke may benefit more from FUS compared with current use of thrombolytic drugs such as the tissue plasminogen activator (tPA) (Daffertshofer and Hennerici, 2003). Liquefaction of a clot inside a blood vessel can be enhanced by the collaborative use of focused ultrasound, microbubbles and thrombolytic agents at lower energy (Stone et al., 2007; Medel et al., 2009). For ischemic stroke, the dissolved residues can be dissipated by normal circulation, while for hemorrhagic stroke, those pieces need to be taken away using other draining techniques. This treatment modality is still under preclinical investigation in order to optimize treatment parameters (Schafer et al., 2005; Ivancevich et al., 2010).

The most promising application of FUS is referred to as targeted drug delivery. The blood brain barrier (BBB) represents an obstacle for delivering macromolecular drugs to the central nervous system (Hynynen et al., 2001b; Hynynen et al., 2005; McDannold et al., 2005). The safe and noninvasive opening of the BBB can be accomplished using ultrasound and microbubbles at lower intensity levels. Focused ultrasound in combination with microbubbles may enhance the BBB permeability (Meairs and Alonso, 2007); and the microbubbles can lower the threshold for cavitation, hence this mechanical bio-effect may facilitate the BBB disruption at further lower signal levels (McDannold et al., 2006). The focused ultrasound mediated delivery can be applied for various substances such as genes, antibodies, growth factors and chemotherapeutic agents (Kinoshita et al., 2006; Kinoshita et al., 2007; Treat et al., 2007). The effectiveness of this approach for various sized therapeutic agents across the BBB and into the central nervous system has been tested and shown to be reproducible and controlled (Choi et al., 2010). Furthermore, focused ultrasound combined with encapsulated nanoparticles may prove to be more effective than delivering the drug alone, partly for eliminating the possible toxic side effects of the drugs (Rapoport et al., 2007).

2.2.3.2 Liver, Kidney, Pancreas Cancers

Sharing similar position information of location behind the rib cage, the upper abdominal organs of liver, kidney and pancreas are attributed to the same category as 'trans-costal sites'. In the UK each year, about 3,960 cases are diagnosed as primary liver cancer, among which 85 % cases are with hepatocellular carcinoma (HCC) (data from Cancer research, UK). Because of tumour multifocality, portal vein invasion and underlying advanced cirrhosis, only less than 20 % of patients with HCCs are suitable for surgical resection (Wu et al., 2005b). Particularly, the high prevalence of HCC in China has created specific needs of affordable and successful treatment solutions. In recent years, various non-surgical, minimally invasive techniques, such as the ethanol ablation therapy, cryotherapy, microwave therapy, radiofrequency ablation therapy and laser therapy have been developed and increasingly used for patients with small-volume HCCs (< 3-4 cm in diameter) (Garcea et al., 2003). With the advent of modern imaging techniques, the practical applications of extracorporeal FUS for the treatment of HCCs are becoming possible. Early clinical studies of hepatic FUS showed that it was both safe and feasible

to induce complete coagulative necrosis in the liver (Vallancien et al., 1993; Kennedy et al., 2004b; Illing et al., 2005; Wu et al., 2004a, b; Wu et al., 2005b; Ng et al., 2011). In Wu *et al.* (2004c), 55 patients with large-volume, advanced HCCs (tumour size ranged from 4 to 14 cm in diameter) were treated with FUS. Large areas of coagulated necrosis were accomplished by moving the therapeutic transducer extracorporeally. Less severe postoperative complications and side effects have been recorded as pain, fever, skin burn, local infection, tumour bleeding or large vessel rupture, hepatic dysfunction, bowel perforation, etc. The respective survival rates at 6, 12, and 18 months were 86.1%, 61.5%, and 35.3%. Wu et al. (2005b) and Jin et al. (2011) also indicated that FUS used in combination with transcatheter arterial chemoembolization (TACE) could offer median survival benefit in the treatment of large-volume, advanced-stage HCCs.

Kidney cancer ranks as the eighth most common type of cancer in the UK, and more than 9,286 patients are diagnosed each year. Though surgery remains the gold standard treatment solution for renal tumours, it is accepted that a non-invasive, nephron sparing way is highly preferred, given the particular risks of surgery in the elderly population (Vallancien et al., 1993; Wu et al., 2003b; Roberts, 2005; Whelan, 2006; Deane and Clayman, 2006). Illing *et al.* (2005) demonstrated the preliminary western experience in the FUS treatment of 30 patients with hepatic and renal tumours (27 evaluable patients). It has been seen that only favourable adverse event profiles (mild discomfort, skin toxicity, subcutaneous oedema and low-grade fever) were reported after extracorporeal FUS ablations. However, tumours in the kidney were killed less consistently than tumours in the liver, which can be explained as the greater depth of kidney tumours and presence of the perinephric fat. Ritchie et al. (2010) documented the FUS management of small renal masses (SRMs) in 17 patients (2 patients were abandoned because of intervening bowel). Findings from their study suggested that extracorporeal renal FUS might be effective in appropriately selected cases, since ablation of tumours lying close to bowel or gall bladder runs the risk of visceral perforation.

Pancreatic cancer is the tenth most common type of cancer, and each year about 8,364 people get pancreatic cancer in the UK. Due to the difficulty in early detection of small pancreatic tumours using current abdominal imaging techniques, ~80 % of patients are first diagnosed with late stage, unresectable tumours. The reported median survival time for patients with locally advanced pancreatic cancer is usually about 6 - 10 months; for

patients with metastatic disease, it is reduced to 3 - 6 months only. The five year survival rate is the lowest among other cancer types, as only 2 %. Till now, no effective treatment modality has been shown to offer survival benefits for patients with pancreatic diseases. Although those minimally invasive strategies mentioned for the hepatic and renal tumours have also been investigated for the pancreatic tumours, FUS may play a more prominent role in future as a result of its non-invasiveness, conformal capabilities of ablating large tumours and pain relief (Zaitsev et al, 1996; Ganaha et al., 2005). Wu *et al.* (2005c) reported their initial experience of FUS in the treatment of 8 patients with advanced and unresectable pancreatic cancer. The follow-up results showed that only occasional minor complications (e.g. abdominal pain, pancreatitis, peritonitis, jaundice, skin burn, tumour bleeding, large vessel rupture and gastrointestinal perforation) were detected after the pancreatic FUS therapy. The preoperative pain disappeared immediately after the FUS ablations and the median survival time was substantially increased to about 11.25 months (range, 2 - 17 months). Randomized controlled trials are now needed to evaluate the effectiveness of FUS for various trans-costal tumours.

2.3 Technical Obstacles to Trans-costal Focused Ultrasound Surgery

2.3.1 Presence of Rib Cage

Although FUS has already been used clinically in the treatment of tumours in the upper abdominal organs (liver, kidney and pancreas), there are some technical limitations. One particular concern is the thermal damage to skin/subcutaneous tissue and ribs in the ultrasound beam pathway, as seen in Figure 2.16 and Table 2.4, as well as the decreased efficacy of cancer treatment at deep targets due to the influences of the layered structures of the abdominal wall. Along the beam path from transducer to liver, kidney, or pancreas, strong reflection, attenuation and diffraction of ultrasound occur at interfaces between tissues with significantly differing acoustic impedances, i.e. the skin surface, the rib cage, the abdominal muscle and the perinephric fat. Due to the higher absorption coefficient of rib bone and the spatial structure of the rib cage, the ribs cause unwanted absorption of the ultrasound beam and hence not enough energy transmitted to the target region. Zhu *et al.* (2009) performed partial ribs resection prior to therapeutic FUS procedures for 16 patients with HCCs. Ribs 6 to 10 (mostly, ribs 7 - 9) at the lower right chest wall were partially removed to obtain an adequate acoustic window to allow HIFU delivery. Even

though this measure might offer the best chance of increased survival rate and complete tumour ablation to patients who have no other treatment options, it lost the benefits of being non-invasive.
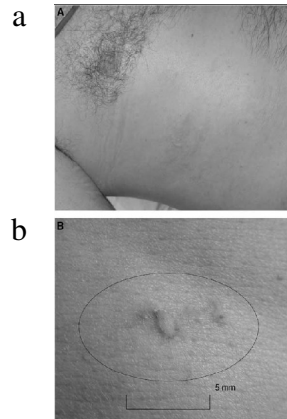
Figure 2.16 Grade 1 skin toxicity after inter-costal FUS treatment to a liver metastasis: (a) right chest wall, (b) Close-up view of lesion, *from Illing et al. 2005*

Table 2.4 Complications of FUS for hepatic and pancreatic cancer, *from Jung et al., 2011*

	Hepatic tumors	Pancreatic cancer
Hospital stay (average, median, range)	5.4 days, 5 days (2 – 15 days)	9 days, 6 days (4 – 29 days)
Skin redness and edema	In all 79 patients	In all 35 patients second-degree burn in one third-degree burn in one
Necrosis of beam pathway	Rib necrosis in all patients	Subcutaneous layer fat necrosis in 10, vertebral necrosis in all
Pain		
None	27 (34%)	10 (29%)
Grade 1	30 (38%)	15 (43%)
Grade 2	18 (19%)	6 (17%)
Grade 3	4 (9%)	4 (11%)
Post-ablation syndrome	9 (11.4%)	6 (11.7%)
Asymptomatic pleural effusion	38 in 53 patients with artificial effusion at the 2-week follow up	N/A
Remark	Transient pancreatitis in one	Transient pancreatitis in six

2.3.2 Abdominal Organ Motion Caused by Respiratory Movement

One other concern is the movement of target organs during the FUS exposures. Previous studies (Bryan et al., 1984; Davies et al., 1994) revealed that the abdominal organs can move up to 20 mm within a respiratory cycle and the moving speed can be up to 15 mm/s. The respiratory and cardiac motion induced organ movements will lead to misdirected energy delivery, which may cause thermal damage to the surrounding normal tissue as

well as incomplete ablation of the target tumour. Early clinical trials (Visioli et al., 1999; Allen et al., 2003) reported poor FUS treatment outcomes due to organ movements. In current clinical studies, epidural or general anesthesia with endotracheal intubation and mechanical ventilation is usually employed for the ablation of tumours located behind the ribs (Kennedy et al., 2004b; Wu et al., 2004b). This measure enables single lung ventilation on either side and hence controls the respiratory movement of the target organ. However, it may result in significantly longer treatment times than desirable, and it will also lose its real benefits of being non-invasive.

2.3.3 Highly Perfused Organs

Another challenge in the upper abdominal organs is related to perfusion, which describes the process of heat transfer from warmer regions to cooler regions by blood flowing through capillaries and blood vessels (Cobbold, 2007). Different from conventional hyperthermia (43 - 45 ℃), the rapid deposition of FUS energy leads to a dramatic rise in temperature in the heated region which may be less dependent of cooling by vascular perfusion or blood flow. The effect of perfusion on the generated HIFU lesion size was studied in *in-vivo* rat livers by Chen et al. (1993a, b). Their published results showed that the size difference between a lesion produced with normal blood flow and that with reduced blood flow became significant for exposure durations longer than 3 s. This could be interpreted in a different way that short ultrasound pulses and small focal regions might deliver thermal doses that were nearly perfusion independent. Further effects of different vessel sizes on FUS lesions and the effects of FUS on the vessels near the target region (e.g. to occlude the feeding blood vessels of tumours) are undergoing histological and radiological investigation in Dr. Gail ter Haar's group in the Institute of Cancer Research, UK and other labs (Chen et al., 2011).

2.3.4 Prolonged Treatment Times

Depending on the tumour size, location and blood supply, the trans-costal FUS treatment durations are typically 2 - 8 hours with the peak intensities ranging from 5,000 to 20,000 $W \cdot cm^{-2}$ (Illing et al., 2005). However, only less than 20 % of the duration is active for tumour ablation, giving the extra time between successive ultrasonic exposures to allow

surrounding tissue to cool down, as listed in Table 2.5. Longer treatment durations can result when considering the need to frequently verify the focus position within the target region by imaging. This considerably long time makes FUS much less favourable compared with alternative treatment options of surgical resection or other minimally invasive techniques. Also, clinical FUS procedures are performed under either general or regional anesthesia, which are selected on the basis of preoperative patient parameters, treatment time, etc. The prolonged anesthesia time may cause serious problems to elderly patients or patients in poor physical conditions. However, the treatment time can be reduced with the technological and methodological developments of this technique and/or in combination with other methods, such as mechanical cavitation. In addition to the main mechanism of tissue heating, at high exposure levels, the ultrasound-induced cavitation is also inseparably responsible for tissue damage caused by FUS. Previous results (Holt et al., 2001; Coussios et al., 2007; Coussios et al., 2008) have shown that acoustic cavitation could enhance heating and use of contrast agent microbubbles could increase the rate of tissue ablation. In future this technology may prove to be useful to enhance treatment efficacy in clinical applications.

Table 2.5 Patient treatment parameters, *from Illing et al. 2005*

	Mean (min)	Range (min)
Anesthesia time	209	150 -271
Patient positioning	17	8 -14
Time to locate tumour and plan treatment	46	8 - 133
Treatment duration	123	20 - 189
Total exposure	20	0.2 - 43.5

2.4 Strategies for Improving Treatment Accuracy of Trans-costal Focused Ultrasound Surgery

The commercially available image-guided FUS systems include key components of the imaging unit, treatment unit, positioning unit, and console operator. The treatment unit integrates the function generator, power amplifier, power-meter, matching circuit, active transducer and cooling device, while the console operator controls the treatment planning and operation. In this section, strategies for improving the precision and efficiency of trans-costal FUS therapy will be summarized in these four units.

2.4.1 Imaging Unit

For accurate preoperative treatment planning, and intra- and post-operative monitoring of tissue damage progression, advanced imaging techniques are required for higher temporal and spatial image resolutions. In most clinical trials, identification and localization of target tumours, monitoring and assessment of thermal coagulative necrosis have been achieved by means of real-time ultrasound imaging or magnetic resonance imaging (ter Haar, 2001; Kennedy et al., 2003; ter Haar, 2007b). It has been known that these modern imaging techniques provide sufficient information for relatively safe and effective energy delivery. Both approaches have advantages and weaknesses. B-Mode US imaging provides real-time images and the bright (hyper-echoic) region appearing in ultrasonic images correlates well with the ablated volume in tissue, though difficulty has been proven in the absence of bubbles. MRI offers superior soft tissue contrast and is the best option for tumour detection, target definition and tissue coagulation detection. The real-time feedback of temperature changes in MRI images as well as the thermal dose maps displayed are able to guarantee the safety of patients during ablation. However, the non-real time imaging and higher cost of the MRI scanner may limit its use in economically undeveloped areas compared with conventional B-mode US imaging.

In clinical studies, some early-stage, small tumours located deep within these upper abdominal organs cannot be detected using current imaging techniques. It is therefore impossible to perform FUS ablations in patients with these malignancies. More promising imaging techniques such as themoacoustic tomography, MR diffusion weighted imaging, MR elastography, ultrasound elastography, acoustic radiation force imaging, etc., may play important roles in future (Jin et al., 2005; Jacobs el al., 2010; McDannold and Maier, 2008; Hou et al., 2011; Hertzberg et al., 2010). Some research groups have also reported their efforts towards dual-modality and/or multi-modality imaging applications, e.g., US imaging combined with CT or MRI. As a reference, Petropoulos and Saunders (2011) proposed a MRI and US guided treatment method, which characterizes the organ motion and relates it in real-time with faster imaging modalities. During this procedure, the MR images of the moving region of interest (movement caused by breathing, cardiac or other action) is registered with the real-time ultrasound images so as to locate the region of interest in the ultrasound images and, based on the registered images, to continuous track the organ motion as it moves.

2.4.2 Treatment Unit

Considering the most widely used Model-JC tumour therapy system (Wu et al, 2004a, 2004b, 2004c), the trans-costal thermal ablation of large tumours has been achieved by mechanically moving the therapeutic transducer that is mounted in a water bath and can be electronically driven to move in six orthogonal and rotational directions. The plane, single-element piezo-ceramic transducers (aperture of 120 mm, operating frequencies of 0.8 and 1.6 MHz) fronted by series of acoustic lenses (focal length ranging from 90 to 160 mm) need to be selected for a given tumour location. It is therefore impossible to avoid ultrasound radiation on the ribs when using these single-element transducers. Instead, new technology incorporating the multi-element phased array and advanced focusing algorithms (e.g. phase conjugation and time reversal methods) may allow larger amounts of tissue to be destroyed in one single shot, and with versatile beam steering, for example to avoid the rib structures during the treatment (Civale et al., 2006; Liu et al., 2007; Aubry et al., 2008; Quesson et al., 2010; Bobkova et al., 2010). Also, new transducer design may facilitate exploitation of mechanical cavitation effects in addition to thermal effects (Melodelima et al., 2004).
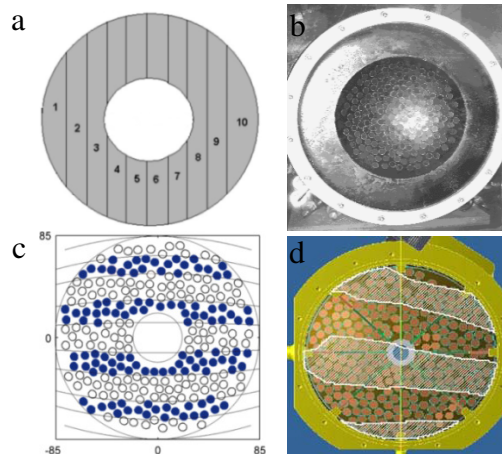
Figure 2.17 (a) 10-element, 1.7 MHz transducer, *from Civale et al., 2006*; (b) 200-element, 1 MHz array, *from Aubry et al., 2008*; (c) 254-element, 1 MHz array, *from Bobkova et al., 2010*; and (d) 256-element array, *from Quesson et al., 2010*

In the case of multi-element phased arrays, as seen in Figure 2.17, the size and number of each individual element, their distribution, the electrical signal applied to each element,

etc, need to be determined with compromise to achieve a satisfactory acoustic field (in terms of size, shape and position) and maximum acoustic power. This procedure may increase the focal volume that can be ablated in a single shot, hence reducing the treatment time. One particular problem associated with the arrays is the grating lobes caused by ultrasound energy spreading away from the intended central lobe; this happens when the element spacing is larger than a half wavelength. In the literature, the random array design may minimize this effect and further reduce the treatment duration.

Ideas of creating contiguous lesion arrays throughout the intended volume by combined electronic and mechanical scanning of the HIFU beam may greatly enlarge the regions of thermal damage. Adjustment in the speed of lesion positioning or the scanning speed of the therapeutic transducer could be further improved to compensate for large-scale organ motion and always keep the target tumour within the therapeutic window (Pernot et al., 2004; Marquet et al., 2011).

2.4.3 Positioning Unit

For all the FUS systems mentioned above, the active transducer can be generally described as a single-element transducer or an electronically-steered phased array transducer, mounted on a moveable frame inside the patient table. These transducers allow for mechanical and/or electronic focus repositioning, however their spatial beam steering abilities are limited to a few centimeters. In addition, these transducers can only provide ultrasound access from below the body. To overcome these problems and further improve the precision and efficiency of the FUS therapy, the concept of robot-assisted intervention is proposed (Krafft et al., 2010). Compared with current commercially available FUS systems, this combined robotically assisted FUS system, as illustrated in Figure 2.18, may provide more flexible positioning of the therapeutic transducer and more superior directing of the ultrasound beam, for example for the purposes of substantially avoiding the rib structures and targeting the moderately moving organs.
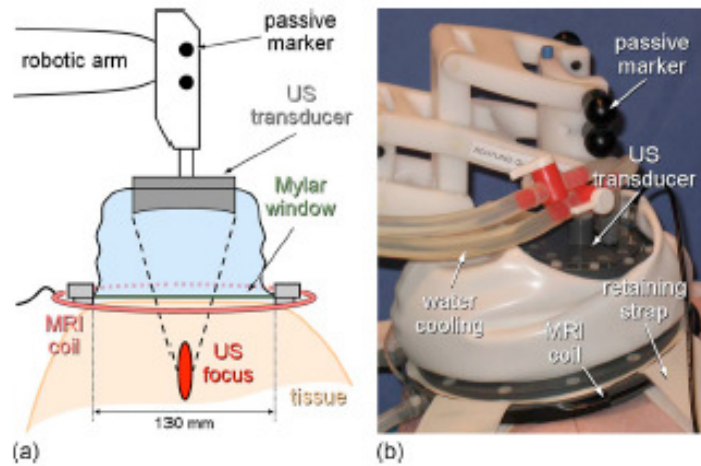
Figure 2.18 Combined robotically assisted FUS system, *from Krafft et al., 2010*

2.4.4 Advanced Treatment Planning

To improve the safety and effectiveness of image-guided FUS in the treatment of large tumours, a fast and accurate treatment planning method is necessary. The treatment planning procedure refers to the numerical determination of optimal FUS exposure parameters satisfying the therapeutic purposes at the target tumours and sparing other structures at risk, e.g., the ribs, on the basis of the pre-treatment images, e.g. CT scans (McGough et al., 1996; Liu et al., 2005; Liu et al., 2010a; Marquet et al., 2009). For a specific patient case, the ultrasound-induced temperature and thermal dose distributions (the volume of induced tumour solidification, as discussed in Section 2.1.3) can be estimated by the dosage calculation formula including variables such as the frequency, the acoustic intensity or power level, the ultrasound emission time, the complex internal structures, the acoustic and thermal properties of various tissue and/or bone, etc. A safe treatment can be guaranteed by implementing a robust and effective spatial-and-temporal temperature or thermal dose controller (Arora et al., 2005; Zheng et al., 2010). If it fails to meet standard safety guidelines, the operator needs to adjust the FUS power or stop the procedure immediately.

In the trans-costal FUS applications, since ultrasound is reflected and distorted at the interfaces and is greatly attenuated in the rib bone, an adequate acoustic window is required to enable the beam to reach the targeted region, while avoiding other challenging obstacles of lung, rib, and bowel. The rib bone can be problematic due to its high attenuation, varying thickness and density, just as the human skull. The non-uniform soft

tissue can cause scattering and diffraction of the beam, and also need to be considered in treatment planning. To date, many different methods have been used to model the ultrasonic beam scattered and diffracted by the rib cage. These include the 2D finite difference time domain method combined with the time reversal technique (Aubry et al., 2008), the 3D finite difference frequency domain solution of the KZK equation (Li et al., 2007; Liu et al., 2010b), the modified Rayleigh-Sommerfeld integral method (Liu et al., 2007), simple analytical solutions of parabolic approximations of diffraction theory (Khokhlova et al., 2010), and a boundary element approach based on a generalized minimal residual (GMRES) implementation of the Burton-Miller formulation (Gelat et al., 2011), and others (Bobkova et al., 2010). Nevertheless, knowledge of the influence of ribs on the propagation of focused ultrasound or even its possible impacts on the safety and efficacy of trans-costal FUS treatment are still quite fragmented and limited.

2.5 Discussion

A review of the literature has revealed that image-guided FUS is a promising non-invasive treatment modality for tumour ablation. Its ability to ablate a wide range of tumour types has been demonstrated in clinical studies. However, the relevant results have all been obtained from non-randomized clinical trials. Large-scale long-term randomized controlled studies will therefore be necessary to fully understand the potential role of this novel treatment technique, in particular for trans-costal applications. The technical hindrances addressed in Section 2.3 need to be overcome in preclinical laboratory or animal studies prior to entering into the clinical stage. Following the work presented in Section 2.4, the aims of the present investigation are to study the various influencing factors associated with the presence of the rib cage in extracorporeal FUS treatment of liver, kidney, and pancreas tumours; to optimize the sonication protocols for different tumours encountered in practice; and to minimize heating of the ribs for different tumour positions. This thesis covers devices, equipment, and systems that have been used, material and samples that have been fabricated, and models that have been built during the application and investigation of acoustic and thermal effects in HIFU technique in general and in trans-costal FUS in particular. Special attention has been paid to representative rib cage mimics and samples and qualitative studies relating to them.

CHAPTER 3 EXPERIMENTAL STUDY OF FUS TREATMENT THROUGH THE RIB CAGE

This Chapter details the materials and experimental methods employed in addressing issues related to the presence of the rib cage. Prior to any experiment, both single-element focused ultrasonic devices and tissue-mimicking phantoms for HIFU are characterized first. This is critical for accurately estimating their acoustic and thermal performances. These measurements include electrical impedance and acoustic beam profiling of the HIFU devices (Section 3.1), and acoustic and thermal characterization of the tissue-mimicking HIFU phantoms (Section 3.2). Basic effects during the HIFU procedures are then investigated by delivering series of sonications to the phantoms (Section 3.3). Experimental methods used to investigate specific issue in trans-costal FUS are further presented in Sections 3.4 and 3.5. The effects of focal beam distortion through the rib cage sample (mimics), which result in insufficient energy deposition at the focal region, are presented, and the heating effects at the focus and the ribs, and its frequency dependence are investigated. Section 3.6 furthers the investigation by testing a geometric rib sparing solution with binary manipulation of elements in 2D phased arrays, which aims to avoid overheating of the ribs and enhance localized heating at the target region in clinical trans-costal FUS applications.

3.1 Characterization of HIFU Devices

3.1.1 Single-element Transducers

In this work, three commercial single-element focused ultrasound transducers supplied by Precision Acoustics, UK were used, as shown in Figure 3.1. Their general specifications including the operational frequency, f, the aperture, $2R_s$, and the focal length, Z, are listed in Table 3.1. For ease of description, the devices were named using their corresponding product numbers.
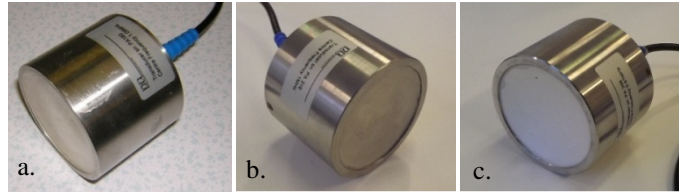
Figure 3.1 Single-element transducers: a) PA160, b) PA316, c) PA356.

Table 3.1 Summary of single-element transducers

Device Name	Active Material	f (MHz)	$2R_s$ (mm)	Z (mm)	$f\#$ ($Z/2R_s$)
PA160	PZT (PZ 54)	1.09	60	75	1.25
PA316	PZT (PZ 54)	1	60	75	1.25
PA356	PZT (PZ 54)	0.67	60	75	1.25

N.B. PA = Precision Acoustics Ltd. Dorset, UK;

Typical components of these single-element transducers include the active piezoelectric material, associated electronics and case for handling. The relevant material properties of the PZ 54 are listed in Table 3.2. The low dielectric loss, tan δ, and low mechanical loss, Q_m, combined with high permittivity, ε, of the material make it particularly suitable for HIFU applications (Wolny, 2005; Zhang et al., 2005). The thickness of the active material in the direction of ultrasound propagation, l, determines the resonant frequency of the transducer, f_r:

$$f_r \propto \frac{c}{2l}$$

(3 - 1)

where c is the speed of sound in the active material.

Table 3.2 Typical material properties of the new HIFU material, PZ 54

Parameters	
ρ (kg/m^3)	7760
$\varepsilon_{3,r}$	2867
tan δ	0.003
T_c (°C)	225
k_p	0.585
k_t	0.485
d_{33}	4.79e-10
Q_m	> 3000

Data from (http://www.ferroperm-piezo.com)

For the spherical bowl focusing transducer, a matching layer may be added to the front

surface of the piezoelectric element to reduce the acoustic impedance mismatch between the electronically active material and the propagating medium, hence improving the energy transmission efficiency. The thickness of the matching layer can be assumed to be equal to a quarter wavelength of the operating frequency of the transducer (λ/4). At this thickness, the reflected waves from the rear and front surfaces of the matching layer will be cancelled due to destructive interference with the forward propagating signal. However, in practice, this presents challenges for fabricating a well-controlled thickness matching layer in a curved shape to precisely match the curvature of the bowl. Moreover, a backing layer made of high attenuative material with the same acoustic impedance of the active material can be added to the rear surface of the piezoelectric element to shorten the ringdown time of the transducer i.e. to reduce reverberation in the piezoelectric material. For the air backed HIFU transducers, as shown in Figure 3.1, potential hot spots may be formed on the surface of the active materials when they are driven with extremely high powers, and may result in damage to the active material, e.g., de-poling and crack formation (Mulvana, 2007).

3.1.2 Electrical Impedance Measurement

A determinant performance indicator of the HIFU devices is their electrical impedance behaviour. Electrical impedance, Z (unit: Ohms), in an alternating current (AC) electrical circuit is determined by

$$Z = \frac{V(t)}{I(t)} \tag{3 - 2}$$

This parameter is unique to the resistance in a direct current (DC) electrical circuit for the inclusion of the time-dependent characteristics, for which it can be represented in the complex format as

$$Z = R + jX, |Z| = \sqrt{R^2 + X^2}, \theta = \arctan\left(\frac{X}{R}\right) \tag{3 - 3}$$

where the real component R is the resistance and the imagine part X is the reactance.

In practical uses, the electrical impedance spectroscopy is represented by the impedance magnitude, |Z|, and phase, θ; or sometimes in the terms of R and X. For the commercial single-element transducers used throughout the investigation (PA160, PA316, PA356), their electrical impedance spectral (impedance magnitude, |Z| and phase, θ) were measured using an impedance analyzer (4395A, Aglient Technologies Ltd., UK), as shown in Figure 3.2. Measurements of electrical impedance were performed with the piezoelectric elements immersed in water to simulate real operation conditions, and the acoustic absorbing material was used to prevent ultrasound reflections that may affect the impedance measurement results. The GPIB data acquisition and import data to Excel was used for data processing.
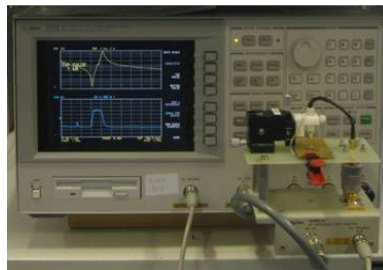
Figure 3.2 4395A Network/Spectrum/Impedance Analyzer.

The resonant frequency (also called as the electrical resonance), f_r, occurs at the impedance minimum of the representative piezoelectric system. At the resonant frequency, the piezoelectric element achieves the highest conversion efficiency from electrical energy to mechanical energy. Transmitting devices should therefore normally work near this frequency. Conversely, the anti-resonant frequency (or mechanical resonance), f_a, occurs at the impedance maximum, and is thus suitable for receiving devices. When an electrical impedance mismatch exists between the HIFU device and associated drive system, the driving power or energy is lost as heat, resulting in an inefficient system and potential risk of damage to the equipment. For the purpose of improving energy transfer capabilities, an additional electrical impedance matching circuit using either standard transformers or matching networks needs to be implemented to influence the electrical resonant behaviour of the device, and match closer to 50 Ω of associated power supply units (Mulvana, 2007).

3.1.3 Beam Profile Measurement

Beam profiles of all single-element HIFU transducers (PA160, PA316, PA356) were characterized by means of acoustic field mapping. The results can provide useful information about the HIFU devices in use, such as field pattern, position of the focus, and the size of the focal region, etc (Canney et al., 2008). Acoustic field measurements were conducted with low power drive conditions (without signal amplification). The standard experimental set-up used throughout the device characterization is shown in Figure 3.3a, in which distinct functions with respect to the acoustic signal generation and transmission (function generator, transducer under test), reception (needle hydrophone, DC coupler), and observation (data acquisition unit (DAQ), PC), etc, are included. In each case, the measurement was performed in degassed water.
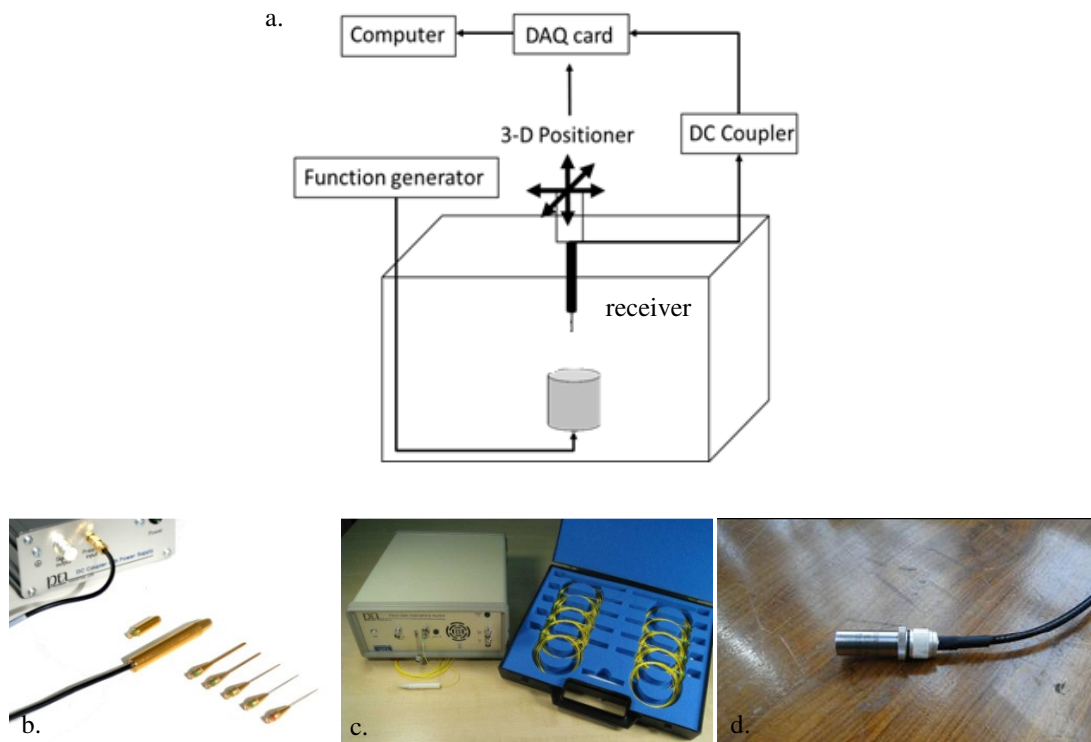
Figure 3.3 Three-dimensional ultrasound scanning system for field mapping.

The electrical input in either forms of a short pulse of energy or continuous energy can be fed into the HIFU devices for the purposes of signal generation and transmission. Throughout the work, continuous sine waveforms with predetermined frequencies and amplitudes were used, due to the requirement of continuous wave HIFU exposures for clinically-relevant ablation. Unless otherwise stated, the drive signals were emitted from a

functional generator (33220A, Agilent, UK), that each transducer under test (fixed on a transducer holder) were driven at relevant resonant frequency, f_r, and with an equivalent amplitude of 8 V_{p-p}.

To detect the output signals, a variety of receiving devices e.g. lab-made receiving transducer, needle hydrophone (Figure 3.3b), fiber-optic hydrophone (Figure 3.3c), membrane hydrophone, etc, can be selected depending upon their suitability and need. For basic signal reception, the lab-made receiving transducer and commercial non-destructive testing (NDT) devices could be used for their fair sensitivities and easy manipulation. In the instances of highly attenuated signals, a pulser-receiver (DPR300, JSR Ultrasonics, USA) could be used for signal amplification. For more accurate acoustic field measurements with finer axial and lateral resolutions, a series of small-diameter needle hydrophones with active sensing diameters of 0.2, 0.5, and 1 mm, respectively (Precision Acoustics, UK), could be used. Unless otherwise noted, the 0.5 mm diameter needle was employed for all the devices under investigation: PA160 (wavelength of $\lambda \approx 1.38$ mm), PA316 ($\lambda = 1.5$ mm), and PA356 ($\lambda \approx 2.24$ mm). The electrical signal output received from the needle hydrophone was then fed to a DAQ unit (CH-1350 PCI DAQ card, Acquitek, France) through a DC coupler (Precision Acoustics, UK), and recorded using a self-developed Labview program. All signal connections were made using 50 Ω co-axial cables.

During device characterization, the needle hydrophone was mounted to a combined 3-D positioner (XSlide and UniSlide, Velmex, USA) and could be scanned in two orthogonal directions, e.g. in the transverse focal plane for the cases, under control of the computer-driven stepping motor controller (VXM, Velmex, USA). The needle hydrophone was advanced in increments as small as 0.01 inches (0.254 mm) in both directions, and a record of the peak to peak signal from the reception device at each location was used to build a 2D matrix of signal amplitudes representative of the acoustic field. The measuring areas were selected to cover the maximum useful field, and one practical indicator was the ability to distinguish the signals from background noise. In the water tank, an acoustic absorber board was placed on the 3-D positioner to prevent reflections of the transmitting wave.

For supplemental investigation of high power characterization, the drive signal emitted

from the signal generator needs to be amplified with a power amplifier (1020L RF power amplifier, E&I, USA) in advance of transmitting to the transducer. Rather than the continuous wave mode mentioned above, the transducer should be driven with pulsed signals in order to prevent overheating or possible damage to the receiving device, and the appropriate amplitudes should also be selected on the basis of avoiding cavitation. In order to detect the high power signals, a novel fibre-optic hydrophone (Precision Acoustics, UK), that simultaneously measure the acoustic pressure and temperature will be used instead (Zhou et al., 2006).

3.2 Characterization of Tissue-mimicking Phantoms for HIFU Exposures

3.2.1 Fabrication of HIFU Phantoms

In fundamental laboratory studies, tissue-mimicking phantoms including Bovine Serum Albumin (BSA) phantom and egg white phantom have been recognized as useful tools for calibration of HIFU transducers and real-time visualization of HIFU-induced lesion evolution (Takegami et al., 2004; Divkovic and Jenne, 2005; Divkovic et al., 2007; Lafon et al., 2001; Lafon et al., 2005). Their corresponding compositions are listed in Table 3.3, and detailed fabrication procedures can be found in the work presented by Takegami et al. (2004) and Lafon et al. (2005).

Table 3.3 Fabrication protocols of tissue-mimicking phantoms for HIFU

Egg White Phantom	BSA Phantom
Degassed, distilled water	Degassed, distilled water
	1mol/L TRIS buffer (PH 8)
Egg white	BSA
Acrylamide/Bis-acrylamide, 19:1 ratio	Acrylamide/Bis-acrylamide, 19:1 ratio
10% (w/v) APS	10% (w/v) APS
TEMED	TEMED

The polyacrylamide gel is formed by polymerization of acrylamide monomer crosslinked by N,N'-methylene-bis-acrylamide (BIS). Since the acrylamide monomer and BIS are nonreactive between themselves when mixed, ammonium persulfate (APS) and -N,N,N',N'-tetramethylethylene diamine (TEMED) are required to start the polymerization reaction. Because the acrylamide monomer is a potent neurotoxin affecting the central and peripheral nervous systems, appropriate safety precautions

(Lafon et al., 2005) must be taken during the fabrication procedures. Although the polyacrylamide gel might be considered to be non-toxic, care should also be taken when handling the gel for the possible presence of free acrylamide monomer.

Having the same temperature-sensitive benefits to BSA, egg white is far less expensive. In the work, the resulting mixtures, which consisted of 30% (v/v) of egg white, provided satisfactory visualization of HIFU exposures (Takegami et al., 2004). The mixtures could be transferred to any desirable mold or container to polymerize. The polymerization reaction was slightly exothermic, and took about 20mins to complete. The polymerized egg white phantom could then be stored in vacuum-sealed, plastic bags to avoid dehydration or swelling.

To date, some research groups have attempted to characterize the tissue-mimicking phantoms acoustically. Lafon et al. (2005) measured the acoustic and optical properties of BSA-embedded polyacrylamide hydrogels as a function of BSA concentration and temperature; Takegami et al. (2001) presented the acoustic property characterization of polyacrylamide gels with different egg white concentrations. However, very limited research has been conducted on the thermophysical characterization of tissue-mimicking phantoms for HIFU; except that Divkovic et al. (2007) reported on the thermal properties and temperature-dependent acoustic properties of egg white phantoms. But, in their study, the thermal conductivity, k, and specific heat capacity, C, were measured separately using the hot-wire method and conventional calorimetry, which are not available in most standard ultrasound labs.

In this study, both acoustic and thermal properties of the egg white phantoms were characterized. The longitudinal wave velocity, c, and attenuation, α, measurements were performed using a non-contact through-transmission ultrasound system for the egg white phantoms with various egg white concentrations ranging from 0 - 40% v/v (by 10 % v/v interval, as shown in Figure 3.4), and concentrations of other ingredients were similar to those reported in Takegami et al. (2004): 19:1 ratio Acrylamide/Bis-acrylamide (24.8 % v/v), 10 % (w/v) APS (0.5 % v/v), TEMED (0.2 % v/v), etc. A relatively simple step-wise transient plane source (TPS) method has been used to simultaneously measure the thermophysical properties of these egg white phantoms for HIFU applications.
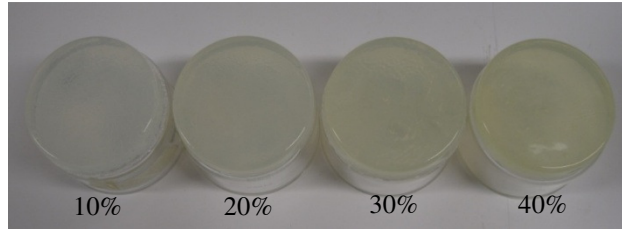
Figure 3.4 Egg white phantoms with different egg white concentrations: 10% to 40%.

3.2.2 Ultrasonic Through Transmission Technique

The most concerning acoustic properties of HIFU phantoms include acoustic impedance, Z, and attenuation, α. The acoustic impedance is determined by multiplying the density of the phantom, ρ, and its longitudinal wave velocity, c. The phantom density is calculated as the mass divided by the volume of the test sample.

Standard non-contact through-transmission techniques using either continuous wave or pulsed signal, are well established for acoustic characterization of isotropic materials (Selfridge, 1985). The continuous wave methods have disadvantages of introducing errors due to reflections, mode conversions and other interfering signals, while the pulsed technique can isolate the transmitted pulse from unwanted signals in the time domain, e.g., reflections and reverberations, and hence offers a more attractive approach.

As illustrated in Figure 3.5, this non-contact through-transmission system uses a pair of 5 MHz plane immersion transducers (SLIH5-10, Sonatest, UK) (Figure 3.3d) which act as a transmitter and a receiver respectively; the upper transmitter, excited in a short-pulse mode (single five-cycle pulses), was mounted on the STAUBLI robot (STAUBLI RX90), while the lower receiver was fixed at the bottom of the water tank; and they were vertical-aligned against each other. A test sample with a known thickness was then inserted between the two devices, with the devices positioned normal to the surfaces of the test sample. The received signal from an amplified receiver (DPR300, JSR Ultrasonics, USA) was displayed on an oscilloscope (TDS2024, Tektronix, USA). All measurements were carried out under water at room temperature.
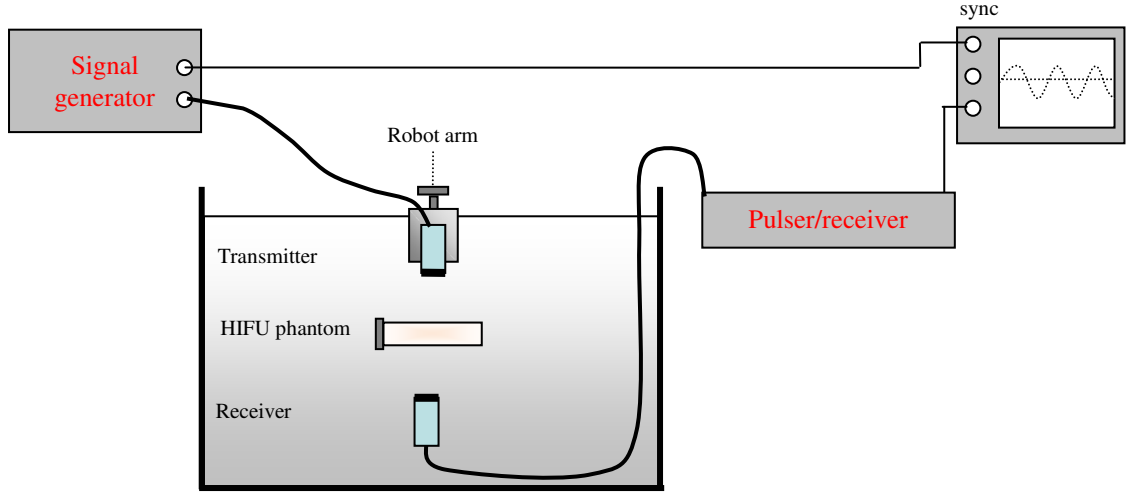
Figure 3.5 Non-contact through-transmission ultrasound characterization system.

The longitudinal wave velocity through a test sample was determined by measuring the time of flight between the excitation pulse and the received pulse of a reference signal in water; and then measuring the time of flight with the test sample inserted; the time difference between these two signals, Δt, was used to calculate the velocity in the non-contact through-transmission mode:

$$V_L = d/[\frac{d}{V_i} - \Delta t] \qquad (3 - 4)$$

where V_L is the longitudinal wave velocity through the sample; V_i is the longitudinal wave velocity in water; d is the thickness of the sample; Δt is the time difference between the two signals.

The time of flight of the two signals without and with inclusion of the test sample refer to the corresponding difference between the excitation time and the arrival time. However, the pulse shape could change when transmitted through a material, especially lossy materials, so that it becomes difficult to assess the arrival time accurately and the data reading process becomes quite subjective. Based on different experimental criteria for accessing the transit time (first arrival, 10% threshold, first zero crossing), as illustrated in Figure 3.6, different times may be recorded resulting in variation in the calculated longitudinal wave velocity. In this thesis, the first arrival method was applied in all measurements for its easy determination.
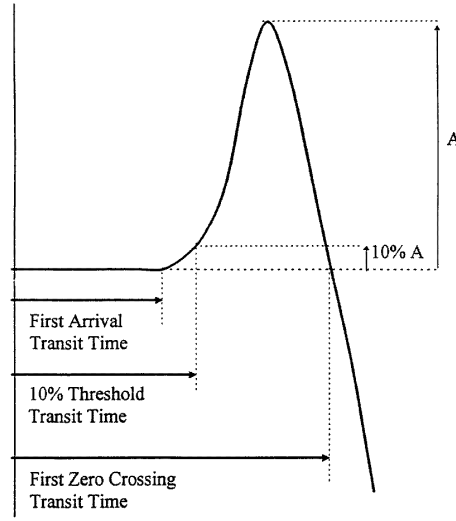
Figure 3.6 Criteria for transient time measurement, *from Nicholson et al., 1996.*

The same experiments were performed to determine the attenuation of the test sample, with the amplitudes of the two signals compared. The attenuation, α (dB/mm), can be calculated as:

$$\alpha = 20 * \log_{10}(T_L \frac{A_w}{A_s}) \bigg/ d \qquad (3-5)$$

where A_w is the amplitude of the reference signal through water; A_s is the amplitude of the transmitted signal through the sample; d is the sample thickness in mm; T_L is the total longitudinal transmission coefficient through both interfaces of the sample. T_L equals to:

$$T_L = \frac{4 Z_w Z_L}{(Z_w + Z_L)^2} \qquad (3-6)$$

where Z_w is the acoustic impedance of the wave in water; Z_L is the acoustic impedance of the wave in the test sample.

Another particular interesting acoustic property i.e., the nonlinear parameter B/A, can be determined with an advanced technique, i.e., the finite amplitude insert-substitution technique that is based upon the comparison between numerical simulations and experimental measurement (Lafon et al., 2005). An estimation of the B/A coefficient at

room temperature from the work mentioned above (B/A = 5, similar to that of water, since it was greatly composed of water) is employed for later numerical analysis in Chapter Four.

3.2.3 Step-wise Transient Plane Source Technique

3.2.3.1 Measurement Principle

As shown in Figure 3.7, the principle of the step-wise TPS method is a relatively new methodology for the measurement of thermophysical properties of solid materials (Kubicar and Bohac, 2001; Tye et al., 2005; Yu et al., 2006; Lei et al., 2009). The test sample is divided into three sections with different thicknesses. A thin layer of a planar heat source is located between layers I and II; while, a fine diameter thermocouple is placed between layers II and III. Applying electric current $I(t)$, in the form of a step-wise function, through the heat source, the resulting temperature response $T(x, t)$ at a distance x from the heat source can be recorded using the thermocouple.
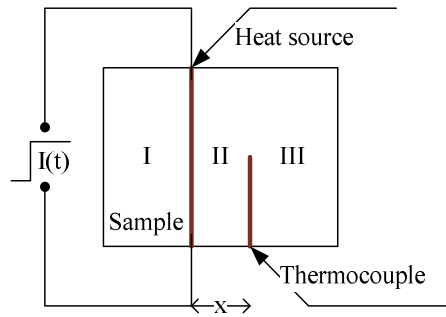
Figure 3.7 Schematic diagram of the step-wise TPS method.

Supposing that the test sample has no heat exchange with surrounding environment and the thickness of the planar heat source is zero, the measurement principle could be taken as the one-dimensional unsteady-state heat conduction problem in semi-infinite solids (Kubicar and Bohac, 2001; Yu et al., 2006):

$$\frac{\partial^2 T}{\partial x^2} = \frac{1}{\alpha}\frac{\partial T}{\partial t}, \quad (0 < x < +\infty) \tag{3 - 7}$$

The initial conditions:

$$T = 0 \ (t = 0)$$

$$k \frac{\partial T}{\partial x} = f(t) \ (x = 0)$$

(3 - 8)

The boundary conditions:

$$T \to 0 \ (x \to \pm\infty)$$

$$\frac{\partial T}{\partial x} \to 0 \ (x \to \pm\infty)$$

(3 - 9)

where $T = T(x, t)$ is the temperature difference between the real temperature and the initial temperature, α is the thermal diffusivity, k is the thermal conductivity, and $f(t)$ is the imposed constant heat flux. In the case of the step-wise TPS method, $f(t)$ is given as

$$f(t) = q = \begin{cases} 0 & (t = 0) \\ \dfrac{I^2 R}{2A} & (t > 0) \end{cases}$$

(3 - 10)

where I is the electric current, R is the electrical resistance of the heat source, and A is the area of the heat source.

By applying the corresponding Laplace transform and inverse Laplace transform to Eqs. (3 – 7) – (3 – 9) (Yu et al., 2006), an analytical solution of the temperature change, $T(x, t)$, could be obtained for the step-wise heating method:

$$T(x,t) = \frac{q}{k} \left\{ 2\sqrt{\frac{\alpha t}{\pi}} \exp\left(-\frac{x^2}{4\alpha t}\right) - x\,\mathrm{erfc}\left(\frac{x}{\sqrt{4\alpha t}}\right) \right\}$$

(3 - 11)

where erfc(x) is the complementary error function, defined as

$$\operatorname{erfc}(x) = \frac{2}{\sqrt{\pi}} \int_x^\infty e^{-t^2} \, dt \qquad\qquad (3\text{ - }12)$$

Based on the one-dimensional unsteady-state heat conduction equation and its analytical solution, the required thermophysical properties (k, α, and c) can be calculated simultaneously. In Eq. (3 - 11), two unknown thermophysical parameters, k and α, exist. However, due to the linear independence of their sensitivity coefficients (see more detailed information in Section 3.2.3.3), both parameters can be estimated using the curve-fitting method or least-squares parameter estimation method (Yu et al., 2006). Another thermophysical parameter, the specific heat capacity, c, can then be calculated with the conversion $c=k/(\rho\alpha)$, where ρ is the density.

3.2.3.2 Experimental Setup

In the experimental work, the testing tissue-mimicking phantoms consisted of varied egg white concentrations ranging from 0 to 40 % v/v (by 10 % v/v interval). As shown in Figure 3.8, the samples to be tested were divided into three sections by inserting a 53 mm diameter, 408 Ω heat source (flexible kapton heater, Omega Engineering, UK) and a thermocouple (Type K thermocouple, T.M. Electronics Ltd., UK) into the samples. The corresponding thicknesses of different sections were $x_{II} = 8$ mm, $x_I = x_{III} = 20$ mm, respectively, and the surface dimensions of the samples were the same as those of the heat source. A constant voltage power supply (Type SVA 4, variable power supply, Zenith Electric Co. Ltd., UK) was used to generate a 40 V step-wise signal for the heat source. The temperature change at one single point of the sample, $T(x, t)$, and the k, α and c values were determined using an USB-based eight-channel data logger (USB-TC, Measurement Computing Corporation, USA) and one customized Labview program. The nonlinear curve fit VI based on the nonlinear Levenberg-Marquardt algorithm (LMA) and the error function VI were selected to calculate the least-squares coefficients that best fit the input data points. The measuring time and fitting time window were determined according to the methods discussed in Section 3.2.3.3.
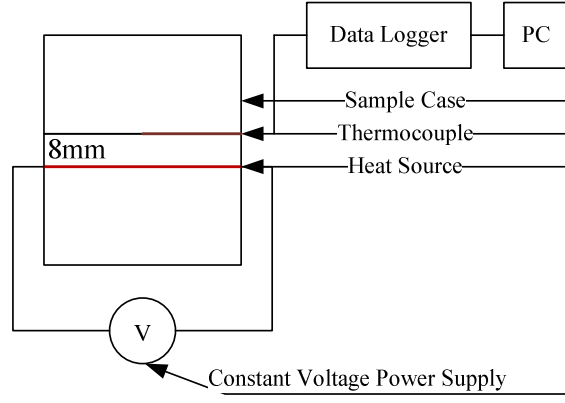
Figure 3.8 Scheme of the experimental setup for the step-wise TPS method.

3.2.3.3 Determination of Measuring Time and Fitting Time Window

In practical terms, the measuring time and fitting time window are two key factors affecting the accuracy of the step-wise TPS technique. One method of predicting the measuring time and fitting time window is based on the correlation analysis of function $\gamma(F)$. Introducing the Fourier number F as

$$F = \alpha t / x^2, \tag{3 - 13}$$

the temperature change $T(x, t)$ could be rewritten as

$$T(F, x) = \frac{qx}{k} \times \left[2\left(\frac{F}{\pi}\right)^{1/2} \exp\left(-\frac{1}{4F}\right) - \mathrm{erfc}\left(\frac{1}{2\sqrt{F}}\right) \right] \tag{3 - 14}$$

Considering the sensitivity coefficient of the thermophysical parameter, β_p, as

$$\beta_p = p \frac{\partial T(F, x)}{\partial p} \tag{3 - 15}$$

where p is the thermophysical parameter to be analyzed i.e., thermal conductivity, k, or specific heat capacity, α. The sensitivity coefficient of the thermal conductivity, β_k, and the sensitivity coefficient of the thermal diffusivity, β_α, have the forms as follows

62

$$\beta_k = -\frac{qx}{k}\left[2\left(\frac{F}{\pi}\right)^{1/2}\exp\left(-\frac{1}{4F}\right)-\mathrm{erfc}\left(\frac{1}{2\sqrt{F}}\right)\right] = -T(F,x)$$

$$\beta_\alpha = \frac{qx}{k}\left[\left(\sqrt{F\pi}+\frac{1}{\sqrt{F\pi}}\right)\exp\left(-\frac{1}{4F}\right)\right]-T(F,x) \qquad (3-16)$$

The correlation coefficient of these two sensitivity coefficients, $\gamma(F)$, is then defined as

$$\gamma(F)=\beta_\alpha/\beta_k \qquad (3-17)$$

Theoretical calculations of these sensitivity coefficients, β_k and β_α, and the correlation coefficient, $\gamma(F)$, were performed using Eqs. (3 - 13) – (3 - 17) (Kubicar and Bohac, 2001; Yu et al., 2006), based on the proposed experimental setup and material properties presented in Divkovic *et al.* (2007), $\rho = (1045 \pm 5)$ kg·m^{-3}, $k = (0.59 \pm 0.06)$ W·m^{-1}·°C^{-1}, and $c = (4270 \pm 365)$ J·kg^{-1}·°C^{-1}. As shown in Figure 3.9, the measuring time could be identified by the moment when the correlation coefficient of the sensitivity coefficients starts to be high, i.e., up to $F = 4.48$ ($t \approx 36$ min) for the case; and the fitting time window could be determined when the correlation coefficient of the sensitivity coefficients remains low, or to say when the sensitivity coefficients are linearly independent, i.e., in the interval $0.7 < F < 3$ (5.6 min $< t <$ 24 min). And because the correlation coefficient is usually high at the beginning of the heating process, the fitting time window is shorter than the measuring time.
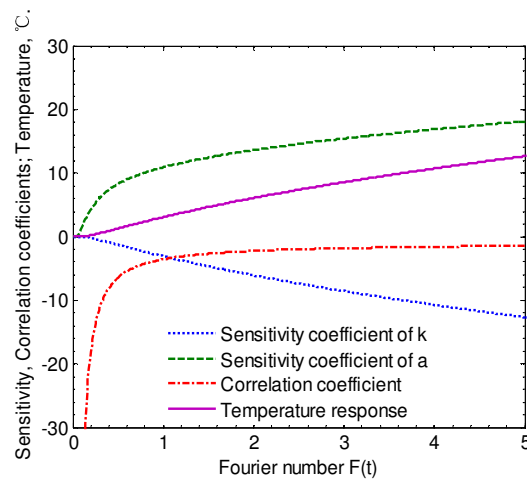
Figure 3.9 Calculated temperature change, sensitivity coefficients, and correlation coefficient as functions of F.

The other method of determining the measuring time and fitting time window, the difference analysis method, will also be discussed in Section 5.1.2.2. Detailed discussion about this method can be found in Kubicar and Bohac (2001).

3.3 HIFU Effects on Tissue-mimicking Phantoms

3.3.1 Visualization of HIFU Ablation

The effect of the HIFU procedure was explored on the 30 % (v/v) egg white phantom for its acoustic similarity to human tissue as well as its thermal sensitivity. Using the robot assisted high power experimental setup (as shown in Figure 3.10), all the experimental work described here were conducted in degassed water. A series of thermal ablation tests were thereafter performed by a customized Labview program to automatically control the excitation signal from the signal generator and the movement of the robot arm. In all instances, the HIFU transducer, PA160 (resonant frequency of 1.09 MHz, aperture of 60 mm and focal length of 75 mm), was driven by a continuous wave mode, and followed by an active cooling-off period.
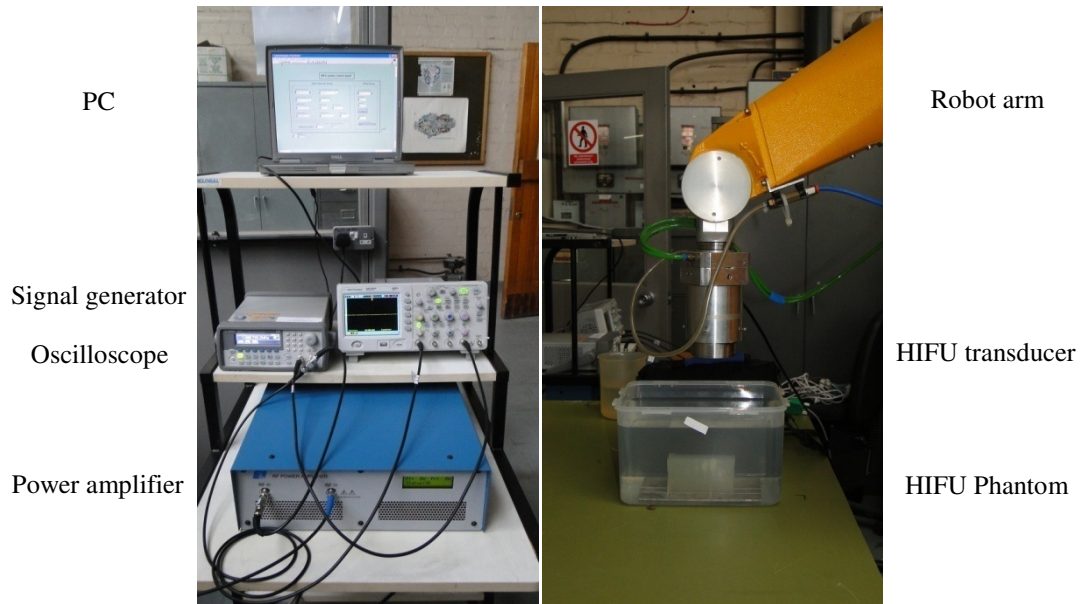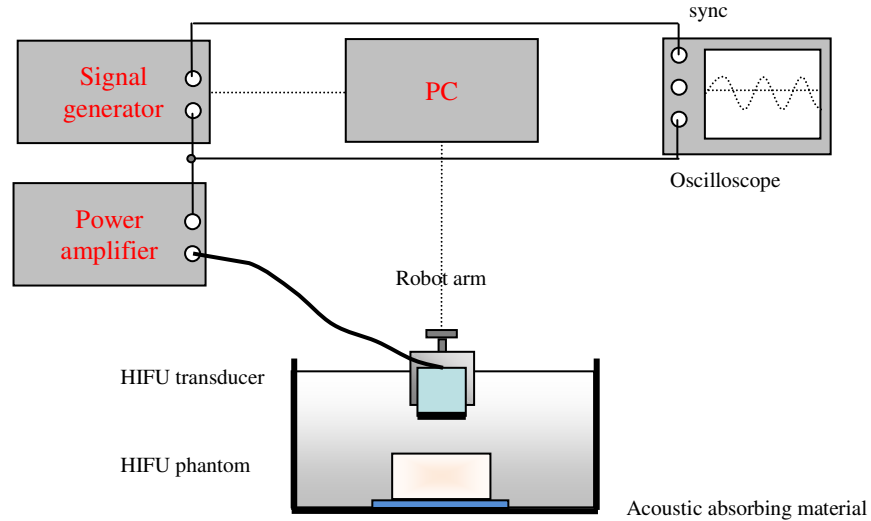
Figure 3.10 Robot assisted HIFU system for visualization of HIFU effects on TMMs.

As functioned in the Labview program, various experimental parameters, e.g., driving signal (frequency, amplitude, etc.), sonication duration, movement routine (controlled by the V+ program in the robot arm system), and distance between adjacent sonication positions (set to be 7 mm, if not specified) could be defined. During this investigation work, three basic heating strategies were discussed:

a). with fixed sonication duration (t_{on} = 30 s), whilst varied driving powers (P = 15, 27, 38, 58, 74 W);

b). with fixed driving power (P = 38 W), whilst varied sonication durations (t_{on} = 10, 20, 30, 40, 50, 60 s);

c). with fixed driving power and sonication duration (P = 38 W and t_{on} = 30 s), whilst varied cooling-off periods (t_{off} = 0, 10, 20, 30, 40, 50, 60 s).

N.B. P denotes the electric power, but not the acoustic power delivered to the focal region.

3.3.2 Recording of Focal Temperature Change

To record the real-time temperature change at the focal region during thermal ablation, a fiber-optic hydrophone (Precision Acoustics, UK) was inserted into the 30 % (v/v) egg white phantom under water, as shown in Figure 3.11. Special care must be taken to ensure the safety of the fiber-optic sensor, and guarantee a good coupling with the surrounding TMM.
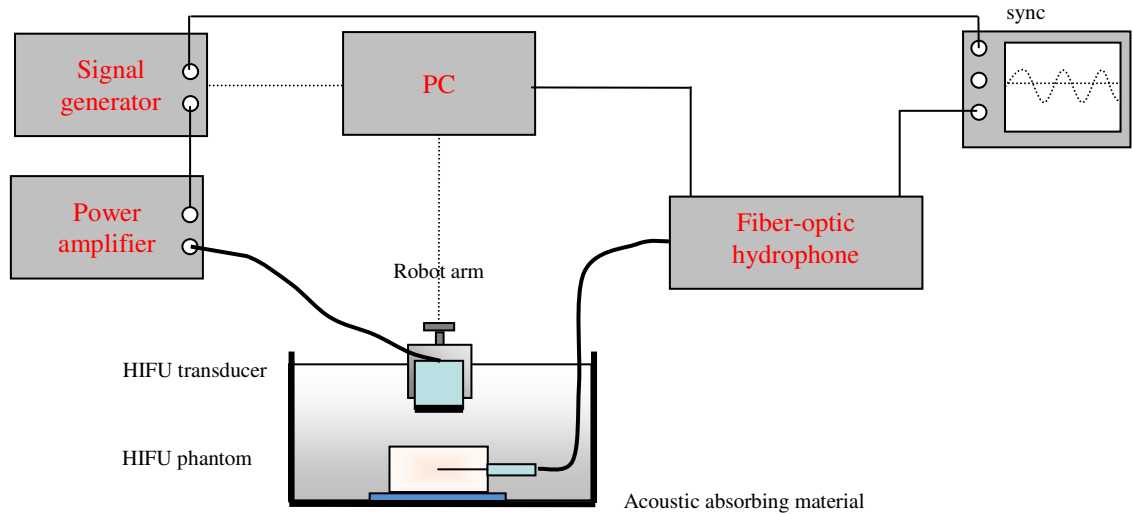
Figure 3.11 Robot assisted HIFU system for temperature measurement at the focus.

The HIFU transducer and hydrophone were positioned perpendicular to each other. To achieve the coincidence of the tip of the hydrophone with the focus of the HIFU transducer, it was essential to mechanically move the transducer mounted on the robot arm until maximum pressure amplitude was observed on the oscilloscope, during which process the transducer was driven at a lower signal level. The temperature signals acquired from the fiber-optic hydrophone at high power amplitudes were then recorded by its supporting Labview program.

In some additional cases, the temperature responses at the geometric focus were recorded using a conventional thermocouple connected to the USB-based eight-channel data logger (USB-TC, Measurement Computing Corporation, USA) and saved by one customized Labview program in PC.

3.3.3 Effect of Perfusion

The effect of perfusion was initially investigated by developing the egg white phantom with a water path in it, as seen in Figure 3.12, which allowed water or even blood to pass through it, if the proper tubes were connected. The speed of water flowing (0 ~ 24 ml/s) could be controlled by an adjustable DC water pump.
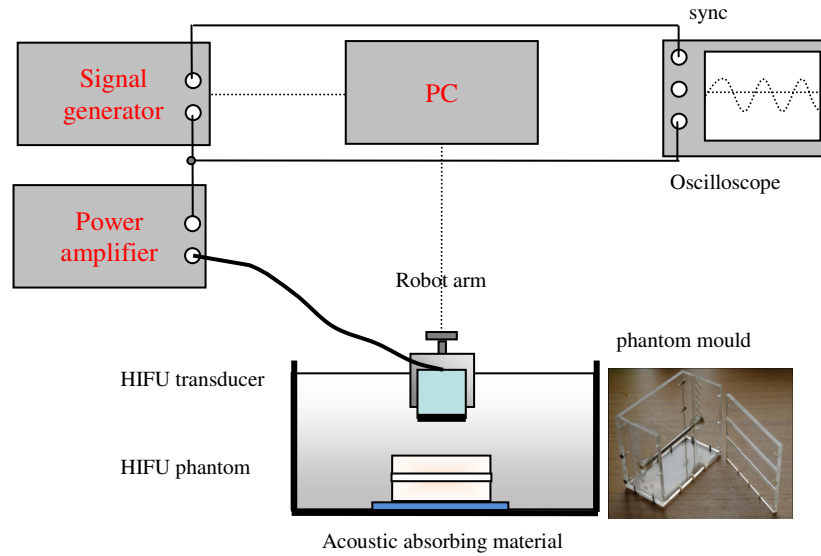
Figure 3.12 Robot assisted HIFU system to investigate the perfusion effect.

This experimental section extended the investigation to include the thermal behaviour on the tissue-mimicking phantoms. The experimental results may provide the opportunity of a better understanding of the factors that influence the HIFU-induced lesions, e.g., driving power, sonicating duration, cooling duration, and perfusion rate; and may work towards the optimum sonication protocols required to generate the specified ablation results.

3.4 Transmitted Beam Distortion and Pressure Reduction in Trans-costal FUS

3.4.1 Field Mapping of Focused Ultrasound Propagation through the Rib Cage

As presented in Section 2.3.1, the presence of the rib cage is a significant hindrance to the clinical applicability of FUS for various internal organs including the liver, kidney, and pancreas. The main problems associated with the rib cage were considered to be: the strong reflections that occur at the soft tissue/rib interfaces; the highly attenuating effect of the ribs; and the scattering and diffraction that occur at the ribs boundaries. In this study, the ultrasonic beam profiles in the transverse focal plane (the X-Y plane) without and with propagation of focused ultrasound through the rib cage were determined using the customized 2D high speed ultrasound scanning system (see in Section 3.1.3), as depicted in Figure 3.13. In particular, a porcine rib cage sample and two other rib cage mimics (an epoxy rib cage mimics and an acoustic absorber rib cage mimics, see in

Section 3.4.2 - 3.4.4) were developed and tested.
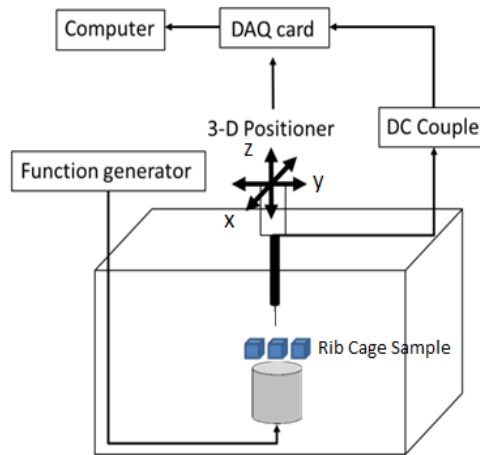
Figure 3.13 Ultrasound scanning system for trans-costal beam profiling.

The single-element spherical focused source, PA160, was used, with the aperture of 60 mm, the focal length of 75 mm and the centre frequency of 1.09 MHz. During the experiments, the porcine rib cage sample and the rib cage mimics were positioned on the transducer holder in water and their positions relative to the acoustic source were adjusted manually. 2D pressure distributions in the transverse focal plane were measured with a calibrated 0.5-mm needle hydrophone. This was held vertically, facing downwards, with the transducer facing upwards, and scanned by a 3D positioning system. All the measurements were performed in degassed water, and a piece of ultrasonic absorber was attached to the hydrophone holder to prevent reflections back to the source from the surface of the water.

3.4.2 Porcine Rib Cage Sample

All porcine rib cage samples were obtained from a butcher's shop. For the porcine rib cage sample, as shown in Figure 3.14, the four rib strips in the lower part of the porcine rib cage were selected. The widths of the inter-costal muscle (~20 mm) are nearly twice as wide as the widths of the ribs (~10 mm). For consideration in the experiment, three different target positions relative to the rib cage sample were investigated by directing the beam axis through: (i) the second rib, (ii) the third rib and (iii) the inter-costal space between the second and third rib strips, respectively, as high-lightened in Figure 3.14.
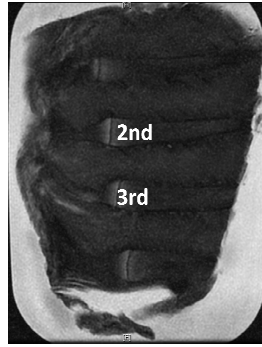
Figure 3.14 T2-weighted MR image of the porcine rib cage sample (2nd and 3rd present the solid ribs).

3.4.3 Epoxy Rib Cage Mimics

An epoxy rib cage phantom was developed by InSightec Ltd., as shown in Figure 3.15. It presents a realistic rib cage in 3D anatomic shape and geometry and is embedded in an acoustically transparent tissue-mimicking phantom. In this model, the average width of the epoxy strips and the spacing between adjacent rib strips are both around 15 mm. For a comparative study, ten different target positions in the focal plane were chosen for all the experiments with this epoxy rib cage phantom. These ten target locations relative to the epoxy rib cage phantom were shown in Figure 3.15 (line 1, points a-e; line 2, points a-e).
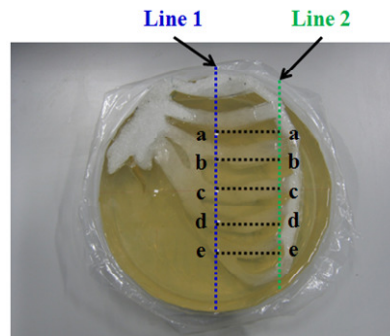
Figure 3.15 Epoxy rib cage mimics.

For later use, a similar rib cage mimics with four rib strips, as seen in Figure 3.16, was produced in lab, which was reconstructed based on the CT images of patient's thoracic cage and then fabricated by a fast prototyping machine. This rib cage model could be embedded in the absorbing egg white phantom and hence could be used for thermal measurements repeatedly.

Figure 3.16 Rib cage mimics reconstructed from patient data.

3.4.4 Acoustic Absorber Rib Cage Mimics

As shown in Figure 3.17, another rib cage mimics used in this study was made of acoustic absorber Aptflex F28 (Precision Acoustics, UK) with the properties given in Table 3.4. It consisted of three parallel strips, each $90 \times 15 \times 10$ mm in dimension, and with spacing between of 15 mm. These dimensions of the absorbing rib cage mimics are within the typical range of clinical inter-costal muscle width (for patient 1, 17.3 ± 7.2 mm; patient 2, 13.5 ± 5.6 mm; patient 3, 21.1 ± 9.3 mm) and rib width (for patient 1, 13.3 ± 6.0 mm; patient 2, 17.5 ± 6.3 mm; patient 3, 13.4 ± 3.9 mm), as described in Liu et al. (2007).
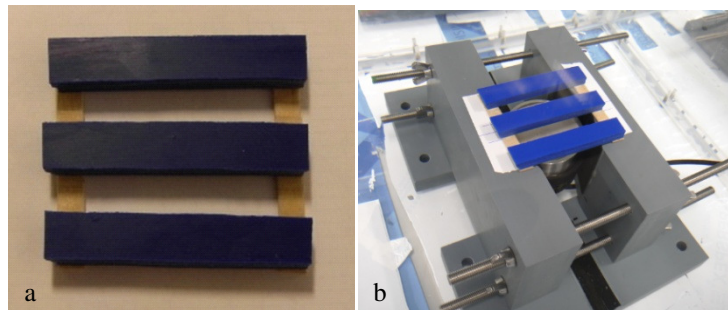
Figure 3.17 (a) Acoustic absorber rib cage mimics and (b) its positioning on the holder.

Table 3.4 Material properties of the absorbing rib-mimics

Parameters	
ρ, kg m^{-3}	1010
c, m s^{-1}	1500
α, dB cm^{-1} MHz^{-1}	22.9

A set of acoustic measurements were performed using the rib cage mimics made of ultrasonic absorber: (i) pressure profile in a free field, without the rib cage mimics; (ii) pressure profile by directing the beam axis through the centre of the inter-costal space; (iii)

pressure profile by directing the beam axis through the centre of the middle rib; (iv) pressure profile by directing the beam axis through the centre of the middle rib and with a 10 mm further transducer-to-rib distance.

3.5 Trans-costal Heating and its Frequency Dependence

The sonicating frequency is thought to be an important factor on the safety and efficacy of trans-costal FUS. To date, a wide range of frequencies ranging from 0.4 to 1.7 MHz have been examined in laboratory studies and clinical trials (Liu et al., 2010a - *400 kHz*; Liu et al., 2007, Botros et al., 1998 - *500 kHz*; Bobkova et al., 2010 - *0.8-1.25 MHz*; Pernot et al., 2007, Aubry et al., 2008, Ballard et al., 2010, Khokhlova et al., 2010, Gelat et al., 2011 - *1 MHz*; Li et al., 2007, Liu et al., 2010b - *1.13 MHz*; Cochard et al., 2009 - *1.5 MHz*; and Civale et al., 2007 - *1.7 MHz*), however no consensus has been achieved on addressing the optimal sonicating frequency in these trans-costal applications yet.

In this experimental section, the trans-costal heating results (particularly the rib heating) were investigated on the acoustic absorber rib cage mimics over a range of frequencies. The thermal ablation experiments were conducted using the ExAblate 2000 platform (InSightec, Israel) which is clinically used for the treatment of uterine fibroids, integrated into the 1.5 Tesla HDx MRI (GE Healthcare, USA). In the ExAblate 2000 system, the 208-element combined concentric-ring and sector-vortex phased array (150 mm radius of curvature and 120 mm aperture) is housed inside a sealed water bath in the patient table and connected to a 4 degree of freedom motion system. The applied voltage amplitude and phase in each element can be adjusted independently by the electric controller. Acoustic propagation is enabled through a thin Mylar membrane on top of the platform. The temperature evolution was monitored with real-time MRI thermometry. MR images are obtained with the imaging coil integrated into the platform, and the MRI thermometry utilizes the temperature-dependent proton resonance frequency shift occurring in water molecules (Holbrook et al., 2009). In this method, the background phase information is collected before sonication, and the baseline subtraction is performed correspondingly. The accuracy of temperature measurements in MRgFUS is of three degrees.
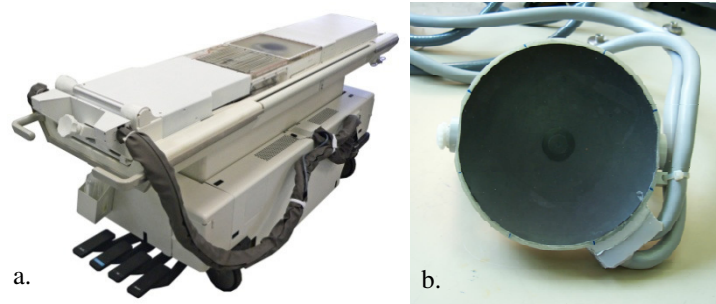
Figure 3.18 ExAblate 2000 System: a) patient table, b) 208-element, 1 MHz phased array.

The relative positions of the HIFU phased array, acoustic absorber rib cage mimics and tissue-mimicking phantoms are shown in Figure 3.19. The rib cage mimics was positioned tightly between two solid tissue-mimicking phantoms to ensure continuous ultrasound wave propagation along the beam path and direct measurement of temperature changes at the surface of the rib mimics. A certain volume of degassed water was filled into the plastic container to ensure good acoustic coupling. The 208-element phased array was then driven at different frequencies between 0.95 - 1.35 MHz, with 0.05 MHz in step. An acoustic power of 50 W and a sonication period of 20 s were used in all the measurements. Each sonication was followed by a 5-minute cooling-off period, during which time the temperature could reduce to slightly higher than ambient temperature.
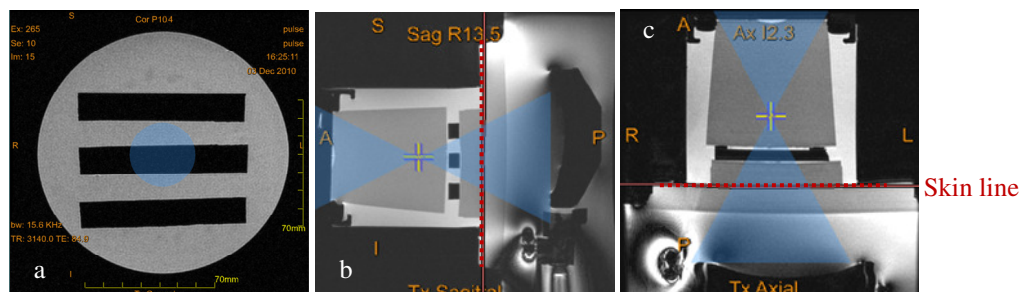
Figure 3.19 ExAblate 2000 System: MR images showing the experimental setup for the trans-costal sonications (a- coronal, b- sagittal and c- axial planes).

3.6 Optimized Operation of 2D Phased Arrays to Avoid Overheating of Ribs

The rib necrosis or even rib fracture in the beam pathway remains major challenge for patients with hepatic tumours. To avoid or minimize overheating of the ribs and overlying tissue, while simultaneously enhancing localized heating at target tissues within the rib cage is important during trans-costal FUS. In the literature, the most attractive approach is the adaptive focusing technique based on the concept of time reversal (Aubry et al.

2008; Cochard et al., 2009), which improves the focusing quality and considerably decreases the rib heating in the trans-costal FUS procedures. However, although it is easily explained in mathematics as a spatiotemporal matched filter, time reversal is currently difficult to implement in clinical activities, as an acoustic source at the target position is always required, which makes the procedure lose its benefits of complete non-invasive surgery. A non-invasive implementation of time reversal in the trans-cranial treatments has been developed by Aubry et al., 2003; Pernot et al., 2007; Marquet et al., 2009. However, great challenges still exist in translating the technique to the trans-costal applications, e.g., movement of the rib cage during sonications (Marquet et al., 2011). In this section, efforts have been made to reduce the adverse effects of rib overheating and increase the efficacy of ultrasound treatment at the focal region through a relatively simple and straightforward geometric rib sparing approach.

3.6.1 Binary Manipulation of Elements in 2D Phased Arrays

In order to reduce unwanted ultrasound exposure on the ribs, the geometric rib sparing method referring to binary manipulation of elements in 2D phased arrays and without phase adjustment has been explored, i.e., 0 – element should be switched off and 1 – element should be switched on. This method was proposed on the basis of the slight difference in the focusing quality between with and without phase correction (Marquet et al., 2011). For a given experimental configuration, shown in Figure 3.20, the idea is that based on central projection from the focus, the transducer elements located in front of the ribs should be switched off whereas the transducer elements located in front of the inter-costal spaces should be switched on, Algorithm #1, as illustrated in Figure 3.21(a). The other algorithm, Algorithm #2, as illustrated in Figure 3.21(b), has also been performed to identify the transducer elements affected by ribs shadowing that should be switched off, however, this algorithm is based on the parallel projection from infinity. Other than the full spherical wave front, a binary wave front will be formed following these algorithms (Liu et al., 2007; Bobkova et al., 2010; Quesson et al., 2010).
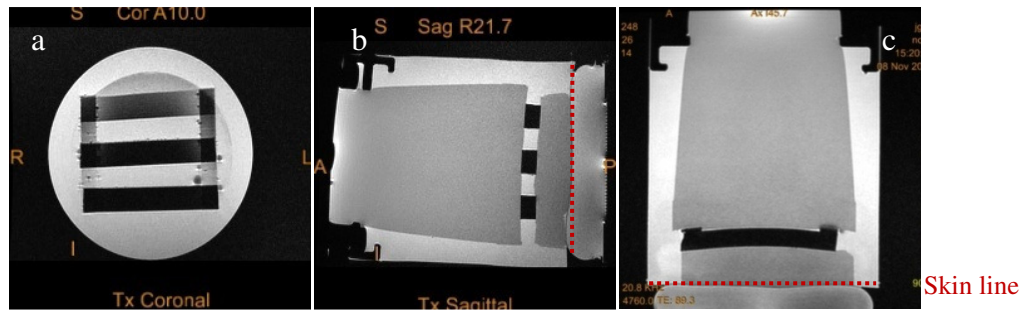
Figure 3.20 ExAblate 2100 system: MR images showing the experimental setup for the geometric rib sparing study: (a- coronal, b- sagittal and c- axial planes).
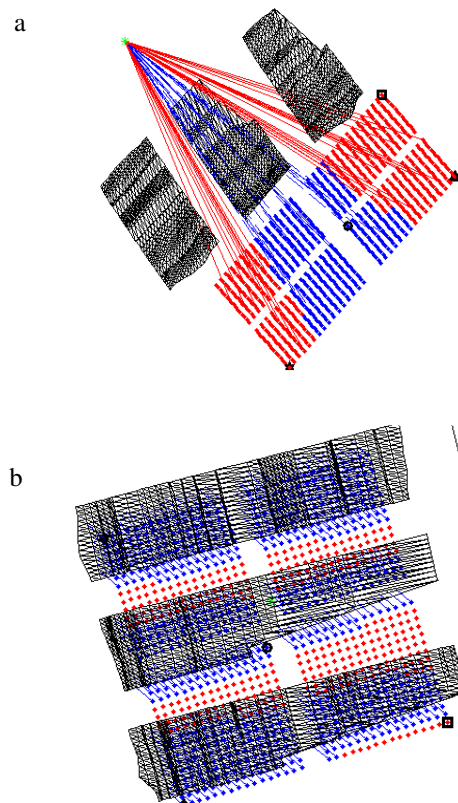
Figure 3.21 Illustration of the geometric rib sparing methods: (a) Algorithm #1 – central projection and (b) Algorithm #2 – parallel projection, on the ExAblate 2100 conformal bone system. The red elements are switched on while the blue ones are switched off.

3.6.2 Acoustic Absorber Rib Cage Mimics

3.6.2.1 ExAblate 2100 system

As illustrated in Figures 3.20 and 3.21, the trans-costal thermal ablations were performed using the modern ExAblate 2100 conformal bone system (CBS) (InSightec, Israel)

integrated into the 1.5 Tesla HDx MRI (GE Healthcare, USA), that is designed for the treatment of bone metastasis. The high density (> 1000 elements) matrix phased array in the ExAblate 2100 system, as seen in Figure 3.22, allows more flexible transducer positioning during the FUS procedures. Good acoustic coupling is provided with the water-permeable membrane and active cooling processes can be accelerated due to the integrated built-in skin cooling system.
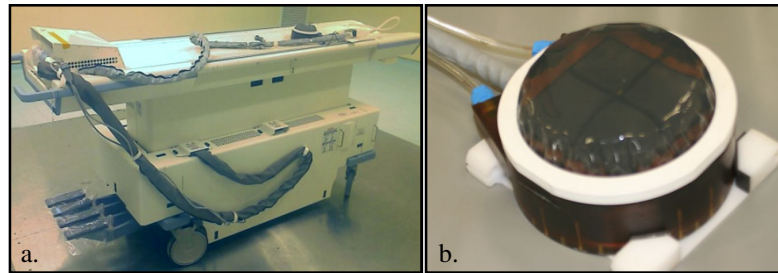
Figure 3.22 ExAblate 2100 System: a) patient table, b) 1000-element, 550 KHz phased array.

In the updated ExAblate system, the *x*, *y* and *z* coordinates of each transducer element can be tracked automatically in the 3D MR coordinate system. The rib strips could be detected using MR imaging and drawn using the testing files produced by the workstation software in the ExAblate 2100 platform. A MATLAB program was then used for the determination of the transducer elements that intersected with the ribs when straight lines from the geometric centres of the elements to the focal point were drawn (Algorithm #1, Figure 3.21a); or when straight lines from the geometric centres of the elements to infinity were drawn (Algorithm #2, Figure 3.21b). These selected elements were then electronically switched off.

In the cases with the acoustic absorber rib cage mimics (as seen in Figure 3.20), the focal point was selected to be ~ 90 mm above the matrix phased array, with the distance from the 'skin line' (red-dotted line) to the frontal rib plane approximately 25 mm, and the distance between the dorsal rib plane and the focus of 35 mm. For the given focal position behind the middle rib-mimics, three types of sonications with and without employing the geometric rib sparing methods (both Algorithm #1 and #2) have been performed for comparison, during which procedures the acoustic power and sonication duration were kept fixed at 25 W and 60 s. Real-time MR thermal images were obtained with particular consideration of temperature changes at the focal point and near the

rib-mimics respectively. Using this CBS system, two other target locations, i.e. 106 mm and 71 mm above the transducer (transducer-to-rib distance was 38 mm), were sonicated respectively.

3.6.2.2 ExAblate 2000 system

The same geometric rib sparing procedures were repeated using the high frequency ExAblate 2000 system, and the experimental setup screened with MRI was similar to Figure 3.19. However, having no testing files produced by the ExAblate 2000 system (workstation software), the tasks of detecting and drawing the ribs cannot be accomplished using this system solely. Therefore, it is necessary to make the calibration using the ExAblate 2000 system and copy its results for use in the novel ExAblate 2100 system. The sonications (without and with manipulating transducer elements) were performed using the ExAblate 2000 system software. The sonications had parameters with a frequency of 1.15 MHz, acoustic power of 25 W and duration of 60 s. In one case, as shown in Figure 3.23, the focal position was approximately 130 mm above the bowl shaped phased array, the distance between the 'skin line' (red-dotted line in Figure 3.19) and the frontal rib plane was ~ 90 mm, and the distance from the dorsal rib plane to the focus was ~ 30 mm. While the same amount of energy was delivered to a slightly lower axial position of around 125 mm. Advanced experimental results with varying transducer-to-rib distance or transducer elevation value (0 to 32 mm) will also be given in Chapter 5.4.1.1 using the ExAblate 2000-2 system in Israel, which provides an extra degree of freedom for the bowl array to move in the axial direction.
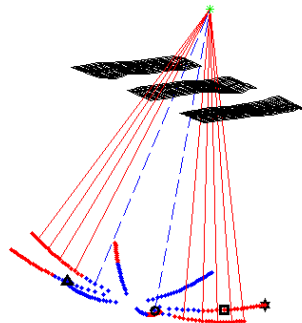
Figure 3.23 Illustration of the geometric rib sparing method (Algorithm #1 – central projection) on the ExAblate 2000 system. The red elements are switched on while the blue ones are switched off.

3.6.3 Epoxy Rib Cage Mimics

The feasibility study of this geometric rib sparing method on the epoxy rib cage mimics has also been investigated. In practical terms, this approach used the imaging capability of the MRI and automatic tracking capability of the 1000-element phased array platform in order to reconstruct the relative positions of the 2D phased array and the rib strips along the beam propagation pathway and hence to identify the appropriate elements that should be switched off on the 208-element phased array. The same continuous wave sonications were performed with an acoustic power of 25 W and sonication duration of 60 s.
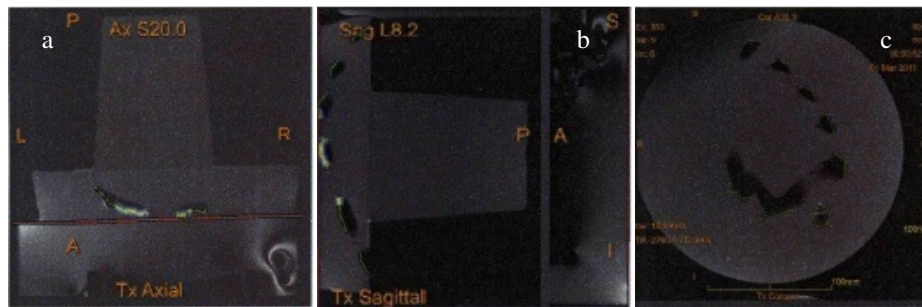
Figure 3.24 ExAblate 2000 System: MR images showing the experimental setup with the epoxy rib cage mimics (a- coronal, b- sagittal and c- axial planes).

3.6.4 Thiel-embalmed Cadaver

Thiel-embalmed human cadavers have been successfully used as medical simulators in laparoscopic surgery, neurosurgery and oral surgery training and research activities (McLeod et al., 2010). The feasibility of using the Thiel cadaver models for MRgFUS (Volovick et al., 2010a; Volovick et al., 2010b) are currently undergoing evaluation in University of Dundee. The novel embalming technique developed by Professor Em. Walther Thiel relies on the use of a mixture containing 4-chloro-3-methylenphenol, various salts, boric acid, ethylene glycol and low amounts of formalin for the functions of tissue fixation, disinfecting, preservation of tissue plasticity, etc (Thiel, 1992; Thiel, 2002). Immersed in the resulting solution for few weeks (4 – 6 weeks) and then stored at 4 – 6 ℃ in sealed environment in vacuum, the embalmed cadavers allow for repeated use of up to 3 years. Major advantages of the Thiel embalming method are the excellent

preservation of the flexibility and plasticity of the body (tissues and organs), and their color are very similar to *in vivo* conditions. This technique is also preferred for not releasing harmful substances into surrounding environment, and the formaldehyde concentration in room air is below the limit of detection. Compared with live animal studies, no anesthesia is needed on the soft embalmed cadavers and there is no time limit for performing sessions of focused ultrasound sonications. However, no blood flow or perfusion occurs, for which it may cause accumulation of bubbles during these sonications.

The Thiel embalming technique provides easy access to human anatomy with more straight-forward ethical procedures. In the experimental setup with the Thiel-embalmed cadaver, as seen in Figure 3.25, the 1000-element phased array transducer was positioned at the cadaver's left upper abdomen, and various MR imaging sequences have been evaluated for imaging of human ribs. Continuous wave sonications with applying the geometric rib sparing method were then evaluated for targeting the kidney organ behind the rib cage.

Figure 3.25 Photograph of the experimental setup with the Thiel-embalmed cadaver.

CHAPTER 4 NUMERICAL ANALYSIS OF FUS TREATMENT THROUGH THE RIB CAGE

This Chapter introduces the algorithm backgrounds and modelling issues in both finite element (FE) methods, PZFlex and SpectralFlex, which are designed for short and long distance ultrasonic wave propagations (Section 4.1), details the corresponding numerical models built for investigation of basic acoustic and thermal behaviours of HIFU (Section 4.2), and investigates related issues in advanced treatment planning in trans-costal FUS, including the transmitted beam distortion and pressure reduction (Section 4.3); the frequency-dependent heating effects in full spherical radiation patterns (Section 4.4); and the efficiency of the geometric rib sparing method proposed for improved treatment outcomes (Section 4.5).

4.1 Introduction of Finite Element Methods

4.1.1 Electromechanical Finite Element Method

During the course of study, an explicit-implicit time-domain finite element code designed for solving problems involving the piezoelectric materials and/or wave propagation in biological media was used. All the simulation work in PZFlex can be divided into two main types: the acoustic model and the coupled/uncoupled thermal model. The acoustic model is used to calculate the ultrasonic wave propagation in the domains of interest. The resulting acoustic energy deposition is used as the initial heat load for the thermal model.

Acoustic Model

The electromechanical finite element method (PZFlex, Weidlinger Associates Inc., USA) reduces the governing piezoelectric constitutive equations and the equations of mechanical and electrical equilibrium to a global system of ordinary differential equations (ODEs) in time in the computational domain (Wojcik et al., 1993).

$$M_{uu}\frac{d^2u}{dt^2}+C_{uu}\frac{du}{dt}+C_{u\psi}\frac{d\psi}{dt}+K_{uu}u+K_{u\phi}\phi=F \qquad (4-1)$$

$$K_{u\phi}^T u - K_{\phi\phi}\phi = Q \qquad (4-2)$$

$$M_{\psi\psi}\frac{d^2\psi}{dt^2}-C_{u\psi}^T\frac{du}{dt}+C_{\psi\psi}\frac{d\psi}{dt}+K_{\psi\psi}\psi=0 \qquad (4-3)$$

The elemental system of ODEs governs the dynamic elastic Eq. (4 - 1), quasi-static electric Eq. (4 - 2), and dynamic acoustic Eq. (4 - 3) fields, respectively. In the equations above, the unknowns u, ϕ, and ψ represent the elastic displacement vector, the electric potential vector, and the velocity potential vector, respectively; F is the applied external force vector and Q is the charge vector. All vectors are defined by field values at all nodes over the model domain. While **M**, **C**, and **K** indicate various 'mass', 'damping', and 'stiffness' matrices, respectively.

To determine the ultrasonic wave phenomena in various applications, a step-by-step integration of the electromechanical equations is performed in either an explicit (which decouples the current solution vector and eliminate the global system solve, e.g. in equations 4 - 1 and 4 - 3) or an implicit way (which couples the current solution vector and the global system of ODEs must be solved at each time step, e.g. in equation 4 - 2). The time-domain solutions on a set of discrete space-time points can then be represented by a summation of elemental systems of linear equations on the unknown field values at nodes of discretization (Wojcik et al., 1993; Wojcik et al., 1994).

As it has been noted, the time updating equations of the nodal velocity, v, displacement, u, and force, F, for a computational element can be written as follows (Wojcik et al., 1995):

$$v^n = v^{n-1} + \frac{\Delta t \cdot F^{n-\frac{1}{2}}}{m}$$

$$u^{n+\frac{1}{2}} = u^{n-\frac{1}{2}} + v^n \cdot \Delta t \qquad (4-4)$$

$$\vartheta^{n+\frac{1}{2}} = div u^{n+\frac{1}{2}}$$

$$p^{n+\frac{1}{2}} = p_0 + A\left[\vartheta^{n+\frac{1}{2}} + \frac{B}{A}\frac{\left(\vartheta^{n+\frac{1}{2}}\right)^2}{2}\right] \rightarrow F^{n+\frac{1}{2}} \qquad (4\text{ - }5)$$

where m is the lumped mass, Δt is the time step smaller than the CFL limit - the shortest wave transit time between neighboring nodes in a grid, the superscripts n and $n \pm 1/2$ refer to time levels e.g., at $n \cdot \Delta t$, and the subscript 0 means the ambient condition. Also, $\vartheta = \rho / \rho_0 - 1$ is the dilatation, $A = \rho_0 \cdot c_0^2$, and B/A is the nonlinearity parameter in the truncated Taylor series.

Thermal Model

Following this, the acoustic energy deposition during one single cycle of wave propagation at the centre frequency can be calculated (named as 'loss' array) and saved as the initial heat load for the thermal model. After implementing a conversion of energy to power by multiplying the loss array and the frequency, the thermal analysis can be performed based on the discrete form of the bio-heat transfer equation as introduced in Wojcik et al., (1995):

$$\left(\frac{2}{\Delta t}\mathbf{M} + \mathbf{K}\right)T^{n+1} = F^{n+1} + \mathbf{M}\left(\frac{2}{\Delta t}T^n + \tau^n\right)$$
$$\tau^n = \frac{2}{\Delta t}\left(T^n - T^{n-1}\right) + \tau^{n-1} \qquad (4\text{ - }6)$$

where T is the nodal temperature vector, τ is the rate of change vector, $\mathbf{M}$ and $\mathbf{K}$ are the heat capacity and thermal conductivity matrices, respectively, F is the heat load term, and n and $n \pm 1$ refer to the time levels. In Eq. 4.6, perfusion contributes to both $\mathbf{K}$ and F.

Modelling Technique

In PZFlex, the spatial accuracy increases with the mesh density and a minimum of 15 elements per wavelength is recommended from previous experience (at this mesh density, the errors of wave dispersion can be limited to less than 1 %) (Wojcik et al., 1993). Typically, appropriate radiation boundary conditions are necessary for the purpose

of reducing finite element model size and saving computer memory. For another issue of frequency-dependent material attenuation characterized by $\alpha = af^b$ (f is the frequency), PZFlex simulates the absorption mechanism by using the two most convenient damping models e.g., the stiffness-proportional damping (b = 0) and mass-proportional damping (b = 2), or their linear combinations i.e., the Rayleigh damping (0 < b < 2), and the viscoelastic damping (0 < b < 2). Proper choice of damping models can be made for their operational and algorithmic properties. The material nonlinearity can also be included in the models (Wojcik et al., 1995).

4.1.2 Pseudo Spectral Method

The regular PZFlex can be most efficiently used for 2D models at > 10s wavelengths propagation range, e.g., for a 100×50 wavelengths model in 2D with the mesh density of 70 elements per wavelength, a total of 24.5 million elements will be created; however, for the corresponding 3D model, it would be around 86 billion elements instead, which is not realistic on current commodity hardware. For the practical needs of long distance wave propagation (> 100s wavelengths) in complete 3D modelling, the pseudo-spectral technique (SpectralFlex, Weidlinger Associates Inc., Los Altos, USA) is applied. This algorithm is accurate for many hundreds of wavelengths propagation, and needs only 2 elements per minimum wavelength for simulation accuracy.

In SpectralFlex, it solves the governing partial differential equations (PDEs) formed by the momentum and constitutive equations (Wojcik et al., 1997; Wojcik et al., 1999a):

$$\rho \frac{\partial^2 u}{\partial t^2} = -\nabla^2 p$$
$$p = -K\nabla \cdot u$$

(4 - 7)

where u is the displacement vector, p is pressure, and $K = \rho \cdot c^2$ is the bulk modulus. By differentiating equation (4 – 7) with respect to time, it yields the first order system on the velocity vector v and pressure rate,

$$\frac{\partial v}{\partial t} = -\frac{1}{\rho}\nabla p$$

$$\frac{\partial p}{\partial t} = -K\nabla \cdot v$$

(4 - 8)

The discrete, 3D form of equation (4 – 8) can be defined by sampling velocity and pressure on the N points of an $N = N_x \times N_y \times N_z$ Cartesian grid. Defining N-vectors on velocities v_x, v_y, v_z, and pressure p, the system of discrete equations is as follows:

$$\frac{\partial (v_x, v_y, v_z, p)^T}{\partial t} = \left(-\frac{1}{\rho}\frac{\partial p}{\partial x}, -\frac{1}{\rho}\frac{\partial p}{\partial y}, -\frac{1}{\rho}\frac{\partial p}{\partial z}, -K\left(\frac{\partial v_x}{\partial x} + \frac{\partial v_y}{\partial y} + \frac{\partial v_z}{\partial z}\right)\right)^T$$

(4 - 9)

where the superscript T denotes the transpose.

The discrete ultrasonic wave equation (4 – 9) is reduced to a system of ODEs, which is to be integrated in time using either explicit or implicit integrator schemes, e.g., the 4th order Adams-Bashforth time integrator in the case (Mould et al., 1999). The iterative process can be interpreted as: a) Load new values of v_x, v_y, v_z, and p in equation (4 – 9); b) Calculate the spatial derivatives of v_x, v_y, v_z, and p at the N grid points Cartesian mesh system with applying the FFT-based procedures; c) Evaluate Eq. (4 – 9) and integrate the system of equations at each time step. The solution algorithm is thus repeated adequate time steps to capture the wave propagation in heterogeneous media. While it is worth noting that in SpectralFlex, the pressure is loaded on the interior of the element rather than adding the pressure to the element surface as done in PZFlex. Given the same amplitude of the driving load, the SpectralFlex model will generate a pressure twice higher than in the PZFlex model, for avoiding the waves propagating in two opposite directions.

Modelling Technique

The SpectralFlex model is highly accurate with small discontinuities (Mould et al., 1999), but when used for structures like tissue/bone, it becomes less accurate. Another technical limitation of this method is its spatial periodicity, for which the wave exiting one side of the model will enter from the opposite side, and the attenuation at the boundaries will cause reflections. One solution in SpectralFlex is the employment of a highly attenuative

and non reflective perfectly matched layer (PML) (Wojcik et al., 1997; Wojcik et al., 1999a). The pseudo spectral method combined with the perfectly matched layer works well for large-scale wave propagation problems in heterogeneous tissue models. For example, an eight element PML boundary can reduce reflections by more than 80 dB. In SpectralFlex, a sufficient small time step, Δt, is selected to be $\Delta t = \tau \cdot \Delta x/c = 0.3 \cdot \Delta x/c$ (where τ is the stability factor or called as the CFL number i.e., the shortest wave transmit time across any element, Δx is the element size and c is the wave speed), while in PZFlex $\tau > 0.8$ for solution accuracy. To simulate the attenuation mechanism, simple stiffness and mass-proportional damping, as well as an appropriate viscoelastic-dispersive model can be implemented. The harmonic distortion caused by weak shock effects can be involved by solving the nonlinear wave equation (Wojcik et al., 1999b).

4.2 HIFU Effects on Tissue-mimicking Phantoms

4.2.1 Geometric Model

To numerically explore the fundamental acoustic and thermal behaviour during the HIFU procedures, 2D axisymmetric PZFlex models comprising the single-element focused transducer (PA160) and the egg white tissue-mimicking phantom were created in accordance to Figure 3.10, as illustrated in Figure 4.1. For acoustic and thermal field investigations, the inclusion of the piezoelectric active element (PZ 54) will considerably increase the calculation time, due to the necessity of complete matrix manipulation at each time step in the implicit solver. And also it results in much denser element allocation in order to avoid ripples that may be observed in the loss array in the focal region, hence it will further increase the required computation time and memory usage. In the model proposed here, the piezoelectric element was replaced by a spherical pressure load with the same focal length, $Z = 75$ mm, and aperture size, $2R_s = 60$ mm. In all instances, the thickness of the phantom used was set to 88 mm and the distance between the transducer and surface of the phantom was $D = 28.2$ mm. The material properties of water and the egg white phantom for HIFU were referred to the measurement results from Section 3.2, and the non-linear parameter of the phantom material was supposed to be similar to water, e.g., B/A = 5.
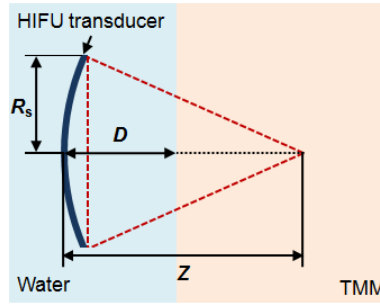
Figure 4.1 Schematic illustration of HIFU exposures on egg white phantoms.

4.2.2 Modelling Techniques

For a compromise between computational accuracy and run time, a uniform mesh density with 32 elements per wavelength was used in the acoustic model. The axisymmetric boundary condition and the absorbing boundary conditions were implemented to the transducer axis and other surrounding boundaries respectively. Focused ultrasound beam was generated by applying a desired acoustic pressure signal (amplitude, p_0; phase, θ) to the concave surface of the HIFU transducer. The ultrasonic wave propagation and acoustic pressure changes in the whole field was calculated. Once the acoustic wave propagated through the computational domain and the model reached its steady state condition, a loss array, i.e., one single cycle of acoustic energy deposition, was deposited as the heat source input for the following thermal prediction procedures. In the thermal model, less dense mesh with fewer elements per wavelength (16 elements per wavelength in the case) was selected, and the boundaries and initial conditions were set to 37 ℃. The temperature histories at the focal region were recorded and thereafter the thermal necrosis volume was predicted by calculating the thermal dosimetry, as described in Section 2.1.3.

As described in the experimental evaluation in Section 3.3.1, different heating strategies were discussed in the FE simulations:

a). with varying initial pressure amplitude, p_0, (0.4 – 1.2 MPa, with an elevation of 0.4 MPa);

b). with varying sonication duration, t_{on}, (3 – 15 s, with an elevation of 3 s);

c). with varying cooling-off period, t_{off}, (0 – 25 s, with an elevation of 5 s),

d). with varying perfusion rate, w_b, (0 – 20 kg/m^3/s, with an elevation of 5 kg/m^3/s).

In the thesis, numerical simulation of the piezoelectric element was not performed for the

thermal exploration; while it was used for validation of the free-field acoustic field measurement as described in Section 3.1.2. Based on our knowledge, the most crucial issues concerning transducer modelling include accurate transducer geometries, accurate piezoelectric material properties and poling direction. Assuming that the transducer geometries are fixed as provided, small modifications in the material properties can be made to achieve a better fit between the simulated and measured electrical and/or acoustic behaviour. The electrical impedance response can be changed with particular adjustments of the piezoelectric stress constant, e_{33}, the relative permittivity, ε_R^s, the elastic stiffness, c_{33}, the mechanical damping, Q, etc.

4.3 Transmitted Beam Distortion and Pressure Reduction in Trans-costal FUS

4.3.1 Geometric Model

The geometric configuration of HIFU propagation through the rib cage is shown in Figure 4.2. The geometries and material properties used in the FE model are based on those of the experimental setup for the acoustic absorber rib cage mimics as described in Figures 3.13 and 3.17. The rib cage is simplified as a set of three parallel rectangular sectional ultrasonic absorbers, where L_r and L_i are the widths of the rib mimics and the inter-costal spaces respectively, $L = L_r + L_i$ is one period of the structure, and H is the thickness of the rib mimics. In clinical practice, ribs 7 - 9 of the lower chest wall are mostly intersected by the HIFU beam (Zhu et al. 2009), indicating that three rib mimics are enough for both experimental analysis in Section 3.4.4 and simulation work presented here. Other relevant parameters are R_s, the radius of the ultrasonic source; Z, the focal length of the source; D_z, the distance from the source to the front (outer) surface of the ribs; and D_y, the distance from the focus to the centre of the middle rib in the transverse direction. Hence, $Z - D_z$ and R_e represent the depth of the focus (target) measured from the surface of the ribs and the beam radius there. Main factors affecting the acoustic beam patterns after propagation of focused ultrasound through the rib cage are investigated as follows:

a)   the dimensions of the rib cage: $L_r + L_i = 30$ mm and $L_r / L_i = 0.5, 1, 2$; $H = 10$ mm.

b) the position of the intended target relative to the rib cage: $Z - D_z = 11.2 \sim 61.2$ mm, with a step of 5 mm; $D_y = 0, 3.75, 7.5, 11.25, 15$ mm.

c) the F-number of the ultrasonic source: $f\# = Z / 2R_s = 1.25, 0.9375, 0.75, 0.625$, for which $Z = 75$ mm and $R_s = 30, 40, 50, 60$ mm.

d) the driving frequency of the ultrasonic source: $f = 0.55, 0.7, 0.85, 1.0, 1.15$ MHz.
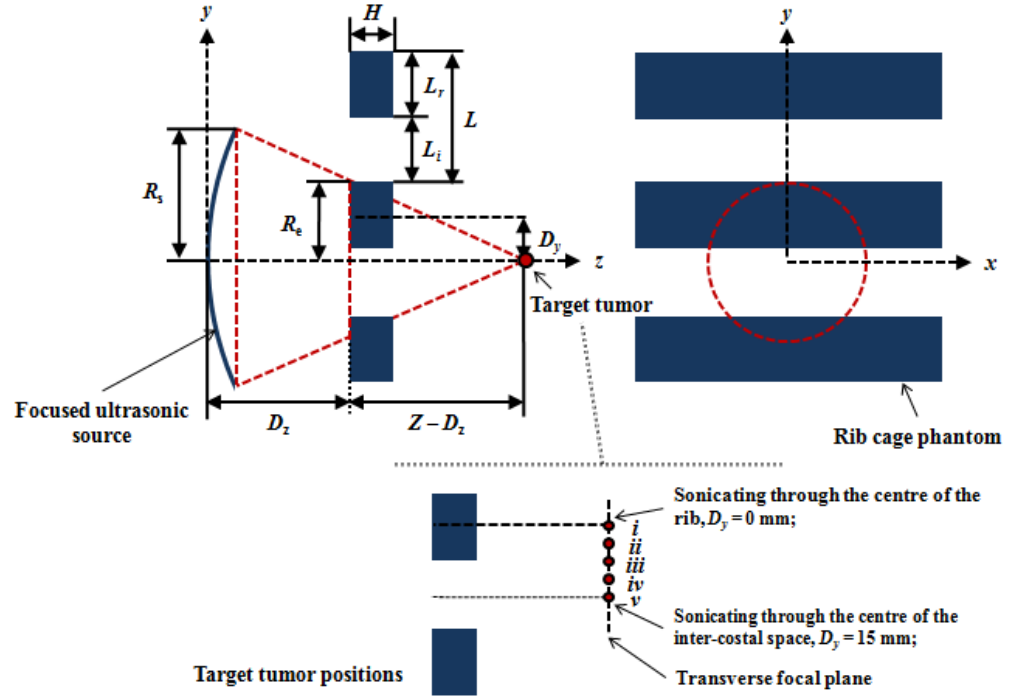
Figure 4.2 Geometric configuration of propagation of focused ultrasound beams through the rib cage. The variables L_r and L_i are the widths of the rib mimics and the inter-costal spaces respectively, $L = L_r + L_i$ is one period of the rib structure. $2R_s$ and Z are the aperture and the focal length of the ultrasonic source. D_z and D_y are, respectively, the distance from the source to the front surface of the ribs and the distance from the focus to the centre of the middle rib in the transverse direction.

4.3.2 Modelling Techniques

In Section 4.2, a spherical cap pressure load, radius of curvature Z and aperture $2R_s$, was used to model the focused ultrasonic source. This allowed use of the axisymmetric boundary condition. However, the rib mimics can be simulated only in a complete 3D model or a 2D plane strain model. The large 3D model produces more accurate results, but at the expense of increased computation time (to more than 10 hr) and memory (as much as 1200 GB). The 2D model can significantly reduce the solution time and the

amount of memory, and is also effective enough to solve the proposed problem. Absorbing boundary conditions were employed to truncate the model in space, and a uniform mesh of 30 elements per wavelength was used in all simulations as a compromise between accuracy and computation time. With this mesh density, a 2D plane strain model required roughly 20 min to reach a steady state with 24 GB memory, depending in detail on the model size. In this study, the ultrasonic pressure distributions affected by the ribs were calculated numerically. Although the intensity distributions could be evaluated from these with $I = p^2/2\rho c$, considering $\rho_{water} \cdot c_{water} \approx \rho_{rib\text{-}mimics} \cdot c_{rib\text{-}mimics}$, the resulting pressure distribution adequate represented the intensity distribution directly. The normalized target pressure value was determined as functions of dimensions of the rib cage, position of the intended target relative to the rib cage, F-number and driving frequency of the ultrasonic source.

4.4 Trans-costal Heating and its Frequency Dependence

4.4.1 Geometric Model

This section aims to understand the effects of transmitted beam distortion and intensity reduction caused by the abdominal structure and to examine the effects of different ultrasound frequencies (0.4 – 1.2 MHz, with an elevation of 0.2 MHz) in the trans-costal treatment of tumours in the upper abdomen organs e.g. the liver, kidney, and pancreas. A configuration diagram encompassing components of the HIFU transducer, the coupling medium and the chest anatomy was built using PZFlex. This simplified multi-layer model was closely matched to the anatomical structure as shown in Figure 4.3(a). The absorbing boundary conditions were used to truncate infinite domains in order to perform computations. In Figure 4.3(b), the ultrasonic source used for trans-costal sonications has an internal radius of $R_s = 60$ mm and a focal length of $Z = 135$ mm (F-number of $f\# = 1.125$). $L_r = 14$ mm and $H = 8$ mm are the width and thickness of the rib bone, $L_i = 26$ mm is the width of the inter-costal muscle, and $L = L_r + L_i = 40$ mm represents one period of the rib structure. These representative values of ribs were selected within the range in variation in human adults (Liu et al., 2007). The target positions relative to the acoustic source or the rib cage are indicated by two parameters of $Z - D_z$ (ranging from 20 to 100 mm, with a step of 10 mm) and D_y (0, 10, 20 mm), where D_z is the distance from the acoustic source to the frontal surface of the rib plane, and D_y is the distance from the

target to the centre of one rib in the transverse direction. Another parameter, R_e, is the effective beam radius in the frontal rib plane.
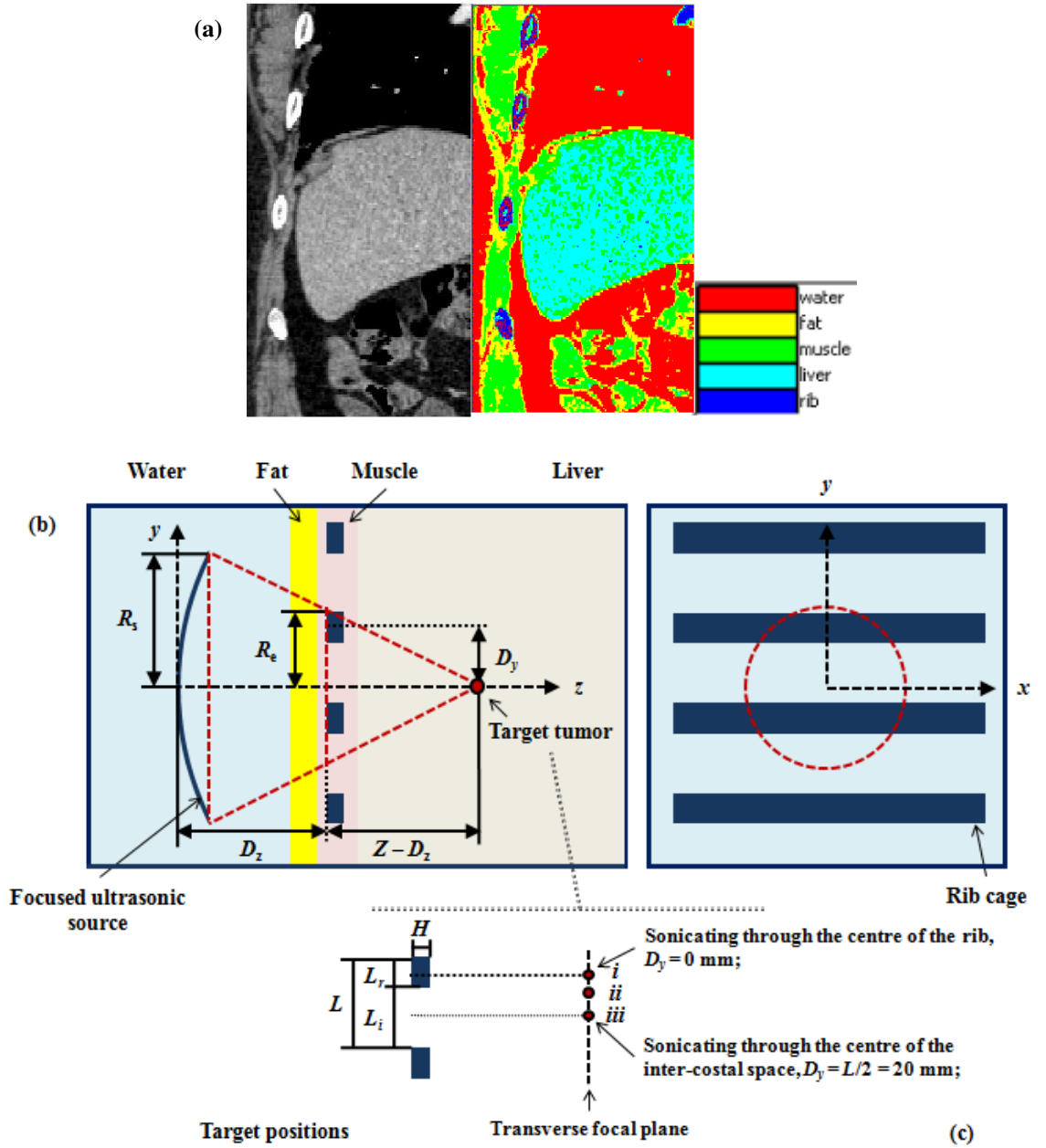
Figure 4.3 (a) Images showing the chest anatomy, from patient data. (b) Geometric representation of trans-costal delivery of focused ultrasound energy. Representative tissue layers of the abdominal structure include fat (12 mm in thickness), muscle (18 mm), rib (8 mm), and liver in sequence. (c) Three lateral distances were $D_y = 0$ mm (sonicating through the centre of the rib), $D_y = L/4 = 10$ mm, and $D_y = L/2 = 20$ mm (sonicating through the centre of the inter-costal muscle), respectively.

4.4.2 Modelling Techniques

Ultrasound at frequencies of 0.4, 0.6, 0.8, 1.0, and 1.2 MHz have respective wavelengths of 3.75, 2.5, 1.875, 1.5, and 1.25 mm in water. An equivalent Cartesian mesh resolution with the element size of 0.0625 mm was achieved by assigning appropriate numbers of elements per wavelength. A full 3D model with the same mesh resolution would contain over 15 billion elements and is therefore undesirable with current hardware systems considering their limited storage space and limited computing capability. It is reasonably assumed that the 2D models could function as a satisfactory alternative approach in trans-costal research (Aubry et al., 2008). For all of the thermal models considered, the boundaries and initial conditions were set to 37 ℃, and the mesh resolution was adjusted to 0.125 mm instead. To access the heating efficiency of different driving frequencies, the acoustic power was maintained at the same level, with the initial pressure amplitude of 0.4 MPa. A 15 s active heating session following by a 45 s cooling-off period was then evaluated. Throughout the study, the frequency-dependent heating at the target and the intervening ribs were estimated. The ratio of ultrasonic power density at the target and the ribs, the time-varying spatial distribution of temperature, and the ablated region of each sonication were regarded as key indicators to determine the optimal sonicating frequency in clinical trans-costal FUS applications.

4.4.3 Material Properties of Rib Bone

The reliability of FE simulations depends on several factors such as mesh resolution and material properties. However to date, very little literature exists on the acoustic and thermal properties of rib bone and much of the relevant work has been accomplished in femoral bone or cranial bone. In the study, the ribs are simplified as a homogeneous material. The uniform mass density, longitudinal wave speed, and longitudinal attenuation coefficient with $\rho_{\text{-rib}}$ = 2100 kg·m^{-3} (Williams, 1990), $c_{\text{-}l\text{-rib}}$ = 3200 m·s^{-1} (Goss *et al.*, 1980), and $\alpha_{\text{-}l\text{-rib}}$ = 6.9 dB·cm^{-1}·MHz^{-1} (Duck, 1990) were assigned to the rib bone for simulation of acoustic wave propagation through it. Previous results of FE computations with and without shear wave generation within a bone revealed the effects of generally higher energy deposition in the shear bone model (Nell and Myers, 2010); in particular, a slightly lower temperature rise on the axis of the ultrasound beam as well as higher

temperature rises at increasing transverse distances from the axis were observed (the largest difference in temperature rises between the shear and no shear supporting models was ~30 %). Hence, it is necessary to include shear wave propagation in the determination of acoustic and thermal effects in the bone structures. The values of the shear wave speed, c-$_{s\text{-rib}}$ = 1800 m·s^{-1} (Mehta and Antich, 1997), and the shear attenuation coefficient, α-$_{s\text{-rib}}$ = 10 dB·cm^{-1}·MHz^{-1} (Nell and Myers, 2010), were incorporated into the models, effectively simulating acoustic propagation in the transverse direction. The ultrasonic attenuation coefficients of rib bone, α-$_{l\text{-rib}}$ and α-$_{s\text{-rib}}$, were both assumed to increase approximately linearly with the frequency (b = 1) in the frequency range of 0.2 - 1.7 MHz (Chaffai et al. 2000). The value of the nonlinear coefficient of rib bone was set to zero, only accounting for linear wave propagation.

The thermal conductivity in rib bone, k-$_{\text{rib}}$, is also an important parameter to demonstrate the ability of rib bones to dissipate heat generated by ultrasound and to predict the potential production of hot spots in ribs under sonication. Hot spots might be produced by the formation of standing waves between the frontal and dorsal surfaces of the ribs leading to local areas of greater heating. A high k-$_{\text{rib}}$ value can thus reduce the effect of standing waves by rapidly dissipating local hot spots into surrounding cooler rib bone. As noted earlier, a single representative value of k-$_{\text{rib}}$ is sufficient for thermal simulation in the ribs. As the rib bone appears to be structurally different to the femoral bone, measurements from the bones of the cranial skull were used, e.g., k-$_{\text{rib}}$ = 0.435 W·m^{-1}·°C^{-1} and C-$_{\text{rib}}$ = 1370 J·Kg^{-1}·°C^{-1} (Liu et al., 2007). All the acoustic and thermal properties used in the simulations can be found in Table 4.1.

Table 4.1 Properties of materials used in the simulations

	water	fat	muscle	rib	Liver
ρ (kg m^{-3})	1000	921	1138	2100	1055
c-$_l$ (m s^{-1})	1500	1445	1569	3200	1547
c-$_s$ (m s^{-1})	-	-	-	1800	-
α-$_l$ (dB cm^{-1} MHz^{-1})	0.002	0.608	0.782	6.9	0.782
α-$_s$ (dB cm^{-1} MHz^{-1})	-	-	-	10	-
k (W m^{-1}°C^{-1})	0.615	0.248	0.54	0.435	0.512
C (J Kg^{-1} °C^{-1})	4180	2490	3700	1370	3600

4.5 Optimized Operation of 2D Phased Arrays to Avoid Overheating of Ribs

4.5.1 2D PZFlex Models

To verify the effectiveness of the geometric rib sparing techniques mentioned in Section 3.6, 2D acoustic and thermal models were constructed using the PZFlex code following details as described in Figure 3.20, in which setup the tissue-mimicking phantom with inclusion of the acoustic absorber rib cage mimics was sonicated by the 1024-element matrix phased array. As illustrated in Figure 4.4, three types of sonications were investigated: a) full spherical radiation, b) Algorithm #1 – central projection and c) Algorithm #2 – parallel projection. For both rib sparing algorithms, those transducer elements located within the effective areas of $S \sim A_1$ and $A_2 \sim T$, or $S \sim B_1$ and $B_2 \sim T$, should be activated, respectively. And their relative pressure amplitudes were adjusted to deliver the same power output.
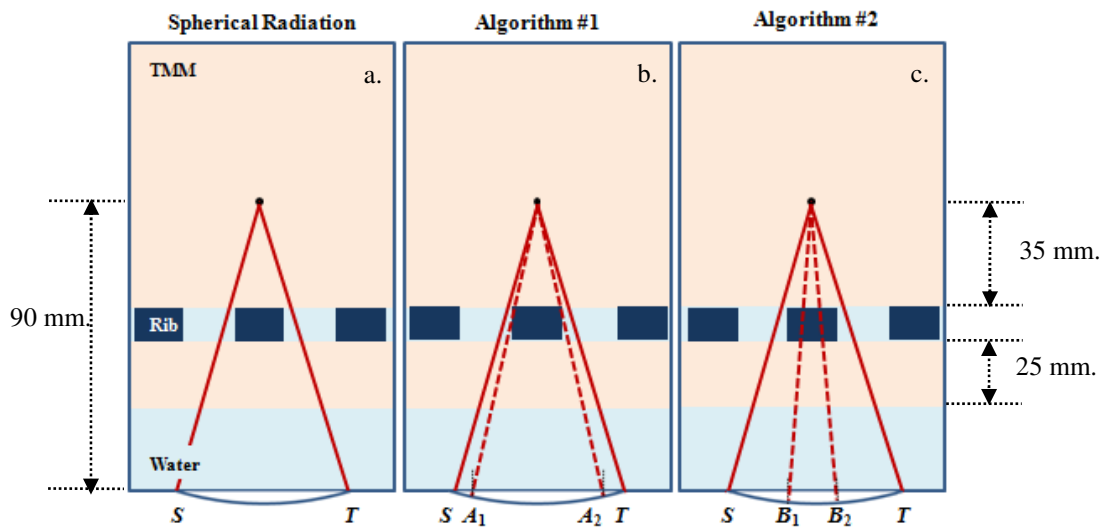
Figure 4.4 Geometric representation of binary manipulation of elements in the phased array: (a) Full spherical radiation, (b) Algorithm #1 – central projection, and (c) Algorithm #2 – parallel projection.

To further evaluate the effectiveness of the geometric rib sparing method with respect to more complex abdominal structure and varying target locations, 2D FE simulations were built as shown in Figure 4.5. The geometric information and modelling techniques, such as the spatial and temporal discretization, material damping, boundary conditions, etc, included in the models were the same as those presented in Figure 4.3, only with varied

pressure load conditions. For example, using Algorithm #1 – central projection, only transducer elements located within the unshadowed intervals of $S \sim A_1$ and $A_2 \sim A_3$ (y axis) were activated (Figure 4.5). The acoustic intensity on the surface of the transducer was maintained at the same level, with the initial pressure amplitude of 0.4 MPa. The optimal centre frequency derived from Section 4.4 was applied, and the mesh resolution of 0.0625 mm was obtained then. In this part, only the acoustic models were calculated, and the ratio of ultrasonic power density at the target and the ribs was compared with and without implementation of the elemental manipulation. Various target positions relative to the rib cage (D_y = 0, 10, 20 mm, respectively; D_z = 76 mm and 20 mm $\leq Z - D_z \leq$ 100 mm), were numerically steered without mechanical movement of the phased array.
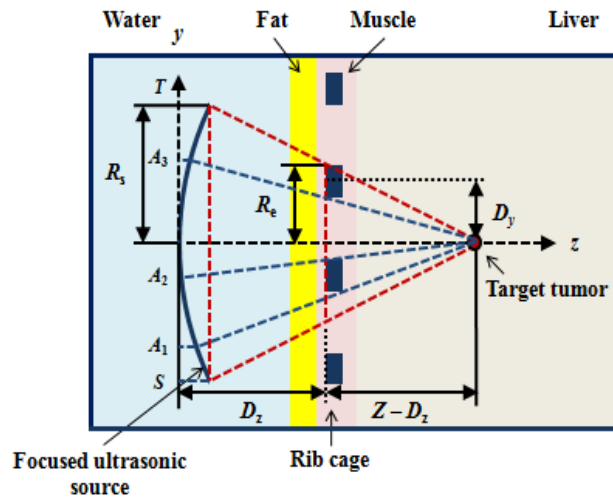
Figure 4.5 Geometric representation of binary manipulation of elements in the phased array: Algorithm #1 – central projection.

4.5.2 3D PSFlex Models

Binary manipulation of the >1000-element matrix phased array was simulated in complete 3D SpectralFlex models, where the linear propagation media remained unchanged as shown in Figure 4.4. The positions of transducer elements in the matrix phased array are displayed in Figure 4.6. Other than the typical 15 ~ 20 elements per wavelength at the highest frequency of interest in PZFlex, 4 elements per wavelength at the highest frequency of interest were assigned to the SpectralFlex models. In this FFT-based algorithm, the best model efficiency is achieved when the number of cells in each direction is a power of 2, 3, or 5. Therefore, it was possible to find out that the actual

number of elements allocated did not equal what was requested. As SpectralFlex only models acoustic materials like water and biological tissue, so no shear wave velocity and attenuation in the rib bone was included in these cases. Also the viscous damping is no longer available in SpectralFlex and the recommended acoustic damping was used for all materials here instead. The perfectly matched layer (PML) boundary conditions were used to prevent signal looping, e.g., 20 PML elements with attenuation factor of 0.2 were allocated at the edges of the grids. Under these configurations, both acoustic and thermal simulations (driving load: an initial pressure amplitude of 0.4 MPa, and heating session: a 15 s active heating session following by a 45 s cooling-off period) were conducted with and without appropriate transducer elements switched off.
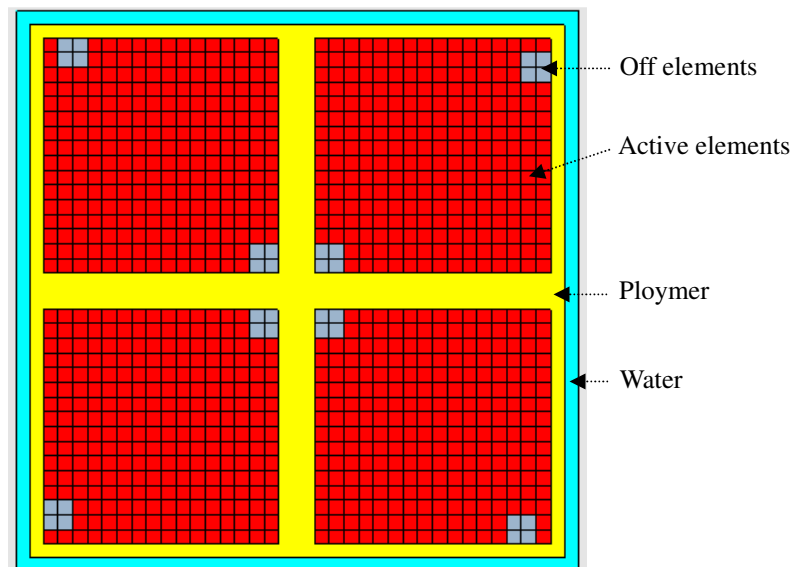
Figure 4.6 Geometric illustration of the 1000-element matrix phased array.

CHAPTER 5 RESULTS AND DISCUSSION

Chapter Five presents the results and discussion gathered during the course of the work. Section 5.1 begins with a summary of characterization results of all single-element focused ultrasound devices used throughout the investigation in terms of electrical impedance and acoustic field behaviour (Section 5.1.1). Section 5.1.2 presents the acoustic and thermal properties of the heat-sensitive tissue-mimicking phantoms introduced to test the HIFU devices and explore functional behaviour during the HIFU procedures. The experimental and numerical results relevant to the fundamental acoustic and thermal effects of HIFU are then presented in Sections 5.1.3 and 5.1.4, thus providing a solid foundation for follow-up trans-costal studies. This chapter also contains the results from the application investigation conducted for the treatment of upper abdominal tumours through the rib cage. A variety of rib cage models including two rib cage mimics, porcine rib cage samples and a Thiel-embalmed cadaver are used to investigate the effects of HIFU propagation through the rib cage in trans-costal FUS (Sections 5.2 to 5.4). The results of the investigation presented here are addressed in all aspects of the developed procedures: the focused ultrasonic devices (the geometry and the driving frequency of the device), the anatomical configurations (the geometry of the human rib cage and the anatomical relation of the tumour with the ribs), the relative positioning of the device, the ribs and the target tumours. Following the full investigation, discussion is provided on the exploration of optimal sonication protocols, paying particular attention to the problem of overheating of the ribs.

5.1 Fundamental Acoustic and Thermal Effects of HIFU

5.1.1 Electrical Impedance and Beam Profiles of HIFU Transducers

5.1.1.1 Electrical Impedance

The electrical impedance response can reveal useful information about the performance of an ultrasonic device and is an important indicator for use. This section presents the electrical impedance data for each of the commercial single-element HIFU devices used

in the investigation including PA160, PA316 and PA356. In these cases, water was used as the acoustic load.
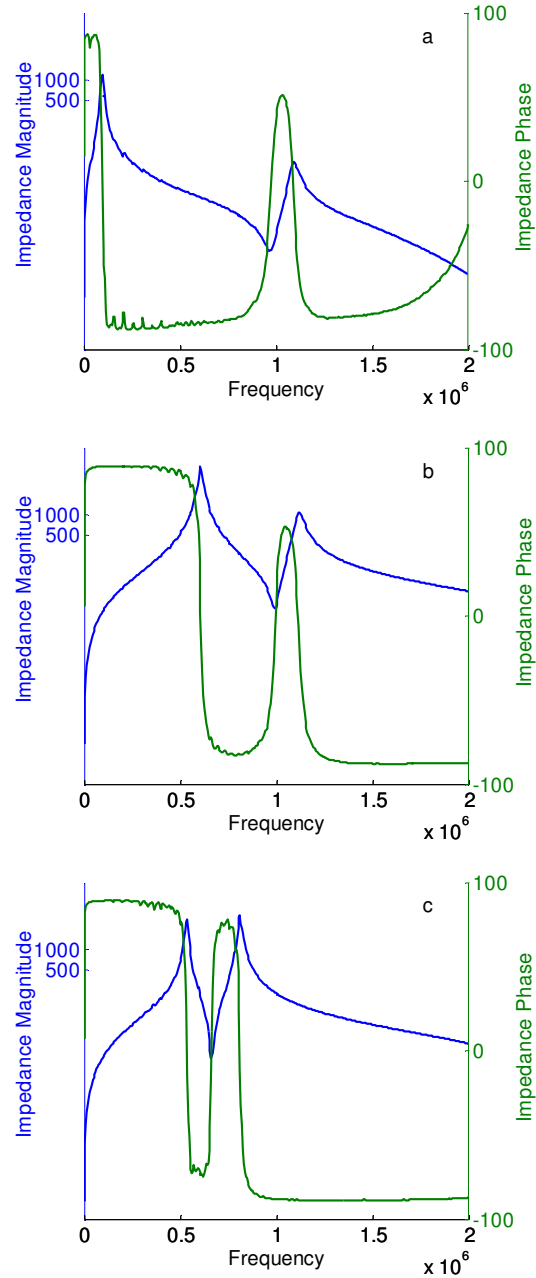
Figure 5.1 Impedance magnitude, |Z|, and phase, θ: a) PA160, b) PA316, and c) PA356.

The impedance magnitude curve, |Z|, of a standard piezoelectric transducer with no electrical matching, shows an exponentially decreasing trend with frequency as a capacitor, and the phase remains at -90°; while within the interval of the resonance pair, from the electrical resonance (impedance minimum or resonant frequency) to mechanical resonance (impedance maximum or anti-resonant frequency), it behaves as an inductor,

and the phase is close to $+90°$. The impedance phase is close to zero at the electrical and mechanical resonance frequencies. However with implementation of impedance matching, e.g., LC (inductance-capacitance) circuitry or a transformer, the resulting changes in the impedance magnitude, $|Z|$, and phase, θ, can be detected, as shown in Figures 5.1(a) - (c).

The impedance magnitudes, $|Z|$, at the electrical and mechanical resonances of the devices supplied with impedance matching are summarized in Table 5.1. At the electrical resonant frequency of 0.965 MHz, the transducer PA160 has an impedance magnitude of 2.89 Ω, while at the mechanical resonant frequency of 1.09 MHz, it has the impedance magnitude of 60.92 Ω. Thus, in contrast to the conventional choice of electrical resonance, the working frequency of PA160 is taken as near the mechanical resonance of 1.09 MHz for simpler implementation of electrical impedance matching (close to 50 Ω) between the transducer and the external drive equipment.

Table 5.1 Summary of electrical impedance data relevant to each device

Device	Electrical resonance (MHz)	Impedance magnitude, $\|Z\|$ (Ω)	Mechanical resonance (MHz)	Impedance magnitude, $\|Z\|$ (Ω)	Suggested frequency, $\|Z\| = 50\ \Omega$
PA160	0.965	2.89	1.09	60.92	1.078
PA316	0.99	40.41	0.605	5308	1
			1.12	1093	
PA356	0.66	24.53	0.535	2849	0.67
			0.81	3209	

5.1.1.2 Beam Profiles

This section presents the results relating to acoustic field measurements of all HIFU devices available. Descriptions of the measurement system can be found in Section 3.1.3 and in these instances, the measurements were made under the same driving signal amplitude of $V_{\text{p-p}}$ = 5 V for comparison. Resultant beam profiles for each device are presented in the form of contour plots measured with the calibrated 0.5-mm needle hydrophone (sensitivity coefficient of 359.2 mV/MPa and uncertainty of 13 % at the frequency of 1 MHz). Further demonstration of the acoustic performance of each device can be achieved through axial and lateral focal plots of these receiving signal amplitudes.
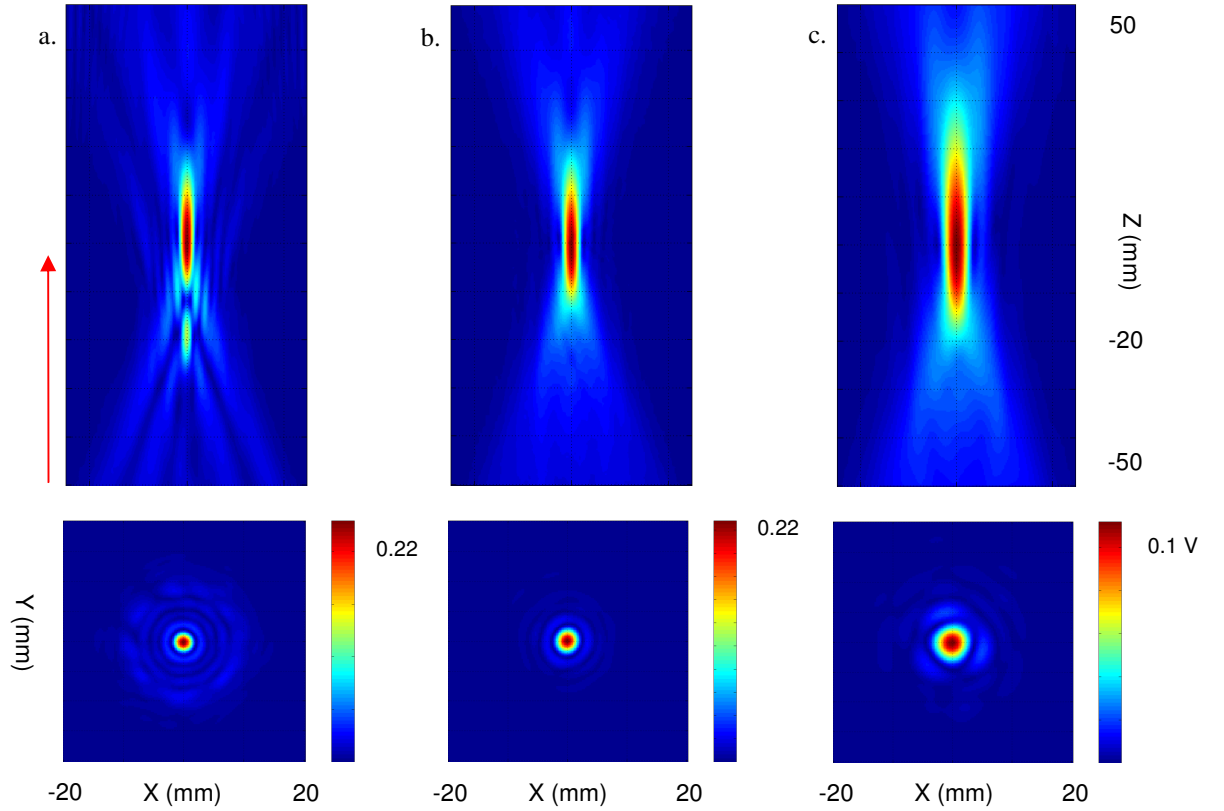
Figure 5.2 Acoustic field mapping: a) PA160, b) PA316, and c) PA356.

Table 5.2 Summary of -6 dB focal zone of each device

Device	dx (mm)	dy (mm)	dz (mm)	cross-sectional focal area at focus (mm^2)
PA160	2.38	2.41	34.14	4.5
PA316	2.89	3.12	25.63	7.08
PA356	4.41	4.58	39.4	15.86

Figure 5.2 displays the separate focal characteristics of each device (the point of peak voltage/pressure value was taken as the origin), and a more direct comparison among the dimensions of -6 dB focal volume are listed in Table 5.2. A less concentrated focal region of the low frequency device, PA356 (0.67 MHz), in comparison to the high frequency ones, PA316 (1 MHz) and PA160 (1.09 MHz), can be seen clearly from the measured axial and lateral behaviour of all devices. The results also show the devices to have excellent field uniformity with approximate axial focal lengths of 71.4 mm (PA160), 74.3 mm (PA316), and 74.7 mm (PA356), close to the radius of curvature of the focusing bowls. However, the sub-focal zone at the small axial depth of around 50 mm from the

device front face (PA160) will limit its performance in thermal ablation, as an unintentional thermal lesion will be produced there.

Of particular importance, the most intensively used HIFU device, PA160, was calibrated prior to use. Exploring the relationship between the voltage output of the signal generator to the 53 dB power amplifier (1020L RF power amplifier, E&I, USA) and the resultant voltage reaching the piezoelectric element, a linear relationship between the two can be seen preceding a certain input voltage of 200 mV_{pp}; however, following that value the relationship ceases to be linear, as shown in Figure 5.3(a). This nonlinear distortion occurring at higher input-signal levels reveals the reliable operating range for the power amplifier. The calibration procedure was completed by measuring the transducer output pressure at the focus against the voltage input to the active element after the amplified driving system. The resultant calibration curve is shown in Figure 5.4.
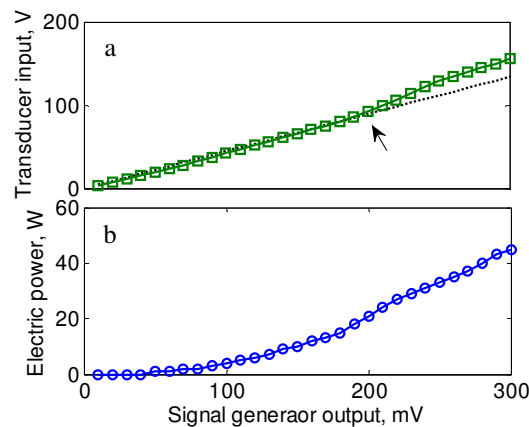
Figure 5.3 Calibration curve of PA160.
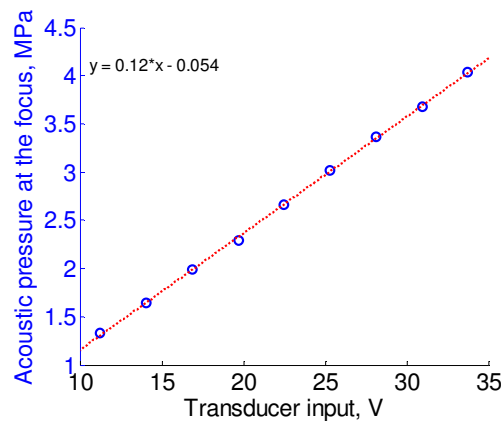
Figure 5.4 Calibration curve of PA160: output pressure at the focus.

Data gathered during calibration may provide useful information for future investigations. For example, for subsequent focused ultrasound sonications, the power amplifier driven with a 50 mV$_{pp}$ (35.4 mV$_{rms}$) signal yields an input of 19.4 V$_{pp}$ (13.7 V$_{rms}$) to the active piezoelectric element. This will produce a peak-to-peak pressure of 2.29 MPa at the focus, and a consequent intensity of around 13 W/cm^2 in the free field condition. In all instances, the device is capable of producing focal intensities of at least 1700 W/cm^2 (acoustic power of 85 W).

5.1.2 Acoustic and Thermal Properties of HIFU Phantoms

A new experimental model of a transparent polyacrylamide (PAA) gel embedded with egg white was employed in the follow-up investigation of HIFU for non-invasive ablation. In this section, results regarding the acoustic and thermal characteristics of these egg white tissue-mimicking phantoms are presented.

5.1.2.1 Acoustic Properties

Fundamental acoustic properties of these egg white phantoms including the longitudinal wave velocity (or speed of sound) and acoustic attenuation coefficient were measured using the standard through transmission technique described in Section 3.2.2. Using this method, the acoustic signal only has to transmit through the sample once, so that even highly attenuative materials can be characterized easily. During the experiment, the phantoms with varying egg white concentrations (10 % - 40 %, with a step of 10 %) were held with a phantom holder. Although the sample can be placed directly on top of the bottom transducer in water (Figure 3.5), it is difficult to ensure that the phantom does not move at all.

The longitudinal velocity was measured at 5 MHz and the attenuation between 3 and 5 MHz. The measured acoustic properties of these tissue-mimicking phantoms with varying egg white concentrations at room temperature are shown in Figure 5.5. The densities of the phantoms were close to that of water, and were almost independent of egg white concentration within the investigation range of 10 % - 40 %. The longitudinal velocities ranged from 1539 to 1548 m/s, as shown in Figure 5.5a. Phantoms with higher

egg white concentration had higher speed of sound, and a high correlation coefficient of 0.969 between the speed of sound and the egg white concentration was seen. As shown in Figure 5.5b, the attenuation of each egg white phantom varied quasi-linearly over the investigated frequency range. The frequency range (3 - 5 MHz) was determined by the centre frequency (5 MHz) of the transmitting and receiving devices in use. Although this does not match the most useful frequency in HIFU applications (~ 1 MHz), reasonable outcomes can be estimated by assuming a linear relationship between the attenuation coefficient and the frequency. Thus, the attenuation coefficients of 0.449, 0.456, 0.528, and 0.587 dB/cm were produced for the 10 %, 20 %, 30 % and 40 % egg white phantoms at 1 MHz respectively. The attenuation coefficient was also noted to increase with the egg white concentration.
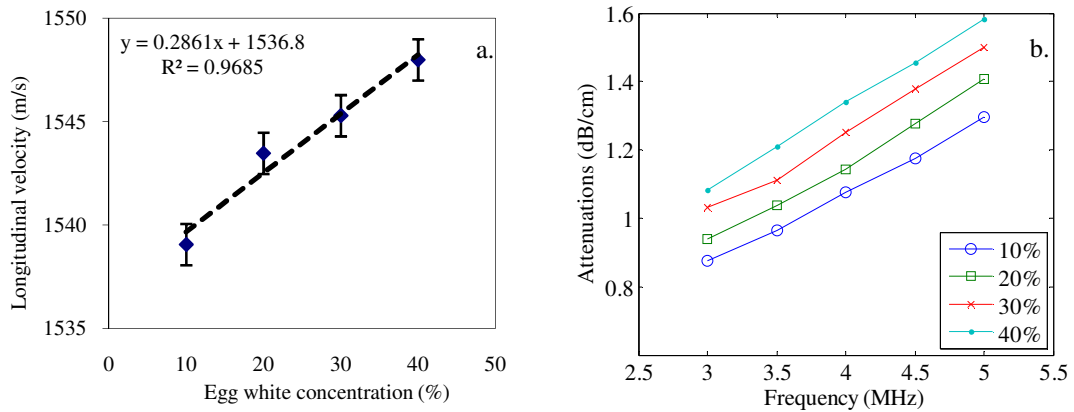
Figure 5.5 (a) Longitudinal velocity and (b) attenuation coefficient of egg white phantom vs. egg white concentration ranging from 10 % to 40 %.

In comparison, the longitudinal wave velocities of these phantoms were similar to that of soft tissue, though their acoustic attenuation coefficients were smaller than that of soft tissue, e.g., 0.782 dB/cm/MHz for liver. Regarding the uncertainty of determining the dimensions of the sample and digitizing errors, the relative errors were assumed to be 2 % and 5 % for the measured longitudinal velocity and attenuation coefficient, respectively.

5.1.2.2 Thermophysical Properties

Thermophysical properties of these egg white phantoms, namely the thermal conductivity, specific heat capacity and thermal diffusivity, were estimated using the step-wise

transient plane source (TPS) method in correspondence with Section 3.2.3. Egg white phantoms with gradually increased egg white concentrations ranging from 0 to 40 % v/v, by 10 % v/v interval were tested. Of particular importance, a measuring time of 15 min was chosen based on the discussion in Section 3.2.3.3 for this step-wise TPS method. At each egg white concentration level, measurements of the temperature changes were repeated three times at room temperature (~20 °C) and the mean values were obtained by averaging. Figure 5.6 shows the averaged temperature responses at the distance of 8 mm from the heat source during the heating processes. For all the samples the maximum temperature rises were more than 11 °C at the end of the 15 min heating period. A good linear relationship between the egg white concentration and the maximum temperature rise existed, especially in the range of 10 % to 30 % ($R^2 = 0.992$).
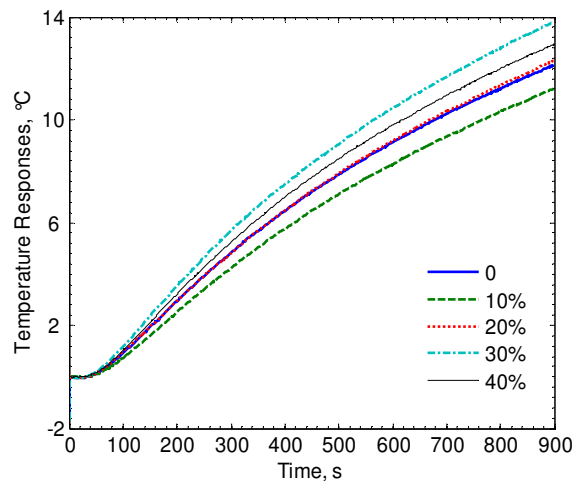
Figure 5.6 Averaged temperature rises in 15 min heating period for egg white phantoms with different egg white concentrations (0 to 40 %).

The difference analysis method (Kubicar and Bohac, 2001) used for determination of fitting time window is based on sequential fitting of Eq. (3 - 11) to the measured temperature change curve. A time interval of 25 s was selected, within which period the fitting procedure was applied to an individual part of the measured temperature response curve. The time interval was consecutively shifted over the measured curve starting from 0 up to 15 min (i.e., 0 s to 25 s, 25 s to 50 s, ⋯, 875 s to 900 s). Discrete fitted values of the thermal conductivity and thermal diffusivity of the 10 % egg white phantom are shown in Figure 5.7 as a function of t (s). Data stability is good in the interval of 100 s to 500 s.
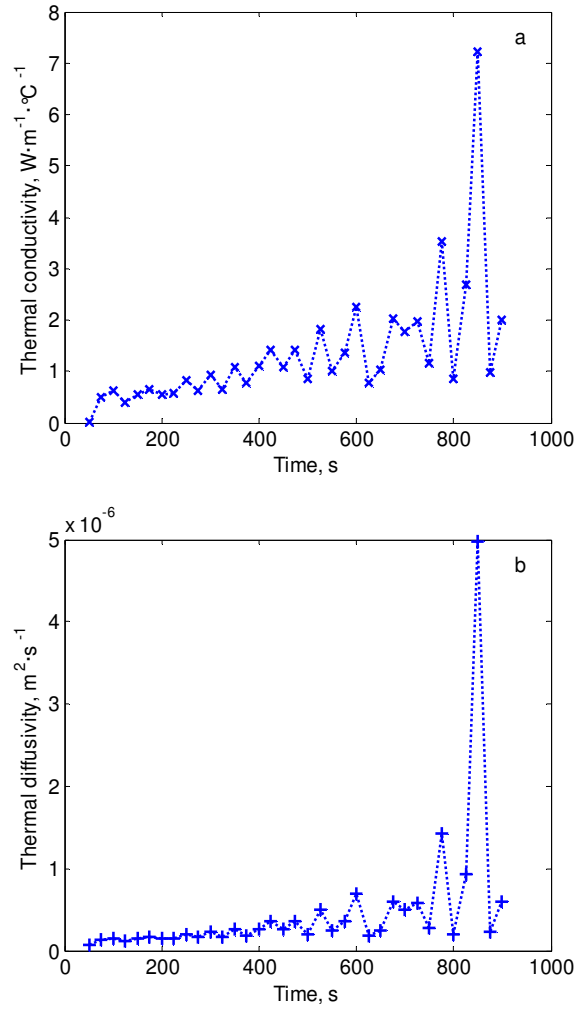
Figure 5.7 Difference analysis of the 10 % egg white phantom: (a) thermal conductivity and (b) thermal diffusivity.

According to the difference analysis results of the 10 % test sample, the curve fitting procedures were applied to the heating period of 100 s to 500 s for all test samples. Table 5.3 summarizes the measured k, α, and C values of all samples at room temperature. In Table 5.3, the measured thermal conductivity, k, increases linearly from $0.722 \, \text{W} \cdot \text{m}^{-1} \cdot {}^{\circ}\text{C}^{-1}$ (0 %) to $0.759 \, \text{W} \cdot \text{m}^{-1} \cdot {}^{\circ}\text{C}^{-1}$ (40 %) within the entire egg white concentration range of 0 to 40 %, and the R-squared value, R^2, is around 0.95. The measured thermal diffusivity, α, also shows a linear increase trend in the concentration interval between 0 and 40 % (especially in the range of 10 % to 30 %, $R^2 = 0.9998$), while the measured specific heat capacity, C, decreases with increasing egg white concentration.

Table 5.3 Measured thermophysical properties of egg white phantoms with different egg white concentrations (0 to 40 %)

Egg White Concentration	k	α	C
units	$W \cdot m^{-1} \cdot °C^{-1}$	$m^2 \cdot s^{-1}$	$J \cdot kg^{-1} °C^{-1}$
0 %	0.722	1.866×10^{-7}	4230.5
10 %	0.737	1.826×10^{-7}	4304.9
20 %	0.744	2.019×10^{-7}	3670.4
30 %	0.747	2.221×10^{-7}	3743.9
40 %	0.759	2.253×10^{-7}	3271.9
R^2	0.95	0.88	0.84

Comparing the data reported in this thesis and those published in Divkovic et $al.$ (2007) (k = (0.59 ± 0.06) $W \cdot m^{-1} \cdot °C^{-1}$ and C = (4270 ± 365) $J \cdot kg^{-1} °C^{-1}$, 9 % to 10 % w/w egg white protein, 5 % acrylamide, 26 °C), the specific heat capacity values are identical and the difference between the thermal conductivity values is about 12.4 %; while, comparing the data reported here with those published in Lafon et $al.$ (2001, 2005) (k = (0.70 ± 0.07) $W \cdot m^{-1} \cdot °C^{-1}$ and C = (5100 ± 500) $J \cdot kg^{-1} °C^{-1}$, 7 % BSA, 7 % acrylamide, 22 °C), the thermal conductivity values are similar and the difference between the specific heat capacity values is about -19.7 %. The differences of the measurement results could be explained by variations in the compositions of the egg white phantoms and the measurement conditions. It is important to notice that the thermophysical properties of these egg white phantoms were similar to those of real tissues, e.g., liver (k = 0.512 $W \cdot m^{-1} \cdot °C^{-1}$ and C = 3600 $J \cdot kg^{-1} °C^{-1}$).

The transient methods for the determination of thermophysical properties, including the hot-wire method, the hot-strip method, the hot-disk method, the hot-plate method, the pulse transient method, the step-wise transient method, the laser flash method, etc., perform the measurements during the process of heating (ISO 22007, 2007; Gustafsson et $al.$, 1979; Al-Ajlan, 2006; Bilek et $al.$, 2006; Huang and Liu, 2009). The relatively short duration of the experiments eliminates unwanted physical or chemical changes of the test sample, and hence reduces the measurement errors caused by time. The relatively simple experimental setup also makes the measurements cost effective. However, one disadvantage of the transient technique is that its signal processing is more complicated than that of the steady-state technique.

The major problems of the step-wise TPS technique mainly result from the differences

between a real experimental setup and ideal model, as summarized in Table 5.4. For the issue of finite sample size (Table 5.4 - 1), as the experimental design criteria of the step-wise TPS method has not been set yet (Lei *et al.*, 2009), we reasonably assume it is similar to that of the pulse TPS method. Based on the criteria proposed by Kubicar (Kubicar and Bohac, 2001; Tye *et al.*, 2005) ($x_{II} < 0.4R$, $x_{II} H/k < 0.1$, $x_{I, III} > 1.4x_{II}$, where R is the diameter of the sample, H is the heat transfer coefficient ($H_{air} = 25$ W·m^{-2}·K^{-1}, $H_{vac} = 1$ W·m^{-2}·K^{-1}), and k is the thermal conductivity), the required sample sizes were estimated as: $R = 53$ mm, $x_{II} = 8$ mm, $x_I = x_{III} = 20$ mm in the study, which were also thought to be effective for the problem mentioned in Table 5.4 - 5. Moreover, considering the relatively small thermal contact resistance between the sample pieces in comparison with the thermal resistance of the samples (Table 5.4 - 4), and the relatively high thermal conductivity of the sample pieces in comparison with that of air (Table 5.4 - 6), the ideal conditions were thought to be satisfactorily approximated and the measurement errors of the thermal conductivity and thermal diffusivity of approximately 20 % were accepted (Kubicar and Bohac, 2001; Yu *et al.*, 2006).

Table 5.4 Differences between real experiment and ideal model

	Ideal model	Real experiment
1.	geometrically non-limited sample size	limited sample size
2.	negligible thickness of the heat source equivalent thermophysical properties	actual thickness of the heat source unique heat capacity of the heat source
3.	negligible mass of the thermocouple negligible heat capacity of the thermocouple	actual mass of the thermocouple actual heat capacity of the thermocouple
4.	ideal thermal contact between individual parts of the sample pieces	possible thermal contact resistance between individual parts of the sample pieces
5.	equal power output on both sides of the heat source	possible unequal power output on both sides of the heat source
6.	boundary and initial conditions valid for vacuum environment	experiments conducted in air surroundings

5.1.3 Experimental Exploration of Thermal Issues in HIFU

The optically transparent polyacrylamide hydrogels with the egg white concentration of 30 % were used for real-time visualization of HIFU induced thermal coagulative necrosis. Their general material properties are summarized in Table 5.5. As shown in Figure 3.10, the egg white phantom was subjected to continuous ultrasonic exposures from the fixed focus HIFU transducer, PA160. During HIFU sonications, the focal region was heated and the thermal ablation zone turned white due to protein denaturation.

Table 5.5 Acoustic and thermophysical properties of the 30 % egg white phantom

Parameters	
ρ (kg/m^3)	1000
c (m/s)	1545.3
α (dB/cm/MHz)	0.528
B/A	5
k (W·m^{-1}·°C^{-1})	0.747
α (m^2·s^{-1})	2.221×10^{-7}
C (J·kg^{-1}·°C^{-1})	3743.9

Figure 5.8 shows the change in white color of the coagulated area in a 30 % egg white phantom, in which sonications were performed at respective electric powers of 15, 27, 38, 58 and 74 W, during the uniform heating duration of 30 s (Section 3.3.1). The top image shows the cross-sectional view of the coagulated regions, and the bottom one shows the axial view (HIFU transducer was positioned above the image). These generated elliptical lesions are easily visualized in the gel phantom and the size/volume of the lesion highly depends on the power in this case. The sub-lesions seen at lower signal levels (15, 27 and 38 W) verified the existence of the sub-focal region for PA160, as shown in Figure 5.2(a). In some cases, the gas bubbles and material inhomogeneity in the gel phantom may cause irregular shaped lesion formation.
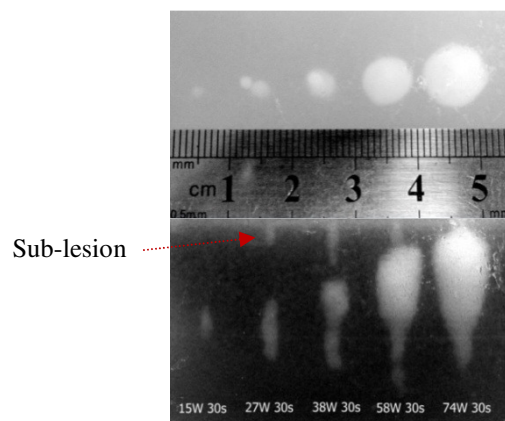
Figure 5.8 30 % egg white phantom irradiated by HIFU beams: electric powers of 15, 27, 38, 58 and 74 W, respectively, and heating duration of 30 s.

Figure 5.9 demonstrates the effect of different heating durations under the same electric power of 38 W. With the increasing heating duration from 10 to 60 s, the formed lesion changed and grew toward the transducer. It was seen that at the early stage of lesion formation ($t < 20$ s), the lesion size correlated well with the heating duration, however, after that the lesion size hardly changed due to the heat dispersion to the surrounding

tissue and the change of the attenuation coefficient in the focal region. Besides, no observable change in the lesion size has been noticed with investigation of the cooling-off periods, as seen in Figure 5.10, due to the rapid temperature drops in the field.
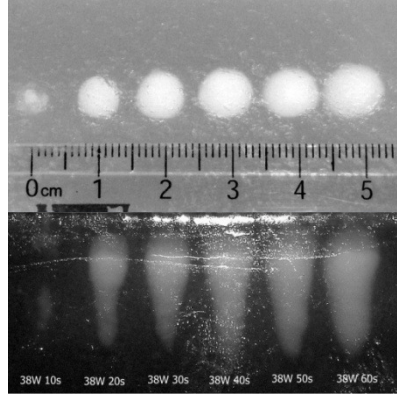
Figure 5.9 30 % egg white phantom irradiated by HIFU beams: electric power of 38 W and heating durations of 10 - 60 s, with a step of 10 s.
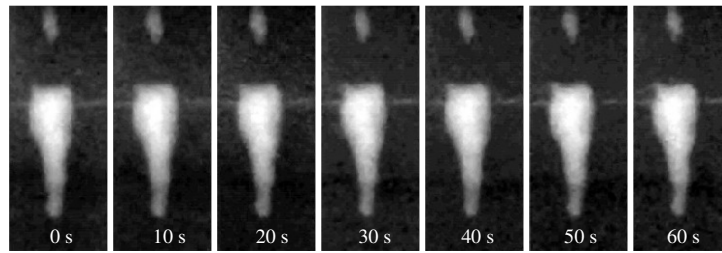
Figure 5.10 30 % egg white phantom irradiated by HIFU beams: electric power of 38 W, heating duration of 30 s, and cooling-off periods from 0 to 60 s, with a step of 10 s.

The HIFU outcomes are mainly dominated by the power deposition level i.e., the electric power output from the power amplifier and the heating duration. Figure 5.11 shows the focal temperature rise with respect to different electric powers and heating durations during the ultrasound heating process. As described in Figure 3.11, this was measured using a fibre-optic hydrophone (FP11-25T, sensitivity of 101.64 mV/MPa and uncertainty of 13 % at the frequency of 1 MHz). The electric power outputs of 1 and 4 W generated the peak-to-peak pressures of 2.26 and 4.33 MPa respectively, which equaled to the free-field intensities of 12.9 and 51.6 W/cm^2 at the focuses. In this study, each set of sonication parameters were repeated at least three times. The rapid temperature rise at the beginning of the heating period and the following relatively flat temperature dependence with time indicate a standard heat energy deposition and transfer process. However, for all the sonications described in Figures 5.11, no visible lesion formation was noticed. It

could also be explained by the limited temperature rises of 10 and 40 °C, for which the resultant temperatures were still below the threshold coagulation temperature of 67 °C for the egg white phantom, considering the room temperature of 20 °C.
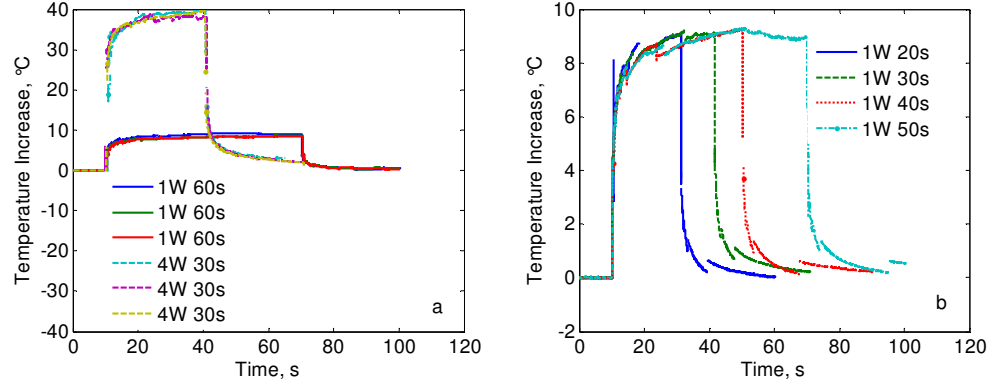
Figure 5.11 Measured focal temperature rises: (a) electric power, (b) heating duration.

Figure 5.12(a) shows the disturbed temperature plots at the relatively high power of 9 W (equaling to free-field intensity of 116 W/cm^2), which may be attributed to the initiation of thermal coagulation and possibly the combined effect of bubble activities. Although a robust temperature history can be obtained using a fine-diameter thermocouple at higher power situations (e.g., electric power of 43 W, equaling to free-field intensity of 554.2 W/cm^2), as shown in Figure 5.12(b), one disadvantage with the conventional thermocouple was that it was not possible to accurately locate the focus as the fibre-optic hydrophone by adjusting the HIFU transducer to find the location presenting the maximum peak-to-peak pressure.
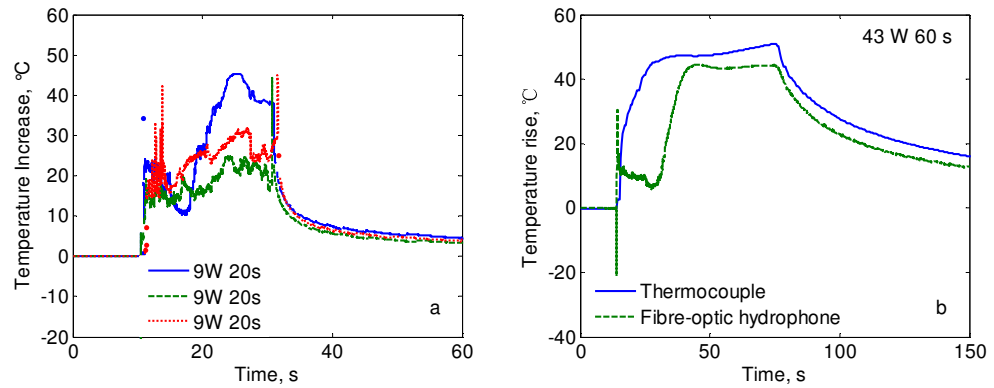
Figure 5.12 Measured focal temperature rises at higher power levels.

Perfusion rate is another influencing factor on the propagation and distribution of acoustic and thermal energy, and was also investigated in this study. As shown in Figure 3.12, the simplified water path with diameter of 5 mm was used to mimic the large blood vessel, and various flow rates of 0, 7.16, 12.25, 18.7, and 24 ml/s were tested. It was seen in Figure 5.13 that the boundaries of these lesions did not change significantly with the cooling effect of water flow; and as seen in Figure 5.14, the temperature rise at the focus of the HIFU field decreased with water flowing through the channel.
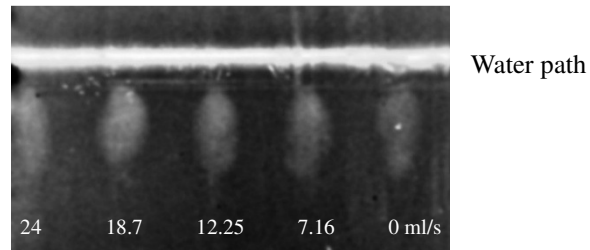
Figure 5.13 30 % egg white phantom irradiated by HIFU beams: electric power of 38 W, heating duration of 60 s, and water flow rates of 0, 7.16, 12.25, 18.7, and 24 ml/s.
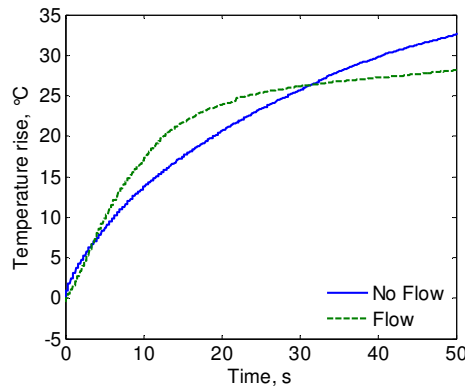
Figure 5.14 Measured focal temperature rises without and with water flow through the perfusion phantom.

5.1.4 Numerical Exploration of Thermal Issues in HIFU

In this study, the finite element modelling using PZFlex was investigated to understand the ultrasound propagation in the tissue-mimicking phantoms, to quantify the ultrasound interaction with the tissue-mimicking phantoms, and to plan and optimize the sonication outcomes. The models were built with inclusion of the piezoelectric element (to simulate the acoustic field mapping experiment for transducer PA160, as described in Section 3.1.3) and those evaluating the acoustic and thermal fields only (to simulate the thermal ablation

experiments in the egg white phantoms, as described in Section 3.3). Material properties provided by the manufacturer of Ferroperm and those listed in Table 5.5 were used. The nonlinear effect was considered in both model types.

As seen in Figure 5.15, the accuracy of the HIFU transducer modelling was verified by comparing the measured and simulated acoustic pressure distributions in the axial and transverse directions. Even better match results could be obtained by adjusting the relevant geometry and material properties used in this model. A corelational relationship between the driving voltage of the HIFU transducer and the imposed pressure loads in other FE models can be established. For example, a driving voltage amplitude of 8 $V_{p\text{-}p}$ and an initial pressure load of 0.068 MPa (peak-to-peak) result in an equivalent maximum peak-to-peak pressure of 1.14 MPa at the focus. With an increase in the initial pressure load to e.g., 0.4, 0.8, and 1.2 MPa, the corresponding transducer input could be around 55.8, 112.3, and 170.6 V, respectively (ref. Figures 5.3 and 5.4).
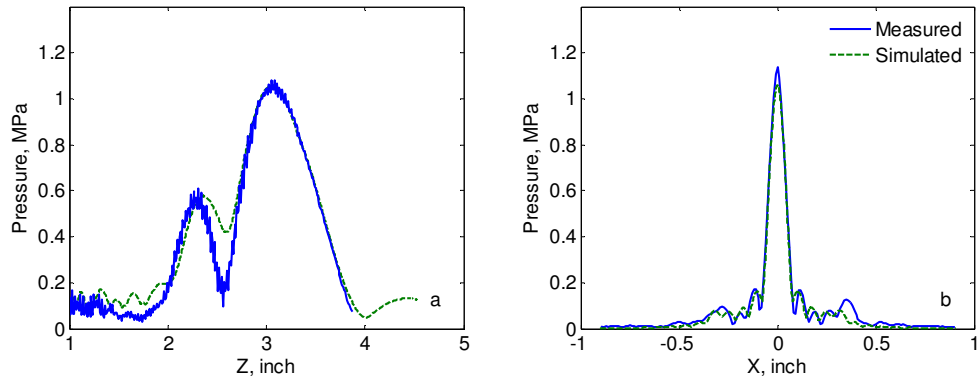
Figure 5.15 Measured and simulated acoustic pressure distributions of transducer PA160: (a) axis direction, (b) transverse direction.

Based on the numerical configuration shown in Figure 4.1, the acoustic pressure and the temperature fields were simulated for the given frequency and geometry of the transducer PA160, the measured acoustic and thermal properties of the tissue-mimicking phantom, and fixed positioning of the HIFU transducer relative to the tissue-mimicking phantom. As shown in Figures 5.11(b) and 5.16, the thermal modelling agreed satisfactorily with the experimental measurements at low power levels, where the relative difference in the peak temperature rise was less than 2 % (9.1 °C in experiment vs. 9 °C in FE results).
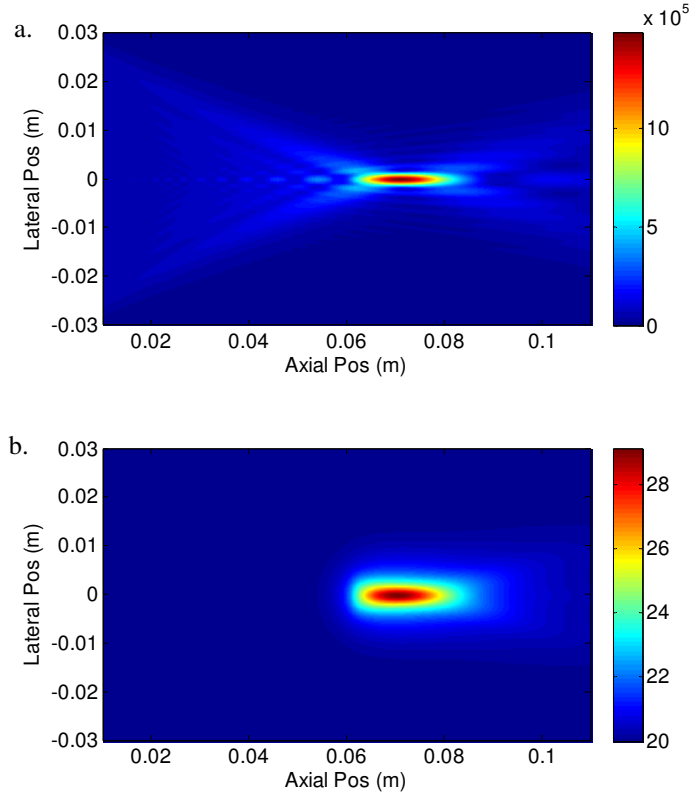
Figure 5.16 (a) Calculated acoustic field and (b) temperature distribution under continuous wave excitation: $p_0 = 0.16$ MPa (electric power of 1 W), $t_{on} = 60$ s, $t_{off} = 40$ s.

Following this result, the effects of various sonication parameters were discussed, including the driving signal amplitude, p_0, positive heating duration, t_{on}, and cooling-off period, t_{off}. Other models taking into account the blood perfusion and consecutive multiple sonications were introduced as well. Figures 5.17 (a) and (b) show the temperature responses at the focuses of the HIFU fields when the driving signal amplitude, p_0, and the positive heating duration, t_{on}, are varied, respectively. During the heating process, the focal temperature increases with time, especially at the beginning of the heating period, the trend seems almost linear (the greater p_0 produces a higher rate of temperature rise). When the heating time prolongs, the heat conduction term exhibits a significant cooling effect, and the focal temperature rises slowly and gradually stabilized. When t_{on} is a constant, the focal temperature rise increases with the increase of p_0; when p_0 is a constant, the focal temperature rise increases with the increase of t_{on}. However, the resulting peak temperature depends more on p_0 than t_{on}, which means for the same amount of energy delivered to the egg white phantom, a higher temperature rise will be obtained for a higher p_0 even with a shorter t_{on}. Figures 5.17 (c) and (d) show the

accumulation of thermal dose, i.e., the cumulative equivalent minutes at 43 °C (EM_{43}), according to the temperature responses at the focuses of the HIFU fields. The horizontal dashed lines represent the threshold thermal dose of coagulation, i.e., $EM_{43} = 240$ min.
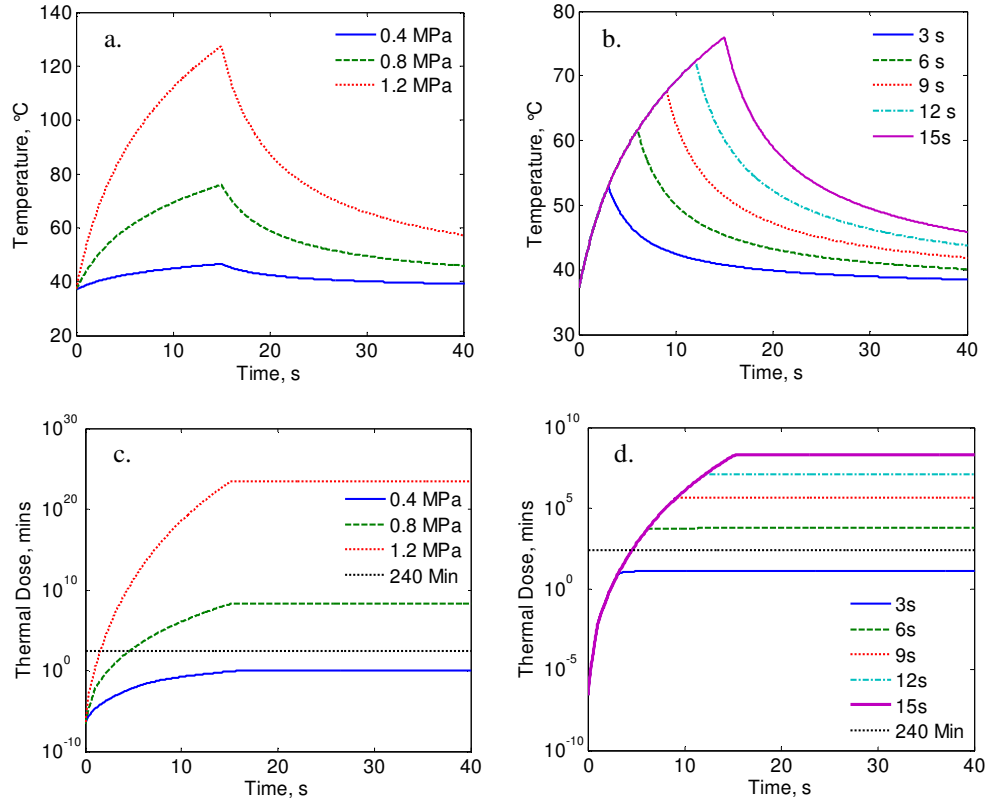
Figure 5.17 Temperature rises and accumulation of thermal doses at the focuses of the HIFU fields: (a, c) $p_0 = 0.4$, 0.8 and 1.2 MPa, $t_{on} = 15$ s, (b, d) $p_0 = 0.8$ MPa, $t_{on} = 3$, 6, 9, 12 and 15 s.

Figure 5.18 summarizes the accumulated thermal doses for all sonication protocols considered in the work. The EM_{43} value is proportional to p_0 and t_{on} during heating, and increases faster with higher p_0. For the lower amplitude of $p_0 = 0.4$ MPa (electric power of 6 W), no thermal lesion will be created within the investigated heating duration range, since EM_{43} is always lower than 240 min. While for the higher amplitudes of 0.8 and 1.2 MPa, the minimum temperatures required to produce $EM_{43} \geq 240$ min at the focuses are 57.94 and 59.62 °C, respectively. These results can be partially validated by the results of the thermal ablation experiments presented in Section 5.1.3. In particular, for the cases driven with lower electric powers of 1 and 4 W, no thermal lesion has been generated within the heating durations of 60 and 30 s, respectively.
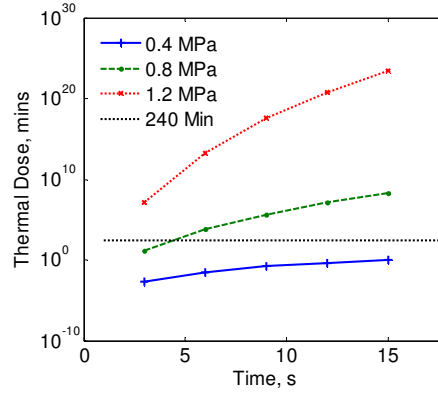
Figure 5.18 Peak thermal doses for different sonication protocols: p_0 = 0.4, 0.8 and 1.2 MPa and t_{on} = 3, 6, 9, 12 and 15 s.

The resulting peak temperature rise and thermal dose at each location within the HIFU field vary, and it declines from the focus to the model boundaries. Figure 5.19 shows the development of the necrotic region (EM$_{43}$ ≥ 240 min) on the axial plane, and the lines represent the predicted boundaries of the necrotic volume. The higher p_0 contributes more to the necrotic domain and also the longer t_{on} produces a larger area of necrosis. It was known in Figures 5.17 (c) and (d) that, the accumulation of EM$_{43}$ is mainly from the active heating duration, t_{on}, while the cooling-off period, t_{off}, contributes little, as the temperature dropped sharply at the beginning of the cooling-off period. As shown in Figure 5.20, no obvious change has been noticed in the size of the necrotic domain (EM$_{43}$ ≥ 240 min) when different t_{off} (0, 5, 15, and 25 s) were considered.

The effect of perfusion was also investigated, however rather than simulating the fluid or blood flow in a vessel, it deals with solving the bioheat transfer equation by introducing the perfusion parameters i.e., specific heat capacity of fluid flowing through the material, C_b, fluid mass flow rate per unit volume, w_b, and temperature of fluid, T_b. As shown in Figure 5.21, the temperature rise at each location decreases slightly with the influence of perfusion hence reducing the level of EM$_{43}$ and its distribution. Although it is generally accepted that the perfusion will reduce the volume of the thermally necrotic region in conventional hyperthermia, for cases of higher intensity and shorter duration heating considered here, the perfusion seems to have limited impact.
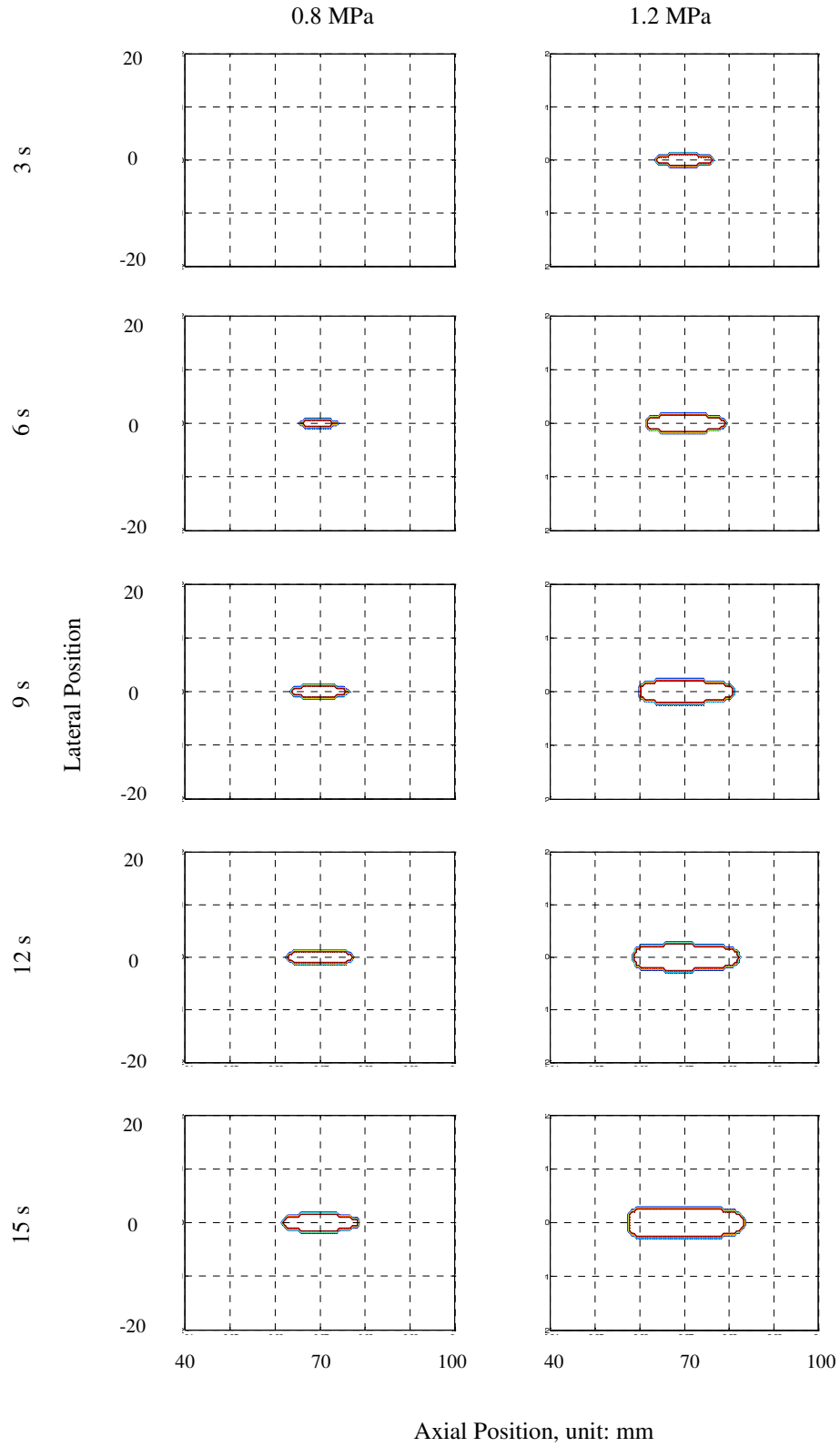
Figure 5.19 The contours of EM$_{43}$ = 240 min on the $x - z$ plane.
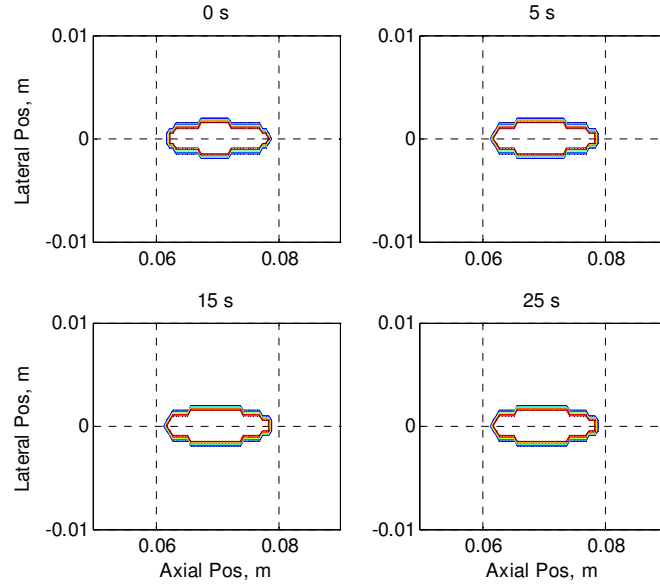
Figure 5.20 The contours of EM_{43} = 240 min on the x – z plane: p_0 = 0.8 MPa, t_{on} = 15 s, and t_{off} = 0, 5, 15, and 25 s.
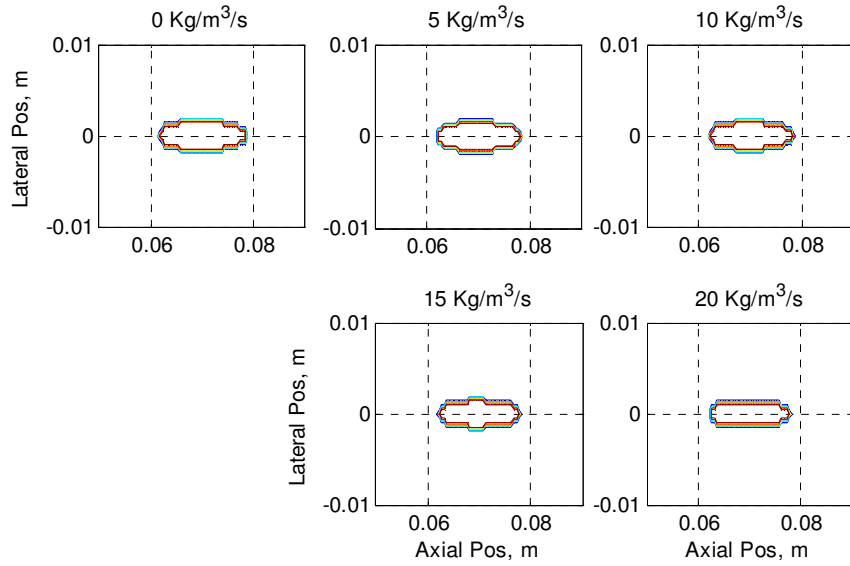
Figure 5.21 The contours of EM_{43} = 240 min on the x – z plane: p_0 = 0.8 MPa, t_{on} = 15 s, t_{off} = 25 s, and w_b = 0, 5, 10, 15, and 20 Kg/m^3/s.

The typical axial and lateral sizes of a single ellipsoidal lesion are about 20 mm and 2 mm, depending on the transducer geometry and treatment parameters, therefore to ensure complete ablation of those large targets, multiple consecutive sonications producing either a series of individual lesions or a strip of lesions are required. To numerically investigate the consecutive heating of a larger area, three focal depths at 90 mm (point 1), 80 mm (point 2), and 70 mm (point 3) were selected. During the heating procedure, the

focus was shifted toward the transducer from point 1 to 3. Figure 5.22 shows the thermal responses during the multiple focal depths heating. The results reveal the accelerated and enlarged lesion formation, and a deeper coagulation necrosis will reduce the ultrasonic energy required for the formation of necrosis at a shallower part. It also illustrates the necessity of sufficient cooling-off periods between consecutive sonication sessions, otherwise the intervening and surrounding normal tissue can be easily damaged due to the rapid accumulation of EM_{43} at higher temperatures, e.g., for points 2 and 3 in Figure 5.22(b). In clinical operations, due to the requirement of reducing the ambient temperature down to near normal body temperature, 37 ℃, this HIFU treatment method will take longer than expected to execute and complete.
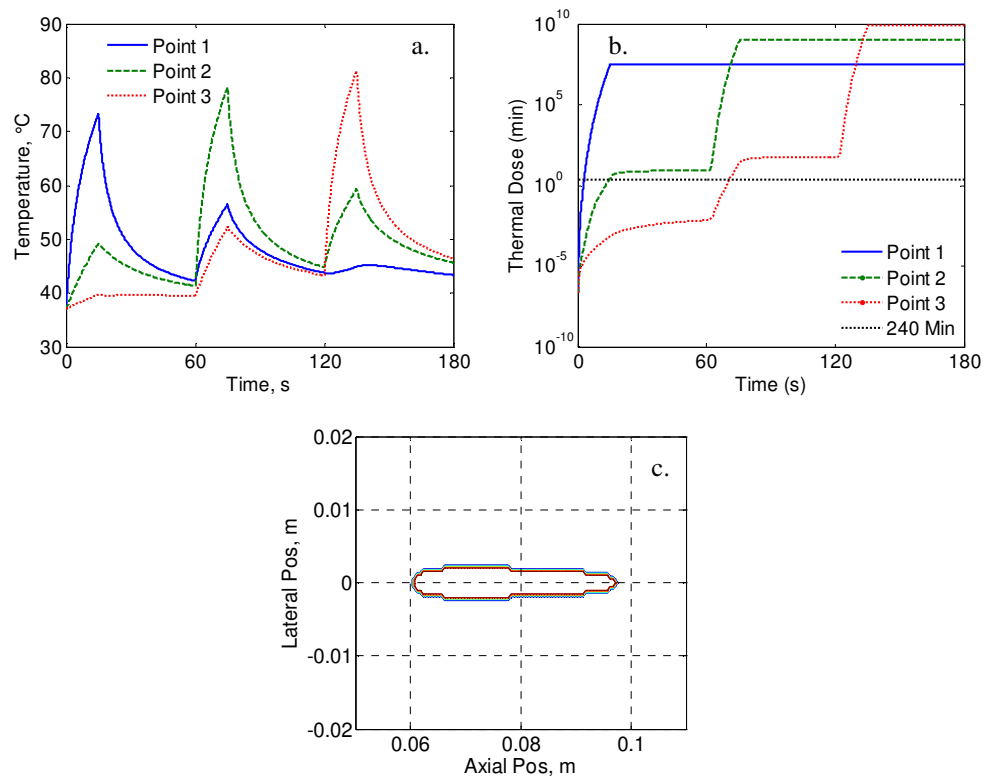
Figure 5.22 (a) - (b) The responses of temperature and thermal dose at three focal depths during a 180 s sonication: p_0 = 0.8 MPa, t_{on} = 15 s, t_{off} = 45 s, w_b = 0 Kg/m^3/s; (c) The contour of EM_{43} = 240 min on the x – z plane.

5.2 Transmitted Beam Distortion and Pressure Reduction in Trans-costal FUS

Section 5.2.1 presents the direct measurement results obtained by the use of different experimental models i.e., the porcine rib cage sample, the epoxy rib cage mimics and the acoustic absorber rib cage mimics. The effects of various influencing factors i.e., the rib cage geometry, the position of the target relative to the rib cage, and the geometry and operating frequency of the transducer on HIFU fields affected by the ribs are numerically analyzed in Section 5.2.2.

5.2.1 Experimental Results

5.2.1.1 Results on Porcine Rib Cage Sample

The transverse pressure distributions in the focal plane after propagation of the focused ultrasonic wave through the porcine rib cage sample were recorded using the high-speed ultrasound scanning system; and the focused bowl transducer, PA160, was used as the ultrasound source throughout the experiments. Three target positions relative to the rib cage sample were investigated by directing the beam axis through the second rib, the third rib, and the inter-costal space between the second and third rib strips, as marked in Figure 3.14. In Figures 5.23 (b) - (d), it can be seen that the beams become distorted or even split after transmitting through the porcine rib cage sample, and the resulting peak pressure amplitudes decreased to 45.5 %, 36.4 %, and 45.5 % of the maximum value of the original focused beam in Figure 5.23 (a).
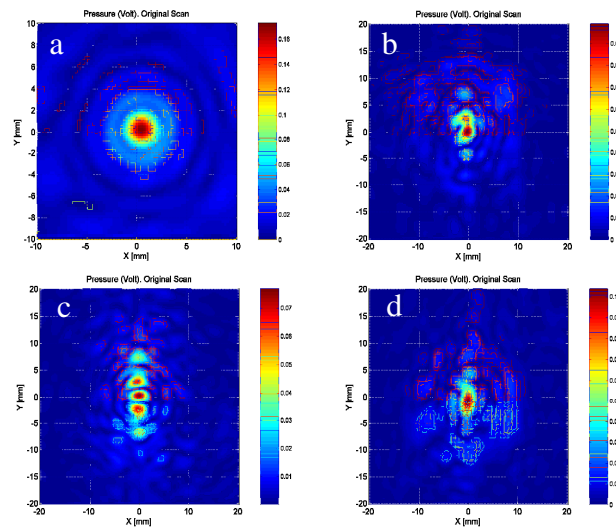
Figure 5.23 Scanned transverse focal fields: a) free field, b) through the 2nd rib, c) through the 3rd rib, and d) through the inter-costal space between the 2nd and 3rd ribs.

5.2.1.2 Results on Epoxy Rib Cage Mimics

Typical pressure distributions in the focal plane behind the epoxy rib cage mimics are shown in Figure 5.24. Similar results were obtained in Figure 5.23 for the porcine rib cage sample: targets blocked by the epoxy strips show more severe focal beam distortion including focus splitting and side foci generation, e.g. position line 1, point e in Figure 3.15; while, targets behind the inter-costal spaces are easier to focus and with small/no side foci generation e.g. position line 2, point b; the resulting peak pressure amplitudes ranged from 32 % to 56 % for all ten targets considered.
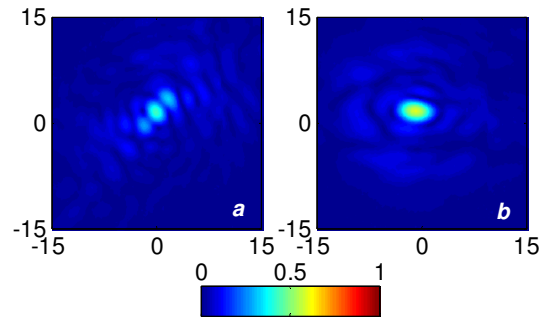
Figure 5.24 Normalized pressure distributions in the transverse focal plane behind the epoxy rib cage mimics: line 1, point e (left); line 2, point b (right). All pressures were normalized to the peak pressure value measured in the free-field case.

5.2.1.3 Results on Acoustic Absorber Rib Cage Mimics

The resultant acoustic patterns in the transverse focal plane were determined for the acoustic absorber rib cage mimics by the four configurations as mentioned in Section 3.4.4. As shown in Figure 5.25 (c), a complex pressure pattern consisting of three main maxima was observed and its peak pressure value decreased dramatically compared with Figure 5.25 (a). However, in Figure 5.25 (b), the effect of focus splitting was not obvious and its peak pressure value was considerably higher than in Figure 5.25 (c). Even worse focus splitting with more foci and lower amplitudes was obtained in Figure 5.25 (d).
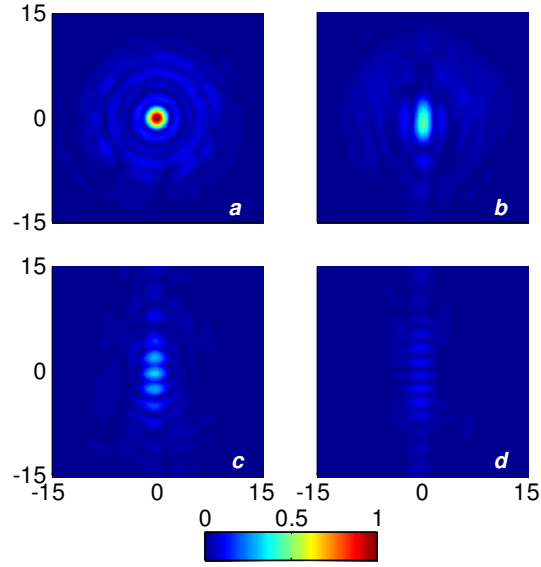
Figure 5.25 Normalized pressure distributions in the transverse focal plane behind the acoustic absorber rib cage mimics: (a) free-field; (b) directing the beam axis through the centre of the inter-costal space; (c) directing the beam axis through the centre of the middle strip; (d) directing the beam axis through the centre of the middle strip and with a greater transducer-to-rib distance.

In brief, comparing results in Figures 5.23 - 5.25, the rectangular absorbers can be validated as satisfactory rib mimics by measuring similar pressure patterns and peak pressure levels at the focal plane after HIFU propagation through the sample of porcine ribs and the two rib cage mimics, even though the shape and geometry of human rib cage are more complex than that of the acoustic absorber rib cage mimics.

5.2.2 Numerical Results

The pressure distributions obtained from the FEA model in Section 4.3 were validated with the measured data. As shown in Figure 5.26, the measured and simulated pressure distributions in the transverse focal plane were compared for the four situations mentioned previously. Compared with the peak value of the free-field in case (i), with the presence of the acoustic absorber rib cage mimics, the peak pressure value decreased to ~45 % in case (ii); and 34 % for case (iii) and 11 % for case (iv), with features that can be considered as multiple foci or as high amplitude side lobes. In all cases, there is generally good agreement between the simulated and experimental results. These results also provide a first indication that the spatial distribution of the pressure and its peak value are

affected by sonication through the inter-costal space and through the solid rib, as well as by the transducer-to-rib distance, which means that the outcome is dependent on the position of the intended target tissue relative to the rib cage in clinical applications.
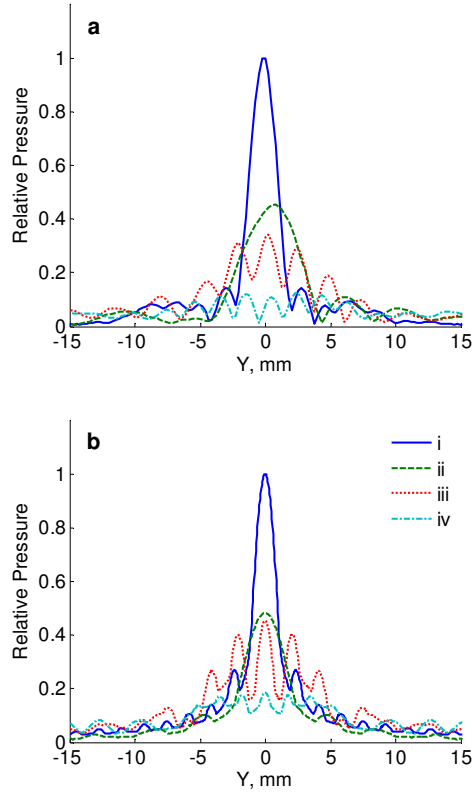
Figure 5.26 (a) Measured and (b) simulated pressure distributions in the transverse focal plane: (i) free-field; (ii) through the centre of the inter-costal space; (iii) through the centre of the middle strip; (iv) through the centre of the middle strip and with a greater transducer-to-rib distance. All pressures were normalized to the peak pressure value measured/simulated in the free-field case.

5.2.2.1 Effects of Rib Cage Geometries and Target Locations

The effects of different simplified rib cage geometries and target locations on the propagation of focused ultrasound through the rib cage were investigated numerically. To do this, the pressures at the focal point of the transducer (with a fixed focal length of 75 mm) were recorded respectively. Here, characteristic geometries of (a) $L_r = L_i/2 = 10$ mm, (b) $L_r = L_i = 15$ mm, and (c) $L_r = 2L_i = 20$ mm were considered for the ribs. The different target locations relative to the ribs were characterized using the target depth measured

from the front surface of the ribs, Z - D_z, and the distance from the target to the centre of the middle rib in the transverse direction, D_y (Figure 4.2). In particular, $D_y = 0$ mm and $D_y = 15$ mm indicate the target positions aligned with the centre of the middle rib and those aligned with the centre of the lower inter-costal space. Figures 5.27 (a) - (c) show the dependences of the normalized target pressure on the quantities Z - D_z and D_y for the various rib cage geometries, and Figure 5.27 (d) shows the relative differences between the pressure at the target behind the centre of the lower inter-costal space, P_i, and that behind the centre of the middle rib, P_r.
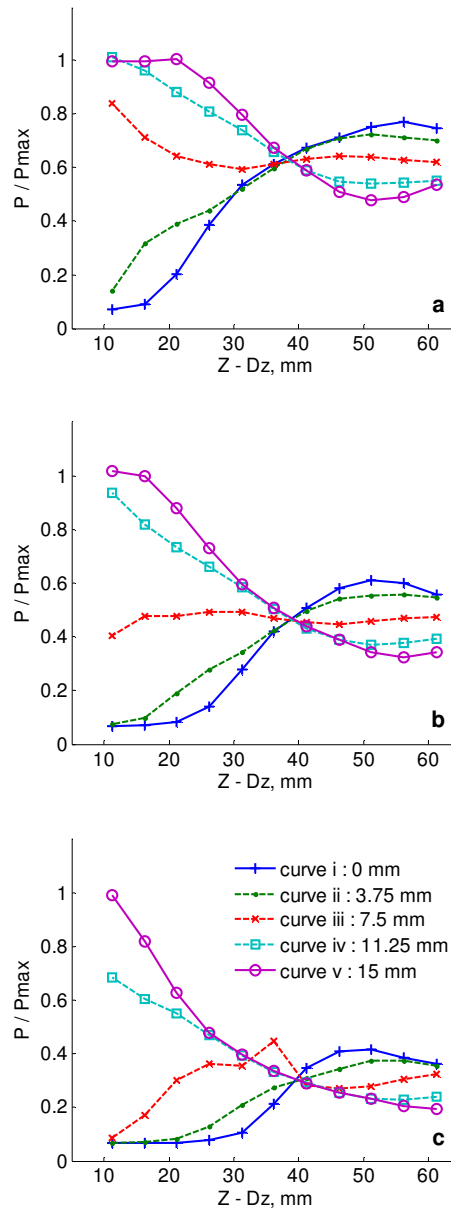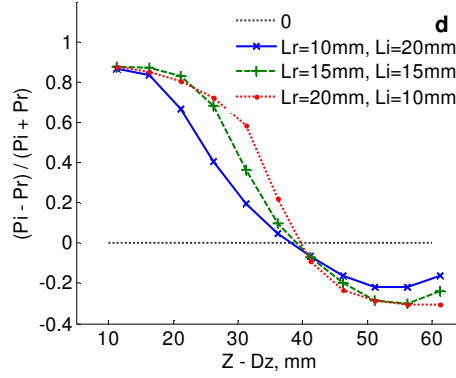
Figure 5.27 Dependences of the target pressure on the target depth, $Z - D_z$, for various anatomical configurations of the ribs and the inter-costal spaces: (a) $L_r = L_i/2 = 10$ mm, (b) $L_r = L_i = 15$ mm, (c) $L_r = 2L_i = 20$ mm. Curves i - v correspond to various target positions relative to the centre of the middle rib in the transverse direction: (i) $D_y = 0$ mm, (ii) $D_y = L/8 = 3.75$ mm, (iii) $D_y = L/4 = 7.5$ mm, (iv) $D_y = 3L/8 = 11.25$ mm, (v) $D_y = L/2 = 15$ mm. All pressures were normalized to the value at the target in the free-field case. (d) Relative differences of the target pressures when the beam axis is aligned with the inter-costal space (P_i, $D_y = 15$ mm) and with the middle rib (P_r, $D_y = 0$ mm).

For all cases discussed in this section, the achievable target depth, $Z - D_z$, was limited by the small aperture and low F-number of the transducer. A maximum of three ribs, i.e. less than two spatial periods of ribs, were intersected along the ultrasound propagation path. As shown in Figures 5.27 (a) - (c), the normalized pressure at the target is highly dependent on the position of the target relative to the ribs (parameters $Z - D_z$, D_y). As the depth of the target, $Z - D_z$, increases, the normalized pressure shows different increasing or decreasing trends when $D_y = 0$ mm, with the beam axis aligned with the rib, and $D_y = 15$ mm, with the beam axis aligned with the inter-costal space. Hence, when the target is just behind the ribs ($Z - D_z \leq 40$ mm), a relatively higher pressure level is obtained by sonicating through the inter-costal space, while for the target farther away from the ribs ($Z - D_z \geq 40$ mm), a relatively higher pressure level is obtained by aligning the beam axis with the rib. For these farther targets, the dependence of the normalized target pressure on D_y becomes insignificant compared with the smaller penetrations.

The increasing or decreasing trend in the amplitude of the normalized target pressure can be explained by the changes in the relative effective beam area not blocked by the ribs, A_{e-p} / A_e, where A_e and A_{e-p} are the entire beam area and positive beam area not blocked

by the ribs (Khokhlova et al., 2010). The crossing point in each graph, i.e. where all the lines meet, indicates that at a certain target depth, $Z - D_z$, the quantities A_{e-p} / A_e are equivalent, no matter which D_y is involved. Considering the case $L_r = L_i = 15$ mm, $A_{e-p} / A_e = 0.5$ is achieved at the target depth $Z - D_z \approx 40$ mm with D_y varying from 0 - 15 mm, which results in production of the same target pressure value in Figure 5.27 (b). Also, with the ultrasonic beam axis aligned with the edge of the middle rib ($D_y = L/4 = 7.5$ mm), the area not blocked by the ribs always occupies half the beam area, so that the pressure at the target does not change with $Z - D_z$, Figure 5.27 (b) curve (iii). Similarly, for anatomical configurations of $L_r = L_i/2 = 10$ mm, $L_r = L_i = 15$ mm, and $L_r = 2L_i = 20$ mm, relatively higher target pressure amplitudes are obtained in the case $L_r = L_i/2 = 10$ mm, in which the ratio of the area not blocked by the ribs is the largest, Figure 5.27 (a).

As shown in Figure 5.27 (d), positive and negative relative differences between P_i and P_r were noted for focusing the ultrasonic beam at depths $Z - D_z \approx 20$ mm and 50 mm respectively. Figure 5.28 shows the acoustic pressure distributions at the targets at $Z - D_z \approx 20$ mm. FEA results are shown for various ratios of the dimensions of the ribs and the inter-costal spaces: $L_r = L_i/2 = 10$ mm, Figure 5.28 (a - c); $L_r = L_i = 15$ mm, Figure 5.28 (e - g); $L_r = 2L_i = 20$ mm, Figure 5.28 (i - k); and target locations relative to the ribs: $D_y = 0$ mm, Figure 5.28 (a), (e), (i); $D_y = 7.5$ mm, Figure 5.28 (b), (f), (j); and $D_y = 15$ mm, Figure 5.28 (c), (g), (k). As shown in Figure 5.28 (m), (n), (o), for the targets located directly behind the middle rib ($D_y = 0$ mm), dramatically decreased peak pressure levels are observed as the ultrasound was mostly blocked by the rib. In contrast, relatively well-defined focal areas with much higher peak pressures are observed for the targets behind the inter-costal space ($D_y = 15$ mm), because of the successful delivery of ultrasound through the inter-costal space. Phenomena of beam bending and shifting are also seen in Figure 5.28 (b), (f), (j), which may prove to have significant practical importance in clinical applications because of the irregular shape of human rib cage. In Figure 5.28 (d), (h), (l), the pressure values in the focal region are higher if the dimensions of the inter-costal spaces are larger than the ribs ($L_i > L_r$), as more energy passes through the rib cage.
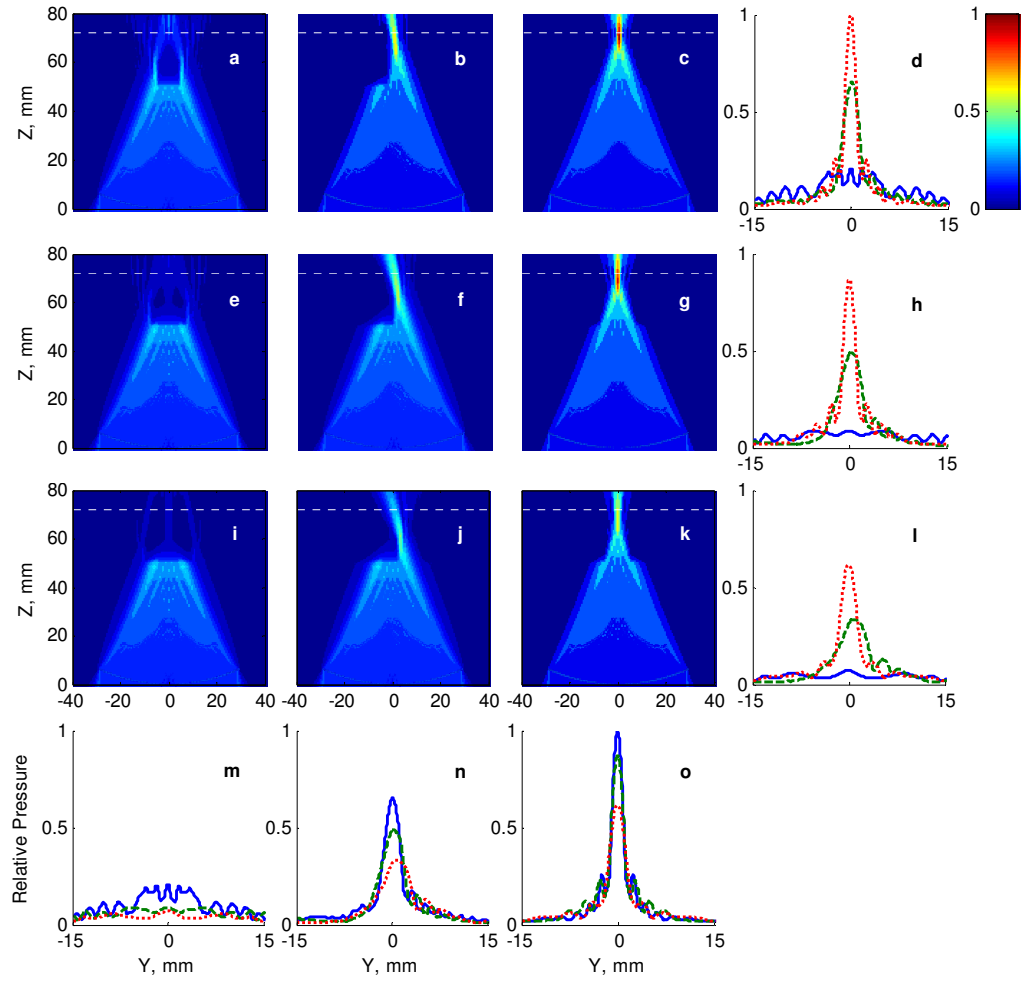
Figure 5.28 Axial pressure distributions in the presence of the absorbing rib cage mimics, with the target depth of ~ 20 mm. Various target positions relative to the rib cage in the transverse direction, $D_y = 0$ mm (a, e, i), $D_y = 7.5$ mm (b, f, j), and $D_y = 15$ mm (c, g, k), were explored for different rib cage configurations of $L_r = L_i/2 = 10$ mm (a - c), $L_r = L_i = 15$ mm (e - g), and $L_r = 2L_i = 20$ mm (i - k). The field of view is $80 * 80$ mm^2 in the y-z plane. Curves corresponding to the pressure distributions at the focal plane are plotted in the last graph in each row (d, h, l) and column (m - o).
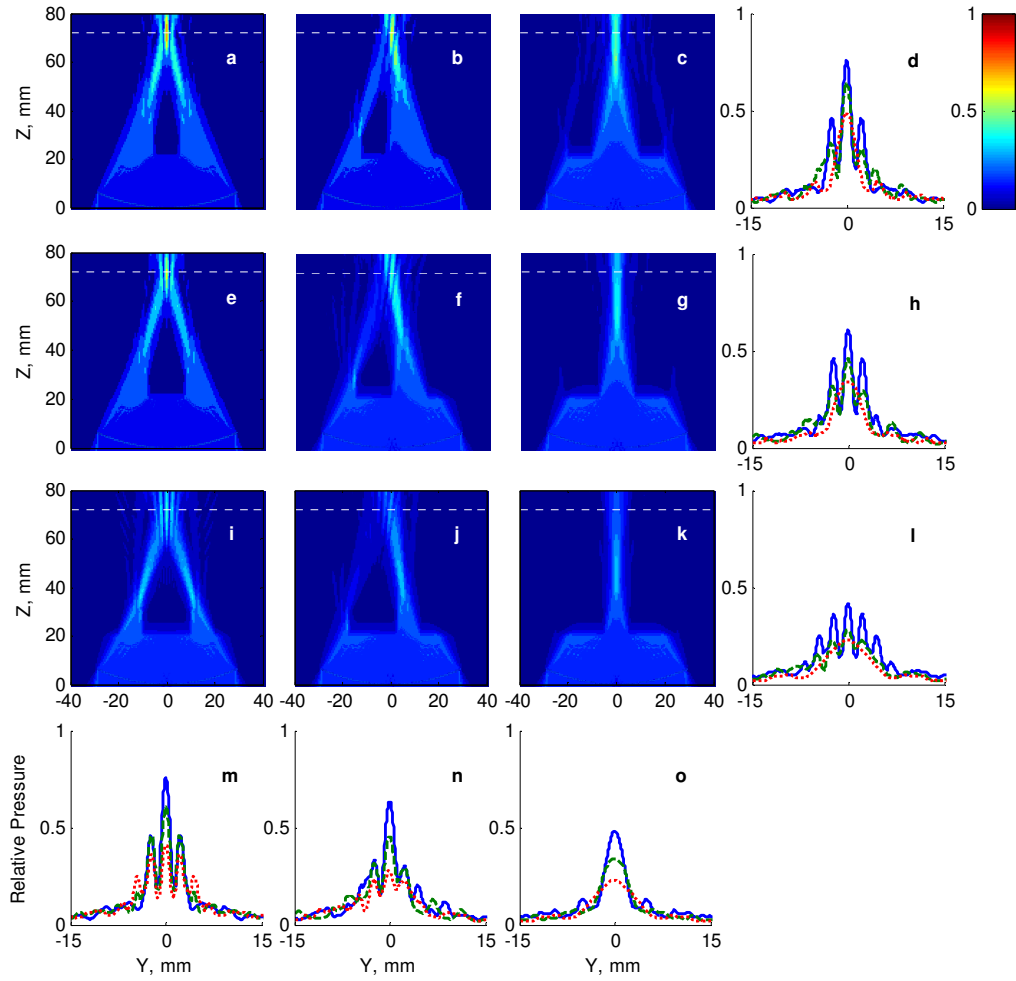
Figure 5.29 Axial pressure distributions in the presence of the absorbing rib cage mimics, with the target depth of ~ 50 mm. Various target positions relative to the rib cage in the transverse direction, $D_y = 0$ mm (a, e, i), $D_y = 7.5$ mm (b, f, j), and $D_y = 15$ mm (c, g, k), were explored for different rib cage configurations of $L_r = L_i/2 = 10$ mm (a - c), $L_r = L_i = 15$ mm (e - g), and $L_r = 2L_i = 20$ mm (i - k). The field of view is 80 * 80 mm^2 in the y-z plane. Curves corresponding to the pressure distributions at the focal plane are plotted in the last graph in each row (d, h, l) and column (m - o).

The pressure distributions at a deeper depth $Z - D_z \approx 50$ mm are shown in Figure 5.29. Compared with the targets behind the inter-costal space, $D_y = 15$ mm, Figure 5.29 (c), (g), (k), relatively higher pressure levels are observed for the targets behind the rib, $D_y = 0$ mm, Figure 5.29 (a), (e), (i). However, the differences in the normalized target pressure between these two situations are considerably less significant. Unlike Figure 5.28, more obvious effects of focus splitting were noticed, with a complex interference pattern producing multiple maxima. The number and dimensions of the maxima, and their

positions and relative amplitudes have been studied previously in Khokhlova et al. (2010). In their research, the number of maxima is determined by the ratio of the dimensions of the ribs and the inter-costal spaces; the sizes of the maxima are determined by the wavelength, the target depth and the beam aperture on the frontal surface of the ribs; the distance between adjacent maxima is determined by the wavelength, the target depth and the period of the rib structure; and the relative amplitudes of the maxima are related to the index number of the maximum and the ratio of the dimensions of the ribs and the inter-costal spaces, etc. However, due to simplifications when the beam dimensions are much larger than one period of the rib structure and in neglecting the influence of D_y in their study, not all conclusions can be applied to the results presented here. Compared with their results on the beam distortion effect, our findings matched qualitatively with their analytical results. As the results from this study have been calculated in the entire physical domain particularly involving a given thickness of rib bone, it therefore offers a more accurate prediction of the experimental situations.

Briefly, the trans-costal FUS is most useful against tumours that are small and near the surface of the abdominal organs, e.g. the liver, kidney, and pancreas. However, for targets deep inside these organs, severe attenuation of acoustic energy occurs so that pure ultrasound thermal ablation with advanced heating patterns will have limited effects in improving the treatment efficiency.

5.2.2.2 Effects of Transducer *F*-Number and Drive Frequencies

The effects of different transducer *F*-numbers have also been investigated with FEA. To do this, transducer apertures were selected from within the range of 60 - 120 mm, with an elevation of 20 mm, and the radius of curvature and driving frequency fixed at 75 mm and 1.09 MHz respectively. To ensure the equivalent target pressure in the absence of ribs, calculations were made to determine the input pressures in situations with different apertures. As a control example, an input pressure amplitude of 0.1 MPa was applied to a 60 mm transducer. Figure 5.30 (a) shows the ratios of target pressures in the presence of the ribs relative to those under free-field conditions for these four apertures. This figure only illustrates sonications with the focus aligned with the centre of the rib, $D_y = 0$ mm, solid line, and with the centre of the inter-costal space, $D_y = 15$ mm, broken line. In Figure 5.30 (b), the dependences of $(P_i - P_r) / (P_i + P_r)$ on $Z - D_z$ are also shown.
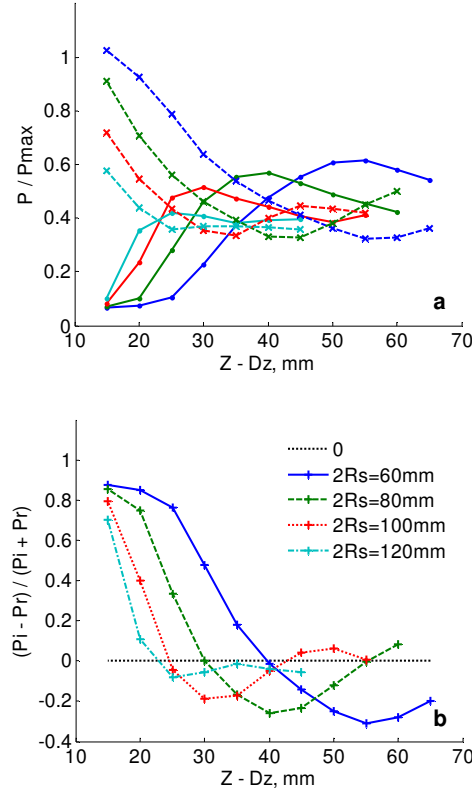
Figure 5.30 (a) Dependence of the target pressure on the target depth, $Z - D_z$, for $L_r = L_i = 15$ mm. Two distinct target positions relative to the rib cage in the transverse direction were considered, $D_y = 0$ mm (solid lines) and $D_y = 15$ mm (broken lines). Curves corresponding to different transducer apertures are displayed as 60, 80, 100, and 120 mm. (b) Relative differences of the target pressures when directing the beam axis through the inter-costal space, P_i, $D_y = 15$ mm, and through the middle rib, P_r, $D_y = 0$ mm.

The results confirm that cancerous tissue at shallow depths can be ablated easily if sonicating through the inter-costal spaces, while it becomes difficult to perform ablations either by sonicating through the inter-costal spaces or in alignment with the ribs for deep targets, even though slightly higher pressure values are achieved by sonicating when aligned with the ribs. For the fixed radius of curvature of 75 mm, the viable target depth is limited for large aperture transducers, e.g., $Z - D_z < 45$ mm for the aperture of 120 mm, and the interval of the target depth resulting in positive relative differences also reduces to $Z - D_z < 25$ mm. The normalized pressure amplitude at the target decreases with increasing transducer aperture. Also the absolute values of positive ($P_i > P_r$) and negative ($P_i < P_r$) relative differences decrease, indicating that the differences between P_i and P_r are decreasing. These results suggest that higher target pressure values will be achieved

with small aperture transducers at clinically relevant depths. However, such a small aperture may reduce the focal spot size and increase the power densities on the ribs; therefore in clinical use, the large aperture transducers are preferred.

Previous results in Figures 5.27 – 5.30 were calculated for f = 1.09 MHz. Subsequently, a wide frequency range from 0.55 - 1.15 MHz was investigated. The aperture size, radius of curvature of the transducer, and the rib cage geometries were the same as those considered in Figure 5.27 (b). The same input pressure amplitude of 0.1 MPa was used to evaluate the efficiency of the five individual frequencies. In Figure 5.31 (a) and (b), the dependence of the target pressure normalized to its value in free-field condition at 1 MHz and the relative difference of P_i and P_r on the target depth are shown.
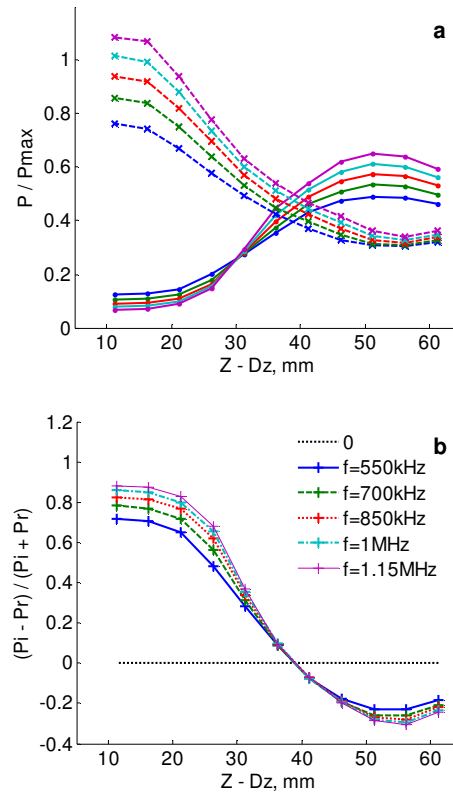
Figure 5.31 (a) Dependence of the target pressure on the target depth, $Z – D_z$, for $L_r = L_i = 15$ mm. Two distinct target positions relative to the rib cage in the transverse direction were considered, $D_y = 0$ mm (solid lines) and $D_y = 15$ mm (broken lines). Curves corresponding to various driving frequencies are displayed as 0.55, 0.70, 0.85, 1, and 1.15 MHz, with a step size of 0.15 MHz. (b) Relative differences of the target pressures when the beam axis is aligned with the inter-costal space, P_i, $D_y = 15$ mm and with the middle rib, P_r, $D_y = 0$ mm.

It can be seen that the normalized target pressure increases with the frequency, except for shallow targets when sonicating with the focused beam aligned with the rib, $Z - D_z < 30$ mm, $D_y = 0$ mm, solid lines. To increase the pressure level in the focal area and also the conversion of ultrasound energy into heat, the high frequency $f = 1.15$ MHz is applicable. However, in clinical use, such a high frequency may lead to more rapid heating of the ribs than the soft tissue, as the frequency-dependent attenuation coefficient of the ribs, 22.15 dB/cm/800 kHz, is higher than that of fat, 0.6 dB/cm/MHz; muscle, 0.78 dB/cm/MHz; and liver, 0.78 dB/cm/MHz (Liu et al. 2007; Liu et al. 2010a).

In this study, both experimental and simulated results showed the effects of beam splitting, bending and shifting with focused ultrasound propagating through the rib cage mimics. For the rib cage geometries and target positions that were considered, the most appropriate treatment settings have been suggested. According to this, trans-costal FUS was particularly useful for the targets lying immediately adjacent to the rib cage and behind the inter-costal spaces, while the worst sonication results in the investigation domain could be found with the cases lying immediately adjacent to the rib cage but behind the ribs. For the targets located away from the rib cage, there were no obvious differences among different lateral target positions, all receiving signals showing low amplitude ratios, which would result in insufficient thermal energy deposition at the focuses. For the aim of further improving the efficiency of trans-costal focused ultrasound ablations, the devices to be employed should be optimized with reasonably larger transducer aperture and driving frequency.

5.3 Optimizing Sonication Protocols in Trans-costal FUS

Results from the previous section show that the transducer dimensions and sonication frequency are important factors that may affect the safety and efficacy of trans-costal FUS treatments. This section discusses the trans-costal heating effects at the target and the intervening ribs by experimental verification (Section 5.3.1) followed by parametric estimation using the PZFlex finite element method (Section 5.3.2). To achieve the goal of successful applications of trans-costal FUS in human patients, certain compromises regarding the ratio of ultrasonic power density at the target and the ribs, the time-varying spatial distribution of temperature, and the ablated focus of each sonication were made.

5.3.1 Experimental Results

As shown in Figure 3.19, the dimensions of the absorbing rib mimics were $90 \times 15 \times 10$ mm, the aperture of the phased array transducer was 120 mm, the steered focal length of the phased array transducer was 130 mm, and the transducer-to-rib distance was 90 mm. The centre frequencies of the transducer could be adjusted within the range of 0.95 to 1.35 MHz and with a step of 0.05 MHz. The focused ultrasound beam was irradiated directly onto the rib mimics (acoustic power of 50 W and heating duration of 20 s). The experimentally measured temperature elevations at the ribs and the target region were summarized in Figure 5.32. In this setup, the intervening rib mimics absorbed the majority of ultrasound energy resulting in ineffective energy delivery to the target region, and hence a more rapid temperature buildup on the ribs than the focal area.
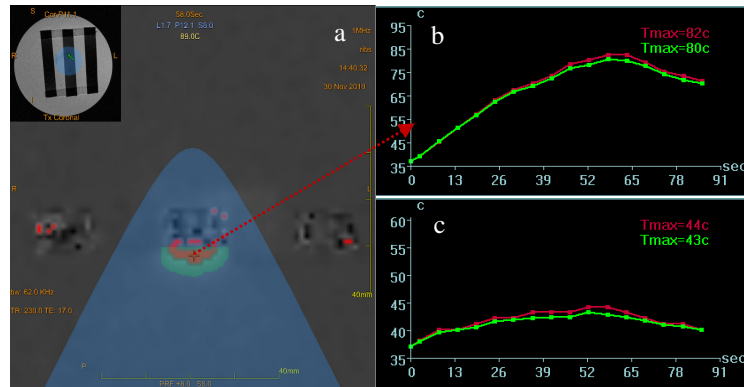
Figure 5.32 ExAblate 2000 system at 1 MHz: (a) Thermal map of rib heating and (b, c) temperature responses near the rib mimics and in the focal region.

Those initial results demonstrated that the trans-costal heating at the target and the ribs could be affected by the target location and the transducer frequency. As seen in Figure 5.33, the experimental results are presented to specify their respective functions. These results show that the trans-costal heating is mostly affected by the transducer elevation value in the hardware system, which is positively correlated with the depth of the target; to put it another way, the heating results will decrease with an increase in the target depth. However in this experiment, no obvious relationship between the rib heating and the frequency was observed, even though the attenuation coefficient of the absorbing rib mimics shows a monotonically increasing trend when higher frequencies are considered.
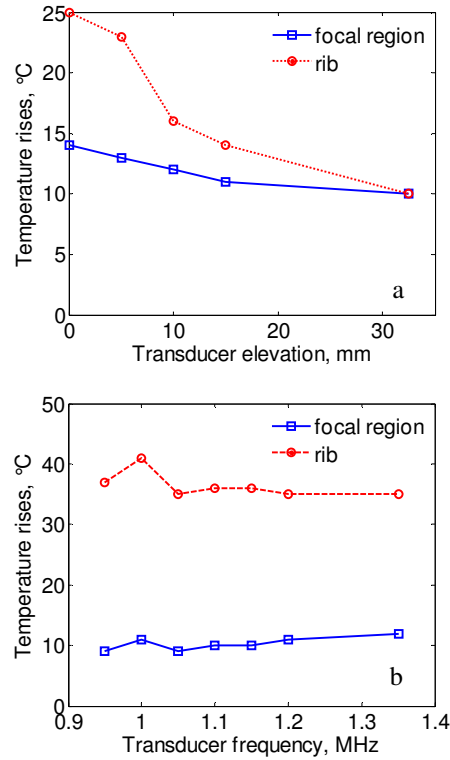
Figure 5.33 Maximum temperature rises in the focal region and near the rib mimics for: (a) different transducer elevation in the ExAblate 2000-2 system, (b) different transducer frequency.

5.3.2 Numerical Results

Further exploring these influence factors in trans-costal FUS, the resultant acoustic and thermal effects were analyzed numerically. To demonstrate how the focal acoustic intensity can be affected after propagation of HIFU through the rib cage, a total of 27 target locations were selected, and these 27 target locations with respect to the chest anatomy were shown in Figure 4.3 (each location was assigned with lateral and axial coordinate values of D_y and $Z - D_z$). The transducer was assumed to be commercial sizes (aperture of 120 mm, focal length of 135 mm).

The frequency-varied acoustic intensities at the targets (scaling to the free-field spatial-peak intensity value at 1 MHz) are correspondingly plotted in Figures 5.34 (a) - (e). Due to the effect of transmitted beam distortion (beam bending, shifting and splitting), resulting from the limited acoustic window and the interference caused by the spatially periodic structures of the intervening ribs, the targets with rib coverage exhibited more

severely reduced intensity levels (< 50 %). Evidently, the normalized focal intensity value strongly depends on the coordinate values of D_y and Z - D_z. For the targets located immediately behind the rib plane (e.g., $Z - D_z < 40$ mm), the maximum focal intensity was achieved when the beam axis intersected the middle of the inter-costal muscle (i.e., $D_y = L/2 = 20$ mm, 'red'); whereas for the targets located away from the rib plane (e.g., $Z - D_z > 40$ mm), slightly higher focal intensities were achieved when the beam axis intersected the middle of the rib (i.e., $D_y = 0$ mm, 'blue'), in which cases, the targets were directly blocked by the dense rib. Also, the frequency characteristics of the normalized intensities at the targets suggest preliminarily that the higher frequencies of 0.8, 1.0 and 1.2 MHz tend to generate higher values compared to the lower frequencies of 0.4 and 0.6 MHz in these trans-costal FUS applications.
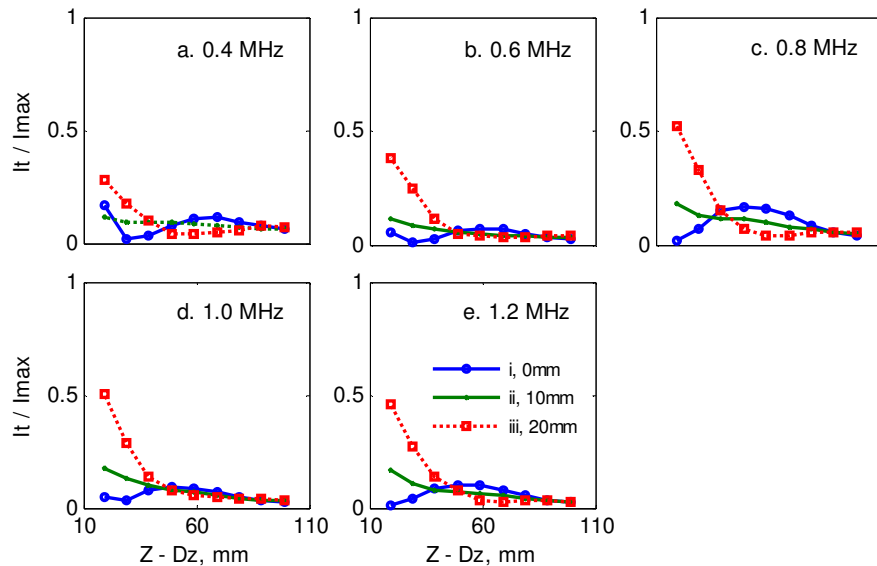
Figure 5.34 Normalized acoustic intensities at the targets under frequencies of 0.4, 0.6, 0.8, 1.0 and 1.2 MHz, respectively. Target positions with various target depth, Z - D_z, and lateral target distance, $D_y = 0$ mm (curve i, 'red'), $D_y = L/4 = 10$ mm (curve ii, 'green'), $D_y = L/2 = 20$ mm (curve iii, 'blue') are presented.

Figure 5.35 then compares the normalized ultrasound power densities (defined as the power absorbed per unit volume) at these 27 target positions (top row) and the intervening ribs (middle row), with the transducer operating at frequencies of 0.4, 0.6, 0.8, 1.0, and 1.2 MHz. The ratios between the data at the target and ribs are also displayed in the bottom row. For the targets located immediately behind the rib plane (e.g., $Z - D_z < 40$ mm), significantly enhanced power density at the target as well as lowered value on

the ribs can be obtained by directing the beam axis through the inter-costal muscle, i.e., $D_y = L/2 = 20$ mm, as seen in Figures 5.35 (c, f, i); while for the targets away from the rib plane (e.g., $Z - D_z > 40$ mm), slightly improved power density at the target as well as lowered value on the ribs can be obtained by directing the beam axis through the solid rib instead, i.e., $D_y = 0$ mm, as seen in Figures 5.35 (a, d, g).
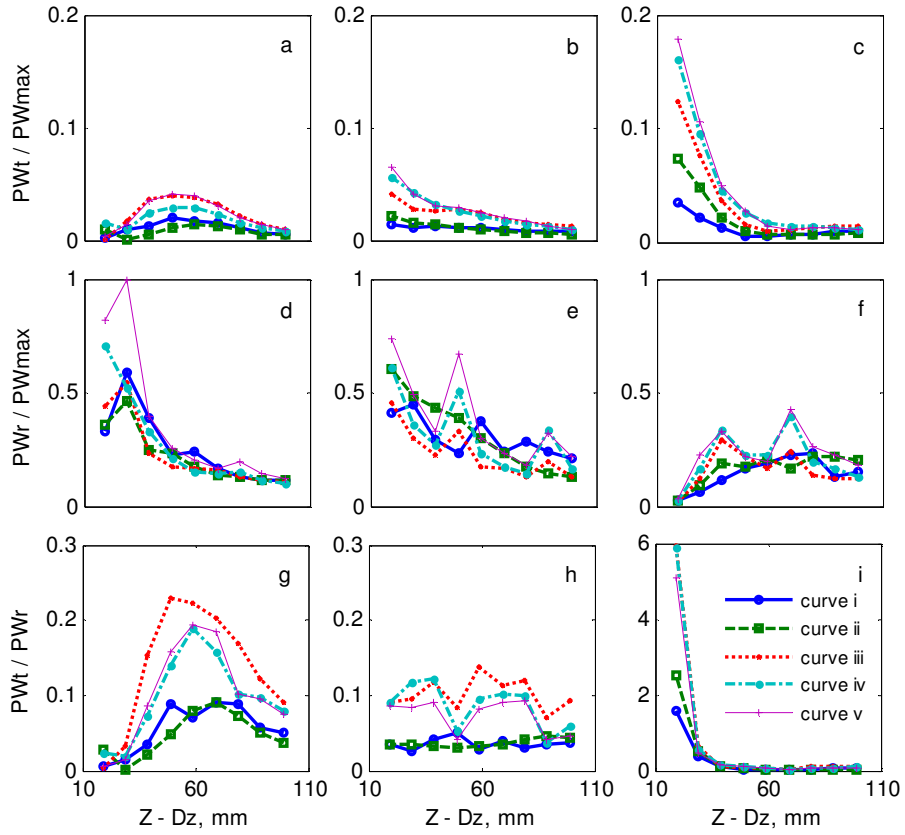
Figure 5.35 Normalized power densities at the targets (a – c), the ribs (d – f), and also the ratios between the values at the targets and the ribs (g – i) under frequencies of 0.4 (curve i, 'blue'), 0.6 (curve ii, 'green'), 0.8 (curve iii, 'red'), 1.0 (curve iv, 'light blue') and 1.2 MHz (curve v, 'purple'), respectively. Target positions with various target depth, $Z - D_z$, and lateral target distance, $D_y = 0$ mm (a, d, g), $D_y = L/4 = 10$ mm (b, e, h), $D_y = L/2 = 20$ mm (c, f, g) are presented.

Observing all these cases, the normalized power density only increased monotonically with the driving frequency at selected target positions, as shown in Figure 5.35 (c). It indicates that for these targets lying behind the inter-costal spaces ($D_y = L/2 = 20$ mm), the heating duration required to reach certain targeted temperatures, e.g., 56 ℃, can be effectively reduced with a higher frequency. However, the normalized power density on

other targets and intervening ribs exhibited no obvious frequency-dependent trends. Assuming that the attenuation coefficient shows a linear increasing trend with frequency, there were no obvious differences in power deposition in the ribs at higher frequencies, even though the attenuation coefficient of rib bone is much higher than that of soft tissue, as listed in Table 4.1. For example, at the target depth of 60 mm under the inter-costal sonications, the dilatational-wave and shear-wave attenuation coefficients of rib bone changed from 2.76 and 4.0 dB/cm (0.4 MHz) to 8.28 and 12 dB/cm (1.2 MHz), respectively; however, the resultant normalized power densities coincided at ~ 0.2, as shown in Figure 5.35 (f). This is because the calculation of power deposition depends not only on the frequency-dependent attenuation coefficient of the material, but also on the frequency component of the propagating wave and the acoustic pressure amplitude at each location (Section 2.1.3).

Another important observation was that the ratios between the corresponding power densities at the target and ribs were maintained at high levels at the sonication frequency of 0.8 MHz, as shown in Figure 5.35 (g) - (i), 'red'; whereas it may shift slightly to higher frequency of 1.0 MHz, 'light blue', with changes in the axial and lateral target positions. Moreover, only at selected target positions, e.g., $D_y = L/2 = 20$ mm and $Z - D_z < 30$ mm, the ratio values were higher than unity, indicating that relatively higher energies can be accumulated at those positions, and rib heating can be greatly avoided

Figure 5.36 shows the resultant peak temperatures at the end of 15 s sonication durations. Similar trends were observed between the peak temperature and the normalized power density. With the spherically curved transducer operating at a certain frequency, satisfactory treatment outcomes (significant heating of the target and preventing over-heating of the ribs) can only be achieved for shallow targets located behind the inter-costal muscle, e.g., $D_y = L/2 = 20$ mm and $Z - D_z < 30$ mm, as seen in Figures 5.36 (c, f, i); for those shallow targets located right behind the solid rib, e.g., $D_y = 0$ mm and $Z - D_z < 30$ mm, the ribs attained much higher temperature rises than the targets, as seen in Figures 5.36 (a, d, g); while for other positions at deeper depths ($Z - D_z > 60$ mm), insufficient temperature rises were generated at both the targets and the intervening ribs. Except at the targets as discussed in Figure 5.36 (c), no apparent evidence of frequency-dependent heating was noticed; of particular interest, little change in the peak temperature rise has been observed at the intervening ribs. Higher relative differences

between temperature rises on the target and ribs can be achieved at the proposed operating frequency of 0.8 MHz or occasionally up to higher frequencies.
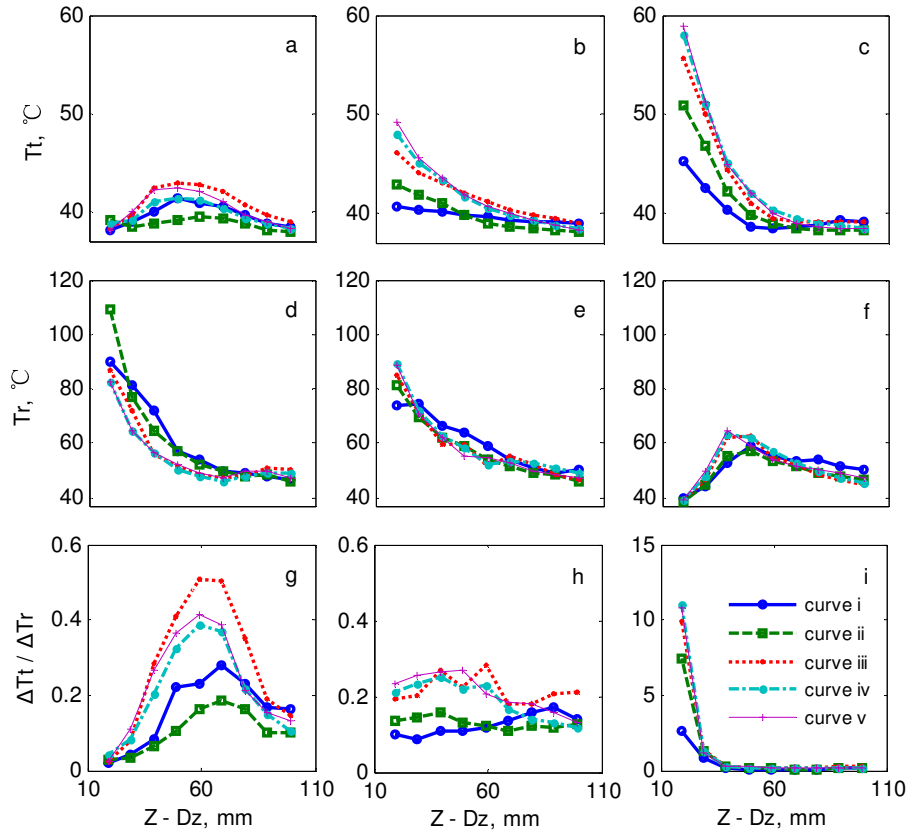
Figure 5.36 Peak temperatures at the targets (a – c), the ribs (d – f), and also the ratios between the change values at the targets and the ribs (g – i) under frequencies of 0.4 (curve i, 'blue'), 0.6 (curve ii, 'green'), 0.8 (curve iii, 'red'), 1.0 (curve iv, 'light blue') and 1.2 MHz (curve v, 'purple'), respectively. Target positions with various target depth, $Z - D_z$, and lateral target distance, $D_y = 0$ mm (a, d, g), $D_y = L/4 = 10$ mm (b, e, h), $D_y = L/2 = 20$ mm (c, f, g) are presented.

These results show that the presence of the ribs in the beam pathway could dramatically decrease the temperature rise at the intended target, due to the effects of transmitted beam distortion and energy attenuation generated in the trans-costal FUS. For the trans-rib sonications, when the target depth, $Z - D_z$, increased, or the transducer elevation value in the hardware system increased, the maximum temperature change at the focal region and the intervening ribs decreased accordingly, as seen in Figures 5.33 (a) and 5.36 (a, d). This may be because the effective beam area transmitted through the rib plane becomes smaller, and the power deposition capability in the rib bone becomes less significant.

During the high intensity short duration heating, the ultrasound power density is useful to rapidly predict the temperature elevation in the biological tissue and ribs, and also the temperature estimation can be regarded as a fairly good indicator of the thermal dose. In this study, two distinct cases capable of generating the most satisfactory heating results at their specified target depths were selected: (1) $D_y = L/2 = 20$ mm and $Z - D_z \approx 30$ mm, (2) $D_y = 0$ mm and $Z - D_z \approx 60$ mm. As shown in Figure 5.37, the results of the two selected cases are illustrated by the normalized power density distributions over the entire computational domain.

With regard to position (1), i.e. the shallow target that was partially blocked by the ribs, and position (2), i.e. the deep target that was directly blocked by the ribs, the focuses shifted apparently toward the transducer at the lower frequencies of 0.4 and 0.6 MHz, as seen in Figures 5.37 (a) - (d). While the higher frequencies of 0.8, 1.0 and 1.2 MHz resulted in more concentrated and compact focal regions and also more energy deposition along the propagation paths, as seen in Figures 5.37 (e) - (j).

According to Figure 5.37, spatially-confined thermal lesions could be generated at the position (1), and similar cases near the surface of the abdominal organ and with only partial rib coverage can be classified as the most ideal candidates in clinical trans-costal FUS. For more practical cases, e.g., position (2), the corresponding power density distributions indicated that split and/or shifted thermal lesions could be generated around the target region when treated at higher frequencies of 0.8, 1.0 and 1.2 MHz. The thermal lesion dimensions and heat deposition in the intervening structures were compensated at the sonication frequency of 0.8 MHz, as shown in Figure 5.37 (f). It could also be noted that, typical thermal lesions at the deeper trans-costal sites could be generated with increased power levels. However in most instances, the resulting peak temperature and thermal dose (TD) might be observed at the intervening ribs rather than at the target regions.
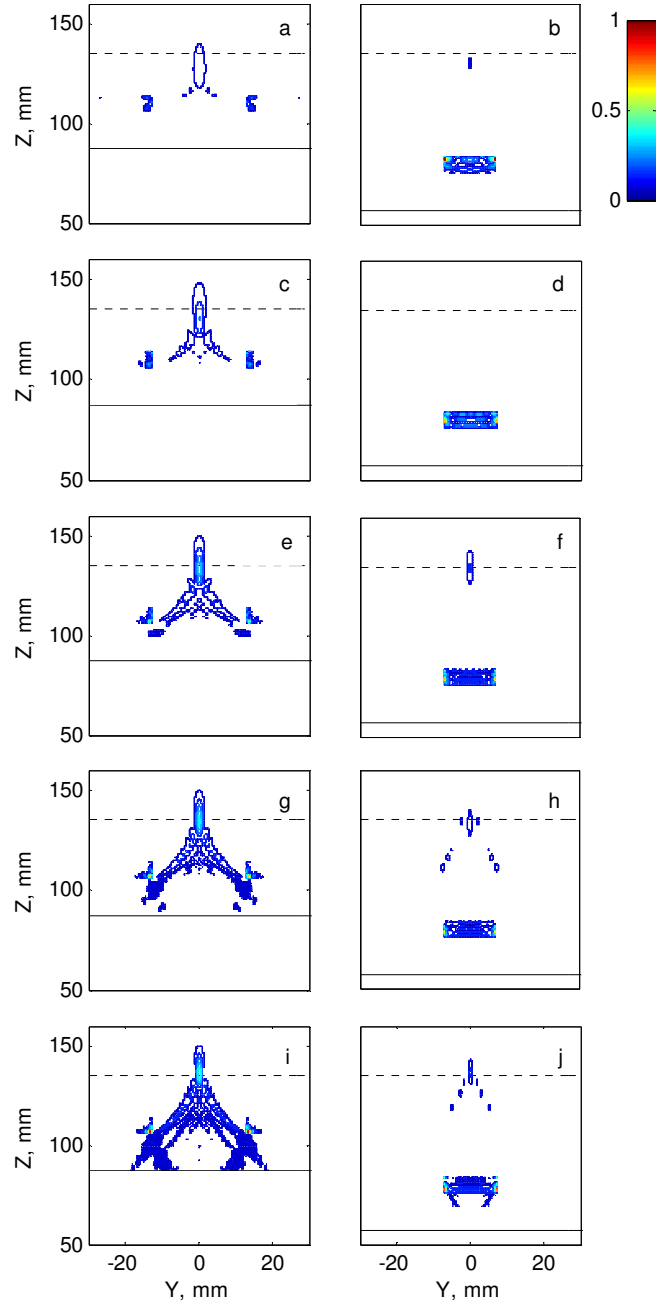
Figure 5.37 Normalized power density distributions over the computational domain under frequencies of 0.4 (a, b), 0.6 (c, d), 0.8 (e, f), 1.0 (g, h) and 1.2 MHz (i, j), respectively. Two selected target positions: (1) $D_y = L/2 = 20$ mm and $Z - D_z \approx 30$ mm (left), (2) $D_y = 0$ mm and $Z - D_z \approx 60$ mm (right) are presented. The calculated values were normalized by the peak value appeared in both cases. Contours are from 0 to 1 in increments of 0.075.

5.4 Avoiding Overheating of Ribs by Optimized Operation of 2D Phased Arrays

In this section, the effectiveness of the geometric rib sparing method to enhance localized thermal coagulation of target tumours and avoid overheating of ribs will be demonstrated both experimentally (Section 5.4.1) and numerically (Section 5.4.2). From the physical point of view, this can be indicated by the ratio of ultrasonic power densities at the target and the intervening ribs. The flexibility and suitability of this strategy for different target positions relative to the rib cage will also be presented.

5.4.1 Experimental Results

Based on the experimental procedures reported in Section 3.6, a preliminary investigation of MR-guided focused ultrasound ablation of trans-costal sites was carried out on the tissue-mimicking and rib-mimicking materials. Two algorithms for avoiding over-heating of the ribs (Algorithm #1 - central projection and Algorithm #2 - parallel projection) were examined experimentally with the 1024-element 550 kHz and the 208-element 1 MHz phased array transducers respectively. For the same phantom/rib setup, sonications were performed with all ultrasonic elements activated and using both rib sparing algorithms. The sonication parameters were maintained at defined values: acoustic power of 25 W and heating duration of 60 s.

5.4.1.1 Results on Acoustic Absorber Rib Cage Mimics

ExAblate 2100 System

The experimental setup using the acoustic absorber rib cage mimics and the 1024-element matrix array was shown in Figure 3.20. The resulting excitation patterns with implementation of both element manipulation algorithms are shown in Figures 5.38 (a) and (b), and the heating results are summarized in Figure 5.39 and Table 5.6. It was found that the rib over-heating problem could be greatly relieved by using the Algorithm #1, as the maximum temperature rise below the rib surface decreased from 27 °C (all elements activated) to 4 °C (Algorithm #1). However, no significant change in the focal heating was detected between the use of all ultrasonic elements and Algorithm #1.
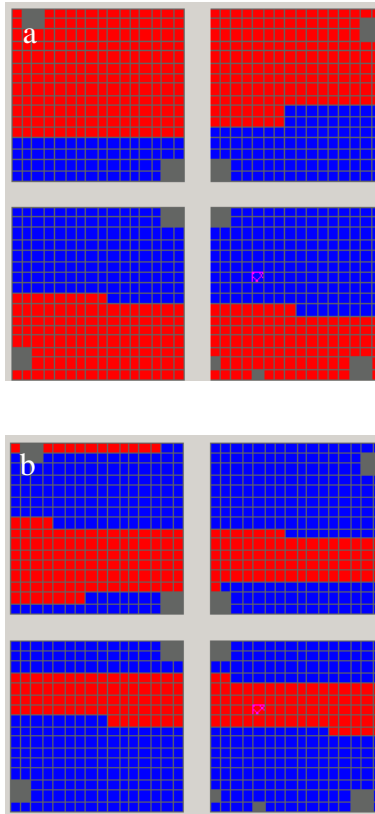
Figure 5.38 Activation/deactivation of elements in the 1024-element matrix array: (a) Algorithm #1 - central projection, (b) Algorithm #2 - parallel projection. The red elements are switched on while the blue ones are switched off.
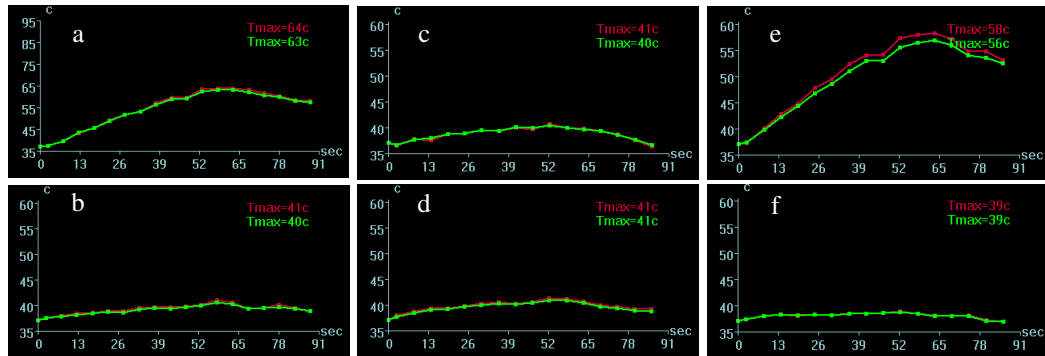
Figure 5.39 Temperature responses near the rib-mimics (a, c, e) and at the focus (b, d, f): all elements activated (left), Algorithm #1 (middle) and Algorithm #2 (right).

Table 5.6 Summary of heating results: excitation patterns

Max temp rise, ℃	Ribs	Focal region
All elements	27	4
Algorithm #1 (575 elements)	4	4
Algorithm #2 (335 elements)	21	2

A further investigation of the Algorithm #1 for two focal lengths of 106 and 71 mm were performed and the heating results are summarized in Table 5.7. It could be seen that the presence of the acoustic absorber rib cage mimics significantly reduced the maximum temperature rise in the focal region, from 20 °C to 4 °C. At the lower depth of 71 mm, a much higher temperature rise on the ribs was observed when sonicating through the solid rib-mimics (44 °C vs. 29 °C), which could be explained by the increase in the power density. This element manipulation method worked well in reliving rib over-heating but is less effective in enhancing heating in the focal zone, and it had more ultrasonic elements remaining active at the lower target depth of 71 mm (576 elements vs. 517 elements).

Table 5.7 Summary of heating results: focal lengths

Max temp rise, ℃	Ribs	Focal region
106 mm - All elements	29	3
106 mm - 517 elements	9	5
71 mm - All elements, no rib presence	-	20
71 mm - All elements	44	4
71 mm - 576 elements	11	6

ExAblate 2000 System

The same procedure was performed using the ExAblate 2000 system and the experimental setup was shown in Figure 3.19. In light of the results obtained for the ExAblate 2100 system, only two types of sonications were performed here, with all elements activated or appropriate elements deactivated using Algorithm #1. The resulting excitation pattern after implementation of this element manipulation algorithm is presented in Figure 5.40. The heating results are summarized in Figure 5.41 and Table 5.8. The maximum temperature rise near the rib-mimics was successfully reduced from 45 °C and 58 °C to 15 °C and 17 °C respectively. Generally, this 208-element 1 MHz bowl array offers enhanced focusing ability (greater focusing gain) than the 1024-element 0.55 MHz matrix array, hence for the same amount of energy delivery, greater temperature rises will be noticed when using the higher frequency bowl array.
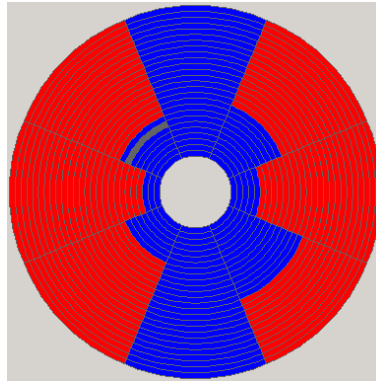
Figure 5.40 Activation/deactivation of elements in the 208-element bowl array: Algorithm #1. The red elements are switched on while the blue ones are switched off.
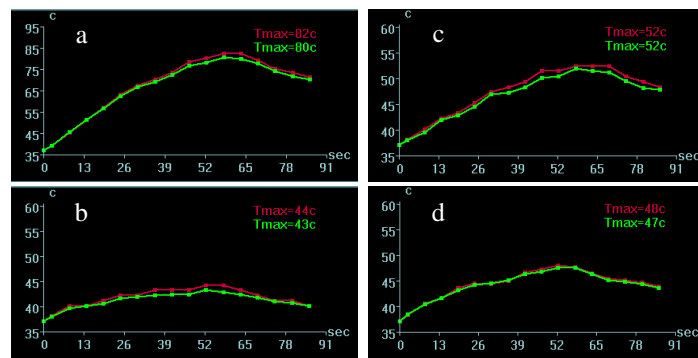
Figure 5.41 Temperature responses near the rib-mimics (a, c) and at the focus (b, d): all elements activated (left) and Algorithm #1 (right).

Table 5.8 Summary of heating results: focal lengths

Max temp rise,℃	Ribs	Focal region
130 mm - All elements	45	7
130 mm - Algorithm #1 (109 elements)	15	11
125 mm - All elements	58	13
125 mm - Algorithm #1 (96 elements)	17	24

ExAblate 2000 System: Transducer-to-Rib Distance

This Algorithm #1 has also been evaluated with respect to different transducer-to-rib distances or different transducer elevations as discussed for the hardware system. Briefly, when sonicating with complete spherical beams (acoustic power of 25 W and sonication duration of 60 s), the maximum temperature rises in the focal region and near the rib-mimics decreased with the increasing transducer elevation value within the investigation range, as seen in Figure 5.33 (a). For these trans-rib sonications with the

targets directly blocked by the middle rib, the number of elements needed to be switched off increased quasi-linearly with the increasing transducer elevation value, e.g., from 94 elements with zero transducer elevation to 128 elements with the transducer elevation of 32.5 mm in the ExAblate 2000-2 system. The heating results after application of the element manipulation algorithm are shown in Figure 5.42, in which the maximum temperature rises in the focal region became less dependent on the transducer elevation, while for the rib-mimics, it increased at higher elevation values. In this setup with the acoustic absorber rib cage mimics, the binary element manipulation method functioned fine to reduce the rib over-heating problem and enhance heating in the focal area, especially in the cases of small transducer elevations.
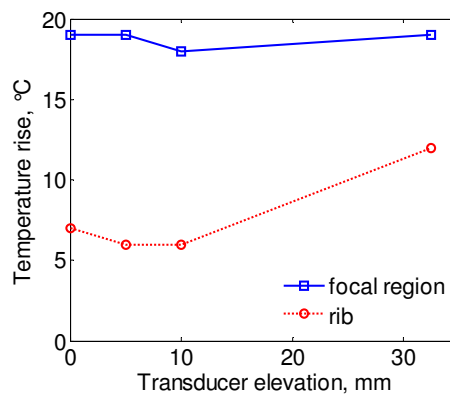
Figure 5.42 Maximum temperature rises in the focal region and near the rib-mimics for different transducer elevation value in the ExAblate 2000-2 system.

5.4.1.2 Results on Epoxy Rib Cage Mimics and Thiel-embalmed Cadaver

In order to assess the applicability of the element manipulation algorithm, or named as the geometric rib sparing method, in complex human anatomy, experiments were conducted on the epoxy rib cage mimics (in Figure 3.15) as well as human cadavers (in Figure 3.24). As seen in Figure 5.43, this element manipulation algorithm could be easily used for this phantom with inclusion of the epoxy rib strips (167 elements on, 41 elements off). However, as shown in Figure 5.44, there were no significant temperature changes at the focus and near the rib strips, due to the transmitting and non-absorbing characteristics of the surrounding gel phantom.
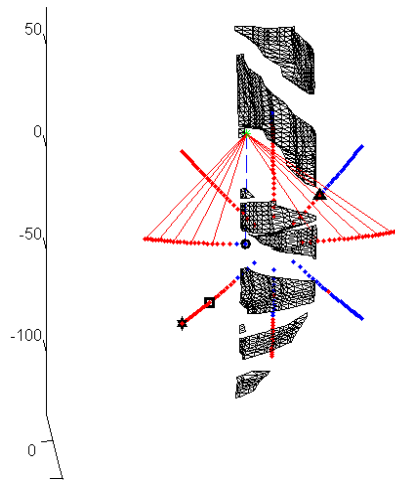
Figure 5.43 Results of elements to switch on/off for the epoxy rib cage mimics: the red elements are switched on whereas the blue ones are switched off. The mesh represents the surface reconstruction of the ribs.
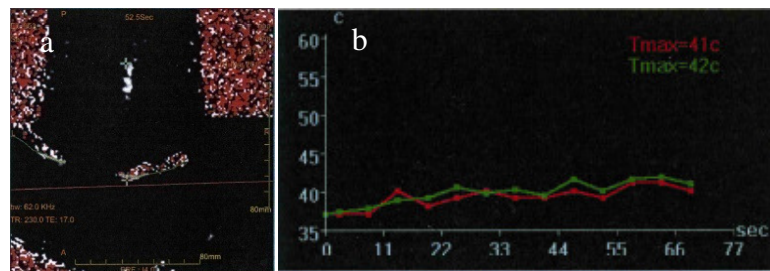
Figure 5.44 (a) Thermal map of rib heating and (b) temperature response at the focus.

The use of Thiel-embalmed cadaver in MRgFUS has been investigated for targeting various organs behind the rib cage. The experiment was performed using the ExAblate 2100 system, where the 1024-element matrix array was located at the cadaver's left upper abdomen. Better imaging qualities of ribs and tissue could be achieved using appropriate MR sequences. After applying the geometric rib sparing method, there were approximately 600 elements remaining active (taking 60 % of the matrix array), as shown in Figure 5.45. However, there were challenges with respect to the complicated internal structures such as the bowel in the pathway that could cause severe distortion and attenuation of the incident beam. The organs being squeezed by the transducer can also cause difficulty in handling the Thiel-embalmed cadaver; however, this may be less problematic on a real patient.
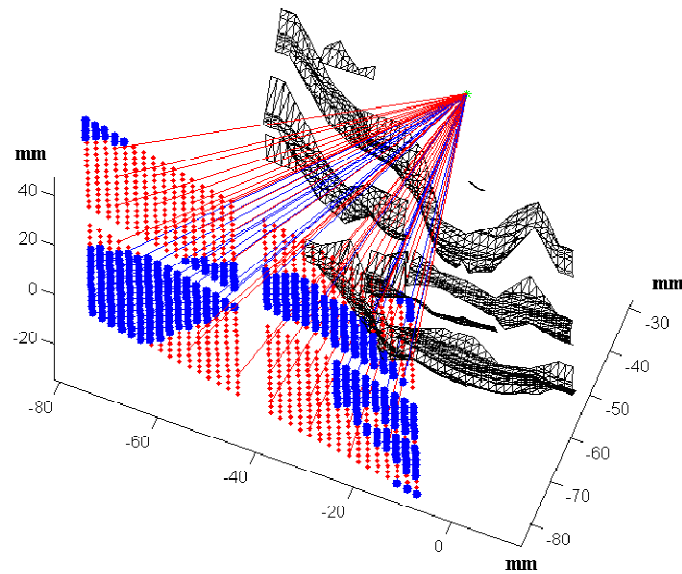
Figure 5.45 Results of elements to switch on/off for the Thiel-embalmed cadaver: the red elements are switched on whereas the blue ones are switched off. The mesh represents the surface reconstruction of the ribs.

Based on this research, the geometric rib sparing method worked for both simplified rib cage mimics and the complex human anatomy. The number of transducer elements needed to be deactivated is affected by the geometric shapes of the rib cage and the relative positioning of essential parts (transducer, ribs and target); usually around half of the elements remain active after implementing the rib sparing procedures. Efficient treatment schemes for optimized heating results in the focal region and on the intervening ribs may be achieved by adjustment of the transducer in different roll and pitch directions and other additional degrees of freedom. For advanced laboratory and clinical research, further experimental and simulation work in terms of parametric and algorithm studies need to be performed as part of the pre-treatment planning procedure.

5.4.2 Numerical Results

The acoustic and thermal models, as shown in Figure 4.4 and Section 4.5.2, were built to simulate the experiments performed on the ExAblate 2100 system. The resulting thermal maps and histories of maximum temperature rises near the ribs and in the focal region are shown in Figures 5.46 and 5.47, respectively. As seen in Figure 5.46, only the Algorithm #1 can prevent the incidence of ultrasound beams to the rib surface, which resulted in

reduced heating of the rib-mimics, with 22 °C less compared to full spherical radiation. However, as presented in Figure 5.37, there were no significant improvements in the focal region for all sonication types.
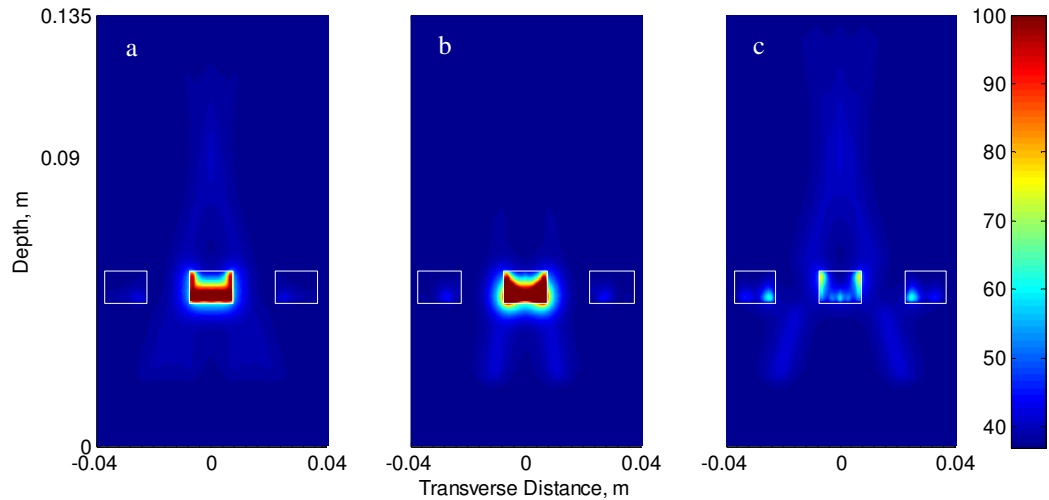
Figure 5.46 Temperature distributions in the presence of the acoustic absorber rib-mimics (white blocks): (a) all elements activated, (b) Algorithm #2, and (c) Algorithm #1.
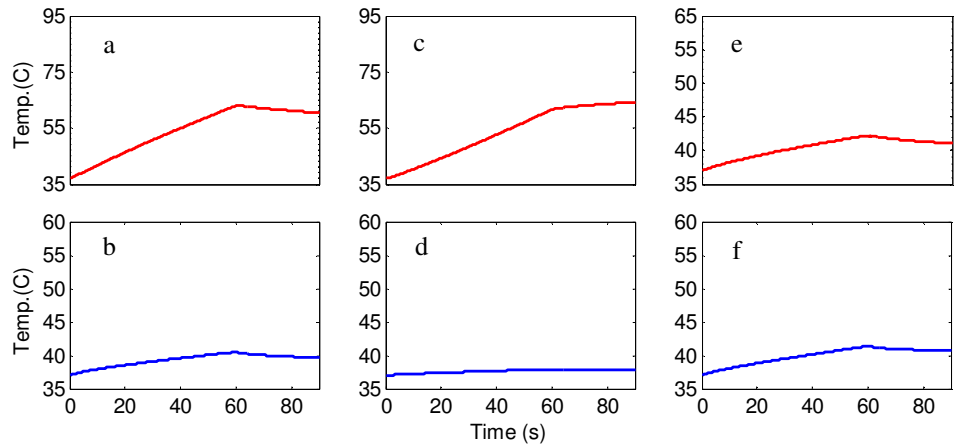
Figure 5.47 Temperature responses near the rib-mimics (a, c, e) and at the focus (b, d, f): all elements activated (left), Algorithm #2 (middle) and Algorithm #1 (right).

Table 5.9 Comparison of measured and simulated heating results

Max temp rise ℃	Measurement		Simulation	
	Ribs	Focal region	Ribs	Focal region
All elements on	26	3	26	3.5
Algorithm #1 – central projection	4	3	5.2	4.4

As summarized in Table 5.9, the measurement and simulation results are in good agreement with each other, and variations can be explained by the differences in geometric configuration, material properties, driving conditions, and also temperature measurement errors in MR thermometry.

5.4.2.1 Effects of Transducer-to-Rib Distances and Focal Lengths

For the fixed-focus single-element transducers, the transducer-to-rib distance, D_z, has to be mechanically adjusted with the target depth, $Z - D_z$, for the given focal length, Z. However, it should not be a problem limiting the efficiency of the trans-costal treatments when multi-element phased arrays are used, since D_z and Z can be altered accordingly for any particular target within the body. For fixed targets with coordinates of D_y and $Z - D_z$ relative to the rib cage, the phased array transducer can be mechanically moved along the coordinate directions and/or the pitch and roll rotations, and the resulting excitation pattern applied to the array can be controlled by binary manipulation of the transducer elements.

In this part, discussion will focus on the movement of the matrix array in the direction of the beam axis as well as the variance in the focal length. Each row in Figure 5.48 shared the same transducer-to-rib distance, D_z, but varying focal length, Z, while each column shared the same focal length, Z, but varying transducer-to-rib distance, D_z. As shown in Figures 5.48 (a), (e) and (i) which represented the same target depth of $Z - D_z = 45$ mm but different transducer-to-rib distances of $D_z = 35$, 45, and 55 mm, the maximum temperature rise in the focal region increased slightly with the decreasing D_z (can be interpreted as elevating the transducer), and the maximum temperature rise near the rib-mimics showed a decreasing trend from 10.9 ℃ to 4.6 ℃; and these simulation results listed in Table 5.10 provided supporting data against the transducer elevation value as shown in Figure 5.42.
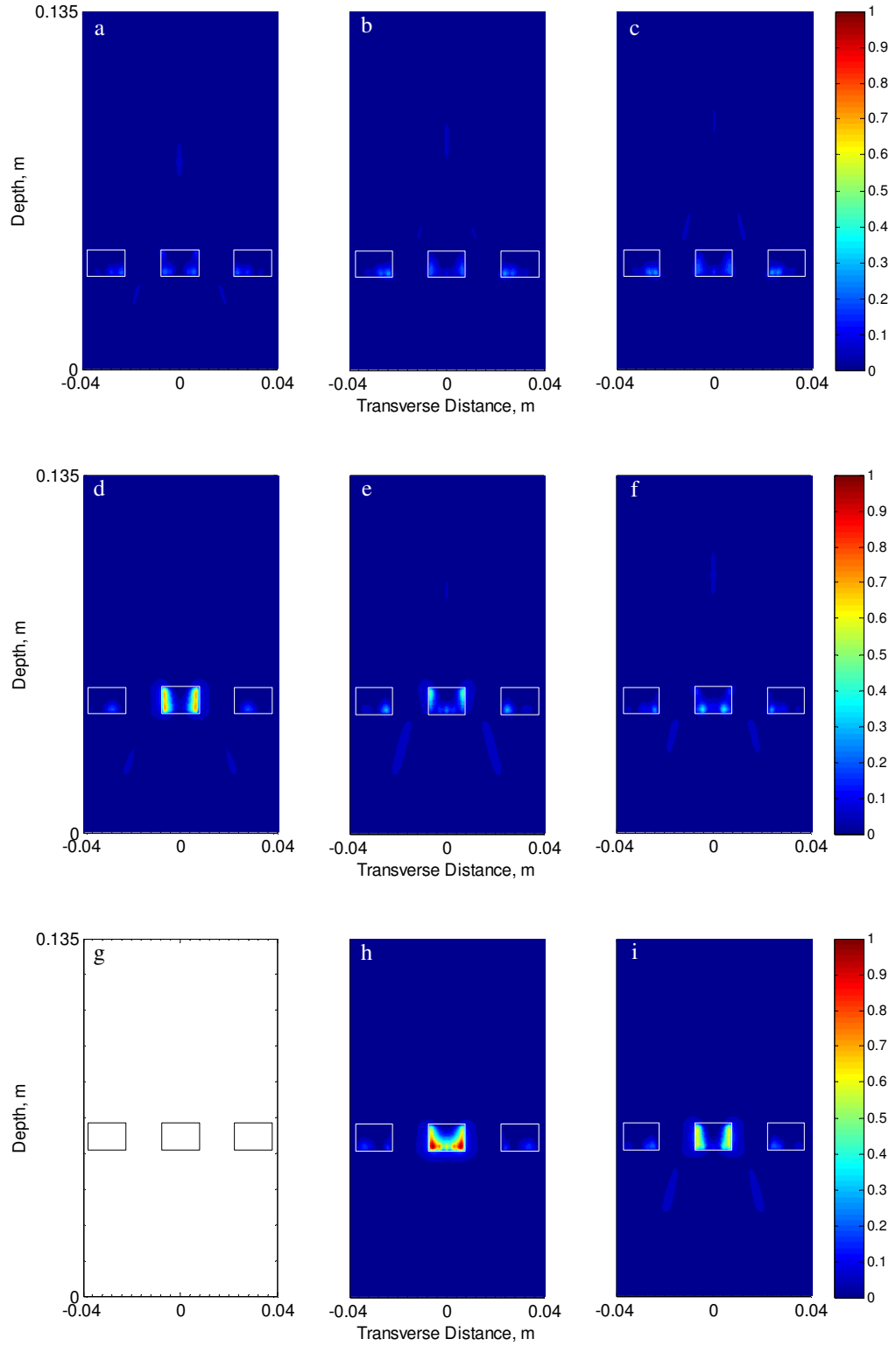
Figure 5.48 Temperature distributions in the presence of the acoustic absorber rib-mimics (white blocks). Rows 1-3 represent different transducer-to-rib distance of 35, 45 and 55 mm and columns 1-3 indicate different focal position of 80, 90 and 100 mm, respectively.

Table 5.10 Maximum temperature rises near the rib-mimics and at the focus, ℃

Max temp rise ℃		Ribs			Focal Region		
		Focal Length (mm)			Focal Length (mm)		
		80	90	100	80	90	100
Transducer-to-rib distance (mm)	35	**4.6**	4	4.2	4.8	4.7	4.4
	45	10.75	**5.2**	7.05	4.3	4.4	4.8
	55	-	19	**10.9**	-	2.6	3.6

5.4.2.2 Effects of Target Locations

There are several influencing factors on the geometric rib sparing solution including the transducer frequency, the transducer dimensions, and the transducer-to-rib distance (related with the transducer elevation value). In this part, discussion will be expanded to application of this rib sparing method for different target locations relative to the rib cage, as discussed in the Sections 5.2 and 5.3, the target coordinates were denoted by D_y and $Z - D_z$ (Figure 4.5). Basic geometric configurations and material properties of the finite element models were the same as those presented in Figure 4.3 and Table 4.1. The proposed frequency of 0.8 MHz as obtained in Section 5.3 was used. For a given target, the array transducer focusing can be achieved by steering the beam focus via the phased array technology. In this parametric study, the axial target depth measured from the front surface of rib bone, $Z - D_z$, ranged from 10 to 90 mm, with a step of 10 mm; while three distinct values of $D_y = 0$ mm (sonicating through the solid rib), $D_y = L/4 = 10$ mm, and $D_y = L/2 = 20$ mm (sonicating through the inter-costal space) were considered for the lateral target distance, where $L = L_r + L_i = 40$ mm represents the width of an individual rib structure. The initial driving pressure was maintained at the same amplitude of 0.4 MPa for different sonications, and the effectiveness of these sonications were evaluated by comparing the ratio of power densities between the target and the intervening ribs.
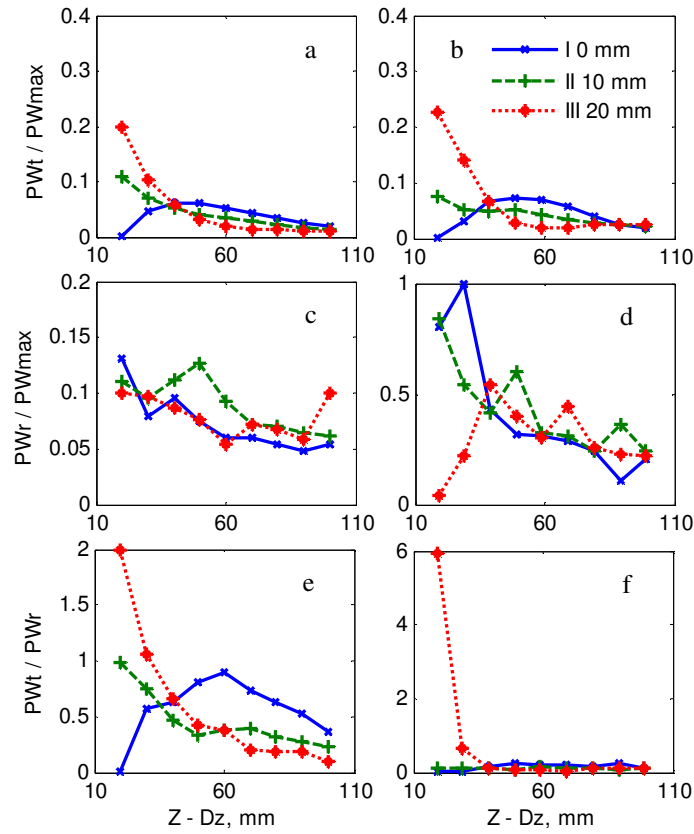
Figure 5.49 Normalized power densities at the targets (a – b), the ribs (c – d), and also the ratios between the values at the targets and the ribs (e – f) under frequency of 0.8 MHz. Target positions with various target depth, Z - D_z, and lateral target distance, $D_y = 0$ mm (curve I, 'blue'), $D_y = L/4 = 10$ mm (curve II, 'green'), $D_y = L/2 = 20$ mm (curve III, 'red') are presented with (a, c, e) and without (b, d, f) application of the rib sparing method.

As seen in Figures 5.49 (a) and (b), the normalized power density at the target showed different increasing or decreasing trend with respect to the target depth, $Z – D_z$, in both cases with and without implementing the element manipulation algorithm. As discussed previously, the reason behind this was the differences in the transducer-to-rib distance and focal length. It can be seen that the normalized power densities at the intended focuses maintained the same levels or had slightly smaller amplitudes, which was caused by the decrease in power when selected elements were switched off. However, under the same power, for example at the axial target position of $Z – D_z = 50$ mm, the normalized power density at the focus when directing the beam axis through the solid rib, 'blue', could be about 1.16 times the value in the full spherical sonication case. This amplification factor also explained the slight improvements in temperature rises in the focal region in

previous experiment session.

In Figure 5.49 (c), the calculated normalized power density at the ribs shows less obvious dependence on the axial and lateral target positions. Compared with those full spherical sonications presented in Figure 5.49 (d), the maximum value after applying the rib sparing method decreased by nearly an order of magnitude, e.g., PW_r / PW_{max} = 0.13 at the target depth of 20 mm when sonicating through the solid rib, and also this value could be modified to around 0.19 when being driven with the same power. However, there was an occasional case resulting in greater power density on the ribs when using the rib sparing method, i.e., for the target position that was close to the rib cage, $Z - D_z$ = 20 mm, and was located right behind the inter-costal muscle, D_y = 20 mm.

In Figures 5.49 (e), (f) and 5.50, the average improvement in the ratio of power densities between the target and the ribs after applying the rib sparing method was about 428 % for all the cases considered here and the maximum improvement could be up to 1800 % at the coordinates of D_y = 0 mm and $Z - D_z$ = 30 mm, referring to the focus located behind the solid rib and was in close proximity to the ribs. In summary, the geometric rib sparing method works fine for most cases, but excluding the targets that were located behind the inter-costal muscle and were either too near or too far from the ribs e.g., D_y = 20 mm, $Z - D_z$ = 20 mm (34%) or $Z - D_z$ = 100 mm (85%). However, for these lower efficiency cases, greatly enhanced improvements can be achieved with combined adjustments of the transducer-to-rib distance and hence the focal length.
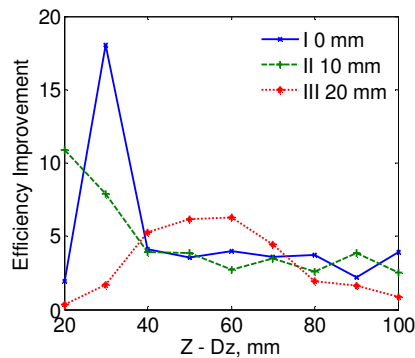
Figure 5.50 Efficiency improvements by using the rib sparing method. Target positions with various target depth, $Z - D_z$, and lateral target distance, D_y = 0 mm (curve I, 'blue'), D_y = L/4 = 10 mm (curve II, 'green'), D_y = L/2 = 20 mm (curve iii, 'red') are presented.

In addition, for successful 'trans-rib' treatment of the upper abdominal tumours, the operator may need to reduce the transducer-to-rib distance and guarantee there is enough water for cooling; whereas for those shallow target tumours located behind the inter-costal muscle e.g., at $D_y = 20$ mm and $Z - D_z = 20$ mm as presented above, one needs to lengthen the transducer-to-rib distance instead. Intensions behind these measures are to increase the effective beam area not blocked by the ribs, A_{e-p} / A_e. This study also demonstrated that there might be limitations in this geometric rib sparing method, in which cases more than half of the active elements would be deactivated. However this could be avoided and enhanced through careful pre-treatment planning procedures.

CHAPTER 6 CONCLUSIONS AND FURTHER WORK

The material presented in the above chapters is summarized in Chapter Six. The initial purposes of this investigation were to explore the basic acoustic and thermal effects of HIFU and the feasibility of using the finite element software packages, PZFlex and SpectralFlex, to simulate the HIFU procedures. Of particular concern was the exploration of the direct thermal ablation for which the indirect damage resulting from mechanical cavitations are temporarily not involved. A review of the available literature shaped the investigation and helped identify the research directions for new researchers in this field. It was noted that there existed a few challenges concerning the wider surgical application of FUS for tumours located in the upper abdomen organs. The investigation that followed therefore was aimed to address the practical issues and solutions related to the physical presence of the rib cage in trans-costal FUS. The chapter draws important conclusions about the relevance of the material presented and its influence on the possible direction of any further work.

6.1 Conclusions

6.1.1 Characterization of HIFU Devices and Assessment of HIFU Effects

The focused acoustic fields were generated with relative ease using single element transducers, the main component of which was the focusing bowl piezo-ceramic element. These devices were driven with a sine waveform at some resonant or matching frequency determined by the electrical impedance response, at which value (MHz range), the resulting impedance magnitude was most closely matched to that of the associated drive equipment impedance of 50 Ω. Such devices showed a uniform focused acoustic field with a predictable and relatively small focal volume, whilst the geometries of focusing bowls could be selected to generate focal zones of comparable volumes. This method of geometric focusing was simpler and cheaper to implement than electronic focusing and beam steering, and provided a more readily available alternative. However, it could be argued that adjustable focusing could only be achieved by alternating the position of the device, when implementation of the device with a scanning system should be considered.

The thermal sensitive egg white phantoms were developed for, and in laboratory use for real-time visualization of HIFU-induced thermal coagulative necrosis. The material was found to exhibit favourable acoustic properties and was well suited to high power, high intensity applications. The concentration of the egg white allowed adjustable material properties, however it was not feasible to increase the amplitude of the attenuation coefficient to that of real tissue with adjustment in the egg white concentration, due to the requirement of optical clarity. In the literature, the speed of sound and attenuation of the egg white phantom were both measured to be temperature dependent, for that the changes in the acoustic properties before and after thermal coagulation may cause thermal defocusing and distorted lesions in the shape. In future, the effects of the temperature dependent acoustic properties on the HIFU procedures need to be figured out.

Moreover, a step-wise transient plane source (TPS) method was used to determine the values of the thermal conductivity, thermal diffusivity, and specific heat capacity of egg white phantoms with elevated egg white concentrations at room temperature. Important experimental parameters, e.g., the sample sizes, the heat output from the heat source, the measuring time, and the time window for the non-linear curve fitting were determined sequentially. This work contributes to the literature not only for publishing relevant data on the thermal properties of egg white phantoms for HIFU, but also for introducing a relatively simple method that can be used in most standard ultrasound labs for the simultaneous measurements of thermophysical properties of most solid samples.

Focusing ensured sufficient focal intensities for the purposes of rapid heat deposition and thermal ablation. This study investigated the quantitative relationship between ultrasonic power deposition, temperature, and thermal dose. It was suggested that the produced lesion position, shape and size were related to various HIFU parameters (frequency, intensity, time duration, focal length, and etc.). Interaction of the devices with materials of temperature sensitivity also appeared to yield indications that the thermal conduction was the dominating factor for the responses of thermal ablation, almost independent of blood perfusion. However, the over-heated cases were usually associated with the formation of cavitation clouds, which were reported to acoustically shield other regions and thus limit the ability to treat the whole target area. Further research is required to fully understand and control these thermal and non-thermal mechanisms, especially cavitation.

This study presents preliminary experimental results from egg white phantoms. However, there are limitations in understanding the HIFU effects on these tissue-mimicking phantoms, as it has notable differences from clinical tumour ablation such as the lack of biological mechanisms in *in-vivo* perfused organs. Further studies regarding the destruction mechanisms by HIFU need to be explored on *ex-vivo* tissue, *in-vivo* tissue, animal studies, and clinical studies in future. HIFU treatment may present specific safety risks, hence further discussion regarding the practical guidelines for its safe use is necessary, though it is generally considered to be difficult due to the differences of tissue condition and the alternation of tissue properties during treatment.

6.1.2 Investigation of Trans-costal FUS towards Successful Applications

The first stage results presented in Section 6.1.1 covered a wide range of subjects from device characterization, fabrication and characterization of tissue-mimicking phantoms, through to application of these devices and phantom materials for the purposes of experimental and numerical studies of HIFU. In later sections, both experimental and computational results demonstrated the effects of decreased ablation efficiency at the targets and overheating of the ribs during trans-costal FUS sonications. However, these unwanted effects might be reduced with the use of the most effective treatment configuration.

The investigations conducted in the first session detailed the results of distorted focal behaviour in trans-costal FUS, which allows for better understanding and pre-planning of the treatment effects that may be encountered in clinical practice. It is favourable for clinical uses that the inter-costal spaces are normally twice as wide as the ribs in human anatomy. For all aspects of the study, the shallow cancerous tissue lying immediately behind the inter-costal spaces can be ablated easily by sonicating through the inter-costal spaces; while for the shallow cancerous tissue lying immediately behind the ribs, an initial solution by mechanically moving the transducer relative to the rib cage can be considered to produce the maximum effective beam area on the ribs plane. Alternatively the solution involving respiratory motion management technique (i.e., respiratory-gating) and breath-hold may be necessary to control active movements of organ to positions right behind the inter-costal spaces during the treatment. Unfortunately, this procedure will

considerably extend the duration of the treatment. For other deep targets, though treatment efficiency can be slightly improved by sonicating through the ribs instead of the inter-costal spaces, novel and promising solutions in combination with cavitation need to be explored for further enhanced localized heating.

As discussed previously, the trans-costal heating can be influenced by a number of factors, including the widths of the ribs and the inter-costal spaces, the positions of target tumours relative to the rib cage, the dimensions and also the driving frequency of the ultrasonic source. In the second session, the temperature developments in terms of magnitudes and profile shapes were significantly affected by the intervening ribs during trans-costal FUS. The results of the model analysis demonstrated that ultrasound at frequencies around 0.8 MHz was optimal for maximizing power density gains (target to ribs) in these sonications. In the investigation, a lower frequency resulted in an enlarged and distorted focus toward the transducer and less energy deposition in the focal region. While a higher frequency offered much tighter focal spots, this was advantageous to reduce temperature elevations in surrounding normal tissue, but would greatly increase the entire treatment time when treating larger tumours. Also, the higher frequency led to increased energy absorption at the intervening tissue, which is undesirable for avoiding over-heating there. Thus, the moderate frequency around 0.8 MHz is more appropriate, and it may shift slightly to higher levels with changes in the axial and lateral positions of target tumours. However, it was worth noting that no obvious relationship between the rib heating and the frequency was observed yet.

In the third session, the effectiveness of the geometric rib sparing solution for reducing the rib-overheating problem in trans-costal FUS was evaluated. With use of multi-element phased arrays and multiple rib cage structures, the proposed method based on central projection from the focus to identify transducer elements affected by rib shadowing which should be switched off. By applying the geometric solution, there were generally 60 % ultrasonic elements remaining active and the maximum temperature rises near the ribs were significantly reduced. The average improvement in the treatment efficiency was approximately 428 % compared with the conventional full spherical radiation. The only exception was the 'inter-costal' tumour lying close to the ribs, where the power density ratio (target / ribs) increased three fold when using the complete spherical radiation. However, the limitation could be solved by increasing the transducer-to-rib distance to

maximize the effective beam area transmitting through the rib plane. As for the 'trans-costal' tumours, the rib over-heating problem could be relieved by reducing the transducer-to-rib distance or advancing the transducer elevation when speaking of the hardware system. Residual temperature rise on the ribs could be further reduced by active cooling as presented in the ExAblate 2100 system, allowing higher energies essential for efficient ablation.

Currently, the correction of beam patterns remains a technological performance and needs to be validated clinically. In particular, organs along the beam pathway may significantly distort and absorb the ultrasonic beam causing insufficient energy delivered to intended tumours and possible damage of organs that are intersected. Although it may pose challenges, this method can be useful if carefully selected and planned, and our findings in the thesis will provide useful information for accurate and reliable treatment planning in clinical practice.

6.2 Further Work

6.2.1 Multi-level Model for Moving Abdominal Organs

This thesis will contribute to the academic world by publishing relevant data to address and solve the problems associated with the rib cage in developing clinical applications of FUS for the liver, kidney, and pancreas tumours. General side effects such as overheating of the ribs, distortion of ultrasound beam behind the rib cage, reduction of intensity in the main focus, etc, have been investigated both experimentally and using numerical models. However, no general model which includes realistic 3D geometries and adequate physical properties of ribs has been developed yet to quantitatively model the clinical conditions.

In this direction, the patient-specific model for treatment planning in trans-costal FUS can be established sequentially by image segmentation to generate layered surface model, ultrasound simulation of HIFU-induced intensity distribution and temperature profiles, and visualization of integrated 3D anatomy and ultrasound simulation. For an ideal tissue model, it should include the inhomogeneous structure of the anatomical tissue, blood flow, the nonlinear acoustic effect, and cavitation, which complicate the treatment outcomes in practice. The problem of motion artifacts is an important research topic particularly in the

treatment of abdominal parts, for which reliable motion detection (e.g., by applying the appropriate registration algorithm for ultrasound images to deduce patient respiratory and cardiac motion) and 3D real-time motion model are needed to simulate the effects of motion during the intervention. Further studies to minimize the general side effects and develop the best heating strategy for irradiation of any specific situation can be evaluated interactively based on the model.

All results of current clinical trials are based on an open-loop concept where the acoustic power is controlled by the operator on the basis of the feedback information obtained during previous sonications. The entire volume is covered by repeating the sonications in multiple locations. This method does not provide an optimal energy delivery and the treatment times cannot be minimized. An alternative method to this is to use image-based thermometry to control the power during the sonication such that desired exposure is induced without wasting energy by overheating the treated volume, as may be found in the case with the open-loop concept. These closed-loop feedback systems reduce the complexity of operating the systems and can optimize the energy delivery and hence minimizing the treatment times. This could be explored in computer simulations with multi-element phased arrays for both single spot sonications and scanned focused ultrasound heating of a large volume.

6.2.2 Cavitation-based Solutions to Further Enhance Localized Heating in Trans-costal FUS

Our previous work has proved the feasibility of delivering acoustic energy through the rib cage safely by using appropriate control schemes of the phased arrays. However, there were no significant temperature changes in the focal region, and the rib heating was still higher than heating at the focus. To mitigate the problem of reduced heating efficiency and prolonged treatment times in clinical trans-costal FUS, potential cavitation-based solutions including the use of micro-bubble contrast agents and optically-activated nanoparticles, could be tested experimentally. The micro-bubble contrast agents previously used in ultrasonic imaging for detection and diagnosis of malignant tumours (Kennedy et al., 2004a), have been shown to increase the volume of tissue that can be coagulated (Kaneko et al., 2005). However, the mechanisms by which micro-bubbles in the ultrasound field cause heating are not fully understood. Enhanced localized heating

has also been achieved by pulsed laser illumination of the light-absorbing nanoparticles when combined with ultrasound field (McLaughlan et al., 2010). However, factors contribute to cell damage in the pulsed-laser based photothermal therapy are not fully understood yet. Following the work introduced here, further experimental studies and clinical trials may be necessary for final successful applications of these methods.

REFERENCES

http://: www.cancerresearchuk.org/

http://www.ferroperm-piezo.com

International Standard ISO 22007, Plastics - Determination of thermal conductivity and thermal diffusivity (2007)

Al-Ajlan S.A., Measurements of thermal properties of insulation materials by using transient plane source technique. Appl. Therm. Eng. 2006; 26: 2184-2191.

Allen M., Rivens I., Visioli A., et al., Focused ultrasound surgery (FUS): a noninvasive technique for the thermal ablation of liver metastases. Proc. 2nd. Int. Symp. Therapeutics Ultrasound 2002; 17-25.

Arora D., Cooley D., Perry T., et al., Direct thermal dose control of constrained focused ultrasound treatments: phantom and in vivo evaluation. Phys. Med. Biol. 2005; 50: 1919.

Aubry J.F., Tanter M., Pernot M., et al., Experimental demonstration of noninvasive transskull adaptive focusing base on prior computed tomography scans. J. Acoust. Soc. Am. 2003; 113: 84-93.

Aubry J.F., Pernot M., Marquet F., et al., Transcostal high-intensity-focused ultrasound: ex vivo adaptive focusing feasibility study. Phys. Med. Biol. 2008; 53: 2937-2951.

Bekeredjian R., Grayburn P.A., Shohet R.V., Use of ultrasound contrast agents for gene or drug delivery in cardiovascular medicine. J. Am. Coll. Cardiol. 2005; 45: 329-335.

Bernassau A.L., Hutson D., Démoré C.E.M., et al., Characterization of an epoxy filler for piezocomposites compatible with microfabrication processes. IEEE T ULTRASON FERR 2011, 58(12) : 2743-2748.

Bilek J., Atkinson J.K., Wakeham W.A., Repeatability and refinement of a transient hot-wire instrument for measuring the thermal conductivity of high temperature melts. Int.

J. Thermophys. 2006; 27(6): 1626-1637.

Blana A., Walter B., Rogenhofer S., et al., High intensity focused ultrasound for the treatment of localized prostate cancer: 5-year experience. Urology 2004; 63: 297-300.

Blana A., Rogenhofer S., Ganzer R., et al., Eight years' experience with high-intensity focused ultrasonography for treatment of localized prostate cancer. Urology 2008; 72: 1329-1333.

Bobkova S., Gavrilov L., Khokhlova V., et al., Focusing of high-intensity focused ultrasound through the rib cage using a therapeutic random phased array. Ultrasound Med Biol 2010; 36: 888-906.

Bryan P.J., Custar S., Haaga J.R., et al., Respiratory movement of the pancreas: an ultrasonic study. J. Ultrasound Med. 1984; 3: 317-320.

Burov A.K., High intensity ultrasonic vibrations for action on animal and human malignant tumours. Dokl. Akad. Nauk. 1956; SSR 106: 239-241.

Canney M.S., Bailey M.R., Crum L.A., et al., Acoustic characterization of high intensity focused ultrasound fields: A combined measurement and modelling approach. J. Acoust. Soc. Am. 2008; 124: 2406-2420.

Catane R., Beck A., Inbar Y., et al., MR-guided focused ultrasound surgery (MRgFUS) for the palliation of pain in patients with bone metastases – preliminary clinical experience. Ann. Oncol. 2007; 18: 163-167.

Chaffai S., Padilla F., Berger G., et al., In vitro measurement of the frequency-dependent attenuation in cancellous bone between 0.2 and 2 MHz. J. Acoust. Soc. Am. 2000; 108:1281-1289.

Chen L., Rivens I., ter Haar G., et al., Histological changes in rat liver tumours treated with high-intensity focused ultrasound. Ultrasound Med. Biol. 1993a, 19: 67-74.

Chen L., ter Haar G., Hill C.R., et al., Effect of blood perfusion on the ablation of liver parenchyma with high-intensity focused ultrasound. Phys. Med. Biol. 1993b, 38: 1661-1673.

Chen W.S., Matula T.J., Brayman A.A., et al., A comparison of the fragmentation thresholds and inertial cavitation doses of different ultrasound contrast agents. J. Acoust. Soc. Am. 2003; 113(1): 643-651.

Chen W.Z., Zhu H., Zhang L., et al., Primary bone malignancy: effective treatment with High-Intensity Focused Ultrasound ablation. Radiology 2010; 255: 967-978.

Choi J.J., Wang S., Tung Y.S., et al., Molecules of various phar-macologically-relevant sizes can cross the ultrasound induced blood-brain barrier opening in vivo. Ultrasound Med. Biol. 2010; 36: 58-67.

Church C.C. and Yang X.M., A theoretical study of gas bubble dynamics in tissue. AIP Conf. Proc. 838: 217-224.

Civale J., Clarke R., Rivens I., et al., The use of a segmented transducer for rib sparing in HIFU treatments. Ultrasound Med Biol 2007; 32: 1753-1761.

Cline H.E., Schenck J.F., Watkins R.D., et al., Magnetic resonance-guided thermal surgery. Magn. Reson. Med. 1993; 30: 98-106.

Cobbold R.S.C., Foundations of biomedical ultrasound. Oxford University Press US, 79-84, 2007.

Cochard E., Prada C., Aubry J.F., et al., Ultrasonic focusing through the ribs using the DORT method. Med. Phys. 2009; 36(8): 3495-3503.

Coleman D.J., Lizzi F.L., Driller J., et al., Therapeutic ultrasound in the treatment of glaucoma – I. Experimental model. Ophthalmology 1985a; 92: 339-346.

Coleman D.J., Lizzi F.L., Driller J., et al., Therapeutic ultrasound in the treatment of

glaucoma – II. Clinical applications. Ophthalmology 1985b; 92: 347-353.

Coleman D.J., Lizzi F.L., Burgess S.E., et al., Ultrasonic hyperthermia and radiation in the management of intraocular malignant melanoma. Am. J. Ophthalmol. 1986; 101: 635-642.

Connor C.W. and Hynynen K., Bio-acoustic thermal lensing and nonlinear propagation in focused ultrasound surgery using large focal spots: a parametric study. Phys. Med. Biol. 2002; 47(11): 1911-1928.

Connor C.W. and Hynynen K., Patterns of thermal deposition in the skull during transcranial focused ultrasound surgery. IEEE Trans. Biomed. Eng. 2004; 51(10): 1693-1706.

Coussios C.C., Farny C.H., ter Haar G., et al., Role of acoustic cavitation in the delivery and monitoring of cancer treatment by high intensity focused ultrasound (HIFU). Int. J. Hyperther. 2007; 23: 105-120.

Coussios C.C. and Roy R.A. Applications of acoustics and cavitation to non-invasive therapy and drug delivery. Annu. Rev. Fluid Mech. 2008; 40: 395-420.

Cracknell A.P., Ultrasonics, Wykeham Publ. (London) Ltd., 1980.

Curie J. and Curie P., Développement par pression de l'électricité pôlaire dans les cristaux hermièdres à faces inclinées. Compt. Rend. 1880, 91: 294-297.

Curie J. and Curie P., Contractions et dilatations produites par des tensions électriques dans les cristaux hémièdres à faces inclines. Compt. Rend. 1881, 93: 1137-1140.

Daffershofer M. and Hennerici M. Ultrasound in the treatment of ischaemic stroke. Lancet. Neurol. 2003; 2: 283-290.

Damianou C. and Hynynen K., The effect of various physical parameters on the size of necrosed tissue volume during ultrasound surgery. J. Acoust. Soc. Am. 1994; 95(3):

1641-1649.

Damianou C.A., Hynynen K. and Fan X.B., Evaluation of accuracy of a theoretical model for predicting the necrosed tissue volume during focused ultrasound surgery. IEEE T ULTRASON FERR, 1995; 42(2):182-187.

Davies S.C., Hill A.L., Holems R.B., et al., Ultrasound quantitation of respiratory organ motion in the upper abdomen. Br. J. Radiol. 1994; 67: 1096-1112.

Deane L.A. and Clayman R.V. Review of minimally invasive renal therapies: needle-based and extracorporeal. Urology 2006; 68: 26-37.

Demore C.E.M., Design of ultrasound transducer arrays for medical imaging. Thesis (PhD), Queens University, Canada, 2006.

Divkovic G. and Jenne W.J., Egg white phantoms for HIFU. Proc. 4th Int Symp Therapeutic Ultrasound, AIP conference proceedings 2005: 143-146.

Divkovic G.W., Liebler M., Braun K., et al., Thermal properties and change of acoustic parameters in an egg white phantom during heating and coagulation by high intensity focused ultrasound. Ultrasound Med Biol. 2007; 33(6): 981-986.

Duck F.A., Physical properties of tissue: A comprehensive reference book. Academic Press London 1990.

Duncan M., Fundamental characterisation and early functional testing of micromoulded piezocomposites. Thesis (PhD), University of Strathclyde, UK, 2010.

Ebbini E.S., Umemura S.I., Ibbini M., et al., A cylindrical-section ultrasound phased-array applicator for hyperthermia cancer therapy, IEEE Trans Ultrason Ferroelectr Freq Control 1988; 35(5): 561-572.

Ebbini E.S. and Cain C.A., Multiple-focus ultrasound phased-array pattern synthesis: optimal driving-signal distributions for hyperthermia. IEEE T ULTRASON FERR 1989;

36: 540-548.

Ebbini E.S. and Cain C.A., A spherical-section ultrasound phased array applicator for deep localized hyperthermia. IEEE Trans Biomed Eng 1991; 38(7): 634-643.

Fan X. and Hynynen K., The effect of wave reflection and refraction at soft tissue interfaces during ultrasound hyperthermia treatments. J. Acoust. Soc. Am. 1992; 91:1727-1736.

Fan, X.B. and Hynynen, K., The effects of curved tissue layers on the power deposition patterns of therapeutic ultrasound beams. Med Phys 1994, 21(1): 25-34.

Fan X. and Hynynen K., A study of various parameters of spherically curved phased arrays for noninvasive ultrasound surgery. Phys. Med. Biol. 1996; 41: 591-608.

Filonenko E. and Khokhlova V., Effect of acoustic nonlinearity on heating of biological tissue by high-intensity focused ultrasound, Acoust. Phys. 2001; 47: 541-549.

Flynn H.G., Physics of acoustic cavitation in liquids. In: Mason W.P. ed. Physical acoustics: principles and methods. New York: Academic Press, 1964: 57-112.

Frizzell L.A., Linke C.A., Carstensen E.L., et al., Thresholds for focal ultrasonic lesions in rabbit kidney, liver and testicle. IEEE Trans. Biomed. Eng. 1977; BME-24: 393-396.

Fry W.J., Mosberg W.H., Barnard J.W., et al., Production of focal destructive lesions in the central nervous system with ultrasound. J. Neurosurg. 1954; 11:471-478.

Fry W.J., Barnard J.W., Fry F.J., et al., Ultrasonic lesions in the mammalian central nervous system. Science 1955; 122: 517-518.

Fry F.J., Precision high intensity focusing ultrasound machines for surgery. Am. J. Phys. Med. 1958; 37: 152-156.

Furusawa H., Namba K., Thomsen S., et al., Magnetic resonance-guided focused

ultrasound surgery of breast cancer: reliability and effectiveness. J. Am. Coll. Surg. 2006; 203: 54-63.

Ganaha F., Okuno T., Lee C.O., et al., Initial experience with the extracorporeal HIFU knife with 49 patients: Japanese experience. 4th International Symposium on Therapeutic Ultrasound 2005; 7-12.

Garcea G., Lloyd T.D., Aylott C., et al., The emergent role of focal liver ablation techniques in the treatment of primary and secondary liver tumours. Eur. J. Cancer 2003; 39: 2150-2164.

Gelat P., ter Haar G., Saffari N. Modelling of the acoustic field of a multi-element HIFU array scattered by human ribs. Phys. Med. Biol. 2011; 56: 5553-5581.

Gelet A., Chapelon J.Y., Bouvier R., et al., Trans-rectal high intensity focused ultrasound: minimally invasive therapy of localised prostate cancer. J. Endourol. 2000; 14: 519-528.

Gianfelice D., Khiat A., Amara M., et al., MR image guided focused ultrasound ablation of breast cancer: histological assessment of effectiveness – initial experience. Radiology 2003; 227: 849-855.

Gianfelice D., Gupta C., Kucharczyk W., et al., Palliative treatment of painful bone metastases with MR imaging-guided focused ultrasound. Radiology 2008; 249: 355-363.

Gooberman G.L., Ultrasonics: theory and application. Hart, 1969.

Goss S.A., Johnston R.L. and Dunn F., Comprehensive compilation of empirical ultrasonic properties of mammalian tissues II. J. Acoust. Soc. Am. 1980; 68: 93-108.

Gustafsson S.E., Karawacki E., Nazim Khan M., Transient hot-strip method for simultaneously measuring thermal conductivity and thermal diffusivity of solids and fluids. J. Phys. D: Appl. Phys. 1979; 12: 1411-1421.

Hamilton M.F. and Blackstock D.T., Nonlinear Acoustics. Academic Press, 1998.

Hertzberg Y., Volovick A., Medan Y., et al., Ultrasound focusing using magnetic resonance acoustic radiation force imaging: application to ultrasound transcranial therapy. Med. Phys. 2010; 37: 2934-2942.

Hindley J., Gedroyc W.M., Regan L., et al., MRI guidance of focused ultrasound therapy of uterine fibroids: early results.   AJR Am. J. Roentgenol. 2004; 183: 1713-1719.

Holbrook A.B., Santos J.M., Kaye E., et al., Real-time MR thermometry for monitoring HIFU ablations of the liver. Magn. Reson. Med. 2009; 63(2): 365-373.

Holt R.G. and Roy R.A. Measurements of bubble-enhanced heating from focused, mhz-frequency ultrasound in a tissue-mimicking material. Ultrasound Med. Biol. 2001; 27: 1399-1412.

Hou Y., Luo J.W., Marquet F., et al., Performance assessment of HIFU lesion detection by harmonic motion imaging for focused ultrasound (HMIFU): a 3-D finite-element-based framework with experimental validation. Ultrasound Med. Phys. 2011; 37: 2013-2017.

Howard S.M. and Zanelli C.I., HIFU transducer characterization using a robust needle hydrophone. Proc. 6th. Int. Symp. Therapeutics Ultrasound 2007; 8-14.

Huang L. and Liu L., Simultaneous determination of thermal conductivity and thermal diffusivity of food and agricultural materials using a transient plane-source method. J. Food Eng. 2009; 95: 179-185.

Hynynen K., Darkazanli A., Unger E., et al., MRI-guided noninvasive ultrasound surgery. Med. Phys. 1993; 20: 107-115.

Hynynen K. and Sun J. Trans-skull ultrasound therapy: the feasibility of using image-derived skull thickness information to correct the phase distortion. IEEE. T. Ultrason. Ferr. 1999; 46: 752-755.

Hynynen K., Pomeroy O., Smith D.N., et al., MR imaging-guided focused ultrasound

surgery of fibroadenomas in the breast: a feasibility study. Radiology 2001a; 219:176-185.

Hynynen K., McDannold N., Vykhodtseva N., et al., Noninvasive MR imaging-guided focal opening of the blood-brain barrier in rabbits. Radiology 2001b; 220: 640-646.

Hynynen K., Clement G.T., McDannold N., et al., 500-element ultrasound phased array system for noninvasive focal surgery of the brain: a preliminary rabbit study with ex vivo human skull. Magn. Reson. Med. 2004; 52: 100-107.

Hynynen K., McDannold N., Sheikov N.A., et al., Local and reversible blood-brain barrier disruption by noninvasive focused ultrasound at frequencies suitable for trans-skull sonications. Neuroimage 2005; 24: 12-20.

Hynynen K., MRI-guided focused ultrasound treatments. Ultrasonics 2010; 50: 221-229.

Illing RO., Kennedy J.E., Wu F., et al., The safety and feasibility of extracorporeal high-intensity focused ultrasound (HIFU) for the treatment of liver and kidney tumors in a western population. Br. J. cancer 2005; 93: 890-895.

Ivancevich N.M., Haworth K.J., Hitchcock K.E., et al., Determination of optimal ultrasound parameters for ex vivo sonothrombolysis. J. Acoust. Soc. Am. 2010; 128: 2440.

Jacobs M.A., Gultekin D.H., Kim H.S. Comparison between diffusion-weighted imaging, T_2-weighted, and postcontrast T_1-weighted imaging after MR-guided, high intensity, focused ultrasound treatment of uterine leiomyomata: preliminary results. Med. Phys. 2010; 37: 4768-4776;

Jin C., Zhu H., Wang Z., et al., High-intensity focused ultrasound combined with transarterial chemoembolization for unresectable hepatocellular carcinoma: long-term follow-up and clinical analysis. Eur J Radiol. 2011, 80(3): 662-669.

Jin X., Xu Y., Wang L.V., et al., Imaging of high-intensity focused ultrasound-induced

lesions in soft biological tissue using thermoacoustic tomography. Med Phys. 2005; 32(1): 5-11.

Johns L.D., Straub S.J., and Howard S.M., Analysis of effective radiating area, power, intensity, and field characteristics of ultrasound transducers. Arch. Phys. Med. Rehabil. 2007; 88: 124-129.

Jolesz F.A. and McDannold N., Current status and future potential of MRI-guided focused ultrasound focused ultrasound surgery. J. Magn. Reson. Imaging 2008; 27: 391-399.

Jung S.E., Cho S.H., Jang J.H., et al., High-intensity focused ultrasound ablation in hepatic and pancreatic cancer: complications. Abdom. Imaging. 2011; 36(2): 185-195.

Kaneko Y., Maruyama T., Takegami K., et al., Use of a microbubble agent to increase the effects of high intensity focused ultrasound on liver tissue. Eur Radiol. 2005; 15(7): 1415-1420.

Kennedy J.E., ter Haar G., Cranston D. High intensity focused ultrasound: surgery of the future? Br J Radiol 2003, 76: 590-599.

Kennedy J.E., ter Haar G., Wu F., et al., Contrast-enhanced ultrasound assessment of tissue response to high-intensity focused ultrasound. Ultrasound Med Biol. 2004a; 30(6): 851-854.

Kennedy J.E., Wu, F., ter Haar, G., et al., High-intensity focused ultrasound for the treatment of liver tumors. Ultrasonics 2004b; 42: 931-935.

Khokhlova V.A., Souchon R., Tavakkoli J , et al. Numerical modelling of finite2amplitude sound beams : shock formation in the near field of a cw plane piston source[J] . J Acoust Soc Am , 2001 ,110 (1) :95 - 108.

Khokhlova V., Bailey M., Reed J., et al., Effects of nonlinear propagation, cavitation, and boiling in lesion formation by high intensity focused ultrasound in a gel phantom. J.

Acoust. Soc. Am. 2006; 119: 1834–1848.

Khokhlova V., Canney M., Bailey M., et al., Efficient heating and localized millisecond boiling in tissue phantoms by high intensity focused ultrasound due to formation of shocks. International Congress on Acoustics, 2007.

Khokhlova V.A., Acoustic propagation in soft tissue. Cargèse Workshop 2009.

Khokhlova V.A., Bobkova S.M., Gavrilov LR. Focus splitting associated with propagation of focused ultrasound through the rib cage. Acoust Phys+ 2010; 56: 665-674.

Kino G.S., Acoustic waves: devices, imaging and analog signal processing, Prentice-Hall, New Jersey, 1987.

Kinoshita M., McDannold N., Jolesz F.A., et al., Noninvasive localized delivery of herceptin to the mouse brain by MRI-guided focused ultrasound-induced blood-brain barrier disruption. Proc. Natl. Acad. Sci. USA. 2006; 103: 11719-11723.

Kinoshita M. and Hynynen K. Key factors that affect sonoporation efficiency in in vitro settings: the importance of standing wave in sonoporation. Biochem Bioph. Res. Co. 2007; 359: 860-865.

Krafft A.J., Jenne J.W., Maier F., et al., A long arm for ultrasound: a combined robotic focused ultrasound setup for magnetic resonance-guided focused ultrasound surgery. Med. Phys. 2010; 37: 2380-2393.

Kubicar L. and Bohac V., A step-wise method for measuring thermophysical parameters of materials. Meas. Sci. Technol. 2000; 11, 252-258.

Lafon C., Kaczkowski P.J., Vaezy S., et al., Development and characterization of an innovative synthetic tissue-mimicking material for high intensity focused ultrasound (HIFU) exposures. Proc. 2001 IEEE Ultrasonics Symp. 2001: 1295-1298.

Lafon C., Zderic V., Noble M.L., et al., Gel phantom for use in high intensity focused

ultrasound dosimetry. Ultrasound Med Biol. 2005; 31(10): 1383-1389.

Lei Z., Zhu S., Pan N., Determination of sample size for step-wise transient thermal tests. Polym. Test. 2009; 28: 307-314.

Li F., Feng R., Zhang Q., et al., Estimation of HIFU induced lesions in vitro: numerical simulation and experiment. Ultrasonics 2006; 44(suppl 1): 337-40.

Li J.L., Liu X.Z., Zhang D., et al., Influence of ribs on the nonlinear sound field of therapeutic ultrasound. Ultrasound Med Biol 2007; 33: 1413-1420.

Liberman B., Gianfelice D., Inbar Y., et al., Pain palliation in patients with bone metastases using MR-guided focused ultrasound surgery: a multicentre study. Ann. Surg. Oncol. 2009; 16: 140-146.

Linke C.A., Carstensen E.L., FrizzeD L.A., et al., Localised tissue destruction by high intensity focused ultrasound. Arch. Surg. 1973; 107:887-891.

Lin W.L., Liang T.C., Yen J.Y., et al., Optimization of power deposition and a heating strategy for external ultrasound thermal therapy. Med. Phys. 2001; 28(10): 2172-2181.

Lippmann G., Principe de la conservation de l'électricité. Ann. Chim. Phy. 1881, 24: 145-178.

Liu H.L., Shih T.C., Chen W.S., et al., Ex-vivo study of cavitation-enhanced heating by combing low (40 kHz) and high (566 kHz) frequency ultrasound. 2004 IEEE Ultrasonics Symposium: 1477-1480, Vol. 2.

Liu H.L., McDannold N., Hynynen K. Focal beam distortion and treatment planning in abdominal focused ultrasound surgery. Med. Phys. 2005; 32: 1270-1280.

Liu H.L., Chang H., Chen W.S., et al., Feasibility of transrib focused ultrasound thermal ablation for liver tumors using a spherically curved 2D array: A numerical study. Med. Phys. 2007; 34: 3436-3448.

Liu H.L., Hsu C.L., Huang S.M., et., Focal beam distortion and treatment planning for transrib focused ultrasound thermal therapy: A feasibility study using a two-dimensional ultrasound phased array. Med. Phys. 2010a; 37: 848-860.

Liu X., Yin C., Gong X., et al., Theoretical and experimental study on temperature elevation behind ribs caused by weakly focused ultrasound. Ultrasound Med. Biol. 2010b; 36: 1704-1712.

Lizzi F.L., Coleman D.J., Driller J., et al., Experimental ultrasonically induced lesions in the retina, choroid and sclera. Invest. Ophthalmol. 1978; 17: 350.

Lynn J.G., Zwemmer R.L., Chick A.J., et al., A new method for the generation and use of focused ultrasound in experimental biology. J. Gen. Physiol. 1942; 26: 179-193.

Madersbacher S., Schatzl G., Djavan R., et al., Long-term outcome of transrectal high-intensity focused ultrasound therapy for benign prostatic hyperplasia. Eur. Urol. 2000; 37: 687-694.

Marquet F., Pernot M., Aubry J.F., et al., Non-invasive transcranial ultrasound therapy based on a 3D CT scan: protocol validation and in vitro results. Phys Med Biol. 2009; 54(9): 2597-2613.

Marquet F., Aubry J.F., Pernot M., et al. Optimal transcostal high-intensity focused ultrasound with combined real-time 3D movement tracking and correction. Phys. Med. Biol. 2011; 56: 7061-7081.

McDannold N., Vykhodtseva N., Raymond S., et al., MRI-guided targeted blood-brain barrier disruption with focused ultrasound: histological findings in rabbits. Ultrasound Med. Biol. 2005; 31: 1527-1537.

McDannold N., Vykhodtseva N., Hynynen K. Targeted disruption of the blood-brain barrier with focused ultrasound: association with cavitation activity. Phys. Med. Biol. 2006; 51: 793-807.

McDannold N. and Maier S.E. Magnetic resonance acoustic radiation force imaging. Med. Phys. 2008; 35: 3748-3758.

McDannold N., Clement G., Black P.M., et al., Transcranial MRI-guided focused ultrasound surgery of brain tumors: Initial findings in three patients. Neurosurgery 2010; 66: 323-332.

McGough R.J., Kessler M.L., Ebbini E.S., et al., Treatment planning for hyperthermia with ultrasound phased arrays. IEEE Trans. Ultrason. Ferroelect. Freq. Contr. 1996; 43: 1074-1084.

McLaughlan J.R., Roy R.A., Ju H., et al., Ultrasonic enhancement of photoacoustic emissions by nanoparticle-targeted cavitation. Opt Lett. 2010; 35(13): 2127-2129.

McLeod G. Eisma R., Schwab A., et al., An evaluation of Thiel-embalmed cadavers for ultrasound-based regional anaesthesia training and research. Ultrasound 2010; 18: 125-129.

Meairs S. and Alonso A. Ultrasound, microbubbles and the blood-brain barrier. Prog. Biophys. Mol. Bio. 2007; 93: 354-362.

Medel R., Crowley R.W., McKisic M.S., et al., Sonothrombolysis: an emerging modality for the management of stroke. Neurosurgery 2009; 65: 979-993.

Mehta S.S. and Antich P.P., Measurement of shear-wave velocity by ultrasound critical-angle reflectometry (UCR). Ultrasound Med. Biol. 1997; 23: 1123-1126.

Melodelima D., Chapelon J.Y., Theillere Y., et al., Combination of thermal and cavitation effects to generate deep lesions with an endocavitary applicator using a plane transducer: ex vivo studies. Ultrasound Med. Biol. 2004; 30(1): 103-111.

Miller D.L., A review of the ultrasonic bioeffects of microsonation, gas-body activation, and related cavitation-like phenomena. Ultrasound Med. Biol. 1987; 13: 443-470.

Miller D.L. and Thomas R.M., Ultrasound contrast agents nucleate inertial cavitation in vitro. Ultrasound Med Biol. 1995; 21(8): 1059-1065.

Morita Y., Takeuchi S., Hikida H., et al., Decreasing margins to the uterine serosa as a method for increasing the volume of fibroids ablated with magnetic resonance-guided focused ultrasound surgery. Eur. J. Obstet. Gynecol. Reprod. Biol. 2009; 146: 92-95.

Mould J.C., Wojcik G.L., Carcione L.M., et al., Validation of FFT-based algorithm for large-scale modelling of wave propagation in tissue. 1999 IEEE Ultrasonics Symposium Proceedings: 1551-1556.

Mulvana H., The potential of parametric acoustic radiation force generation for elasticity estimation to aid in lower limb prosthesis fitting. Thesis (PhD), University of Strathclyde, UK, 2007.

Nandlall S.D., Arora M., Schiffter H.A., et al., On the applicability of the thermal dose cumulative equivalent minutes metric to the denaturation of bovine serum albumin in a polyacrylamide tissue phantom. Proc. 8th. Int. Symp. Therapeutics Ultrasound 2009: 205-209.

Nell D.M. and Myers M.R., Thermal effects generated by high-intensity focused ultrasound beams at normal incidence to a bone surface. J. Acoust. Soc. Am. 2010; 127(1): 549-559.

Ng K.K., Poon R.T., Chan S.C., et al., High-intensity focused ultrasound for hepatocellular carcinoma: A single-centre experience. Ann Surg. 2011; 253(5): 981-987.

Nicholson P.H.F., Lowet G., Langton C.M., et al., A comparison of time-domain and frequency-domain approaches to ultrasonic velocity measurement in trabecular bone. Phys. Med. Biol. 1996; 41: 2421-2435.

Or S.W., Overview of smart materials technology. 2002. Available from: http://resources.emb.gov.hk/physics/articleIE/smartmaterials/SmartMaterials_e.htm

Pernot M., Tanter M., Fink M. 3D real time motion correction in high intensity focused ultrasound therapy. Ultrasound Med. Biol. 2004; 30: 1239-1249.

Pernot M., Aubry J.F., Tanter M., et al., In vivo transcranial brain surgery with an ultrasonic time reversal mirror. J. Neurosurg. 2007; 106: 1061-1066.

Petropoulos L. and Saunders J.K. MRI and ultrasound guided treatment on a patient. United States Patent Application 20110160566.

Pinton G.F., Numerical methods for nonlinear wave propagation in ultrasound. Thesis (PhD), Duke University, 2007.

Poissonnier L., Chapelon J.Y., Rouviere O., et al., Control of prostate cancer by transrectal HIFU in 227 patients. Eur. Urol. 2007; 51: 381-387.

Prat F., Chapelon J.Y., Fadil F.A.E., et al., Focused liver ablation by cavitation in the rabbit: a potential new method of extracorporeal treatment. Gut. 1994; 35(3): 395-400.

Preston R.C., Output measurements for medical ultrasound, Springer-Verlag, 1991.

Pulkkinen A., Huang Y., Song J., et al., Simulations and measurements of transcranial low-frequency ultrasound therapy: skull base heating and effective area of treatment. Phys. Med. Biol. 2011; 56: 4661-4683.

Quesson B., Merle M., Kohler M.O., et al., A method of MRI guidance of intercostal high intensity focused ultrasound ablation in the liver. Med Phys 2010; 37: 2533-2540.

Rabinovici J., Inbar Y., Revel A., et al., Clinical improvement and shrinkage of uterine fibroids after thermal ablation by magnetic resonance-guided focused ultrasound surgery. Ultrasound Obstet. Gynecol. 2007; 30: 771-777.

Rapoport N., Gao Z., Kennedy A. A multifunctional nanoparticles for combining ultrasonic tumor imaging and targeted chemotherapy. J. Natl. Cancer Inst. 2007; 99:

1095-1106.

Ritchie RW., Leslie T., Philips R., et al., Extracorporeal high intensity focused ultrasound for renal tumors: 3-year follow-up. BJU Int 2010; 106: 1004-1009.

Roberts W.W. Focused ultrasound ablation of renal and prostate cancer: current technology and future directions. Urol. Oncol. 2005; 23: 367-171.

Sanghvi N.T., Fry F.J., Bihrle R., et al., Non-invasive surgery of prostate tissue by high-intensity focused ultrasound. IEEE Trans. Ultrason. Ferroelect. Freq. Contr. 1996; 43: 1099-1110.

Sapareto S.A. and Dewey W.C., Thermal dose determination in cancer therapy. Int J Radiat Oncol Biol Phys. 1984; 10(6):787-800.

Schafer S., Kliner S., Klinghammer L., et al., Influence of ultrasound operating parameters on ultrasound induced thrombolysis in vitro. Ultrasound Med. Biol. 2005; 31: 841-847.

Schmitz A.C., Gianfelice D., Daniel B.L., et al., Image-guided focused ultrasound ablation of breast cancer: current status, challenges, and future directions. Eur. Radiol. 2008; 18:1431-1441.

Selfridge A.R., Approximate material properties in isotropic materials. IEEE T. Son. Ultrason. 1985; 32, 381-394.

Shih T.C., Kou H.S., Liauh C.T., et al., The impact of thermal wave characteristics on thermal dose distribution during thermal therapy: a numerical study. Med Phys. 2005; 32(9): 3029-36.

Shou W.D., Huang X.W., Duan S.M., et al., Acoustic power measurement of high intensity focused ultrasound in medicine based on radiation force. Ultrasonics, 2006; 44: 17-20.

Smith N.B., Temkin J.M., Shapiro F., et al., Thermal effects of focused ultrasound energy on bone tissue. Ultrasound Med. Biol. 2001; 27(10): 1427-1433.

Stewart E.A., Gedroyc W.M., Tempany C.M., et al., Focused ultrasound treatment of uterine fibroid tumors: safety and feasibility of a noninvasive thermoablative technique. Am. J. Obstet. Gynecol. 2003; 189: 48-54.

Stone M.J., Frenkel V., Dromi S., et al., Pulsed-high intensity focused ultrasound enhanced tPA mediated thrombolysis in a novel in vivo clot model, a pilot study. Thromb. Res. 2007; 121: 193-202.

Sun J.Q., Zhang A.L. and Xu L.X., Evaluation of alternate cooling and heating for tumor treatment. Int. J. Heat Mass Transfer 2008; 51(23-24): 5478-5485.

Takegami K., Kaneko Y., Watanabe T., et al., Polyacrylamide gel containing egg white as new model for irradiation experiments using focused ultrasound. Ultrasound Med Biol. 2004; 30(10): 1419-1422.

Tanter M., Thomas J.L., and Fink M. Focusing and steering through absorbing and aberrating layers: application to ultrasonic propagation through the skull. J. Acoust. Soc. Am. 1998; 103: 2403-2410.

Tempany C.M., Stewart E.A., McDannold N., High intensity focused ultrasound surgery of uterine leiomyomas: a feasibility study. Radiology 2003; 226: 897-905.

ter Haar G., Therapeutic ultrasound. Eur J Ultrasound 1999, 9: 3-9.

ter Haar G. and Duck F.A., The safe use of ultrasound in medical diagnosis. British Institute of Radiology, 2000.

ter Haar G., Intervention and therapy. Ultrasound Med. Biol. 2000, S1: 51-54.

ter Haar G., Acoustic surgery. PHYS TODAY 2001, 54: 29-34.

ter Haar G., Therapeutic applications of ultrasound. Prog Biophys Mol Biol 2007a; 93(1-3): 111-129.

ter Haar G. Turning up the power: high intensity focused ultrasound (HIFU) for the treatment of cancer. Ultrasound 2007b; 15: 73-77.

ter Haar G., Dosimetry. Cargèse Workshop 2009.

Thiel W., The preservation of the whole corpse with natural color. Ann Anat. 1992; 174: 185–95.

Thiel W., Supplement to the conservation of an entire cadaver according to W. Thiel. Ann Anat. 2002; 184(3): 267-269.

Thomas J.L. and Fink M.A. Ultrasonic beam focusing through tissue inhomogeneties with a time reversal mirror: application to transskull therapy. IEEE. T. Ultrason. Ferr. 1996; 43: 1122-1129.

Treat L.H., McDannold N., Vykhodtseva N., et al., Targeted delivery of doxorubicin to the rat brain at therapeutic levels using MRI-guided focused ultrasound. Int. J. Cancer 2007; 121: 901-907.

Tye R.P., Kubicar L., Lockmuller N., The development of a standard for contact transient methods of measurement of thermophysical properties. Int. J. Thermophys. 2005; 26(6): 1917-1938.

Uchida T., Baba S., Irie A., et al, Trans-rectal high intensity focused ultrasound in the treatment of localised prostate cancer: a multi centre study. Acta Urol. Jpn. 2005; 51: 651-658.

Unger E.C., Hersh E., Vannan M., et al., Gene delivery using ultrasound contrast agents. Echocardiography 2001; 18(4):355-361.

Vallancien G., Chartier-Kastler E., Bataille N., et al. Focused extracorporeal pyrotherapy.

Eur Urol. 1993; 23 Suppl 1: 48-52.

Vallancien G., Harouni M., Guillonneau B., et al., Ablation of superficial bladder tumors with focused extracorporeal pyrotherapy. Urology 1996; 47: 204-207.

Visioli A.G., Rivens I.H., ter Haar G., et al., Preliminary results of a phase I dose escalation clinical trial using focused ultrasound in the treatment of localised tumours. Eur. J. Ultrasound 1999; 9: 11-18.

Volovick A., Eisma R., Melzer A., Feasibility of using Thiel cadaver model for MRgFUS bone treatments. UK Therapy Ultrasound Group, 2010.

Volovick A., Eisma R., Nabi G., et al., Thiel Cadaver as a Model for MRgFUS. 2nd International Symposium on MR-guided Focused Ultrasound, 2010.

Welsby V.J., Underwater Acoustics: The nonlinear interaction of acoustic waves. Wiley–Interscience, 1970.

Whelan P., Non-surgical ablative treatments for small renal tumours less than 4 cm. Eur. Urol. Suppl. 2006; 5: 471-536.

Williams J.L., Ultrasonic wave propagation in cancellous and cortical bone: Prediction of experimental results by Biot's theory. J. Acoust. Soc. Am. 1990; 91: 1106-1112.

Wojcik G.L., Vaughan D.K., Abboud N., et al., Electromechanical modelling using explicit time-domain finite elements. 1993 IEEE Ultrasonics Symposium Proceedings: 1107-1112.

Wojcik G.L., Vaughan D.K., Murray V., et al., Time-domain modelling of composite arrays for underwater imaging. 1994 IEEE Ultrasonics Symposium Proceedings: 1027-1032.

Wojcik G., Mould J, Lizzi F, et al. , Nonlinear modelling of therapeutic ultrasound. 1995 IEEE Ultrasonics Symposium Proceedings: 1617-1622.

Wojcik G., Fornberg B., Waag R., et al., Pseudospectral methods for large-scale bioacoustic models. 1997 IEEE Ultrasonics Symposium Proceedings: 1501-1506.

Wojcik G.L., Mould J.C., Carcione L.M., Combined transducer and nonlinear tissue propagation simulations. 1999a International mechanical engineering congress and exposition proceedings.

Wojcik G.L., Szabo T., Mould J.C., et al., Nonlinear pulse calculations and data in water and a tissue mimic. 1999b IEEE Ultrasonics Symposium Proceedings: 1521-1526.

Wolny W.W., Application driven industrial development of piezoceramics. J. Eur. Ceram. Soc. 2005; 25: 1971-1976.

Wood R.W. and Loomis A.L., The physical and biological effects of high frequency sound waves of great intensity. Phil. Mag. 1927; 4: 417-436.

Wu F., Wang Z.B., Cao D.Y., et al., A randomised clinical trial of high intensity focused ultrasound ablation for the treatment of patients with localised breast cancer. Br. J. Cancer 2003a; 89:2227-2233.

Wu F., Wang Z.B., Chen W.Z., et al., Preliminary experience using high-intensity focused ultrasound for the treatment of patients with advanced stage renal malignancy. J Urology 2003b; 170: 2237-2240.

Wu F., Wang Z.B., Chen W.Z., et al., Extracorporeal focused ultrasound surgery for treatment of human solid carcinomas: Early Chinese clinical experience. Ultrasound Med. Biol. 2004a; 30: 245-260.

Wu F., Wang Z.B., Chen W.Z., et al., Extracorporeal high intensity focused ultrasound ablation in the treatment of patients with large hepatocellular carcinoma. Ann. Surg. Oncol. 2004b; 11: 1061-1069.

Wu F., Wang Z.B., Chen W.Z., et al., Extracorporeal high intensity focused ultrasound

ablation in the treatment of 1038 patients with solid carcinomas in China: an overview. Ultrason. Sonochem. 2004c; 11:149-154.

Wu F., Wang Z.B., Zhu W., et al., Extracorporeal high intensity focused ultrasound treatment for patients with breast cancer. Breast Cancer Res. Treatment 2005a; 92: 51-60.

Wu F., Wang Z.B., Chen W.Z., et al., Advanced hepatocellular carcinoma: Treatment with high-intensity focused ultrasound ablation combined with transcatheter arterial embolization. Radiology 2005b; 235: 659-667.

Wu, F., Wang, Z.B., Zhu, H., et al., Feasibility of US-guided high intensity focused ultrasound treatment in patients with advanced pancreatic cancer: Initial experience. Radiology 2005c; 236: 1034-1040.

Wu F., Wang Z.B., Cao Y.D., et al., 'Wide local ablation' of localized breast cancer using high intensity focused ultrasound. J. Surg. Oncol. 2007; 96: 130-136.

Wu J.R. and Nyborg W., Emerging therapeutic ultrasound. World Scientific Pub Co Inc, 2006.

Xu Y., Ferroelectric materials and their applications. North-Holland, 1991: 117-121.

Yu F., Zhang X.X., He X.W., Measurement of thermal conductivity and thermal diffusivity for materials on transient hot-plane method. J. Astronaut. Metrol. Meas. 2006; 26(6), 13-21.

Zaher S., Gedroyc W., Lyons D., et al., A novel method to aid in the visualisation and treatment of uterine fibroids with MRgFUS in patients with abdominal scars. Eur. J. Radiol. 2010; 76: 269-273.

Zaitsev A.V., Sanghvi N.T., Ikenberry S., et al., High intensity focused ultrasound (HIFU) treatment of human pancreatic cancer. IEEE Int. Ultrason. Symp. 1996; 1295-1298.

Zhang L., Chen W.Z., Liu Y.J. et al., Feasibility of magnetic resonance imaging-guided

high intensity focused ultrasound therapy for ablating uterine fibroids in patients with bowel lies anterior to uterus. Eur. J. Radiol. 2010; 73: 396-403.

Zhang S.J., Xia R., Lebrun L., et al., Piezoelectric materials for high power, high temperature applications. Mat. Let. 2005; 59: 3471-3475.

Zheng X.L. and Vaezy S. A targeting method based on acoustic backscatter for treatment planning in tissue ablation using focused ultrasound. IEEE Trans. Biomed. Eng. 2010; 57: 71-79.

Zhou Y.F., Zhai L., Simmons R., et al., Measurement of high intensity focused ultrasound fields by a fiber optic probe hydrophone. J. Acoust. Soc. Am. 2006; 120: 676-685.

Zhu H., Zhou K., Zhang L., et al., High intensity focused ultrasound (HIFU) therapy for local treatment of hepatocellular carcinoma: Role of partial rib resection. Eur. J. Radiol. 2009; 72: 160-166.

APPENDIX

Simultaneous Measurement of Thermophysical Properties of Tissue-Mimicking Phantoms for High Intensity Focused Ultrasound (HIFU) Exposures

Jing Gao [a], Jiang You [a], Zhihong Huang [a], Sandy Cochran [b], George Corner [c]

[a] School of Engineering, Physics and Mathematics, University of Dundee, Dundee DD1 4HN, UK

[b] Institute for Medical Science and Technology, University of Dundee, Dundee DD2 1FD, UK

[c] Department of Medical Physics, Ninewells Hospital, Dundee DD1 1SY, UK

Abstract Tissue-mimicking phantoms, including bovine serum albumin (BSA) phantom and egg white phantom, have been developed for, and in laboratory use for real-time visualization of HIFU-induced thermal coagulative necrosis since 2001. However, until now, very few data are available concerning their thermophysical properties. In this paper, a step-wise transient plane source (TPS) method has been used to determine the values of thermal conductivity, thermal diffusivity, and specific heat capacity of egg white phantoms with elevated egg white concentrations (0 to 40 % v/v, by 10 % v/v interval) at room temperature (~20 °C). The measured thermophysical properties were close to previously reported values; the thermal conductivity and thermal diffusivity were linearly proportional to the egg white concentration within the investigation range, while the specific heat capacity decreased as the egg white concentration increased. Taking account of large differences between real experiment and ideal model, data variations within 20 % were accepted.

Keywords Egg white phantom; High intensity focused ultrasound (HIFU); Step-wise transient plane source (TPS) method; Thermo-physical properties; Tissue-mimicking phantom

APPENDIX

Ultrasound Beam Distortion and Pressure Reduction in Transcostal Focused Ultrasound Surgery

Jing Gao [a], Sandy Cochran [b], Zhihong Huang [a]

[a] School of Engineering, Physics & Mathematics, University of Dundee, UK, DD1 4HN

[b] Institute for Medical Science and Technology, University of Dundee, UK, DD2 1FD

Abstract Although it has been long expected to extend the use of image-guided focused ultrasound to transcostal treatment of hepatic, renal and pancreatic tumours, the presence of the rib cage remains a significant hindrance. Major side effects described in the literature include pain, bone injuries and insufficient energy delivered to the target organs. Localized hot spots may also exist at the interfaces between the ribs and soft tissue and in the highly absorptive regions such as the skin and connective tissue. This study investigates the factors affecting the acoustic beam patterns with propagation of focused ultrasound through the rib cage. A realistic rib cage model and a simplified absorbing rib cage model with adequate thickness were used in both experimental and analytical studies. The acoustic pressure at the focus (target) was determined as functions of the dimensions of the rib cage, the position of the intended target relative to the rib cage, and the F-number and driving frequency of the ultrasonic transducer. Results show that the varying distortion of the ultrasound beam behind the rib cage, including splitting, bending and shifting, depends on the details of the influencing factors mentioned above. The beam distortion results in a significant reduction of the pressure/intensity at the target and hence will decrease the ablation efficiency there. This qualitative analysis of focusing ultrasound through the rib cage will provide useful information for optimizing sonication protocols i.e. delivering sufficient ultrasound energy into the tumour site and avoiding potential damage to the normal tissue in clinical applications.

APPENDIX

The Development of Therapeutic Ultrasound with Assistance of Robotic Manipulator

Zhen Qiu [a], Jing Gao [a], Sandy Cochran [b], Zhihong Huang [a], George Corner [c], Chengli Song [b]

[a] School of Engineering, Physics and Mathematics, University of Dundee, Dundee, UK, DD1 4HN

[b] Institute for Medical Science and Technology (IMSaT), University of Dundee, Dundee, UK, DD2 1FD

[c] Medical Physics, Ninewells Hospital, Dundee, UK, DD1 9SY

Abstract High Intensity Focused Ultrasound (HIFU) is finding increasing application and acceptance as a non-invasive approach to the treatment of targeted malignancy. Despite the wealth of research and interest in HIFU, there are still a number of issues that need to be overcome to extend its clinical applications. These relate to the accuracy of placing the HIFU beam, the ability to visualize the target volume, and the understanding of the beam interaction with tissue. In this paper, the output characteristics of a single element HIFU transducer have been investigated with the assistance of a six-axis modified industrial robot. It is shown in the experimental results that clearly defined thermal or mechanical damage can be produced by changing the parameters of the HIFU. The nature and patterns of damage produced by pre-programmed treatment are now being investigated in tissue.

APPENDIX

Characterisation and Application of a Custom-made HIFU Transducer for Robotic Manipulation

GA Corner [a], S Daglish [b], Z Qiu [c], J Gao [c], G Brodie [c], S Cochran [d], A Melzer [d], K Mayne [e], Z Huang [c], T Gourlay [b]

[a] Ninewells Hospital and Medical School, Dundee, UK

[b] Doctoral Training Centre in Medical Devices, University of Strathclyde Glasgow, Glasgow, UK

[c] School of Engineering, Physics and Mathematics, University of Dundee, Dundee, UK.

[d] Institute for Medical Science and Technology, University of Dundee, Dundee, UK.

[e] Peizo-Composite Transducers, Aberdeen, UK

Objectives: Areas requiring further research in high-intensity focused ultrasound (HIFU) therapy include treatment time and prevention of heating of tissue outside the treatment volume. Electronic beamforming is helpful for rapid refocusing but still requires ultrasound propagation through common regions of adjacent tissue, thus initiating problems with excess thermal dosage. Another potentially valuable technique is robot-mounting of the transducer or array. The objective of the present work is thus to characterise and apply a custom-made transducer for both ultrasound and MRI-guided (HIFU), with particular reference to its use as a robot-mounted device.

Materials and Methods: The transducer is a spherically-focused piezocomposite device, diameter 60 mm, focal distance 70 mm. This device was designed principally for robotic manipulation but, for flexibility, it has two confocal elements of equal area. It is very lightweight, with foam backing, a lightweight casing, and remote electrical impedance matching, to allow rapid motion. It is MRI-compatible but it also offers the possibility of ultrasound-guided HIFU. The transducer can be mounted on two robots, a high-precision six-axis industrial machine and a five-axis MRI-compatible machine.

Results: In early exploration, the industrial robot has been used for basic transducer characterisation, demonstrating expected performance, and to explore alternative spatial / temporal regimes for lesion creation. The resultant thermal and mechanical tissue damage has been examined microscopically level using various drive parameters calculated from the known transducer behaviour. The transducer has also been mounted on the MRI-compatible robot to demonstrate feasibility of transfer of treatment regimes from the industrial robot.

Conclusions: The development of a lightweight HIFU transducer for robotic manipulation provides indications that this approach offers very significant flexibility and may potentially allow HIFU

performance demonstrated with other systems to be replicated with simplified electronic systems and array design.

APPENDIX

Exploration of Thermal Issues in Treatment Planning for Focused Ultrasound Surgery

Jing Gao [a], Jiang You [a], Zhihong Huang [a], Sandy Cochran [a], George Corner [b], Christine Demore [a]

[a] Institute for Medical Science & Technology, University of Dundee, Dundee DD2 1FD, UK
[b] Department of Medical Physics, Ninewells Hospital, DD1 1SY, UK

Background: Magnetic resonance image-guided focused ultrasound surgery (MRgFUS) has been recognized as a potentially revolutionary technology for treating diseases that affect a large proportion of the population. To ensure and further improve the effectiveness and safety of MRgFUS in the treatment of large tumours, a fast and accurate treatment planning method is essential.

Purpose: The objective of this paper is to report analysis of the thermal-related issues during focused ultrasound exposure, including the ultrasound power deposition, heat conduction, transient temperature distribution, peak temperature, thermal dose (TD) distribution, necrosed volume, and specific absorption rate (SAR).

Methods: For theoretical predictions, finite element analysis software, PZFlex (Weidlinger Associates Inc., CA, USA) has been used to determine the optimal heating strategy, that is the optimal combination of parameters including frequency, power level, heating duration, cooling intermission between the consecutive heating periods, and beam scanning routine. This was done by means of a comprehensive analysis of the above mentioned thermal issues. PZFlex has also been used to investigate the effect of blood perfusion and blood flow on the thermal ablation induced by focused ultrasonic beams. Corresponding experimental measurements on homogeneous polyacrylamide (PAA) gels containing egg white and a custom flow phantom have been performed to validate the numerical simulations.

Results and Discussion: Good agreement between numerical simulations and experimental measurements on both kinds of phantoms has been achieved, including demonstration that blood perfusion / blood flow contributes to time-delay effects in thermal dose formation. In this paper, various factors are discussed that are necessary to achieve good control over thermal lesions, avoid near field heating, and deliver appropriate treatment within a reasonable period of time. However, the effect of thermally induced attenuation change has not been included.

APPENDIX

Simultaneous Measurements of Thermo-Physical Properties of Egg White Phantoms for HIFU by Using the Step-Wise Transient Plane Source Technique

Jing Gao [a], Jiang You [a], Sandy Cochran [a], George Corner [b], Zhihong Huang [a]

[a] Institute for Medical Science and Technology, University of Dundee, Dundee DD2 1FD, United Kingdom
[b] Department of Medical Physics, Ninewells Hospital, Dundee DD1 1SY, United Kingdom

Abstract Tissue mimicking egg white phantom has been developed and used in laboratory studies for the real-time visualization of high intensity focused ultrasound (HIFU) induced thermal coagulative necrosis since 2004. However, till now, very few data has been published regarding to its thermo-physical properties. In this paper, a step-wise transient plane source (TPS) method was employed to simultaneously and rapidly determine the thermal conductivity, specific heat capacity, and thermal diffusivity values of the egg white phantoms with elevated egg white concentrations (0 ~ 40% v/v, by 10% v/v interval) at room temperature. The measured thermo-physical properties of the egg white phantoms are close to those reported values; the measured thermal conductivity (0.722 ~ 0.759 W/(°C m)) and thermal diffusivity (1.866 x 10^{-7} ~ 2.253 x 10^{-7} m^2/s) are both linearly proportional to the egg white concentration within the investigation range, while the measured specific heat capacity (4230.5 ~ 3271.9 J/(kg °C)) decreases in proportion to the egg white concentration. Taking account of the differences between real experiment and idea model (e.g. the limited sample size, the existence of thermal contact resistance, etc), data variations within 20% are accepted for all measurements.

Keywords Tissue mimicking egg white phantom; High intensity focused ultrasound; Thermo-physical properties; Step-wise transient plane source method

APPENDIX

Focusing through the Rib Cage for MR-guided Transcostal FUS

J. Gao [a], A. Volovick [a, b], Y. Pekelny [b], ZH. Huang [a], S. Cochran [a] and A. Melzer [a]

[a] Institute for Medical Science and Technology, University of Dundee, UK
[b] InSightec Ltd., Tirat Carmel, Israel

Abstract The rib cage presents a significant obstacle in transcostal focused ultrasound surgery (FUS). This paper proposes a geometric solution, based on central projection from the focus to identify transducer elements affected by ribs shadowing which should be switched off. Its effectiveness in phantom experiments and simulations is reported, and ways are discussed to further reduce energy deposition on the ribs while enhancing heating at the focus. A tissue-mimicking phantom with phantom of ribs was sonicated using a 208-element 1.15 MHz bowl transducer and a 1000-element 550 kHz planar matrix transducer (both ExAblate, InSightec, Israel). The temperature evolution was monitored with real-time MRI thermometry (GE, USA). Numerical simulations were performed with FEA software (PZFlex, Weidlinger Associates, USA) to investigate different skin-focus and transducer-rib distances. The temperature rise near the ribs was reduced to 16°C and 4°C for the 1.15 MHz and 550 kHz transducers respectively. With the 1.15 MHz transducer, the focal temperature reached the ablation threshold. These measurements are in good agreement with simulations. The proposed method shows promising results for transcostal FUS. Residual temperature rise on the ribs can be further reduced by active cooling, allowing the higher energies essential for efficient ablation.

APPENDIX

Effect of Focus Splitting on Ultrasound Propagation through the Rib Cage in Focused Ultrasound Surgery

J. Gao [a], S. Cochran [a], Z. Huang [a], L. Shi [a], A. Volovick [a, b]

[a] Institute for Medical Science and Technology, University of Dundee, Dundee, UK

[b] InSightec Ltd., Tirat Carmel, Israel

Abstract The presence of the rib cage is a significant hindrance to the clinical applicability of focused ultrasound surgery for various internal organs, including liver, kidney, and pancreas. The main problems associated with the rib cage are considered to be: the strong reflections that occur at the soft tissue/rib interfaces; the highly attenuating effect of the ribs; and the scattering and diffraction that occur at the ribs boundaries. In this study, a 2D high speed ultrasound scanning system was used to directly measure the acoustic field in the focal plane after propagation of focused ultrasound through an acoustic absorber rib-mimicking material and an epoxy rib-mimicking material. Numerical simulations were also performed with finite element analysis software (PZFlex, Weidlinger Associates, USA) to investigate the changes in the acoustic field with different anatomical configurations. Briefly, due to the defocusing nature of the rib-mimics, the acoustic pressure level at the focus was substantially reduced. This study quantitatively analyzed the effect of focus splitting associated with the ribs to provide reference information for further clinical applications.

Keywords Focused ultrasound surgery; Rib cage; Focus Splitting

APPENDIX

Effects of Blood Flow on High Intensity Focused Ultrasound Ablation

Shaozhen Song, Jing Gao, Zhihong Huang, Dong-Sheng Jeng, Huijie Zhang

School of Engineering, Physics and Mathematics, University of Dundee, Dundee DD1 4HN, Scotland, UK

Abstract With the benefits of high accuracy and non-invasive implementation, high intensity focused ultrasound (HIFU) is a promising medical procedure to heat and destroy pathogenic tissue rapidly. However, the relation between the power emitted by the ultrasound transducer and the energy arriving at the target area is complex, interfered by several factors such as the properties of tissue, obstacles of hard tissues or vascularization. In this study, a finite element model was used to simulate the propagation process of focused ultrasound inside tissue phantom and passing the perfused vascular. Then, the resultant sound pressure distribution provided the heat source for heat transfer process simulation. The simulation results were validated with thermocouple measurements in egg white phantoms. This study demonstrated an efficient methodology for estimating the thermal effects in HIFU hyperthermia therapy, especially in the region with large blood vessel. This study will be useful in minimizing difficulties and risks in HIFU induced hyperthermia treatment and facilitate the extension from laboratory to clinic use.

Keywords High intensity focused ultrasound, ultrasound propagation, blood flow, hyperthermia simulation

APPENDIX

MR-guided Transcostal Focused Ultrasound Therapy: Focusing through the ribcage

Jing Gao [a], Alexander Volovick [a,b], Yuri Pekelny [b], Sandy Cochran [a] and Andreas Melzer [a]

[a] Institute for Medical Science and Technology, University of Dundee, UK
[b] Insightec LTD, Tirat Carmel, Israel

Introduction: Two important technical issues hindering the clinical application of MR-guided transcostal focused ultrasound therapy are: a) the organ motion caused by respiratory movements and b) the presence of the ribcage. Previous transcostal clinical trials revealed skin burns and ribs overheating side effects. The side effects were mainly due to the strong reflections occurred at the soft tissue-rib interfaces and the highly attenuating effects of the ribs. Still, because of the defocusing effects of the ribs, the intensities at the intended focuses (behind the ribs) were substantially reduced, and the treatment efficiency was therefore decreased. In our study, we are trying to reduce the side effects of ribs heating and increase the ultrasound efficacy at the focal point.

Methods: In the work reported here, a preliminary investigation of MR-guided focused ultrasound therapy for treatment of transcostal tumours has been carried out on tissue- and rib-mimicking materials. The experiments were conducted using the ExAblate® Conformal Bone System (Insightec, Israel) and a 1.5 Tesla HDx MRI (GE, USA). Two algorithms for avoiding ribs heating (algorithm 1: placing a light source in the focal point, the elements that were shadowed by the ribs were deactivated and algorithm 2: placing a light source at the infinity below the ribs, the elements that were shadowed by the ribs were deactived) were examined numerically using finite element technique and experimentally for the 1024-element 550kHz phased array transducer. For the same ribs setup we performed sonications for every algorithm and with all ultrasonic elements activated. Sonication parameters were acoustic power 25W and heating duration 60s.

Results: We found that the problem of ribs heating has been greatly relieved by using algorithm 1, as the maximum temperature rise just above the rib surface decreased from 30℃ (all elements activated) to 7℃ (using algorithm 1). No significant change in the heating of focal point was detected between the use of all elements and algorithm 1.

Conclusions: This work has proved in a preliminary way the feasibility of delivering acoustic energy through the ribcage safely and efficiently, by using appropriate control schemes for the phased array transducer. More experimental work in terms of parametric studies and algorithm studies will be performed afterward.
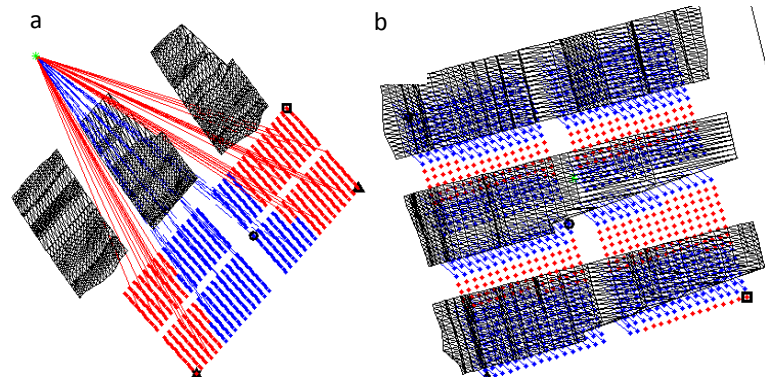
Fig 1: Ultrasonic elements inactivation algorithms (a- algorithm 1 and b- algorithm 2). The blue colored elements will be closed.

APPENDIX

Factors Influencing Treatment Efficacy of Trans-costal Focused Ultrasound Surgery and Possible Solutions

J. Gao [a], A. Volovick [b, c], Y. Pekelny [c], R. Cao [a], G. Nabi [d], Z. Huang [a], S. Cochran [b] and A. Melzer [b]

[a] School of Engineering, Physics and Mathematics, University of Dundee, UK

[b]Institute for Medical Science and Technology, University of Dundee, UK

[c] InSightec Ltd, Tirat Carmel, Israel

[d] Ninewells Hospital, Dundee, UK

Introduction: Two issues hindering the clinical application of image-guided transcostal focused ultrasound surgery are the organ motion caused by cardiac and respiratory movements and the presence of the ribcage. The intervening ribs absorb and reflect the majority of ultrasound energy excited by an acoustic source, resulting in insufficient energy delivered to the target organs of the liver, kidney, and pancreas. Localized hot spots also exist at the interfaces between the ribs and soft tissue and in highly absorptive regions such as the skin. The aim of this study is to clarify the effects of transmitted beam distortion and frequency-dependent rib heating during trans-costal focused ultrasound surgery (FUS), and to propose potential solutions based to reduce the side effects of rib heating and increase ultrasound efficacy.

Methods: Direct measurements of the transmitted beam propagation were performed on a porcine rib cage phantom, an epoxy rib cage phantom and an acoustic absorber rib cage phantom, according to their similarities to the human rib cage. Finite element analysis was used to investigate the rib cage geometry, the position of the target tissue relative to the rib cage, and the geometry and operating frequency of the transducer. Of particular importance, frequency-dependent heating at the target and the intervening ribs were estimated along with experimental verification. The ratio of ultrasonic power density at the target and the ribs, the time-varying spatial distribution of temperature, and the ablated focus of each sonication are regarded as key indicators to determine the optimal frequency. Following that, geometric rib-sparing was evaluated by investigating the operation of 2D matrix arrays to optimize focused beam shape and intensity at target.

Results: Trans-costal FUS is most useful to treat tumours that are small and near the surface of the abdominal organs, such as the liver, kidney and pancreas. However, for targets deep inside these organs, severe attenuation of acoustic energy occurs, suggesting that pure ultrasound thermal ablation with different heating patterns will have limited effects in improving the treatment efficacy. Results also demonstrate that the optimal ultrasound frequency is around 0.8 MHz for the configurations considered, but that it may shift to higher frequencies with changes in the axial and lateral positions of the tumours.

APPENDIX

Conclusions: In our work, we are aiming to reduce the side effects of rib heating and increase the ultrasound efficacy at the focal point in trans-costal treatment. However, potential advanced techniques need to be explored for further enhanced localized heating in the trans-costal FUS study.

APPENDIX

Optimizing Sonication Protocols for Transthoracic Focused Ultrasound Surgery

J Gao [a], A Volovick [b, c], R Cao [a], G Nabi [d], S Cochran [b], A Melzer [b] and Z Huang [a]

[a] School of Engineering, Physics and Mathematics, University of Dundee, Dundee, UK

[b] Institute for Medical Science and Technology, University of Dundee, UK

[c] InSightec Ltd, Tirat Carmel, Israel

[d] Ninewells Hospital, Dundee, UK

Abstract During transthoracic focused ultrasound surgery (TFUS), the intervening ribs absorb and reflect the majority of the ultrasound energy excited by an acoustic source, resulting in pain, bone injuries and insufficient energy delivered to the target organs of liver, kidney, and pancreas. Localized hot spots may also exist at the interfaces between the ribs and soft tissue and in the highly absorptive regions such as the skin and connective tissue. The aims of this study were to clarify the effects of focal beam distortion and frequency-dependent rib heating in TFUS and to propose possible techniques to reduce the side-effects of rib heating and increase ultrasound efficacy. Frequency-dependent heating at the target and the ribs were estimated using finite element analysis (PZFlex, Weidlinger Associates Inc, USA) along with experimental verification on a range of different phantoms. The ratio of ultrasonic power density at the target and the ribs, the time-varying spatial distribution of temperature, and the ablated focus of each sonication were taken as key indicators to determine the optimal operating frequency. Comparison with a patient specific model was also made. TFUS seems to be useful to treat tumours that are small and near the surface of the abdominal organs. For targets deep inside these organs, severe attenuation of energy occurs, suggesting that purely ultrasound thermal ablation with advanced heating patterns will have limited effects in improving the treatment efficacy. Results demonstrate that the optimal ultrasound frequency is around 0.8 MHz for the configurations considered, but this may shift to higher frequencies with changes in the axial and lateral positions of the tumours relative to the ribs. To date, we have elucidated the most important effects and correlated these with idealised anatomical geometry. The changes in frequency and other techniques such as selection of excited element patterns in FUS arrays had some effect. However, more advanced techniques need to be explored for further enhanced localised heating in the TFUS study, if this is to prove fully effective.

APPENDIX

Rapid 3D Human Ribcage and Kidney Modeling For Transcostal HIFU Surgery

Rui Cao [a], Jing Gao [a], Andreas Melzer [b], Ghulam Nabi [c], Zhihong Huang [a]

[a] School of Engineering, Physics and Mathematics, University of Dundee, UK

[b] Institute for Medical Science and Technology, University of Dundee, UK

[c] Department of Urology, Ninewells hospital, Dundee, UK

Abstract A rapid modeling technique for constructing human ribcage and kidney models for high intensity focused ultrasound through the ribcage is proposed and tested. In this study, a 3D model was reconstructed from a patient's CT images provide solutions for the conversion of 3D image data into multi-part volumetric models of kidney and ribcage. The model was imported into PZFlex for simulation of acoustic field analysis. Tissue mimicking materials for the phantom were selected based on the acoustic characterisation result. The effect of the ribcage on HIFU sonication and acoustic pressure distribution were measured in the focal plane. Samples of porcine rib cages were used in experiments for comparison. Results showed that with the presence of the ribcage phantom, the maximum temperature at the focus was reduced to approximately 30-40% and the maximum pressure at the focal zone was halved. Focus splitting with the ribcage in place was demonstrated both in experiments and simulations. The development of this model provides basis for using patient's data for transcostal HIFU research and maximise the efficiency of the HIFU surgery.